Copyright is owned by the Author of the thesis. Permission is given for a copy to be downloaded by an individual for the purpose of research and private study only. The thesis may not be reproduced elsewhere without the permission of the Author.

MASSEY UNIVERSITY
TE KUNENGA KI PŪREHUROA
UNIVERSITY OF NEW ZEALAND

CMOS-compatible Nanostructured Colour Filters for Visible and Near-infrared Regions

by

Ayesha Shaukat

A thesis submitted in total fulfillment for the
degree of Doctor of Philosophy

in the
Department of Mechanical and Electrical Engineering
Massey University

May 2022

Abstract

The human eye is sensitive to electromagnetic radiations with a wavelength range from 380 to 700 nm, and the mechanism of the eye's colour filtering is emulated in colour image sensing devices. Today, image sensing devices can detect colour with distinct hue, brightness, and saturation characteristics. In contrast, spectral imaging filters are developed to perceive electromagnetic radiations, which the human eye cannot perceive. A spectral filter should ideally have narrow bandwidth, high transmission, and independence from incident and polarization angles of incident light. Most importantly, it should be compatible with current power saving CMOS technology for high throughput and cost-effectiveness. Unfortunately, such filters do not exist, and the replacement of pigment-based colour filters is still not realized. Therefore, new designs and materials need to be explored to address the current limitations.

This thesis presents an all-dielectric cascaded multilayered thin film filter for near-infrared (NIR) filtration, which is helpful for spectral imaging applications. With preference to the CMOS compatibility, the material investigation is done through rigorous numerical simulations. Furthermore, the behaviour of the device is observed by varying thicknesses of layered films. This helped in finalizing a design comprised of only eight layers, consisting of amorphous silicon (A-Si) and silicon nitride (Si_3N_4), deposited successively on a glass substrate. Simulation results demonstrate a distinct peak in the NIR region with a transmission efficiency of up to 70 % and full width at half maximum (FWHM) is 77 nm. The results are angle insensitive up to 60° and show polarization insensitivity in Transverse Magnetic (TM) and Transverse Electric (TE) modes.

The design is fabricated and tested at Australian National Fabrication Facility (ANFF). The physical and optical characterization including polarization insensitivity and angle invariance of the thin films are obtained through Spectroscopic Ellipsometry (SE), which shows practical relevance to the theoretical results with angle invariance up to 50°. However, the thicknesses obtained through Scanning Electron Microscopy (SEM) are not helpful, and show discrepancies in the simulated and experimental results. The discrepancy is accredited to the same average atomic mass of the utilized materials.

In addition, rigorous study of CMOS compatible materials led to the usage of tungsten (W) for the design of a three-layered subtractive colour filter based on asymmetric Fabry-Pérot (FP) nanocavity, where titanium oxide (TiO_2) nanocavity is sandwiched between thin tungsten (W) and optically thick aluminium (Al) film. The filter outputs vivid colours with 41.3 % of standard red, green, and blue (sRGB) coverage on the CIE 1931 map. The results show incident angle insensitivity up to 40°. The device is fabricated, but the physical characterization of the sample with the help of an SEM image is not helpful to obtain the thicknesses of the deposited films. However, the

thicknesses obtained with the help of spectroscopic ellipsometry agree with the results obtained from optical characterization.

Declaration of Authorship

I, AYESHA SHAUKAT, declare that this thesis titled, 'CMOS-compatible Nanostructured Colour Filters for Visible and Near-infrared Regions' and the work presented in it are my own. I confirm that:

- The thesis comprises only my original work towards the Doctor of Philosophy except where indicated in the preface;
- due acknowledgement has been made in the text to all other material used; and
- the thesis is fewer than the maximum word limit in length, exclusive of tables, maps, bibliographies and appendices as approved by the Research Higher Degrees Committee.

Signed: _____

Date: _____

Acknowledgements

I want to take the opportunity to extend my heartiest thanks with a deep sense of gratitude and respect to my supervisor Dr. Khalid Muhammad Arif, without whose patience, guidance and help this research would have never been completed. There were moments in this tumultuous journey when things seemed impossible, but it was his insight and knowledge into the subject matter that steered me through this research. Our end-of-meeting discussions and his support in my academic endeavours have made a huge impact on my life.

I am also thankful to my co-supervisor Dr. Frazer Noble, who has always supported this work and has been available to discuss research-related issues.

I would also like to thank Higher Education Commission (HEC) Pakistan for funding my PhD studies at Massey University.

I am thankful to my Amma and all siblings for being moral support throughout this journey.

I am thankful to my husband for all his support, without which I would have stopped this research a long time ago.

Lastly, I take the opportunity to say thank you to my late Dad, who, despite all the odds, gave me wings to fly.

Contents

Abstract i

Declaration of Authorship iii

Acknowledgements iv

List of Figures viii

List of Tables xii

Abbreviations xiii

Symbols xvi

1 Introduction 1
- 1.1 Problem Statement . . . 2
- 1.2 Proposed Solution . . . 3
- 1.3 Thesis Outline . . . 3

2 Background on Imaging Systems 5
- 2.1 Solid-State Image Sensors in Digital Imaging . . . 6
- 2.2 Image Sensing Technologies . . . 7
- 2.3 Colour Vision and Colour Filtering . . . 9
- 2.4 Spectral Imaging . . . 13
- 2.5 Summary . . . 15

3 Literature Review 17
- 3.1 Thin film Colour Filters . . . 18
- 3.2 Plasmons . . . 23
  - 3.2.1 Surface Plasmon Polaritons . . . 23
    - 3.2.1.1 Otto Configuration . . . 24
    - 3.2.1.2 1D Diffraction Grating . . . 25
  - 3.2.2 Localized Surface Plasmonic Resonances . . . 31
    - 3.2.2.1 Nanohole . . . 33
    - 3.2.2.2 Nanohole-Nanodisk Hybrid Colour filters . . . 34
    - 3.2.2.3 Metasurfaces . . . 35
    - 3.2.2.4 Gap Surface Plasmons . . . 38

3.3 Dielectric-based Colour Filter . . . 39
3.4 Liquid Crystal-based Plasmonic Colour Filters . . . 44
3.5 Summary . . . 46
3.6 Knowledge Gap . . . 49

4 Simulation and Fabrication of the Multilayered Thin Films Cascaded Filter 51
4.1 Finite Difference Time Domain Method . . . 52
4.2 Setting-up the Simulation Environment . . . 52
4.3 Proposed Design with its Theoretical Background and Simulated Results 57
4.3.1 Hybrid Etalon . . . 59
4.4 Multilayered thin film Cascaded Filters . . . 65
4.5 Dual Mode Operation . . . 67
4.6 At Various Light Polarization and Incident Angles . . . 67
4.7 Nanofabrication . . . 70
4.7.1 Thin Film Deposition . . . 70
4.7.1.1 Physical Vapour Deposition . . . 70
4.7.2 Chemical Vapour Deposition . . . 71
4.7.2.1 Plasma-Enhanced CVD . . . 73
4.8 Deposition of Hybrid Etalon and Cascaded Multilayered Thin Film Filter 74
4.9 Summary . . . 75

5 Physical and Optical Characterization of Multilayered Thin Films Cascaded Filter 76
5.1 Physical Characterization . . . 77
5.1.1 Dry Etching . . . 77
5.1.2 Electron Microscopy . . . 79
5.2 SEM images for Hybrid Etalon and Cascaded Multilayered Thin Film Filters . . . 82
5.3 Optical Characterization . . . 84
5.3.1 Spectrophotometer . . . 84
5.4 Customization of Spectrofluorometer . . . 86
5.5 Result Analysis of SEM . . . 89
5.6 Spectroscopic Ellipsometry . . . 90
5.7 Summary . . . 94

6 Design of Asymmetric Fabry-Pérot (FP) Nanocavity Incorporating CMOS compatible Tungsten 96
6.1 Design of Asymmetric FP Nanocavity Incorporating CMOS compatible Tungsten . . . 97
6.1.1 Thickness d of TiO_2 . . . 100
6.1.2 Thickness t of W . . . 100
6.2 Resonance Conditions for CMY Subtractive Colours . . . 103
6.3 Commission Internationale del' Elcairage (CIE) 1931 Chromaticity Map . 107
6.3.1 At Various Light Polarization and Incident Angles . . . 111
6.4 Film Deposition . . . 115
6.5 Physical Characterization . . . 116
6.6 Optical Characterization . . . 117

6.7 Summary 117

7 Conclusion and Future Work **118**
7.1 Conclusion 118
7.2 Future Work 120
7.3 Reflection 121

A List of Publications **150**

B FDTD Background **155**
B.1 FDTD Algorithm 157

C Data sheets **159**
C.1 Stepper Motor 159
C.2 Oxford PlasmaLab 100 PECVD 159

D DRC Froms **164**

List of Figures

2.1 Solid-state image sensors in digital imaging . . . 6
2.2 Charge-coupled device versus Complementary metal-oxide semiconductor 8
2.3 Human Eye Anatomy . . . 10
2.4 Human eye's retinal response to white light . . . 11
2.5 Colour filter arrays . . . 11
2.6 Cross-talk in the optical system Image sensor with frontside illumination (FSI) . . . 13
2.7 Multispectral and hyperspectral imaging . . . 14

3.1 Vector diagram for transmission and reflection in FP-cavity . . . 18
3.2 Thin film Filters . . . 21
3.3 Generating Plasmons . . . 26
3.4 1D Diffraction grating-based colour filters . . . 28
3.5 Nanohole and Nanohole-Nanodisk hybrid colour filters: . . . 36
3.6 Metasurfaces . . . 37
3.7 Gap surface plasmons (GSP) . . . 39
3.8 Dielectric-based colour filters . . . 43
3.9 Phases of liquid crystals . . . 45
3.10 Liquid crystal-based colour filters . . . 46
3.11 Key Performance Indicator charts for nanostructure colour filters . . . 48

4.1 Yee cell . . . 53
4.2 Mesh order and overlapping objects . . . 55
4.3 Ansys simulation setup of multilayered cascaded hybrid etalons . . . 56
4.4 Schematic diagram of stack of films . . . 58
4.5 Response of incident light in a 1D ternary photonic crystal with low (Si_3N_4) and high A-Si refractive indices layers. . . . 59
4.6 A simple hybrid filter with two asymmetric etalons joined at a common Si_3N_4. . . . 60
4.7 Refractive index (n,k) values of A-Si from 250 to 2400 nm obtained from Palik. . . . 61
4.8 Refractive index (n,k) values of Si_3N_4 from 250 to 2400 nm. . . . 61
4.9 Transmission and Reflection spectrum of hybrid etalon. . . . 62
4.10 The impact of increase in thickness d_u of upper cavity of hybrid etalon. . 62
4.11 The impact of increase in thickness d_l of upper cavity of hybrid etalon. . . 63
4.12 The impact of film thicknesses on the designed device when $d_u = 2d_l$. . . . 63
4.13 Schematic of hybrid etalon . . . 64
4.14 Schematic of multilayered thin film cascaded filter . . . 66

4.15 Response of cascaded multilayered thin film filters in transmission and reflection mode. . . . 67
4.16 a) The transmission spectrum, when angle of incident is varied from 0° to 70° in TM mode. . . . 68
4.17 a) The transmission spectrum, when angle of incident is varied from 0° to 70° in TE mode. . . . 68
4.18 a) The impact of varying polarization angle(ϕ) of incident light, when it varies from 0° to 90°, where angle of incident is 0° . . . 69
4.19 Chemical vapour deposition (CVD) . . . 72
4.20 Plasma-Enhanced CVD (PECVD) Process . . . 74

5.1 Demonstration of dry reactive ion etching (DRIE) . . . 78
5.2 The electron interaction volume . . . 79
5.3 Schematics of a conventional Scanning Electron Microscope (SEM) and a Transmission Electron Microscope(TEM) . . . 81
5.4 SEM images for a) hybrid etalon and b) cascaded multilayered thin film filters. . . . 83
5.5 Ray Diagram of a typical Spectrophotometer . . . 84
5.6 A typical spectrofluorometer with cell compartment . . . 86
5.7 An L-shaped ray diagram of installed setup inside the cell compartment . 87
5.8 3D illustration of the assembled design of customized spectrofluorometer with a white light source. . . . 88
5.9 a) The in-house built system for customizing spectrofluorometer to spectrophotometer. b) Diced wafer after fabrication. . . . 88
5.10 Theoretical (dotted line) and experimental (solid line) results for reflection spectrum of hybrid etalon with d=40 nm and h= 100 nm. . . . 89
5.11 Theoretical (dotted line) and experimental (solid line) results for transmission spectrum of hybrid etalon with d=40 nm and h= 100 nm. . . . 89
5.12 Theoretical (dotted line) and experimental (solid line) results for multilayered thin films cascaded filter. . . . 90
5.13 The ellipsometric experiment's measurement geometry . . . 91
5.14 Flow chart for ellipsometry data analysis. . . . 92
5.15 Ellipsometric fit to the proposed design extracted at 55°, 65°, and 75°. . . 93
5.16 Transmission spectrum produced with the help of theoritical, experimental and ellipsometry derived data. . . . 94
5.17 Transmission spectrum when incident angle varies from 0° to 60° in TM mode polarization. . . . 95
5.18 Transmission spectrum when incident angle varies from 0° to 60° in TE mode polarization. . . . 95

6.1 Schematic diagram of the proposed design. A 3D perspective of the proposed design of asymmetric Fabry-Pérot cavity with a TiO_2 of thickness d is sandwiched between thin tungsten (W) of thickness t and thick aluminium (Al), grown on a Si substrate. . . . 98
6.2 Refractive index of Titanium oxide (TiO_2) obtained through ellipsometry. 98
6.3 Refractive index of tungsten (W) obtained from Palik's database [208]. . . 99
6.4 Refractive index of aluminium (Al) obtained from Palik's database [208]. . 99
6.5 Contour plot of the visible reflection spectra in accordance to the TiO_2 cavity thickness at t=5 nm. . . . 100

6.6 The reflection dip and absorption peak occur at the resonance wavelength $\lambda_{res} = 625nm$ for cyan colour. . . . 101
6.7 The reflection dip and absorption peak occur at the resonance wavelength $\lambda_{res} = 544nm$ for magenta colour. . . . 102
6.8 The effect of the thickness of W on the reflection spectrum at d = 110 nm. The reflection dip and absorption peak occur at the resonance wavelength $\lambda_{res} = 433nm$ for yellow colour. . . . 102
6.9 Resonance conditions for magenta colour at d=180 nm and t=5 nm. a) Calculated phase shift and the b) corresponding reflection (solid lines) and absorption (dotted line) spectra. . . . 104
6.10 Resonance conditions for magenta colour at d=150 nm and t=5 nm. a) Calculated phase shift and the b) corresponding reflection (solid lines) and absorption (dotted line) spectra. . . . 105
6.11 Resonance conditions for yellow colour at d=110 nm and t=5 nm. a) Calculated phase shift and the b) corresponding reflection (solid lines) and absorption (dotted line) spectra. . . . 106
6.12 CIE 1931 chromaticity map for obtained CMY colour filters. . . . 108
6.13 CIE 1931 chromaticity map for colour filters obtained by varying cavity thickness d from 0 to 500 nm. . . . 109
6.14 Palette of vivid colours obtained by varying nanocavity thickness from 0 to 400 nm. . . . 110
6.15 Reflection spectrum of cyan colour at d=180 nm, when incident angle varies from 0° to 60°. . . . 111
6.16 Reflection spectrum of magenta colour at d=150 nm, when incident angle varies from 0° to 60°. . . . 112
6.17 Reflection spectrum of yellow colour at d=110 nm, when incident angle varies from 0° to 60°. . . . 112
6.18 Reflection spectrum of cyan colour filter (at d=180 nm) when angle of light polarization varied from TM to TE mode in steps of 15°. . . . 113
6.19 Reflection spectrum of magenta (at d=150 nm) colour filter when angle of light polarization varied from TM to TE mode in steps of 15°. . . . 113
6.20 Reflection spectrum of yellow colour filter (at d=110 nm) when angle of light polarization varied from TM to TE mode in steps of 15°. . . . 114
6.21 SEM image for Asymmetric FP nanocavity incorporating CMOS compatible tungsten . . . 116
6.22 Experimental and theoretical results of asymmetric FP nanocavity at d=30 nm . . . 117

A.1 Journal paper: Nanostructured Colour Filters: A Review of Recent Developments. . . . 151
A.2 Poster Presentation: Design of CMOS Compatible Plasmonic Colour Filter for High Selectivity. . . . 152
A.3 Conference Paper: Design of CMOS Compatible Plasmonic Colour Filter for High Selectivity. . . . 153
A.4 All dielectric ultra-thin trans-reflective colour filter. . . . 154

C.1 Oxford PlasmaLab 100 PECVD . . . 163

D.1 RF06 Form . . . 165

D.2 DRC 16 Form1 166
D.3 DRC 16 Form2 167
D.4 DRC 16 Form3 168
D.5 DRC 16 Form4 169
D.6 DRC 16 Form5 170

List of Tables

3.1 thin film colour filters 23
3.2 1D Diffraction-based colour filters 30
3.3 LSPR-based colour filters 40
3.4 All Dielectric-based colour filters 43

5.1 Thicknesses of deposited films extracted with the help of ellipsometry . . 94

6.1 CMY colours due to asymmetric FP nanocavities 107

Abbreviations

AC	**A**lternating **C**urrent
ADC	**A**nalogue to **D**igital **C**onverter
AE	**A**uxillary **E**lectrons
ALCVD	**A**tomic **L**ayer **C**hemical **V**apor **D**eposition
ANFF	**A**ustralian **N**ational **F**abrication **F**acility
AR	**A**nti **R**eflective
APCVD	**A**tmospheric **P**ressure **C**hemical **V**apour **D**eposition
APS	**A**ctive **P**ixel **S**ensor
BSE	**B**ack-**S**cattered **E**lectrons
BSI	**B**ackside **I**llumination
CAGR	**C**ompound **A**nnual **G**rowth **R**ate
CCD	**C**harged **C**oupled **D**evice
CIE	**C**ommission **I**nternationale d**E** l'éclairage
CIS	**C**MOS **I**mage **S**ensor
CL	**C**athod**L**uminance
CMOS	**C**omplementary **M**etal **O**xide **S**emiconductor
CMY	**C**yan **M**agenta **Y**ellow
CVD	Chemical **V**apour **D**eposition
DRIE	**D**ry **R**eactive **I**on **E**tching
EBL	**E**lectron-**B**eam **L**ithography
ED	**E**lectric **D**ipole
ELT	**E**xtraordinary **L**ow **T**ransmission
EOT	**E**xtraordinary **T**ransmission
FDTD	**F**inite **D**ifference **T**ime-**D**omain
FP	**F**abry **P**érot

FIB	**F**ocused **I**on **B**eam
FTIR	**F**ourier **T**ransform **I**nfra **R**ed
FWHM	**F**ull **W**idth at **H**alf **M**aximum
GSR	**G**ap **S**urface **P**lasmon
HSQ	**H**ydrogen hil**S**e **Q**uioxane
IoT	**I**nternet **o**f **T**hings
ITO	**I**ndium **T**itanium **O**xide
IR	**I**nfra **R**ed
LC	**L**iquid **C**rystal
LCD	**L**iquid **C**rystal **D**isplay
LPCVD	**L**ow **P**ressure **C**hemical **V**apor **D**eposition
LSP	**L**ocal **S**urface **P**lasmon
LSPP	**L**ocal **S**urface **P**lasmon **P**olaritons
LSPR	**L**ocal **S**urface **P**lasmon **R**esonance
MD	**M**agnetic **D**ipole
MIMFP	**M**etal-**I**nsulator-**M**etal **F**abry-**P**érot
MOCVD	**M**etal **O**rganic **C**hemical **V**apor **D**eposition
ND	**N**ano **D**isks
NIL	**N**anoimprint **L**ithography
NIR	**N**ear **I**nfra **R**ed
PECVD	**P**lasma-**E**nhanced Chemical Vapour **D**eposition
PML	**P**erfectly **M**atched **L**ayer
PMMA	**P**oly **M**ethyl **M**ethAcrylate
PMT	**P**hoto-**M**ultiplier **T**ube
POC	**P**oint **O**f **C**are
PVD	**P**hysical **V**apour **D**eposition
RIE	**R**eactive **I**on **E**tching
RGB	**R**ed **G**reen **B**lue
SANS	**S**mall **A**ngle**N**eutron **S**cattering
SAXS	**S**mall **A**ngle**X**-ray**S**scattering
SEM	**S**canning **E**lectron **M**icroscope
SERS	**S**urface **E**nhanced **R**aman **S**pectroscopy
SLR	**S**urface **L**attice **R**esonance

SPR	**S**urface **P**lasmon **R**esonance
sRGB	**s**tandarad **R**ed **G**reen **B**lue
TEM	**T**ransmission **E**lectron **M**icroscope
TN	**T**wisted **N**ematic
UNSW	**U**niversity of **N**ew **S**outh **W**ales
UV	**U**ltra **V**iolet
UVCVD	**U**ltra **V**iolet **C**hemical **V**apour Deposition

Symbols

Symbol	Name
A	absorption of spectrum
a	radius
a_m	electric field scattering co-efficient
α	polarizability
α_d	dielectric constant of glass
α_m	dielectric constant of metal
b_m	magnetic field scattering co-efficient
β	propagation constant
Δ	phase difference
d	layer thickness
δ	optical thickness
G	grating diffraction order
H_c	core thickness
L	cavity thickness
ϵ_d	dielectric constant of glass
ϵ_i	imaginary part of refractive index
ϵ_m	dielectric constant of metal
ϵ_r	real part of refractive index
$\epsilon(\omega)$	dielectric function of metal
ϵ_{out}	dielectric constant of the surroundings
k_o	wave propagation in free space
k	extinction co-efficient
k_{SPP}	SPP dispersion
λ	wavelength

N_A	areal density
n	real part of Refractive index
n_{GSP}	refractive index of GSP
n_h	refractive index of core
n_{c1}	refractive index of upper cladding
n_{c2}	refractive index of lower cladding
p	polarizability
ϕ	phase change
T	transmission
R	reflection
r_o	sphere radius
r_p	reflection for p polarization
$\tilde{r}_s$	Fersenel reflection
r_s	reflection for s polarization
t_p	transmission for p polarization
t_s	transmission for s polarization
$\tilde{t}_s$	Fersenel transmission
θ_c	critical angle
θ_i	incident angle
ω	angular frequency
σ	standard deviation
χ	aspect ratio of nanostructures
σ_{ext}	optical extinction
ξ_m	Riccati-Bessel function
ψ	phase shift
ψ_m	Riccati-Bessel function

Chapter 1

Introduction

Recent demand in spectral filtering has led to the development of a wide range of imaging devices, covering ultraviolet (UV) to infrared (IR) regimes of the electromagnetic spectrum, such as thermal imaging sensors [1], medical endoscopes [2], agricultural aerial view imaging cameras [3], security and surveillance cameras, etc.

The optical filters found in commercial image sensors such as laptops, smartphones, tablets etc., emulate the human eye colour acquisition technique (RGB colour filtering) to reconstruct colour images digitally. However, nano-structural spectral filters utilizing different mechanisms such as plasmonics, Mie-scattering and Fabry-Pérot (FP) interferometry are being designed and studied on a nano-scale. They have the potential to outclass decades-old non-recyclable, expensive and environmental unfriendly synthetic and pigment-based filters and can lead the miniaturization race.

In the meantime, researchers have focused on investigating spectral imaging and how it can be used to see what the human eye cannot. It employs multiple bands across the electromagnetic spectrum and collects spectral information from either UV, visible or infrared regions. Spectral imaging is further categorized into multispectral and hyperspectral imaging to facilitate invasive and non-destructive evaluation techniques, such as food inspection, mineral mapping, astronomy, hazardous waste detection, surveillance, thermal imaging, etc. Comparatively, multispectral imaging has fewer spectral bands (typically 3 to 15 bands), and hyperspectral imaging contains as high as 200 narrow bands inside the spectrum, which makes it more like a single continuous band. However, multispectral imaging is preferred over hyperspectral imaging because it provides real-time spectral and spatial information over a discrete spectral range

[4]. Likewise, integrated multispectral filtering methods have the potential to transform imaging and photography by significantly improving colour accuracy over current RGB focal plane arrays while also eliminating the need for external lenses. In fact, the ability to monolithically integrate optical filters on top of an image sensor opens the door to compact, high-speed, and economical spectral cameras, bridging the research-to-industry gap.

There are two image sensing technologies available: 1) charged coupled devices (CCD) and 2) complementary metal-oxide semiconductor (CMOS). In the past, CCDs were mainly used for different image sensing applications like cameras, microscopes and detectors in the field of life sciences, astronomy, and optical microscopy [5]. However, in recent times, CMOS based sensing devices have out-dated their predecessors in performance by demonstrating low power consumption, easy integration, and higher miniaturization capability [6].

1.1 Problem Statement

Ideally, a spectral filter should have narrow bandwidth, high transmission, independence from the incident and polarization angle of the incident light, and have CMOS compatibility along with high throughput and be cost-effective to fabricate. Realistically, a filter with all the qualities mentioned above does not exist, and the replacement of pigment-based colour filters is still not materialized. The main reason is its design's incompatibility to the current power saving CMOS technology and fabrication cost. Hence, what is needed is to explore new designs and materials which can address the aforementioned limitations.

Subsequently, the primary aim of this research is to develop a novel spectral filter design that has the following traits:

- Capability of integration with the available CMOS technology.
- Ease of fabrication in minimal steps to save time and cost.
- Has the minimal impact of environmental changes on its response, such as a change in angle of incident light or direction of polarization of electric field.

1.2 Proposed Solution

In this thesis, a rigorous and powerful tool for modelling nano-scale optical devices called Finite-Difference Time-Domain (FDTD) solutions from Ansys is employed [7].
An extensive simulation study proposes and investigates an economical and highly efficient, lithography-free thin film spectral imaging sensor design for NIR filtration. It comprises only eight thin dielectric films of alternate high and low refractive index amorphous silicon (A-Si) and silicon nitride (Si_3N_4). These dielectric materials are compatible with CMOS technology. The filtered output has transmission efficiency up to 70 %, and the full width at half maximum (FWHM) is 77 nm. Moreover, the angle invariance of 50° is achieved, while the transmission spectrum is not affected by the polarization direction of the incident light. It merely requires deposition of thin film layers using plasma-enhanced chemical vapour deposition (PECVD) for fabrication.
In addition, the design of an asymmetric Fabry-Pérot (FP) nanocavity incorporating CMOS compatible tungsten (W) material is also investigated. It comprises only three layers deposited on the silicon (Si) substrate. Here, the titanium oxide (TiO_2) layer is used as a nanocavity, which is sandwiched between a thick (optically opaque) aluminium (Al) film and a thin W film. The change in cavity thickness sweeps the resonant wavelength across the visible region (400-700 nm) and produces a bright, vivid subtractive colour palette. The reflection spectrum does not change up to 40° incident angle of light, and it is insensitive to a change in light polarization. Moreover, the gamut produced due to this filter covers 41.3 % of the standard red, green, and blue (sRGB) gamut of the CIE 1931 map of chromaticity.

1.3 Thesis Outline

This section contains a brief description of each chapter of this thesis.
Chapter 2 provides a detailed overview of the image sensing devices and their essential parts. The types of image sensing technologies and their advantages and disadvantages are discussed. The process of colour vision and colour filtering is explained with the help of human eye anatomy and its emulated designs implemented in digital devices. Later, spectral imaging and its categories are discussed, and their capabilities are analyzed in terms of their performance as the Vis-NIR filters.

Chapter 3 provides an overview of the research done in the field of the nano-structural colour filter from the last three decades. It includes an explanation and basic working principle of different types of physical mechanisms employed for producing colour filtration, including FP cavity, plasmonics, Mie scattering, etc. The review's outcome is critically evaluated in terms of the key performance indicators such as angle invariance, polarization insensitivity, colour quality and fabrication steps.

Chapter 4 describes the simulation and fabrication process of the cascaded multilayered thin film filters. The chapter begins with an introduction to the Finite-Difference Time-Domain (FDTD) approach, followed by a description of Ansys FDTD Solutions, the software used to simulate all of the optical structures built for this thesis and the simulation environment. The following section provides a detailed theoretical analysis of the chosen design and its constituents. The design is also investigated analytically in its performance, cost, and CMOS compatibility. The second half of the chapter presents the nanofabrication methods and their application for materializing the design. As per design requirements, physical vapour deposition (PVD), chemical vapour deposition (CVD) and plasma-enhanced CVD (PECVD) are discussed.

Chapter 5 provides the physical and optical characterization methods required for obtaining the thicknesses of the deposited films and comparing the experimental and simulated results of the proposed design. For a better understanding of the results, the characterization/fabrication techniques used, such as scanning electron microscope (SEM) and dry reactive ion etching (DRIE), are also explained. Similarly, two approaches to optical characterization have been used, which are explained using diagrams and discussions. The working principles of the used spectrophotometer and spectrofluorometer are also thoroughly explained.

Chapter 6 presents the design of asymmetric FP nanocavity incorporating CMOS compatible tungsten (W), which comprises only three films deposited on silicon (Si) substrate. The produced reflection spectrum produced resulted in a palette of bright, vivid subtractive colours, which covers a large area of standard red, green, and blue (sRGB) gamut of the CIE 1931 map. The design is further evaluated analytically at different light polarization angles and angles of incidence of incident light. The deposition procedure and optical characterization of nanocavity are also provided in this chapter.

Chapter 7 summarises the findings and suggests future research that may be done as a continuation of this work.

Chapter 2

Background on Imaging Systems

This chapter provides the necessary background to understand the main focus of this thesis and its importance.

Section 2.1 gives the information related to solid image sensing devices by briefly demonstrating the working principle of a digital image camera. However, the focus of the discussion is directed towards one of its essential parts, the image sensor.

In an image sensor, the significant parts of concern are its image sensing technology employed to sense the digital image and paint (with the help of colour filters) the image as it is perceived with the naked human eyes. Thus, section 2.2 provides information about image sensing technologies and helps in drawing a comparative analysis between CCD and CMOS technology.

Moreover, the importance of colour filtering in CMOS image sensing devices is explained in section 2.3. It includes defining the capabilities of human eyes to distinguish between different colours followed by different colour filter patterns used in image sensing devices and the challenges to obtaining the " actual" colour.

In the last section 2.4, the detail of spectral imaging, along with information about multispectral and hyperspectral imaging, is also provided. The outcome of this chapter is summarized at the end.

2.1 Solid-State Image Sensors in Digital Imaging

All semiconductor-based electronic devices that detect, transform, and process the information contained in an optical image into an electrical format are known as solid-state image sensors. Personal use, automobile industry [8], object detection systems [9], biomedical imaging [10, 11], and remote sensing [12] are just a few of the numerous industries which employ solid-state image sensors [8]. According to a CMOS image sensor (CIS) market analysis, the market will reach 31.5 billion USD by 2026, growing at a healthy 8.7 % compound annual growth rate (CAGR) between 2021 and 2026 [8].

The acquisition, processing, and storage of a two-dimensional optical image in a

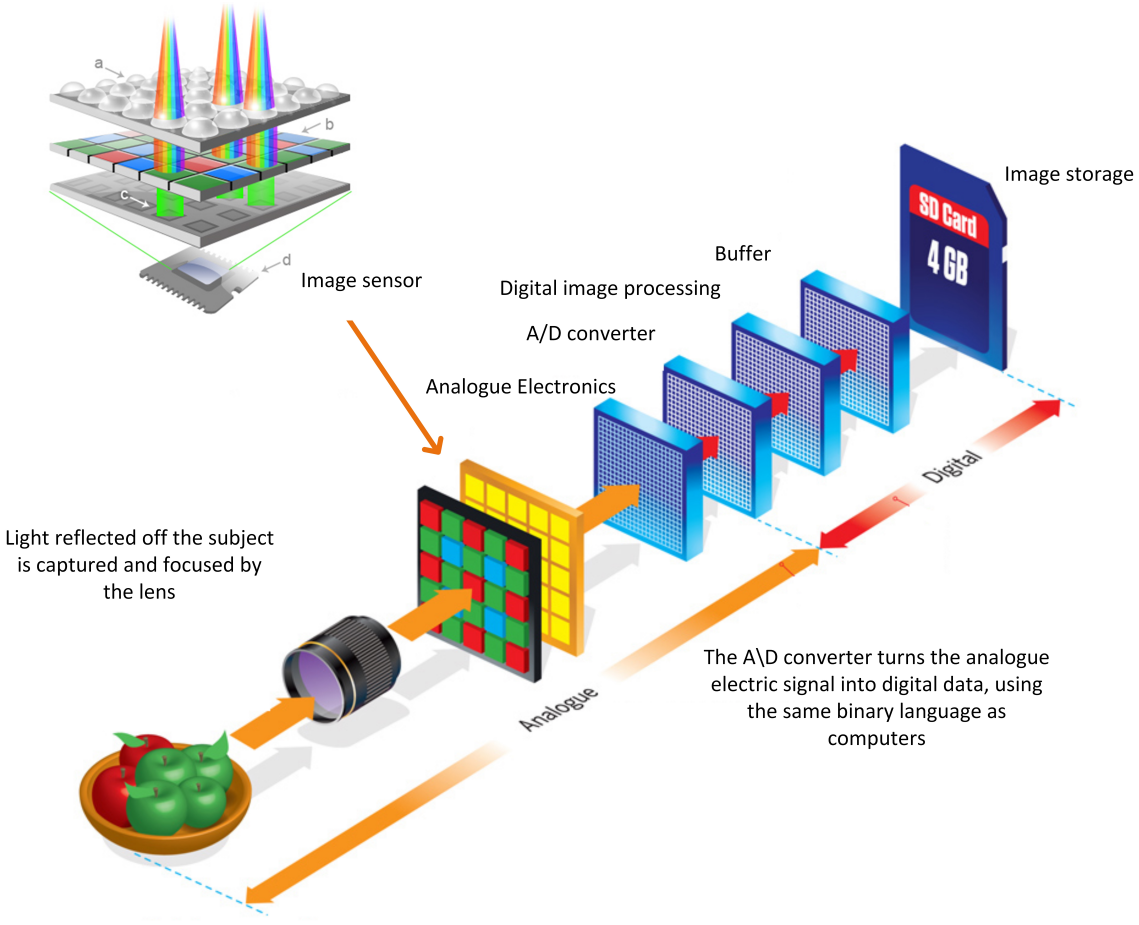

FIGURE 2.1: Figure [13] depicts how a digital camera transforms recorded light into picture pixels. The light reflected from an object or scene is collected by a camera's exterior optics and focused onto the picture sensor. The image sensor absorbs incoming radiation and transforms it into an analogue electrical signal. On-chip circuits then amplify the signal, convert into digital information, and process to conveniently store it in a memory hard drive and later retrieve by the user when needed. The three major components of a typical commercial image sensor are highlighted in the inset [13]: (a) microlens array, (b) colour filter array, and (c) photodetector array

numerical format are typically referred to as digital imaging, as demonstrated in Figure 2.1. Figure 2.1 (inset) shows an image sensor comprised of an array of microlenses, optical filters, photodetectors vertically stacked on top of each other. The incoming electromagnetic energy is spatially collected by each microlens, focused underneath, through the corresponding optical filter, and collected on a single photodetector. An analog-to-digital converter (ADC) converts the charges created at each photodetector into a digital signal, which is processed and stored as a digital reconstruction of a snapshot of the optical image taken at a particular instant in time. The photodetector is the image sensor's light-sensitive component. It transforms incoming electromagnetic radiation into a displacement of electronic charges proportional to the radiation intensity and exposure duration. In digital images, each photosensitive element represents a pixel. A 10 megapixel (MP) camera has an image sensor with around 10 million photodetectors. The higher the spatial resolution of a digital picture, the smaller the pixel size and the higher the density of pixels per area.

The photodetector's capacity to absorb light is directly connected to the semiconductor's bandgap energy. Only photons with greater energy than the bandgap may be absorbed. As a result, the photodetectors of a camera must be made of a semiconducting material that matches the wavelength range being captured. Examples include silicon (Si), which can only detect wavelengths below 1.1 μm due to its bandgap energy. On the other hand, bandgap energy of only 0.18 eV makes indium antimonide (InSb) sensitive to wavelengths below 6.9 μm. As a result, silicon is commonly used for visible imaging, while indium antimonide is best for infrared imaging.

The detecting method of a photodetector (photoelectric, photovoltaic, etc.) may be categorised, and there are various device options for each type of mechanism. Regardless of the physical process that causes electronic charge displacement due to photon energy absorption, most photodetectors are built on a reverse-biased diode-like structure, that is, on an interface between a p-type and an n-type semiconducting material, known as a p-n junction [6].

2.2 Image Sensing Technologies

There are two kinds of image sensing technologies used for digital cameras 1) coupled charge detector (CCD); and 2) complementary metal- oxide semiconductor (CMOS)

active pixel sensors (APSs). The schematic for CCD and CMOS image technologies are shown in Figures 2.2a and 2.2b, respectively. To understand the working principle of CCD and CMOS, a film with 4x4 pixels is considered here.

In CCD image sensing devices, the electrical charge is moved vertically from one pixel

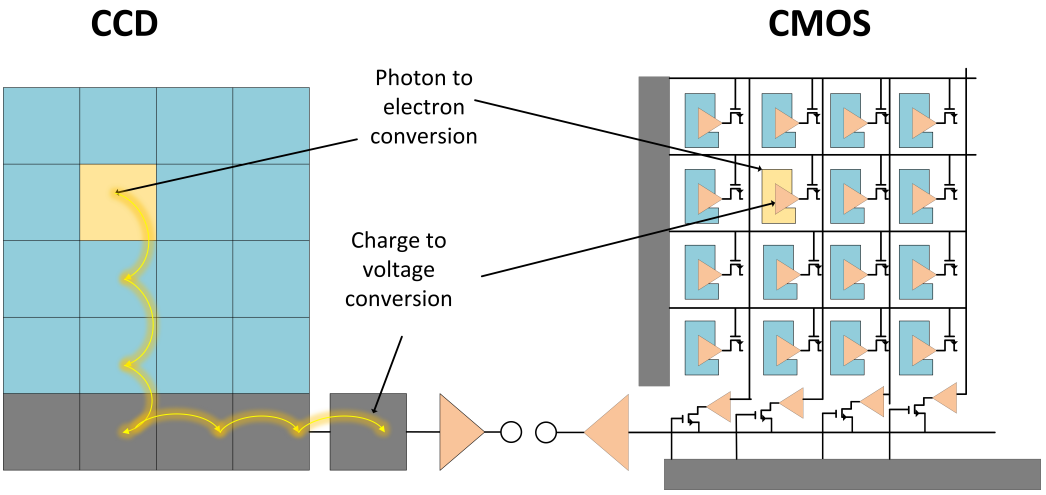

FIGURE 2.2: In a) CCD the electron charge is vertically moved from one pixel to another and is changed from analogue to digital circuit at later stage. b) In CMOS based device the electron to voltage conversion is done at pixel level and it uses separate amplifier for each pixel.

to another to the area where it can be converted to a digital value. The charge movement is accredited to using p-doped metal-oxide-semiconductor (MOS) capacitors. Here at the exposure to electromagnetic waves, the photon is converted to electric charge and is accumulated and transported across the chip and sent to an ADC converter which turns each photosite charge into digital data. In contrast, in a CMOS imaging chip, the electric charges obtained from photosensors are converted to voltage with the help of metal-oxide-semiconductor field-effect transistors (MOSFETs), which further requires additional circuitry on the chip to convert voltage to a digital value [6].

The comparative analysis based on the functionality, results and applications of CCD and CMOS are given as following [6]:

- CMOS image sensors have a higher speed because the signal is processed at the photosite.
- CMOS has low power consumption due to the usage of MOSFET transistors.
- CCD is less susceptible to noise and produces high-quality images comparatively. Hence have been the desired choice for astronomy and digital photography.

- CMOS image sensors are less sensitive as the photosite area is covered with transistors.
- CCDs are manufactured in foundries with specialized equipment, while the manufacturing process of CMOS is more straightforward as it requires conventional fabrication processes.
- CMOS technology allows integration of all the electronic camera functions such as ADC, signal processing and timing control, onto a single chip sensor.

As a result, CMOS APS is now the leading mass-market technology in digital imaging devices such as mobile phones, cameras, tablets, etc. More noise is a reasonable compromise for lower cost and lower power requirements. However, CCD sensors continue to be the preferred choice in applications requiring higher image quality, such as professional digital photography and astronomy [6, 9].

2.3 Colour Vision and Colour Filtering

The colours of the electromagnetic spectrum's visible regime (400 to 700 nm) are subjective to the observer's perception, as colour perception relies on the visual stimulus's responding mechanism. As a result, each of us may perceive the same colour in a slightly different way.

The human eye is sensitive to electromagnetic radiations with a wavelength range from 380 to 700 nm. Figure 2.3 shows a schematic representation of the human eye's anatomy and its colour perception mechanism. The human eye is shown to have a variety of optical components, including the iris, cornea, pupil, vitreous and aqueous humour, a variable-focus lens, and the retina. The reflected electromagnetic energy is focused via the convex cornea and forms an inverted image on the retina's surface with the assistance of other elements. The retina is a multilayered membrane that contains millions of rod and cone photoreceptor cells. The number of rod cells is high, and they are susceptible to light. However, this does not aid in colour discrimination, but it aids several species in detecting prey and predators via their movements and structure.

In contrast, there are three distinct types of cone cells, each set to a distinct wavelength response maximum centred on 430, 535, or 590 nm for blue, green, or red colour

sensitivity. The retinal reaction to RGB is plotted as a function of wavelength in Figure 2.4. As a result, the perceived colour is composed of red, green, and blue (RGB) colours, and the brain input is received via the optical nerve, enabling us to distinguish between millions of different colours [13].

It is a rule of thumb that every commercially available product is created to fulfil

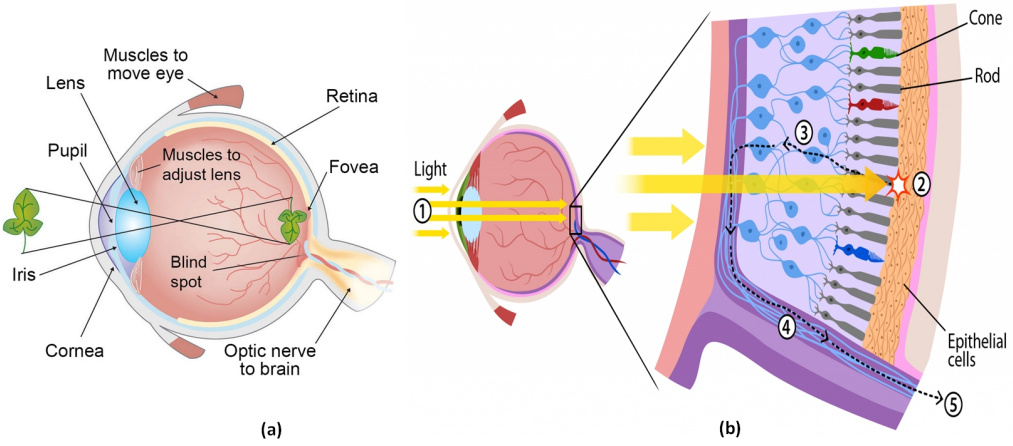

FIGURE 2.3: Illustration of a human eye is a) cross-section and the b) retina's light-absorption mechanism [14]. 1) Light enters the eye through the lens and is focused on the retina at the back of the eye. The retina contains millions of photoreceptors that are classified as rods or cones. 2) When light strikes the discs in the rods and cones' outer segments, photons activate the cells. While rods can be triggered in low light, cones require more illumination. The epithelial cells surrounding them absorb the light that is not absorbed by the rods or cones. 3) The photo-receptors transmit the light they absorb as a signal to brain cells. 4) Information is transmitted between brain cells and eventually reaches the optical nerve. 5) The optical nerve is connected to the brain, which combines the signals to form a complete image

customer requirements. Hence, the fact that commercial image sensors are based on human eye colour acquisition is not surprising. To reconstruct a colour image digitally, image sensors use a pattern of red (R), green (G), and blue (B) filters on top of a photodetector to split incoming light into its major components. This allows an RGB image to be digitally rebuilt from the individual pixels. Transmissive organic or pigmented polymers are commonly used to make colour filters. Each polymer is chemically optimised to pass only a specific colour. However, achieving desirable spectral responsiveness while maintaining the dye's mechanical qualities (such as ease of application, durability, humidity resistance, and other atmospheric stressors). Near-infrared (NIR) cut-off filters are typically required in CMOS image sensors because polymer-based Colour Filter Array (CFA) CFAs and silicon photodetectors are both sound absorbers in that optical range [15].

Most CFAs use an RGB Bayer filter mosaic as their basis. For each 2×2 pixel

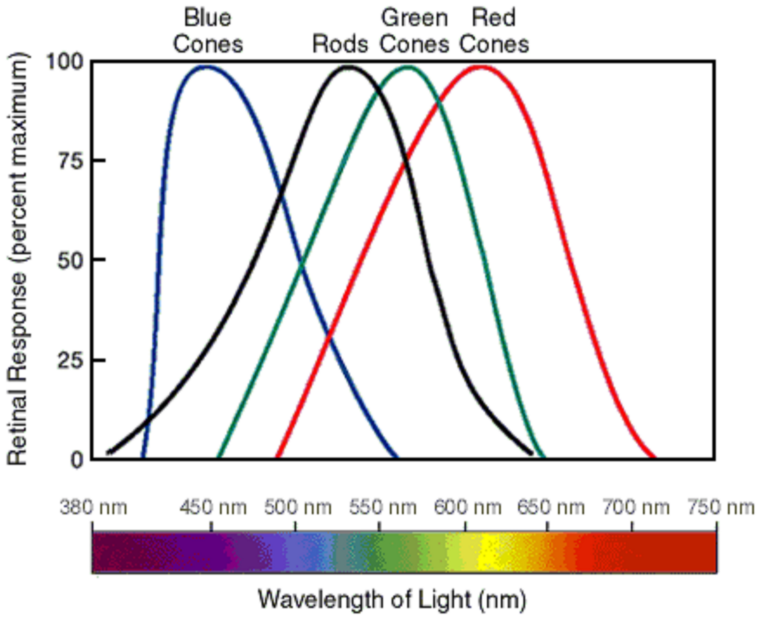

FIGURE 2.4: The human eye's retinal response [14]. Normalized rod and cone absorbance spectra. Although rods cannot discriminate between colours, they allow humans to see in low light. Colour vision, on the other hand, is controlled by cones. To distinguish between colours (or wavebands), the cones in the eye are divided into three categories: blue, green, and red. The stimulus from each cone is merged to provide a variety of colours. Yellow, for example, is created when the green and red cones of the eye are excited, but the blue cones are left unstimulated

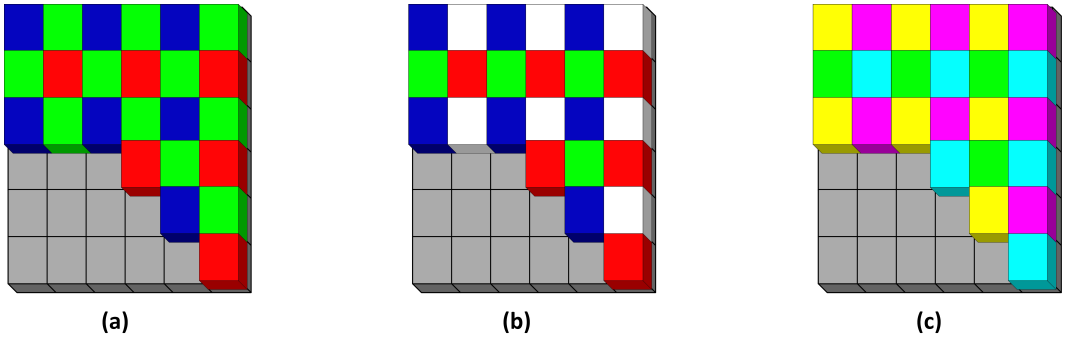

FIGURE 2.5: Colour filter arrays. a) RGB, b) RGBW, and c) CYGM, where R stands for red, G for green, B for blue, W for white, C for cyan, Y for yellow, and M for magenta, are the three most common colours filter array designs used today.

square, one blue filter, one red filter, and two green filters are alternately applied in two orthogonal orientations. This creates the unit cell. The filters are set so that the array's luminance-sensitive element (green) appears at every other array position, guaranteeing that the luminance element dominates in both orthogonal directions. Because the human eye is more sensitive to electromagnetic radiation in the green waveband than red or blue, two times as many green components as red or blue are utilised in the design (see Figure 2.5).

Honda et al. presented an alternate array in 2007 where a "white" pixel, i.e. an optically transparent layer, substituted one of the Bayer array's green pixels. Incorporating the transparent layer increases optical transmission efficiency to nearly 95 %, allowing for more accurate brightness measurements. Using a subtractive CFA, the luminance information may be further enhanced by using the CYGM filter instead of the RGB filter. Because subtractive colours are not actually monochromatic in nature and instead have a high spectrum response, the quality of the colours is degraded.

A Bayer pattern image is the raw output of Bayer-filter cameras. When it comes to video display systems, the pixel is the most basic unit of individual picture processing. In the last section, we learned that each photodetector is equipped with a single, unique colour filter. As a result, because each pixel can only record one of three colours, the data from each pixel cannot correctly identify the red, green, and blue values separately. Using this information, how can the "true" colour of each individual pixel be discovered? If you want a full-colour image, you'll need to digitally interpolate the colour information from the surrounding pixels to assign each pixel a specific hue. For this, different demosaicing methods are implemented [16]. These algorithms rely on the array pattern and are extremely important. High-performing algorithms can even eliminate colour crosstalk caused by filters that aren't optimum, which improves the overall device's colour performance.

The feature size of CMOS technology has increased dramatically during the last few decades. The size of a photodetector has shrunk from over 10 μm to under 2 μm. The expansion of CMOS feature sizes has led to considerable advancements in CIS, allowing for increased spatial resolution and a larger photosensitive area in APS-based digital imaging systems. However, dye-based filtering components suffer from significant optical colour crosstalk at sub-2 μm pixel sizes, resulting in reduced optical efficiency.

The optical crosstalk shown in Figure 2.6 results from a combination of factors: 1) the dye thickness (of the order of few microns), (2) the relatively large distance from the photodiodes beneath them, and (3) the high aspect ratio distance to the active photodiode area, which increases with the scaling in technology [13].

Hence it is implied that due to the dyes' low absorption coefficient, it is not possible to lower the thickness of the organic filters further. It is impossible to move the dyes closer to the photodetectors because they are incompatible with CMOS process materials and, in particular, cannot withstand the high temperatures used in manufacture. In other words, they can only be positioned a few microns above the metal and insulator layers

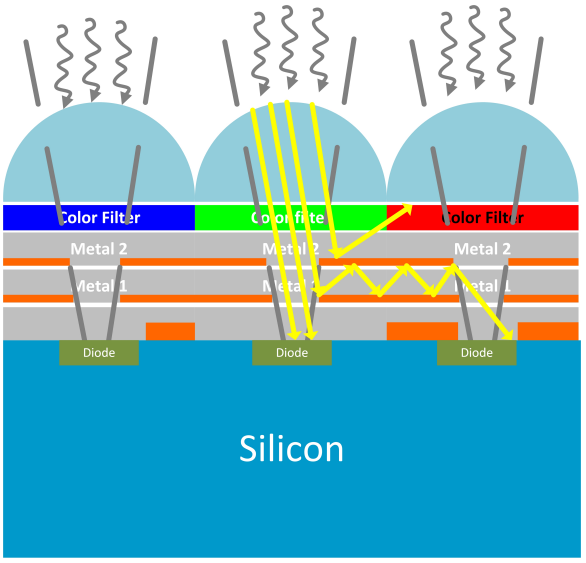

FIGURE 2.6: Cross-talk in the optical system Image sensor with frontside illumination (FSI). The optical cross-talk is caused by a mixture of elements, including i) the dye thickness, (ii) the distance between the filter and the photodiode, and (iii) the high aspect ratio distance between the active photodiode area.

needed to link the pixels. Furthermore, each colour's creation necessitates several process steps, raising the overall production cost and making multispectral devices undesirable. New filter designs that filter light at specific wavelengths in the optical region are highly desirable since they might be more readily integrated into CIS and avoid the above mentioned problems.

2.4 Spectral Imaging

As seen in section 2.3, humans see the visible spectrum (380-700 nm) in three channels: red, green, and blue. However, colour perception is species-dependent. Snakes, for example, can see infrared (IR) radiation [17], while bumblebees can perceive ultraviolet (UV) light [18]. Humans can access many sections of electromagnetic radiation with spectral image sensors. They could allow a bumblebee (UV radiation), a human (visible radiation), and a snake to observe the world simultaneously (IR radiation). The information extracted from an image's spectral data is precious. As a non-destructive and non-invasive assessment tool, spectral imaging has recently gained popularity as a way to identify materials, locate objects, and undertake quality and safety assessments. Its visible range applications include colour measurement, fluorescence imaging [19], skin tone identification [20], chlorophyll concentration mapping [21], blood oxygen saturation

mapping [22], and ocean characterization [23].

Spectral sensors give a digital image with more spectral information than regular colour cameras and have exhibited superior colour fidelity than standard RGB image sensors. A visible spectral sensor registers the colour yellow at its wavelength, not the blue and green contributions. So spectral imaging sensors provide more colour depth.

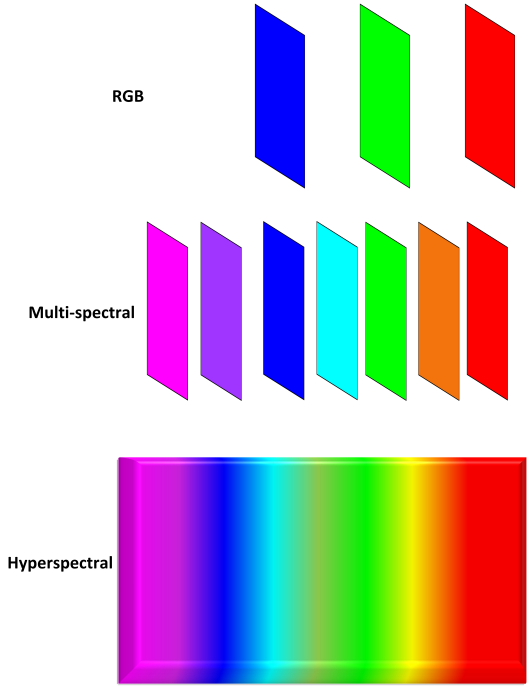

FIGURE 2.7: Spectral Imaging. Multi-spectral refers to a system with a few discrete bands covering a wide range of electromagnetic radiation. Hyperspectral refers to a system with many bands that produce continuous spectra of electromagnetic radiation. Hyperspectral bands typically have an FWHM of 10 nm or less, whereas multispectral bands can have an FWHM of tens to hundreds of nm.

It is possible to classify spectrum imaging techniques as multispectral or hyperspectral depending on the spectral resolution, the number of bands, and width of the acquisition (continuous or discrete) (see Figure 2.7). A hyperspectral sensor produces continuous spectra; a multispectral sensor provides information for discrete ranges of electromagnetic radiation. The precision of these sensors is defined by the spectral resolution of the bands, i.e. the width of each optical filter, which is generally the full-width at half maximum (FWHM). There should be a consideration for the filters' spatial resolution as well. In reality, a vast pixel will produce a reduced image resolution, making it impossible to distinguish between many objects close together. Another problem arises when photo-sensors are used with too small pixels, as the amount of energy captured by each sensor is too low. This results in reduced measurement accuracy due to a reduced

signal-to-noise ratio [24].

Hyperspectral sensors generate enormous amounts of digital data, referred to as the data cube. There are two-dimensional images used to collect information; each image represents a specific wavelength range in the electromagnetic spectrum. These images are taken during scanning procedures. This means that the hyperspectral data cube may demand extraordinarily long data acquisition times and quite large storage capacities, depending on the number of spectral bands. Additionally, processing the data cube can be computationally taxing; however, the whole hyperspectral data cube offers little more information than a small number of multispectral imaging bands (usually 3-8) [25]. Even though some military or scientific research may require hundreds of spectral channels, many more applications require data over a few well-defined wavelengths of interest.

As a result, hyperspectral image sensors capture more spectral information. On the other hand, because they generate vast digital data, even from a single collection, it can be time-consuming, computationally difficult, and resource-intensive to process and store it all. The hyperspectral data cube also contains duplicated information, and many applications only need visual information for a small number of well-defined wavelengths. To make a multispectral imaging system, which is designed to exclusively collect information at various desired wavelengths of light, a more acceptable and cost-effective option, higher spatial resolution, and lower spectral resolution are required [25].

2.5 Summary

It has been concluded from this chapter that CMOS technology is ideal for today's image sensing devices due to its fast, cost-effective, and low power consumption qualities; however, the application of CCD is limited to specific applications where high quality and low noise images are required such as astronomy and digital photography.

On the other hand, decades-old dye/pigment-based colour filters in image sensors are hindering the process of image sensing due to their incompatibility with CMOS technology and have been a reason behind the low colour quality and spatial resolution. This implies that to improve the overall image quality, it is essential to replace the pigment-based colour filter with new designs composed of CMOS compatible materials. The last section explains spectral imaging with multispectral and hyperspectral imaging

comparison, which implies the importance of multispectral imaging due to its vast applications.

Chapter 3

Literature Review

Recent progress in colour filters design, along with the evolution in optical physics [26, 27] and fabrication technology [28–30], has revolutionized colour filtering process and replaced the conventional dry/pigment-based colouring due to its colour tunability, durability, high resolution and environmental friendliness. Today, colour filters are being designed on the nanoscale and play an essential role in the miniaturization of sensors. The idea of nano-structural colour filters is inspired by examples in nature, e.g., butterflies, peacocks, beetles, and Pollia fruits [31]. In structural filters, the working principle is based on the light-matter interaction, where light interacts with the structures designed at the nanoscale and allows colour filtration via light diffraction, scattering, reflection, refraction and transmission at resonant wavelength. This chapter focuses on working principles of nanostructure colour filters and absorbers based on Fabry- Ṕerot (FP) cavity thin film, plasmonics, dielectric and liquid crystal technologies. The significant work in these fields is evaluated in terms of colour quality, spatial resolution, the dependence of output on viewing angle and light polarization, and the required fabrication steps.

3.1 Thin film Colour Filters

Figure 3.1a illustrates that material discontinuity in the propagation path of light from n_1 to n_2 allows light reflection, refraction and transmission and is dependent on the incident angle θ_i.

Mathematically Fresnel equations for transmission (t) and reflection (r) at a material

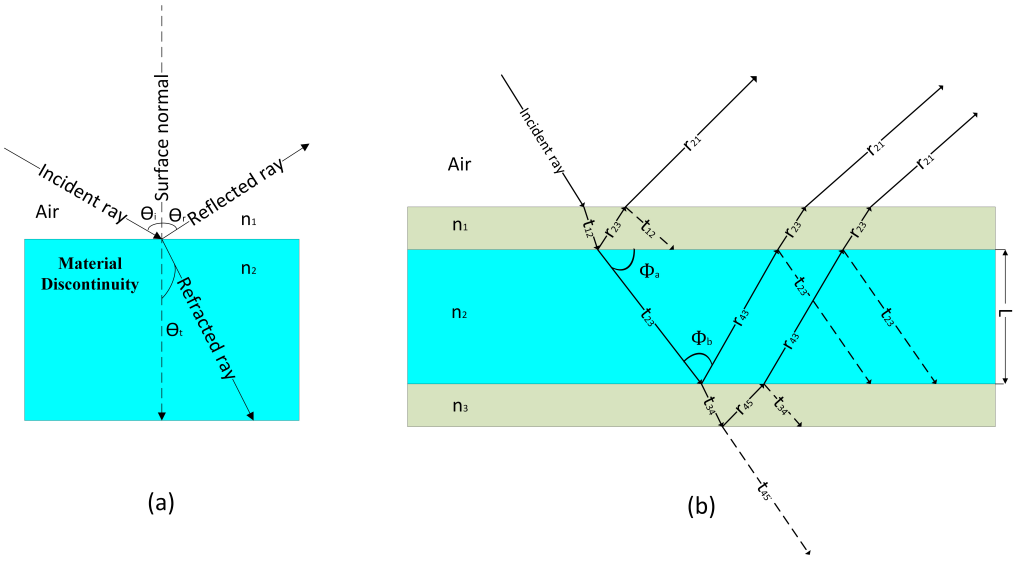

FIGURE 3.1: Vector diagram for transmission and reflection in FP-cavity when light comes across a) Single and b) Multiple material discontinuities.

interface for transverse magnetic (TM) also referred as p, and transverse electric (TE) also referred as s polarization are given as [32–34]

$$t_s = \frac{2n_1 cos\theta_i}{n_1 cos\theta_i + n_2 cos\theta_t}, \tag{3.1}$$

$$t_p = \frac{2n_1 cos\theta_i}{n_2 cos\theta_i + n_1 cos\theta_t}, \tag{3.2}$$

$$r_s = \frac{n_1 cos\theta_i + n_2 cos\theta_t}{n_1 cos\theta_i + n_2 cos\theta_t}, \tag{3.3}$$

$$r_p = \frac{n_2 cos\theta_i - n_1 cos\theta_t}{n_2 cos\theta_i + n_1 cos\theta_t}. \tag{3.4}$$

In another case where light strikes a stack of high refractive index layer n_2 of thickness 'L' sandwiched between two layers with refractive indices n_1 and n_2 as shown in Figure 3.1b. This setup is referred as Fabry-Pérot (FP) -interferometer and allows filtration depending on the FP cavity thickness and refractive index n_1, n_2, and n_3. Here r_{ij} indicates the reflection coefficient at the interface between regions 1 and 2.

At FP resonance, the light gets trapped into the cavity in the form of standing waves and suffers back and forth reflection between two boundaries. In contrast, the rays propagating into the regions adjacent to the films will result in total reflection or transmission from the system. Since these rays travel a different distance within the films, they may have destructive or constructive interference. Hence, in such a case, the intensity of the reflected and refracted waves, along with the material's refractive index, depends on the cavity thickness L and results in filtering out the undesired frequencies. Here $L = m\lambda/2n$, where m is an integer and λ is wavelength in free space.

FP- based filtration is a multifaceted setup for manipulating light propagation. Such as, it allows particular frequency to pass through it or can act as an anti-reflective(AR) coating to reduce light reflection in a design, which may cause destructive interference. There have been numerous applications of FP resonators in different scientific fields such as clinical diagnosis [35, 36], optical communication [37, 38] and sensing [39–41]. The application of metal insulator metal (MIM) based FP interferometers, which exhibit colour filtration by tuning cavity thickness, sandwiched between two metallic mirror layers, is still widely adopted because of its cost-effectiveness, simple design, few fabrication steps [42–46], and easy integration. This section discusses and reviews the remarkable research done to date on FP-based colour filters.

A transmission-based colour filter was designed to filter additive colours (red, green and blue) colours [47]. It comprises silver (Ag) as metallic layers and silicon dioxide (SiO_2) as a dielectric. The devices of different dielectric thicknesses 'h' were fabricated by using plasma-enhanced chemical vapour deposition (PECVD) [30] methodology. The device was further evaluated regarding its polarization sensitivity for oblique incidence, angular dependence, and positional dependence. The minimum reported bandwidth was about 100 nm for green colour, and the colour intensity was 60%. However, for the oblique light incidence, the angular dependence of the relative transmission was up to $\approx 12°$, and the device was insensitive .

Likewise, the centre wavelength showed 10 % variation for the positional dependence. The results were further improved by exploiting titanium oxide (TiO_2) as a dielectric layer with a phase compensating dielectric overlay; it improved the angle insensitivity up to 70°. The design was modified further by using an overlay on the top of the stack [29] (Figure 2a), which allowed dual-mode colour filtering as well as phase compensation. The thickness of TiO_2 cavity allowed the sweeping of resonant frequency across the visible regime. Moreover, the design was flexible enough to change colour saturation

by varying the thickness of one silver (Ag) mirror, with a slight change in transmission efficiency.

Zhangyang Li et al. [48] exhibited the performance of the ultra-thin, large area, lithography free metallic films as super absorbers and additive colour filters. The design comprised of an insulating film (SiO_2) sandwiched between two metallic films (Ag). When used in reflection mode, the design behaved as a super absorber with an optically thick layer at the transmission end, blocking all the transmission through the device. The transmission and absorbance spectra were studied by varying the thickness of the dielectric, i.e. FP cavity. The resonance wavelength swept across the visible and near-infrared regions. The plasmonic effect was not there, and the power absorption was maximum at the metal-dielectric interface. In colour filters, the width of the metallic layers is reduced, and the device performance is examined by changing the width of the layer opposite to the light impinging layer. The leaking mode from the cavity was observed due to the small width of the layer at the transmitting end. Furthermore, the dependence of colour filters on the angle of incidence and modes of polarization of light source is also taken care of. It was observed that the device was more sensitive to -p polarized than s polarized mode and showed angle invariance up to 60°. The results showed 97 % of absorption intensity for super absorbers with a full wave at half maximum (FWHM) of 8 nm. Likewise, transmission colour filters achieved over 60 % transmission across the visible region. Although the examples above have exhibited outstanding results, they suffer from high losses due to the presence of metal [49, 50]. Hence, CMOS-compatible dielectric materials with a high refractive index [51] can help reduce losses and low angle variance.

An ultra-thin design (i.e. less than a quarter wavelength of the light) was proposed where an asymmetric FP cavity implies highly absorbing germanium (Ge) on an optically thick gold (Au) substrate [54]. The obtained results showed maximum absorbance ($1-R$) due to minimum transmission into the substrate.

Since Ge has a high loss and low refractive index than Si, especially its amorphous phase, A-Si is preferred. Moreover, a high refractive index allows angle invariance; therefore, research is inclined towards the material with high refractive indices. An angle robust reflective spectrum filter with high colour purity and ±65 angle invariance is demonstrated by exploiting strong resonance effects in an F-P optical cavity containing lossy media [53] (Figure 3.2c). It acquires improved colour saturation by choosing amorphous silicon (A-Si) with a lower complex dielectric constant. Due to its low

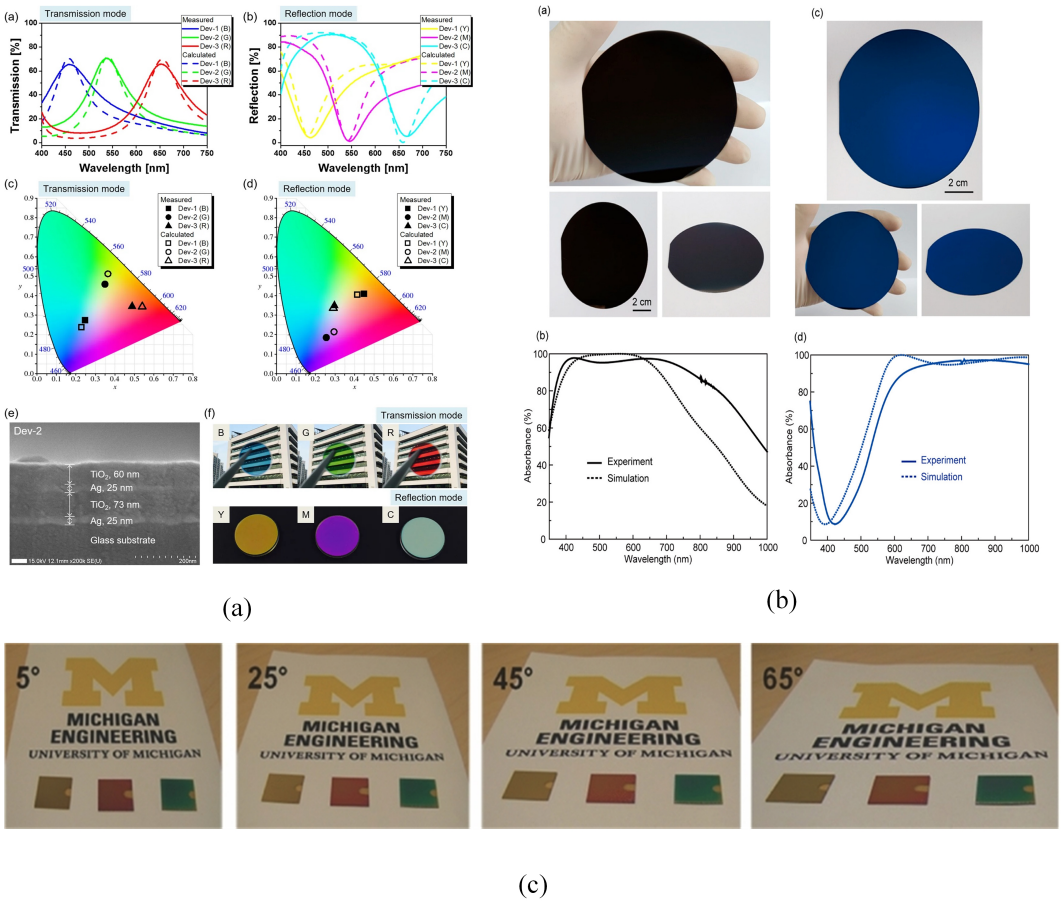

FIGURE 3.2: Thin film Filters: a) Calculated and measured transmission and reflection spectra for the three fabricated devices shows RGB in transmission and CMY in reflection mode. The CIE 1931 further provides the coordinates of the produced results [29]. b) Calculated and measured spectra along with the camera images of broadband visible and near-infrared absorbers implemented with planar nanolayered stacks [52]. c) Demonstration of angle invariance of up to 0 to 65 degrees view angle for fabricated lossy medium-based optical cavity using optical images [53].

absorption and high reflectivity, Ag was used as its metallic layer. The thinner metallic layer at the top (18 nm) allowed the incident light to pass through the structure and simultaneously provided an enhanced reflection from the resonance cavity; however, the bottom Ag is optically thick to block the transmitted light. An organic layer, made from perylene tetracarboxylic bis-benzimidazole (PTCBI), is used to confirm an even thin Ag film that minimizes the scattering.

A CMOS-compatible ultra-thin colour filter containing A-Si deposited on an optically opaque thin aluminium film was demonstrated as a subtractive colour filter [55]. The reported angle insensitivity is up to 60 %. Similarly, a nanoresonator comprising A-Si between two Ag layers showed angle insensitivity up to 65° and a low FWHM value of ≈74 nm in reflection mode [56, 57]. The wide-angle flexible trans transmissive

structural colours with high saturation and efficiency were designed by exploiting multi-cavity resonances [58]. The design consists of alternating Zinc sulphide (ZnS) stack as a dielectric layer and thin Ag films. The high refractive index of the dielectric layer allowed 70° of angle invariance. The design was further coated with a thin ZnS layer as an anti-reflection (AR) from both ends (i.e., top and bottom), enhancing colour efficiency. The device fabrication used simple e- beam evaporation for layer deposition. In order to avoid precise deposition of the thin metallic layer and AR coating, the design was further improved by employing a multilayer semi-transparent structure for suppressing higher order FP-resonances [59]. The FP design is comprised of a transparent ZnS sandwiched between a thin Ag metallic layer and has an overlay at the top for phase compensation. The cavity is designed to have 3rd order FP- resonance, which is helpful to produce good colour quality. However, a 5th order resonance is suppressed by employing a thin lossy material layer (Ge) in the centre of the ZnS cavity. The angle invariance of 60° was reported with an FWHM value as low as 36 nm.

A near-unity absorption as high as 99.58 % is reported by using Cr as a metallic mirror and SiO_2 as a dielectric layer [60]. The results showed ±60°angle tolerance with polarization independence. Similarly, an angle insensitivity of up to 50° was achieved [61] in reflection colour filtering with simple multilayer film deposition. It comprises lossy A-Si material as a dielectric sandwiched by a thin Cr film and a thick Ag layer. The Ag at the bottom of the stack allows the lowest material absorption and highest reflectivity in the visible regime. Likewise, Cr is used as a partial reflection mirror and the absorptive layer. The upper TiO_2 layer is used as an effective anti-reflection layer to chrome film and hence helps in improving the colour saturation. An asymmetric FP-based reflective colour filter was demonstrated [62]. It used lossless metal Cr thin film as an anti-reflection coating on the top of the cavity with a thick Cr layer at the base, which allowed zero transmission. The dielectric consists of lossless material SiO_2. The width of the spacer between Cr and Al allowed colour absorption or reflection across the visible regime. The reported colour sensitivity invariance is up to 60° with spatial resolution up to $50,000dpi$. Although [61, 62] showed promising results, managing thin lossy metals requires special treatment. Recently, a broadband light absorber was constructed with absorption $> 95\%$ in the visible region by utilizing thermally evaporated Ag and Au layer [52] (Figure 3.2b), which exhibit refractive indices much different from the bulk-state value [63]. Nevertheless, the angle invariance was high, i.e. up to 30°.

TABLE 3.1: thin film colour filters

θ_i°	**FWHM (nm)**	**Mode (T/A/R)**	η(%)	**Ref**
12	100	T	60	[47]
70	74	T and R	NG	[29]
60	8	T and A	$A = 97$ & $T = 60$	[48]
60	NG	R	NG	[54]
±65	74	R	NG	[53]
60	70	A	NG	[55]
65	100	R	80	[57]
70	NG	T	70	[58]
60	36	T	54	[59]
±60	NA	A	99.58	[60]
50	NG	R	NG	[61]
60	NG	R	90	[62]
30	NA	A	95	[52]

Note: θ_i°= Angle invariance in degrees NG= Not given, NA= Not Applicable, A= Absorption, T= Transmission, R= Reflection and η=Efficiency.

The summary of all the reported work in terms of FP-cavity performance is given in Table 3.1.

3.2 Plasmons

The emergence of plasmons dates back to the Roman Empire's 4th century AD; the Lycurgus Cup [64] is one of its famous examples. It contains gold nanoparticles on glass and filters different (colours) wavelengths in reflection (green) and transmission (red) mode.

Since its inception, it has been implemented for a number of applications like light emitting diodes (LED) [65], biosensors [66, 67], laser ablation[68] solar cells [69], nanolasers [70], surface enhanced Raman spectroscopy (SERS) [71], waveguides [72] and lithography [73].

3.2.1 Surface Plasmon Polaritons

Surface plasmons [74, 75] is an oscillation of electron density to fixed ions localized at surfaces of metallic structures. The induction of surface charge is accompanied by electromagnetic oscillations and is known as surface plasmon polaritons (SPP), where

polaritons refer to the coupled oscillation of charged particles and electromagnetic waves. Likewise, SPP can travel along with the interface of two materials having negative and positive permittivity materials, i.e., metal-dielectric interface. Moreover, surface plasmon resonance (SPRs) is the resonant excitation of conduction electrons stimulated via incident electromagnetic waves at the metal-dielectric interface.

Figure 3.3 comprises various ways of generating plasmons. As shown in Figure 3.3(a), SPRs generated at the dielectric-metal interface does not have enough momentum (compared to light) to propagate along with the interface. Hence different ways are adopted to fulfil momentum matching needs, such as prisms (Figure 5.7), also called Otto configuration [76] and metallic gratings with period 'Λ', which reflects and transmits light in different diffracting modes as shown in Figure 3.3(c) [77]. Similarly, from Figure 3.3(d), by varying refractive indices and path for incident light and by introducing a waveguide between the periodic grating and substrate, which leads to guided-mode resonances (GMR) shown in Figure 3.3(e). Furthermore, the localization of SPRs is achieved when light impinges on a metallic nanoparticle (MNP) on a dielectric substrate, as shown in Figure 3.3(f). Moreover, the results can be enhanced by increasing the number of MNP in a lattice, which coupling all the localized surface plasmons (LSP) due to each MNP in the lattice. The effect of an increase in the number of MNPs is demonstrated in Figure 3.3(g). Lastly, gap surface plasmon (GSP) can be generated in the dielectric gap between truncated and extended metallic layers as shown in Figure 3.3(h).

In the subsequent sections, the physics behind the different generating mechanisms of plasmons, along with its notable reported works, are discussed in detail.

3.2.1.1 Otto Configuration

Figure 5.7 shows a basic setup of Otto configuration, where a prism consists of a gold layer on one of its rectangular faces. When a coherent lightwave impinges at the glass/metal (usually Au) interface at an angle θ_i, greater than the critical angle $\theta_c(\arcsin(\sqrt{\frac{\epsilon_m}{\epsilon_d}}))$, here ϵ_d and ϵ_m are dielectric constants of glass and metal respectively, and satisfy $\epsilon_d > \epsilon_m$, and the light is totally reflected back into the glass. However, the electric field propagating along x-direction (TM mode) with amplitude decaying exponentially away from the interface represents an evanescent wave. Likewise, the

electric field associated with SPPs is given as [78]

$$E_j = (E_x^j, 0, E_z^j) exp\{i(k_{spp}x - \omega t)\} exp(-\alpha_j |z|), \tag{3.5}$$

where j is 'm' for metal and 'd' for dielectric respectively. It is to be noted that the SPP can only be excited with p polarized light i.e., transverse magnetic (TM) mode propagating along the metal/dielectric interface with amplitude decaying on both sides [78]. The SPP dispersion formula is given as

$$k_{SPP} = \frac{\omega}{c}\sqrt{\frac{\epsilon(\omega)\epsilon_m}{\epsilon(\omega) + \epsilon_m}}, \tag{3.6}$$

where $\epsilon(\omega)$ is the dielectric function of metal and α_j in equation 5.1 is given as

$$\alpha_d = \frac{\omega}{c}\frac{\epsilon_m}{\sqrt{\epsilon(\omega) + \epsilon_m}}, \tag{3.7}$$

and

$$\alpha_m = \frac{\omega}{c}\frac{\epsilon(\omega)}{\sqrt{\epsilon(\omega) + \epsilon_m}}. \tag{3.8}$$

It is to be noted here that equation 5.1 is valid for the negative real part and the negligible imaginary part of $\epsilon(\omega)$. Hence metals like Au, Ag etc., are suitable for generating SPPs in the visible region.

Although the usage of a prism for generating SPRs at the metal-dielectric interface is an obstacle in its miniaturization, it is used in biosensing devices due to its simple design and sensitivity to change in the refractive index caused by adsorption or desorption of molecules on its surface. On the other hand, the grating-based SPRs have been extensively explored due to their miniaturization feasibility and wide range of applications like biosensing [79–82], solar cells [83], spectral imaging [84], and colour filtering [85].

3.2.1.2 1D Diffraction Grating

Grating-based SPRs allow coupling of incident light with SPP through the grating, where resonance conditions are met through diffraction of incident light.

When a plane wave of monochromatic light of wavelength 'λ' incident at an angle θ_i on a periodically corrugated material of periodicity 'Λ', the light is diffracted in

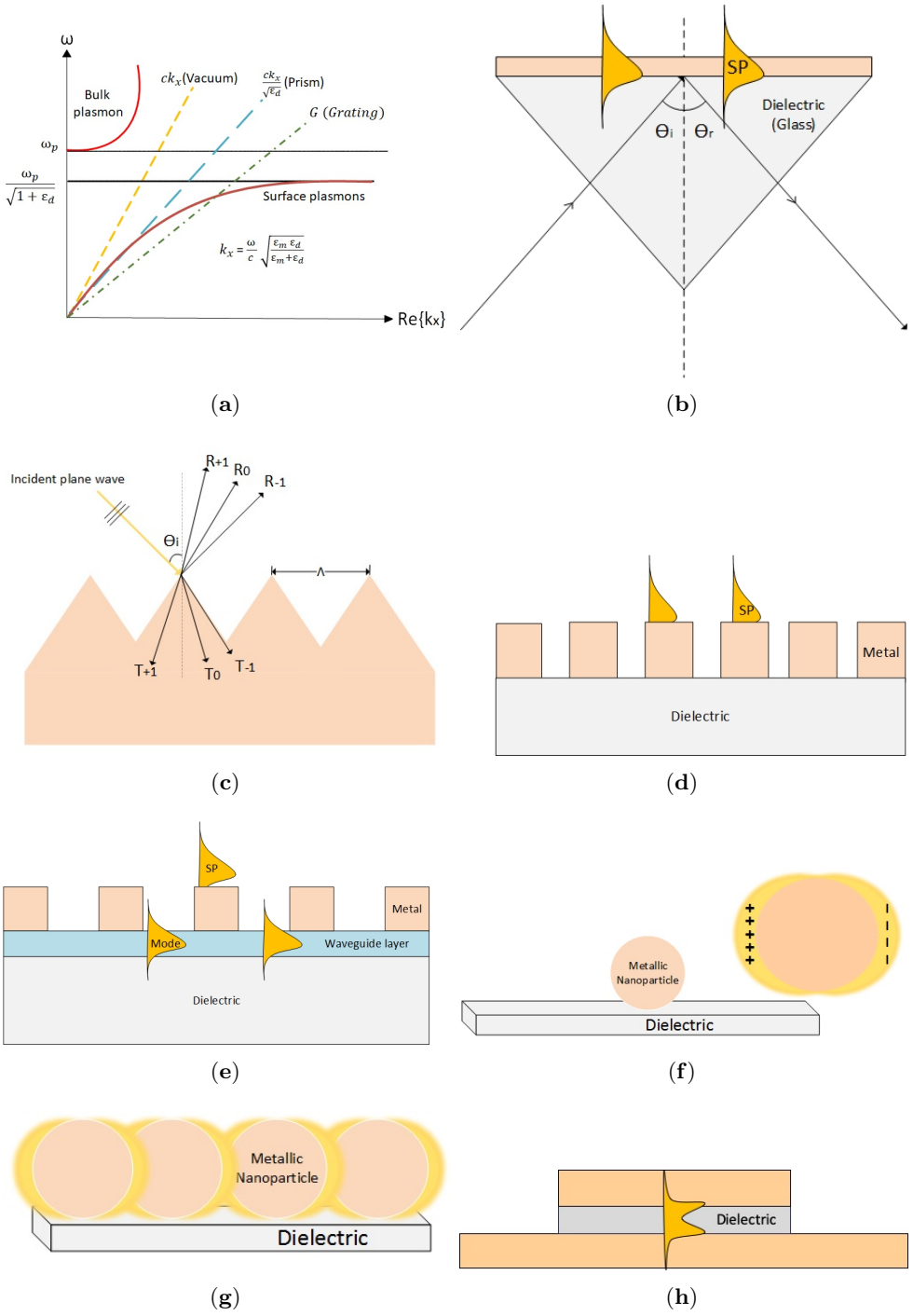

FIGURE 3.3: Generating Plasmons: (a) Dispersion relation of surface plasmons compared to light in vacuum and in the dielectric medium. Incident light on a (b) glass prism with gold sputtered on one of its faces, SPP propagates along the glass and Au interface (c) Diffraction grating with period Λ (d) shows diffraction grating with varying refractive index and path for the incident light (e) represent a GMR-based grating (f) The reaction of single nano-particle on dielectric to the incident light (g) shows the reaction of lattice of nanoparticles to the incident angle and (h) Gap surface plasmon resonance, a special kind of FP- cavity with thin dielectric film and one metallic truncated film on the top.

forward(transmission) and backward (reflection) directions as shown in Figure 3.3(c). The dispersion relation for grating coupling to overcome the momentum mismatch between the energy of impinging photon and of generated electromagnetic waves is given as [78]

$$k_{SPP} = \frac{\omega}{c}\sqrt{\epsilon}_m sin\theta i \pm mG, \tag{3.9}$$

where 'm' is the diffraction order and $G = \frac{2\pi}{\Lambda}$ is the reciprocal lattice with period 'Λ'. The 1D diffraction grating along a waveguide slab (A slab of material between two materials with lower refractive indices from a slab waveguide) is known as waveguide mode coupling. The resonance conditions are met when the angle of the diffracted mode of incident light matches the angle of guided-mode (Figure 3.3(e)). These waves are leaked through the gratings, and the interference of leaky waves and diffracted wave produces a filter response as shown in Figure 3.3(e). Mathematically, the guided mode resonance condition is satisfied by the dispersion relation of the waveguide coupler and is given as [78]

$$m\pi = H_c\sqrt{(k_0^2 * n_h^2) - \beta^2} - \tan^{-1}(\frac{n_h}{n_{c1}})^{2\rho} * \sqrt{\frac{\beta^2 - k_0^2 * n_{c1}^2}{(k_0^2 * n_h^2) - \beta^2}} - \tan^{-1}(\frac{n_h}{n_{c2}})^{2\rho} * \sqrt{\frac{\beta^2 - k_0^2 * n_{c2}^2}{(k_0^2 * n_h^2) - \beta^2}}, \tag{3.10}$$

where H_c is the core thickness, β is the propagation constant; n_h, n_{c1} and n_{c2} are the refractive index of core, upper cladding, and substrate respectively; and k_0 is the wave number in free space. In addition, ρ is 1 and 0 for TM and TE mode respectively. The guided mode resonance occurs at the phase matching between grating vector and the propagation constant for the guided mode of the wave guide [86]. There are numerous reported designs where the waveguide coupler is exploited for colour filtration. Several of the outstanding ones are discussed in this section.

Kaplan et al. demonstrated a highly efficient waveguide coupler based colour filter with tuneable transmission bandwidth [87]. It consists of a waveguide layer (silicon nitride) between the low refractive indices layer, i.e. silicon dioxide. The metallic grating was implemented on the buffer layer at stack (Buffer layer/waveguide layer/substrate) using nanoimprint lithography (NIL) [73, 88]. The impinging source from the grating end was set at TM polarization with zero incidence angle. The wavelength of the transmitted light depended on the grating period, while the bandwidth could be adjusted by changing the buffer thickness, allowing colour tunability by changing the physical dimension of the device. The results were demonstrated experimentally by fabricating

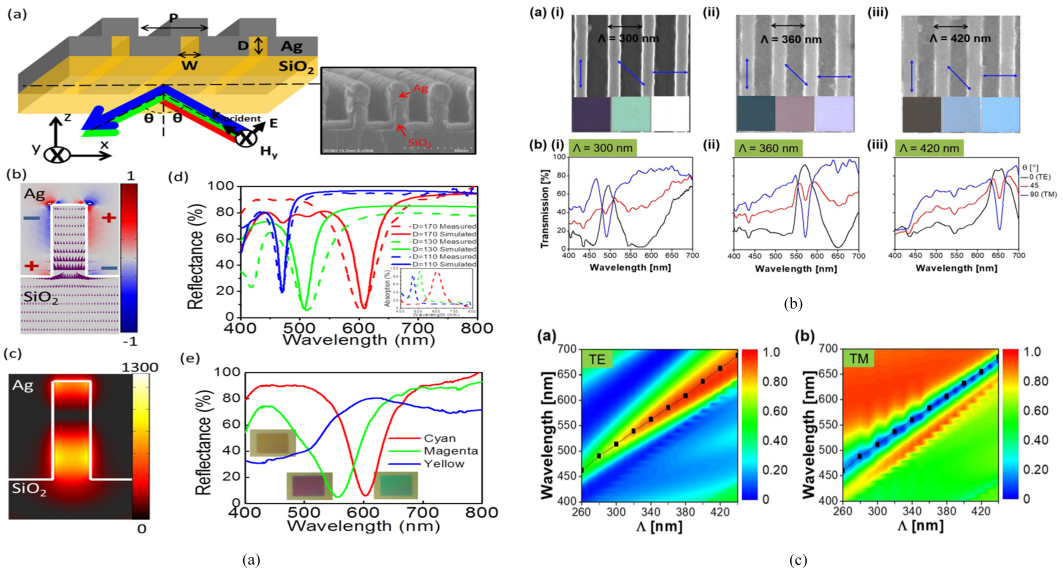

FIGURE 3.4: 1D Diffraction Grating based colour filters a) Schematic of plasmonic nano-cavity along with its fabricated device is illustrated. The charge distribution and Poynting vector direction are shown with a simulator's help. The impact of the dimension of nanoslits on reflection spectra is further shown theoretically and experimentally, and results for CMY colours are produced [89]. b) scanning electron microscope (SEM) images of fabricated multicolour pixel and spectral transmission. Camera image of vivid colour produced shows its dependency on the grating period and angle of polarization c) Verification of GMR for TE and TM mode transmission spectra [90].

two different devices for a red and blue colour generation. The experimental results were in good agreement with the simulated results. Although the obtained results showed transmission as high as 90 %, with tunable bandwidth, it was highly angle sensitive. Likewise, an ultra-thin metal (Al) – dielectric (TiO_2) GMR structure was studied [91]. A thin optical layer of Al was patterned using e-beam lithography as cladding on a dielectric guiding layer. As a result, colour filtration became possible due to the emergence of the incidence wave and the leaky guided modes of the TiO_2 layer. The results showed bandwidth 60,70, and 90 nm for blue, green and red, respectively, with transmission efficiency up to 73 %, but with angle variance. In another study, the impact of core material at a low refractive index contrast was implemented using Al_2O_3 as a core with ultra-thin Al grating [92]. This contrast allowed surface plasmon resonance to occur at Rayleigh anomaly wavelength [93]. The results were promising with 80 % efficiency and $\approx 20nm$ bandwidth. The device was fabricated using a standard lift-off process with the help of laser interference lithography. However, the design exhibited angle sensitivity.

On the other hand, the angle sensitivity of 1D grating was made applicable in a reflection-based dielectric-based guided-mode resonant colour filter design with angle tuneability

for additive colour filters. It showed efficiencies ≈ of 94, 96 and 99 % with green and red colour filters, respectively. The designed silicon nitride grating was patterned on a glass substrate using UV-laser interferometric lithography. The reported pixel bandwidth was 12 nm [94]. Similarly, Koirala et al. [95] presented a highly efficient polarization controlled structural colour filter based on an ultra-thin one-dimensional resonant Al-based grating structure with silicon nitride as a guided layer. It is proposed that a 0.5 duty cycle (required to fulfil the guided mode resonant condition) allows transmission in TE and TM mode. As per our best knowledge, this is the first time such a setup was used in transmission mode. The same design was exploited by replacing Al gratings with hydrogenated amorphous silicon (H:A-Si) grating in an all dielectric polarization-tailored trans-reflective structural multicolour pixels design [90]. It showed 95 and 90 % transmission efficiency in TM and TE mode, respectively (Figure 4a and 4c). However, angle tolerance improved to 35°. Similar results were achieved by Al sub-wavelength grating with slits filled with dielectric (SiO_2) allowing enhanced EOT for TE mode [96] by exploiting GMR. Hence the SPRs are responsible for EOT in TM mode. The gratings are further covered with a thin overlay of SiO_2, which improved the device operation. Although colour intensity improved in TE, the increase in bandwidth resulted in low colour saturation. Likewise, the device remained angle sensitive.

A highly transmissive plasmonic subtractive colour filter was proposed in [97]. The desirable results were achieved by exploiting the counter-intuitive phenomenon of extraordinary low transmission (ELT) [98]. An optically thin silver (Ag) film patterned in 1D nanogratings was fabricated to achieve subtractive colour. The transmission valley, with 60 to 70 % efficiency, can be tuned across the visible regime by varying the periodicity of the silver gratings. Besides, this design is capable of filtering the subtractive colour with only a few nanoslits, close to the optical diffraction limit ($\lambda/2$, i.e. 200 to 350 nm).

The dependence of GMR based colour filters on light incidence angle variance and direction of polarization has been a matter of concern [99, 100]. Symmetric two-dimensional grating pattern, 2D version of [87], resolved the issues faced in the aforementioned examples. A polarization-independent bandpass filtering was made possible by the GMR between orthogonally diffractive waves and both TE and TM mode [101]. The change in grating peak resulted in a change in center frequency. The reported design exhibited arrow bandwidth of 13, 14 and 17 nm for blue, green and red colours. However, the efficiency remains constant at 85 %. Moreover, the

fabrication steps included e-beam lithography and dry etching. Likewise, the 2D version of [102] generated a broad polarization controlled colour gamut [103]. Ryan Wuo et al. [89] numerically and experimentally demonstrated localized resonance in Silver (Ag) nanoslits by light funnelling (Figure 4a). Here the silver was conformally deposited on the silica grating, as shown. The grating design with a certain period, width and periodicity concentrated incident light into silica nano-grooves, which behave more like nanoresonators. When the light impinges on the device from the silica end, it induces charge polarization inside the grooves. This charge induction changes incident light's E-field, trapping it in the grooves. The resonant wavelength is tuned across the visible regime by changing the width and depth of metal-insulator-metal FP (MIMFP) nano-grooves.

The 1D diffraction-based colour filters allow an undesirable angle sensitivity to the results. Although fabrication of angle nanoresonators requires more fabrication steps and advanced technology, it happens to be a better option in terms of its performance, like polarization angle and angle insensitivity.

Recently, diffraction gratings have been studied as wave retarders [102] - capable of changing the direction of light polarization. A 4-fold colour filtering was achieved in the visible region by utilizing a plasmonic phase retarder (PPR). It consists of a periodic array of silver nanowires, which supports LSPRs that can induce substantial phase shift for TM or TE mode [104]. Hence, with the help of a colourless analyzing polarizer, it produced four different colours from one fabricated device.

The summary of the discussed examples is given in Table 3.2, where all the designs are

TABLE 3.2: 1D Diffraction-based colour filters

θ_i°	**FWHM (nm)**	η (%)	**Ref**
0	30	90	[87]
0	60	73	[91]
0	20	80	[92]
0	12	99	[94]
0	NG	90	[102]
35	NG	95	[90]
0	100	70	[96]
0	17	85	[101]
±80	NG	NG	[89]

Note: θ_i°= Angle invariance in degrees NG= Not given and η=Efficiency.

polarization dependable.

3.2.2 Localized Surface Plasmonic Resonances

Localized surface plasmon resonance (LSPR) involves the combined oscillation of Metallic NanoParticle (MNP) and the associated oscillation of the electromagnetic field (Figure 3.3(f)). The resonance wavelength ($\lambda_{(res)}$) depends on the shape, size, composition of MNPs, and the local optical environment of the particles. It generally occurs in the visible to near IR spectra for NP of noble metals (Au,Cu,Ag). Mathematically, dependence of extinction optical (σ_{ext}) on shape, density, dimensions and surrounding environment of a spherical MNP is given as [105]

$$\sigma_{ext}(\lambda) = \frac{24\pi^2 N_A^3 \epsilon_{out}{}^{\frac{3}{2}} a^3}{\lambda \ln(10)} \left[\frac{\epsilon_i(\lambda)}{(\epsilon_r(\lambda) + \chi\epsilon_{out})^2 + {\epsilon_i}^2} \right], \tag{3.11}$$

where N_A is the areal density, a is the radius and ϵ_{out} is the dielectric constant of the surrounding medium of the nanostructure. Here ϵ_m is assumed to be the positive real integer and is independent of λ. It is to be noted that ϵ_i and ϵ_r are the imaginary and real components of the metal dielectric function respectively. However, χ gives the aspect ratio of the nanostructure.

The spectral bandwidth of localized surface plasmon (LSP) is around 80 $\sim$ 100 nm full width half maximum (FWHM), which is far greater than the spectral bandwidth of the change in the reflectance dip of SPPs, i.e., 50 nm. This increased spectral width can be reduced by increasing the number of nanoparticles.

The induced dipole moment p due to electromagnetic field (E) in a single metallic nanoparticle is given as [78]

$$p = \alpha E_0, \tag{3.12}$$

where α is the polarizability and can be obtained using a quasistatic approach. By considering the size of particles smaller than the light involved polarizability can be derived from equation 3.12 as per the following [78]

$$\alpha = 4\pi a^3 \frac{\epsilon(\omega) - 1}{\epsilon(\omega) + 2}, \tag{3.13}$$

where a is the radius of nanoparticle and $\epsilon(\omega)$ is the dielectric constant and α is the measure of effect of applied electric field on the particle. Hence, α is directly proportional to charge displacement within the particle. The resonance occurs due to restoring Coulomb force inside the particles by satisfying $\epsilon(\omega) + 2 = 0$ or $\epsilon(\omega) = -2$. Here the strength of the force determines the resonance frequency while the damping determines resonance width [106].

William L Barnes [107] elucidated the effect of the shape of nanoparticles on the resonance frequency in terms of polarizability. As per the author's mathematical and theoretical explanation, polarizability depends on the composition of the particle and the environment. Besides, it also depends on the net electric field inside the particle.

The quality factor of the resonance is the ratio of resonance wavelength and the width of resonance, and it has the highest value when $Im(\epsilon(\omega) + 2) = 0$. Since the dielectric medium of metal is a complex value, therefore the denominator of equation 3.13 cannot reduce to zero. Later, Wang and Shen [85] proved with their quasi-static approximation that the quality factor actually depends on the dielectric medium of the particle. Hence LSP has been a disappointment for different applications where a high Q factor is desired. A significant improvement in the Q factor arises when two or more than two nanoparticles are brought close together. The interaction of the EM fields between nanoparticles results in coupled SP modes [108] and field enhancement. Similarly, metallic nanoparticles arranged in a lattice experience surface lattice resonance (SLR) due to the coupling of LSP (Figure 3.3). It leads to a significant narrowing of the spectral bandwidth and results in a high Q factor [109]. The position of resonance in a lattice depends on the shape, size, incidence angle, and the refractive index of the metal-dielectric layer [110].

The emergence of extraordinary optical transmission (EOT) [26] due to the coupling of surface plasmons in a surface lattice has been a breakthrough. It has been widely used, and its applications include drug delivery [111], imaging [112], colour filtering [113], high-resolution display [114] and high sensitive sensing [115]. Since the research in the field of plasmonics is expedited with the discovery of new materials and design fabrication techniques [73, 116, 117], this review focuses on and evaluates those developments. The periodic subwavelength nanoparticles of any shape, material and sufficient number for LSPR behave similarly to incident light as electricity to atomic crystals at the subatomic level. In this section, the reported work for photonic crystals is discussed and evaluated in terms of their performance as a colour filter. The section includes nano-porous films,

hybrid structures, metasurfaces and gap surface plasmon-based designs studied so far.

3.2.2.1 Nanohole

A porous metallic film on dielectric when excited by a white light source results in EOT and only allows the light of specific wavelength (λ_{res}) to pass through it. The λ_{res} depends on the periodicity and geometry dielectric constant of metal and dielectric, respectively, and a lattice arrangement of holes [118]. Similarly, the mode of operation, i.e. transmission [119], or reflection [120] of the structure, also depends on the shape of the nanoparticles.

The localized field in nanoholes and nanoparticles is widely investigated [121]. It has been reported that LSPR in nanoholes is dependent on the lattice periodicity; however, it is less affected in a metasurfaces array. Similarly, the fabrication process of nanoholes on metal films is more straightforward than metasurfaces. Nevertheless, an increase in resonance quality in nanoholes is quite challenging [122]. Therefore, the application of a perforated metal film (usually bio-compatible, i.e. Au/Ag) on the dielectric layer is limited to biosensing sensors [123]. On the other hand, the application of subwavelength nanoholes is not limited to electromagnetic waves. It has been theoretically proven that various acoustic absorbers, under coherent conditions, can be attained using the effective deep- subwavelength holey rigid plate, such as steel [124].

A dielectric-based 2D subwavelength dielectric grating was proposed for backside illuminating (BIS) CMOS image sensor (CIS) technologies [125]. It consists of a hexagonal nanohole array for the red and blue colour and a square nanohole array for green colour production with a silicon spacer between the photodiode layer and grating. The device was fabricated with poly-Si materials prepared by amorphous-Si deposition followed by a high-temperature furnace annealing method [126]. The design exhibited promising results, i.e. 60-80 % efficiency with angle invariance up to ±20 %. The high transmission efficiency was achieved due to the high refractive index and low absorption of A-Si, which helps in enhancing the spectral features [127]. Besides, holes of different shapes have also been explored, have shown promising results, and has provided a flexible tuning mechanism. For instance, a CMOS-compatible polarization-switchable array of asymmetric cross-shaped nanoholes in an Al ultra-thin film was reported [128]. The mechanical-based optical filtering enabled a single design to encode two information

states, which could be decoded by changing the polarization angle of incident white light. However, the maximum transmission efficiency of subtractive colours was insufficient, i.e., 14 % with incident angle variance.

The nanoholes with FP etalon have demonstrated efficient results. Chang et al. [129] demonstrated an efficient structural colour printing filter based on plasmonic metasurfaces with a thin MIM stack. In order to avoid colour crosstalk, holes on perforated Ag film were milled through Focus Ion beaming (FIB) [130], in a hexagonal array. The design was further covered with a thin transparent polymer layer, PMMA. The change in λ_{res} due to overlay is covered by geometrical adjustments. The design showed promising results and allowed pure perfect absorption resonances of A$\approx$ 90 % with a high Q factor. Furthermore, the design was angle insensitive up to $\approx 70^o$, accredited to the angle robustness of the FP cavity. However, the usage of Ag in this design had introduced additional fabrication steps like adhesion layer between glass and Ag and PMMA layers to avoid Ag oxidation. Recently, transmission efficiency of 60 % was exhibited by increasing the density of coaxial holes of optimized size in a coaxial hexagonal lattice (with bigger holes) on a MIM stack of Al/glass/Al [131]. However, the design exhibited angle invariance of $\approx 60°$. The colour quality was reduced with the increase in coaxial holes.

3.2.2.2 Nanohole-Nanodisk Hybrid Colour filters

Kumar et al. [132] with a nanohole-nanodisk hybrid structure, to our best knowledge, was the first one who demonstrated a system that could achieve bright-field colour prints with resolution up to diffraction limit (i.e. 10,000 dpi). To obtain the desirable results, the scattering strength of resonators (nanoparticles) was increased by raising them above a metal back reflector (Ag/Au); hence the light of a specific wavelength was reflected back to the viewer‘s eye. A full palette of colours was obtained by changing the diameter and gaps between the nanodisks without varying the periodicity of the array. The dips in the reflected spectrum showed the presence of Fano resonance [133] that was the outcome of a broad spectrum of nanoholes and nanodisks with sharp peaks of surface plasmon resonances (SPRs). This work was further extended by using aluminium instead of Ag. It paved the way towards a cost-effective and stable structure, as compared to the short shelf life of Ag [134]. Its high-throughput lithography approaches also give it an edge over Au and Ag. Moreover, the range of printable plasmonic colours was expanded from

$\approx$ 15 to more than 300 colours by spatially mixing and adjusting the nanoscale spacing of the aluminium-based discrete nanostructures [135] (Figures 3.5a and 3.5b).

Recently, a spatial resolution of $\approx 141,000$ *dpi* with a wide gamut and large angle invariant was achieved by implementing circular nanohole-nano-disk hybrid nanostructure arrays based on the uncoupled localized surface plasmon polaritons (LSPPs) [136] (Figure 3.5c). The λ_{res} spanned across the visible regime by varying the diameter of the nanodisk-nanohole structure rather than its periodicity. Hence a single nanodisk-nanohole could be operated as an individual pixel resulting in sub-diffraction limit resolution. The results included theoretical as well as experimental results for subtractive colours.

An ultra-thin hexagonal nanodisk-nanohole hybrid structure array generated high gamut, high colour brightness, and polarization-independent subtractive colours with 77,000 *dpi* [137]. Here, the excitation of short-range SPR [138], and LSPR contributed to the ELT effect for the designed structure.

A structural design was demonstrated to generate structural colour through triangular-latticed square nanohole arrays in Al film with bottom Al nanodisks [139]. The design was fabricated using e-beam lithography and metal deposition by adjusting the period and the side length of nanohole arrays colours across the visible regime, with tunable brightness, hue and saturation, and pixel density of 12,700 dpi. However, the filtered colours were highly saturated.

An angle-insensitive of scratch-resistant hybrid disk-hole plasmonic-based colour filter was demonstrated by utilizing the PMMA layer on glass substrate [140]. For fabrication, nanoimprint lithography (NIL) was employed, where the silicon masters used for embossing was fabricated using EBL and subsequent dry etching. Furthermore, the samples were made using hot embossing and metal evaporation. Later, Al was deposited using electron-beam evaporation. The hybridization of plasmonic modes due to nanodisks and nanohole array offered angle-insensitivity up to 60°.

3.2.2.3 Metasurfaces

Metamaterials with subwavelength thicknesses such as nanodisks, nanospheres, nanotubes and thin film are capable of manipulating the wavefront of impinging light by changing its phase [141], amplitude [142], or angle of polarization [143]. Its applications include cloaking [144], polarization manipulation [145], high resolution lenses [146], and

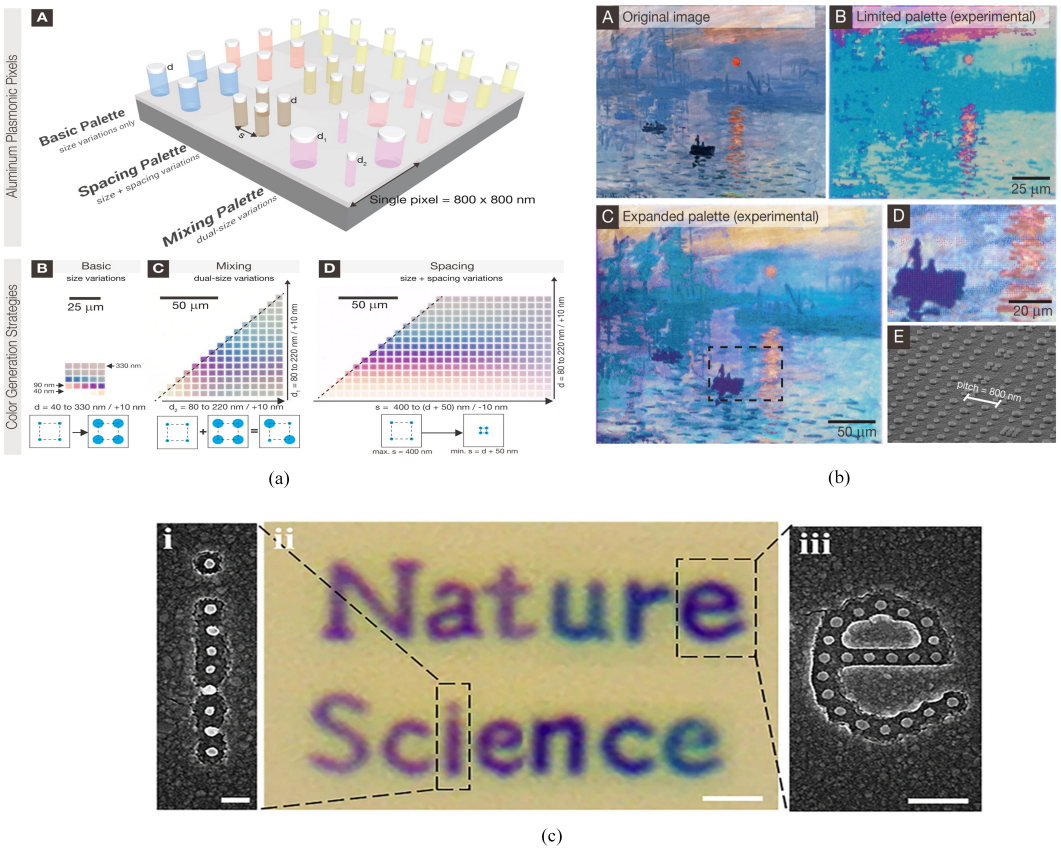

FIGURE 3.5: Nanohole and Nanohole-Nanodisk hybrid colour filters: a) schematic diagram of aluminium based nanohole- nanodisk hybrid structure. b) The impact of variation in diameter , periodicity and (spacing) diameter and periodicity on the colour image due to colour toning and mixing is demonstrated experimentally [135] c) colour printing resolution test pattern for LSPP based nanostructures at the scale bar of i) 200 nm, ii) 1μm and iii) 500 nm. [136]

perfect absorbers [147]. The metasurfaces based colour filter has shown remarkable results, and this section includes the reported work in this field.

An ultra-thin Ag patch array on silica was demonstrated [148] (Figure 3.6b). The Ag was deposited using magnetron sputtering, followed by FIB. The λ_{res} is affected by the change in patch dimensions; hence it can be swept across the visible regime. The structure showed the angle sensitivity up to 60° in transmission and reflection modes. The angle insensitivity is credited to LSPR at the nano patch array. However, the transmission efficiency is up to 40 %, and usage of Ag for CMOS devices has its disadvantages [149].

A 2D array of opaque but physically thin Al nano patch array on glass demonstrated highly efficient plasmonic subtractive colour filtering by capitalizing on SP-mediated selective transmission through it. Here the transmission was suppressed by opaque nano-patches instead of ELT. The spectral position of the transmission valley was governed by

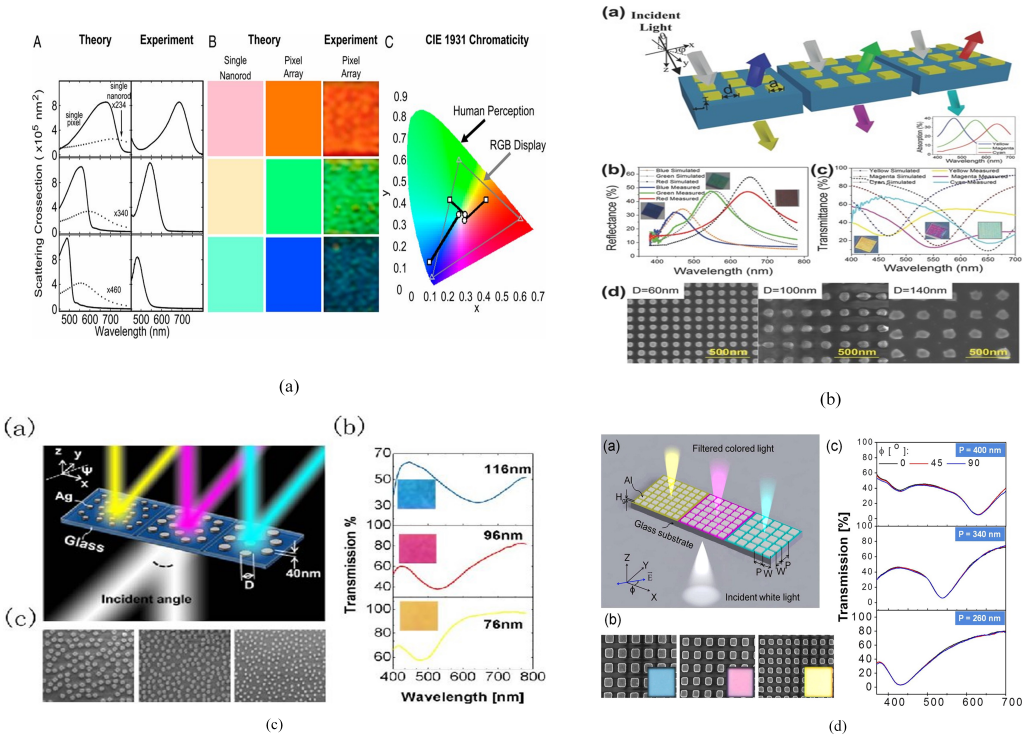

FIGURE 3.6: Metasurfaces: a) Experimental and theoretical results of vivid colours produced due to Al nanorod as a single nanorod and in hexagonal array [150]; b) Schematic diagram of Ag nano patch on a glass substrate with different periodicities allowing angle invariant (up to 60°) additive and subtractive colour filtration in transmission and reflection respectively. The simulated and experimental spectra plot shows the obtained results with the colour image inset. SEM gives a close look at the fabricated nano patch array [148]; c) schematic diagram of randomly distributed Ag nanodisks, the λ_{res} was swept by varying the diameter of the nanodisks. The transmission spectra with a colour image in the inset show the colour quality produced [151]; and d) Schematic diagram of thin Al nano patch array on a glass substrate, this design filters out white colour into distinct subtractive colours by varying the pitch of array. The colour quality is evident in SEM and camera images of the fabricated filters. The polarization independence is verified by plotting reflection spectra at different polarization angles [152].

varying the periodicity of the nano patches and realized a palette of subtractive colours [152] (Figure 3.6d).

A highly polarized angle-sensitive CMOS-compatible aluminium nanorods arranged in a hexagonal lattice and excited via a prism produced vivid, high-contrast colours of 100:1 with a footprint of 25 μm × 25 μm (Figure 3.6a). Here the far-field diffracting coupling is exploited to narrow the bandwidth down [153], and the physical dimensions of nanorod allowed additive colour tuning across the spectrum. However, using a prism for excitation is a hurdle in its integration and miniaturization.

An array of two dimensional randomly distributed silver nanodisks on a glass substrate with improved angle insensitivity up to 60° for reflected colour filters was demonstrated

[151] (Figure 3.6c). It was possible by defying hybridized LSPR and isolating the nano-disks. The uncoupled LSPR allowed better angle sensitivity as compared to the coupled LSPR. The colour was tuned by varying the diameter of the nanodisks, while the minimum distance, to avoid LSPR coupling, between nanodisks was kept up to 80 nm. A broad series of colour filters with colours varying from yellow to cyan were shown fabricated with the nanodisk diameter ranging from 66 to 166 nm. The circular shape of the nanostructure allowed polarization insensitivity and showed good brightness and high colour contrast across the visible region. The angle insensitivity was further improved to 70° with randomly distributed nanodisks and nanoholes fabricated with hydrogen silsesquioxane (HSQ), and Ag films on silicon substrate [154]. The LSPR-based colour filters are further summarized in Table 3.3.

3.2.2.4 Gap Surface Plasmons

A gap surface plasmon (GSP) is a special kind of plasmon metasurface where a subwavelength dielectric spacer is sandwiched between a thick optical metal and metallic subwavelength particles arranged in a periodic or quasi-periodic arrangement [155]. The subwavelength-thin dielectric spacer enhances the field in MIM and allows near-field coupling between the SPP of the two interfaces [156] (Figure 3.3(h)).
The FP resonance condition for MIM with truncated upper metallic layer of width w is given as [157]

$$w\frac{2\pi}{\lambda}n_{GSP} = m\pi - \phi. \tag{3.14}$$

Here n_{GSP} is the effective refractive index of GSP, λ is the vacuum wavelength, ϕ is the unknown phase change due to reflection at the nanodisk boundary, and m is a positive integer account for resonance mode. The applications of GSP resonators include flat lenses [158], surface wave couplers [159], holograms [160], beam-steerers[161] absorbers [162], polarization controllers [163], and dynamically reconfigurable metasurfaces [164]. As per the focus of this review, the reported work on GSPR-based colour filters is discussed and reviewed in this section.

A plasmonic colour filter with the subwavelength resolution based on MIM configuration capable of supporting GSP was demonstrated [165] to effectively reflect different colours at subwavelength scale (Figure 3.7). Here an array of 340 nm period containing circular gap-plasmon resonators of Au $/SiO_2$ and Au was fabricated with single-step electron

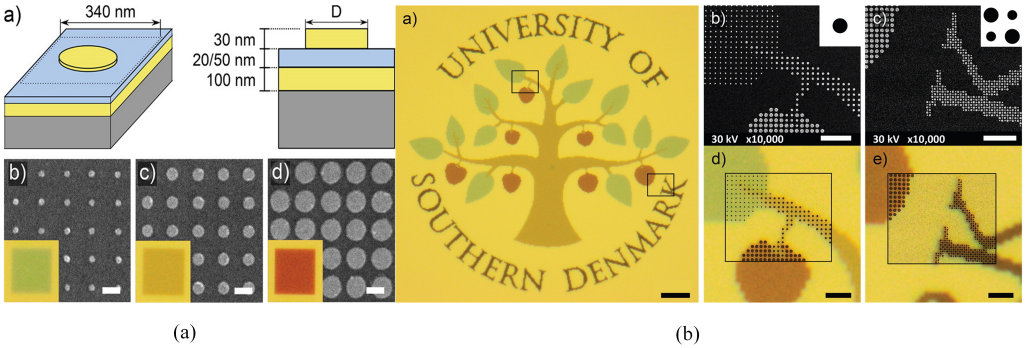

(a) (b)

FIGURE 3.7: Gap surface plasmons (GSP): a) Schematic diagram of a circular gap plasmonic nano microscopic images of the highly uniformed colours due to an array b) Precise colour printing on an optical microscopic image demonstrate bright colours with high contrast, and demonstrate that even single pixel details are coloured and discernible [165].

beam lithography. Here λ_{res} is varied by varying the diameter of the nanodisks and allows angle insensitivity up to 60°with polarization dependence. Furthermore, the λ_{res} is immune to the presence of overlay; hence it allows chemical and mechanical stability to the device.

The performance of the aforementioned example was further improved by utilizing $Al/Al_2O_3/Al$ MIM stack in nanodisk GSP resonators [166]. Here each resonator is treated as an individual colour element. Hence, the resultant colour obtained is the effect of colour absorption due to each of the resonators in an array. The nanodisk diameter and array periodicity change covered the entire visible regime with saturated colours and dark colours at the optical diffraction limit. The presence of Al makes it robust and reliable, hence discarding the need for overlay, which can be red shift λ_{res} in this case.

3.3 Dielectric-based Colour Filter

As per scattering theory, all scattering bodies can be represented by effective magnetic and/or electric polarizability densities. Light scattering by small particles is based upon the Mie solution of the diffraction problems. The scattered field of a single isolated dielectric sphere with radius r_o and relative refractive index n can be decomposed into a multipole series with the 2^m-pole term of the scattered electric field proportional to [34]

$$a_m = \frac{n\psi_m(nx)\psi'_m(x) - \psi_m(x)\psi'_m(nx)}{n\psi_m(nx)\xi'_m(x) - \xi_m(x)\psi'_m(nx)}, \tag{3.15}$$

TABLE 3.3: LSPR-based colour filters

θ_i°	FWHM (nm)	η (%)	Spatial resolution (dpi)	Ref
Nanohole				
±20	NG	60-80	NG	[125]
0	NG	14	NG	[128]
70	55	98	NG	[129]
60	145	60	NG	[131]
Nanohole Hybrid				
NG	NG	NG	100,000	[132]
±40	NG	NG	141,000	[136]
0	NG	60	77000	[137]
0	NG	NG	127,000	[139]
60	NG	NG	NG	[140]
Meta surface				
60	NG	40	100,000	[148]
±8	NG	75	100,000	[152]
60	NG	NG	100,000	[151]
Gap Surface Plasmon				
60	110	NG	100,000	[165]
60	NG	NG	100,000	[167]

Note: θ_i°= Angle invariance in degrees NG= Not given, NA= Not Applicable, A= Absorption, T= Transmission, R= Reflection and η=Efficiency.

whereas 2^m-pole term of the scattered magnetic field is proportional to

$$b_m = \frac{\psi_m(nx)\psi'_m(x) - n\psi_m(x)\psi'_m(nx)}{\psi_m(nx)\xi'_m(x) - n\xi_m(x)\psi'_m(nx)}, \tag{3.16}$$

where $x = k_o r_o$,k_o is the free-space wavenumber and $\psi_m(x)$ and $\xi_m(x)$ are Riccati-Bessel functions. The primes indicate derivation with respect to the arguments. The scattering coefficient a_m and b_m are related to the electric and magnetic response of the sphere, respectively.

Here the first and second highest wavelength resonances of dielectric spheres correspond to the electric and magnetic dipoles [168]. The dielectric resonators [169] are capable of concentrating electromagnetic energy in different modes with a high refractive index n, which results in a higher Q factor and allows sharp Mie resonances in small spherical particles with a large permittivity [170]. Similarly, the magnetic response of dielectric resonators in reaction to the magnetic component of external electromagnetic waves has

significance in the implementation of negative-index metamaterials (NIM) with isotropic properties [171]. In contrast, the metallic nanoparticles mostly demonstrate anisotropic optical, magnetic response. They are prone to significant ohmic losses, which aggregate with the increase in frequency, hence making it unsuitable for lower wavelength signals like blue colour in the visible regime [172]. Due to a high Q-factor and low loss, dielectric-based colour filters with high permittivity material have been studied and demonstrated extensively. This section includes state-of-the-art research work done in this field.

Full colour printing with titanium oxide (TiO_2) metasurfaces with trapezoid-shaped nanostructures arranged in the square lattice was demonstrated in [173]. High reflection peaks and bright contrast were obtained across the visible regime. The fabrication involved a typical lift-off process. Taking advantage of the Fano resonances, the reflected colour was also achieved from TiO_2 metasurface with much smaller pixel sizes. Thus bright, high contrast and high-resolution structure colours were generated (Figure 8a and 8b).

It has been noted that colour saturation for higher desired wavelength is impaired due to the presence of high order Mie resonances (quadruple mode) at lower wavelength [174]. This was addressed by exploiting multi dielectric metasurfaces with SiO_2, TiO_2 and Si_3N_4 from top to bottom on silica substrate [175]. The index matching between layers allows multipolar modes suppression at non-resonant wavelength and extraordinary enhancement in the monochromaticity of reflection spectra. It expanded unprecedentedly and acquired 171 % sRGB space, 127 % Adobe RGB space and 57 % CIE space.

Recently, it has been proposed that applying Rayleigh anomalies at a relatively short wavelength in Si_3N_4 (nanopillars) metasurface on quartz substrates results in higher modes suppression. However, the lateral angle of incidence was employed for producing vivid colours in transmission modes [176]

A cross-shaped A-Si-based 2D array of nanoresonators demonstrated by Vishal et al. [177] showed insensitive polarization results with high quality and a wide colour gamut (Figure 8c). High purity colours were obtained by optimizing resonance properties, which were easily tuneable through changes in structural parameters. The obtained resonant wavelength is further tuned by varying the aspect ratio of nanoresonators. The obtained results showed polarization insensitive independent resonances with high transmission efficiency. However, the issue of incidence angle could not be addressed.

All-dielectric polarization dependent reflection colour pixels with a subwavelength

resolution of up to 85,000 dpi have been demonstrated [178]. Here the C-Si nano block resonators were arranged in a square lattice allowing distinct vivid colours across the visible regime by varying its physical geometry. The results showed that these individual pixels could be distinguished easily in a chequered pattern and do not allow colour mixing. However, an incidence angle insensitivity of only 20° was achieved. The subwavelength resolution was further improved to 100,000 dpi by exploiting monocrystalline Si nano-disks resonators with a metal mask on them [179]. This offered a high resolution by weakening the interaction between two resonators to such an extent that even with a pixel containing a single nanoresonator, the filtered colour will not be mixed.

A subtractive CMY colour filter showed high efficiency and colour quality with A-Si-Al hybrid nanodisk metasurfaces on Si substrate [180]. The nanodisk supported MD resonance mode and was confined to the nanodisk due to an Al nanodisk at the top. A near-zero reflection dip was reported and swept across the visible regime by changing the diameter of the nanodisks. However, incidence angle invariance of only 25° was reported. The results for yellow colour could further be improved by implementing a rectangular lattice as theoretically presented [181].

Ninety-percent efficient reflective colour filters with hydrogenated A-Si nanodisks in a square lattice were realized by [182] (Figure 8d). ED and MD resonance govern the wavelength-dependent filtering characteristics via Mie Scattering. The vivid subtractive colours were tuned by varying structural parameters like the period and radius of the nanodisks.

All dielectric-coloured silicon-based metasurfaces (silicon nanopillars) etched on a glass substrate with the period of $1\mu m$ were theoretically and experimentally studied [183]. The farther apart nanopillars defied the coupling, and each nanoresonator worked as an individual colour filter, where the response of ED and MD can be tuned by changing the aspect ratio of each nanoparticle.

Furthermore, an economical solution for broadband anti-reflection through Si surfaces textured by the laser-based method has been proposed [184]. The study showed that well-ordered Si nanowires (NW) with high aspect ratios improve the UV-visible-NIR performance. Likewise, the decoration of Si with MNPs also reduced the optical reflection. The hybrid anti-reflection surfaces demonstrated reflection below 1 %.

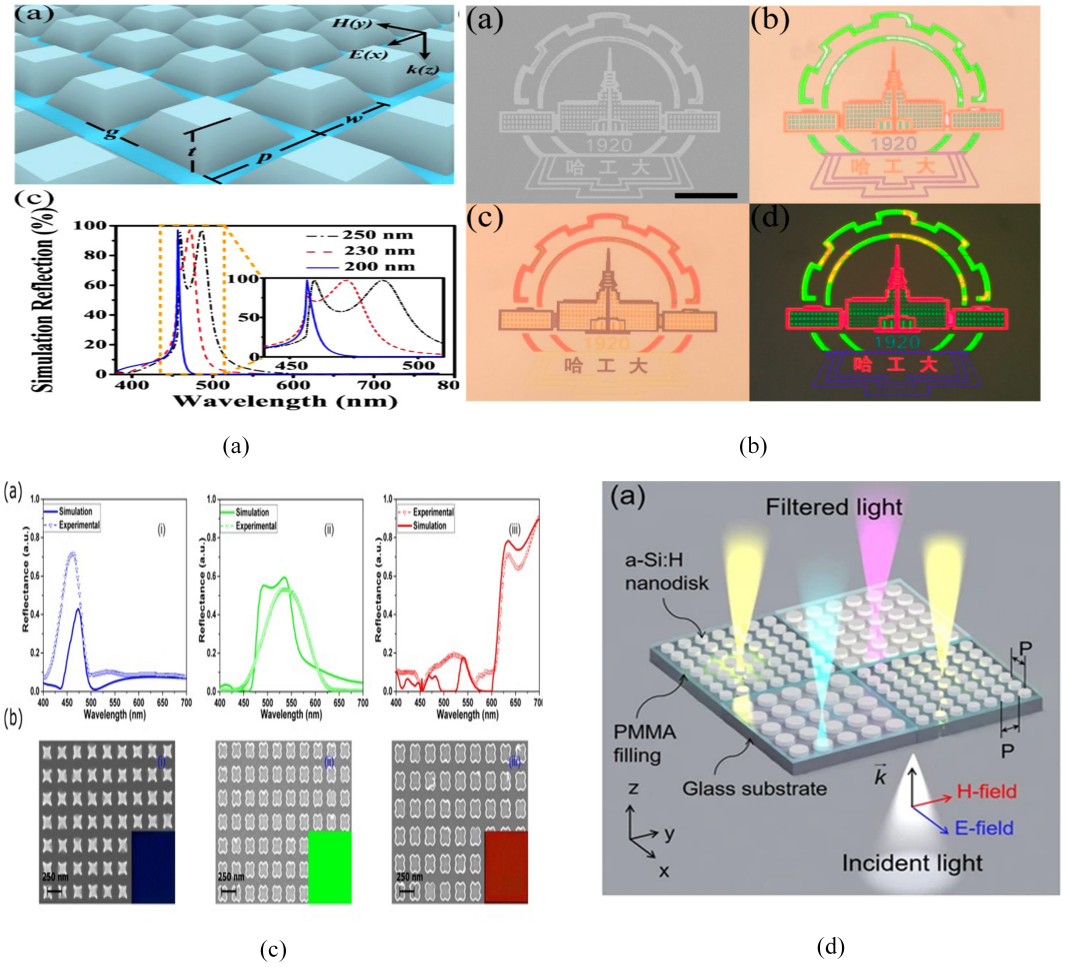

FIGURE 3.8: Dielectric-based colour filters: a) Schematic diagram of TiO_2 based colour filter, the reflection spectra shows the dependence of filter on the device dimensions (here the width of the bottom face w is varied from 200 to 250 nm). b) colour image printing is exhibited with the top view SEM image of the logo with transmission and reflection colourful images under bright field microscope [173]. c) Simulated and experimental results for additive colours of all dielectric metasurfaces based on cross-shaped resonators [177] d) Schematic diagram of a 2D lattice of A-Si:H nanodisks on a glass substrate [182].

TABLE 3.4: All Dielectric-based colour filters

θ_i°	**FWHM (nm)**	η (%)	**Spatial resolution (dpi)**	**Ref**
60	30	64	16000	[173]
20	NG	NG	85,000	[178]
NG	NG	100	100,000	[179]
26	50-65	Near Zero (A)	NG	[180]
0	NG	90	NG	[182]
0	NG	NG	25,400	[183]

Note: NG =Not given.

All studied Mie-scattering-based colour filters made of high refractive index nanoresonators are summarized in Table 3.4.

3.4 Liquid Crystal-based Plasmonic Colour Filters

Active plasmonic colour filters are the colour filters that can encode more than one colour state. These devices generally employ active mediums such as liquid crystal [185], elastic polymer [186], chemical reduction/oxidation [187], and molecular machines [188]. However, liquid crystal stands out from all the kinds above, with the highest birefringence on the refractive index, a low threshold on transition among different states, and versatile driven methods to create transitions. Moreover, their large birefringence span across the visible regime and near-infrared [189], high throughput, compatibility with optoelectronic materials, and flexible control of the alignment of liquid crystals, i.e., via light, electricity, and acoustic waves, makes it the best candidate.

In general, there are three phases of liquid crystals, 1) nematic,2) smectic and 3) cholesteric. In the nematic state (Figure 3.9(a)), the molecules are obeying the translational order only, while in the smectic phase, there is translational as well as orientation order in all the molecules (Figure 3.9(b), 3.9(c)). In the cholesteric phase, a special kind of nematic phase (Figure 3.9(d)), the phase of the liquid shows the distribution of molecules at several planes that are perpendicular to the helical axis. The molecular chirality governs the twist direction, i.e., right-handed or left-handed.
The most remarkable characteristic of liquid crystals is their anisotropic refractive index. One refractive index corresponds to light polarized along with the director of liquid crystals, while the other is for light polarized perpendicular to the director. Hence, magnetic and electric field components will propagate through the liquid crystal at different speeds, which results either in or out of phase at the exit from the crystal. Furthermore, the polarization state of light will change at the exit due to optical anisotropy. Likewise, the birefringence decreases with the decrease in temperature and ends up at the isotropic phase [190].

Since the orientational order and birefringence can be tailored easily via electric, weak magnetic and optical fields, it has been used in numerous applications such as liquid crystal display (LCD) for watches, television, cell phones, spatial light modulators for adaptive optics in real-time optical imaging, phased optical array for beam steering, and

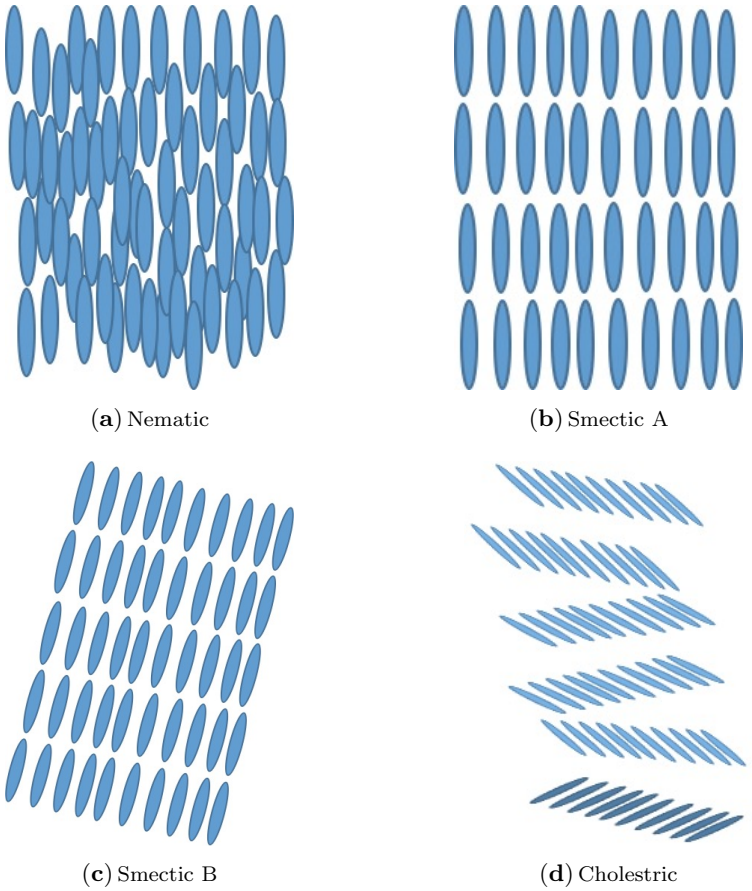

(**a**) Nematic (**b**) Smectic A

(**c**) Smectic B (**d**) Cholestric

FIGURE 3.9: Phases of liquid crystals

attenuators for telecommunications [193].

In this section recent research examples of liquid crystal plasmonic-based colour filters are studied and reviewed. A highly efficient electrically tuneable colour filter with dichroic resonators was achieved by exploiting an LC-based polarization rotator [191] (Figure 10a). The variation in applied voltage rotated the polarization in LC and affected the results from the dichroic resonators. The dichroic resonators are comprised of guided-mode resonance through an Si_3N_4 dielectric layer and the diffraction due to 2-D rectangular Al-grating. The LC-based polarization rotator allowed electrical colour tuning across the visible regime with high efficiency, including narrow bandwidth.

An Al- grating with a twisted nematic liquid crystal (TN-LC) integrating cell was studied for dynamic colour filtering [194]. The cell comprises Al-grating metasurfaces fabricated on indium tin oxide (ITO) glass as a top layer. The bottom plate consists of ITO glass with spin-coated PMMA. The TN-LC was injected via capillary action into the gap between the plates. The TN-LC allows change in the polarization of incident light, while this change can be varied by varying voltage across the plate, allowing electrical

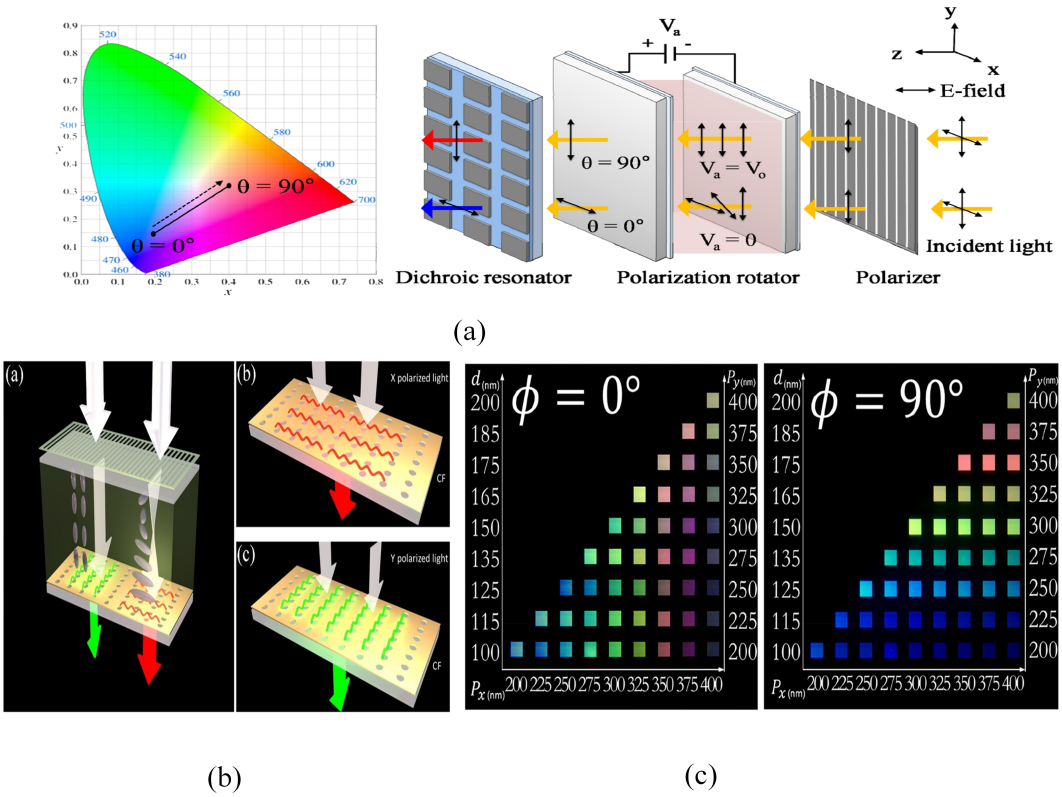

FIGURE 3.10: Liquid crystal-based colour filters: a) Setup of electrically tunable colour filter exploiting a visible dichroic resonator with subwavelength metal-dielectric resonant structure in conjunction with a LC-based polarization controller [191]. b) Schematic diagram of electrically tunable colour filter exploiting TN-LC and rectangular lattice of nanoholes on Al film to control the polarization of incident light, and c) Optical photographs of printed colours in TM and TE mode [192].

colour tuneability. The idea was further implemented in an electrically colour switching LSPR by exploiting TN-LC [192] (Figure 10b and 10c).

Here one of the polarizing plates of TN-LCD is replaced by Al-based rectangular nanohole array film; however, an indium tin oxide (ITO) coated glass substrate was used as another electrode. The LC layers formed between substrates are mutually orthogonal to achieve the TN-LC configuration when light enters the display. Here the asymmetric nanohole array as an output filter allows two different colours in TE and TM mode, and the change in polarization can be induced by applying a voltage across TN-LCD.

3.5 Summary

Ideally, a colour filter should have high colour quality, a wide gamut, incident angle invariance, high spatial resolution, CMOS compatibility and independence of angle

of polarization along with high throughput and cost-effective fabrication techniques. Realistically, a structural colour filter with all the above-mentioned qualities does not exist, and the replacement of pigment-based colour filters is not materialized yet. However, there are examples studied in this review that are exemplary in their own right. So, there is still a need for material exploration and new design technologies to investigate improvements in present designs. This review is further summarized in Figure 3.11. It gives an overall comparison of key performance indicators of discussed technologies for nanostructure colour filters.

From this study, it is inferred that FP-based colour filters with lossy materials allow high angle invariance and polarization independence. Furthermore, the FP cavity fabrication requires simple deposition methods and is cost-effective, but dealing with thin lossy films (proved to have lower losses than its counterparts Au, Ag, and Al) becomes tricky and requires special care. Lately, new methodologies are being adopted to obtain suitable metallic refractive indices, such as using the evaporated form of Au/Ag, etc., which has shown efficient results and deserve to be further investigated in the future. In terms of results, generally, it has the low colour quality and limited colour gamut and spatial resolution.

Despite the usage of noble metals in the pioneering designs of the plasmonic colour filter, today, Al is preferred over Au, Cu and Ag. This preference is accredited to its compatibility with CIS devices, durability and robustness. Likewise, it is the third most abundant material on earth and also has recycling capabilities.

In general, 1D grating-based structures are prone to viewing angle sensitivity with reasonable colour quality. Similarly, it is to be noted that GMR-based colour filters produce high-quality colours but usually with low spatial resolution. Although it does not require sophisticated fabrication steps, it requires more gratings and results in a large footprint. Likewise, its asymmetric geometry strictly depends on polarization, but it also makes it a good candidate for polarization tunable colour filters.

From LSPRs based structures, it can be deduced that nanoholes due to their high angle variance, low spatial resolution and limited colour gamut are substituted with advanced structures. The first nanohole-nanodisk hybrid structure employing Fano resonance has paved the way for spatial resolution up to diffraction limit and been an epitome for designs where spatial resolution more than or equal to diffraction limit are desired. Likewise, metasurfaces have shown better performances but still have lower angle invariance due to LSPRs, which can be further refined by employing novel

techniques. Lastly, GSP-based colour filters also allowed high angle invariance and spatial resolution with limited colour gamut.

In addition, the advancement in nano-fabrication technologies and simulation methodologies has paved the way for precise and controlled plasmonic-based nanostructures fabrication. Hence, it makes plasmonic-based colour filters stand out among their counterparts with high research potential. However, the strong dependence of λ_{res} on the device geometry requires a tight critical dimension control, especially in the fabrication process of metasurfaces, GSP- based colour filters and nanohole-nanodisk hybrid structure.

All the studied dielectric-based colour filters made of high refractive index (like

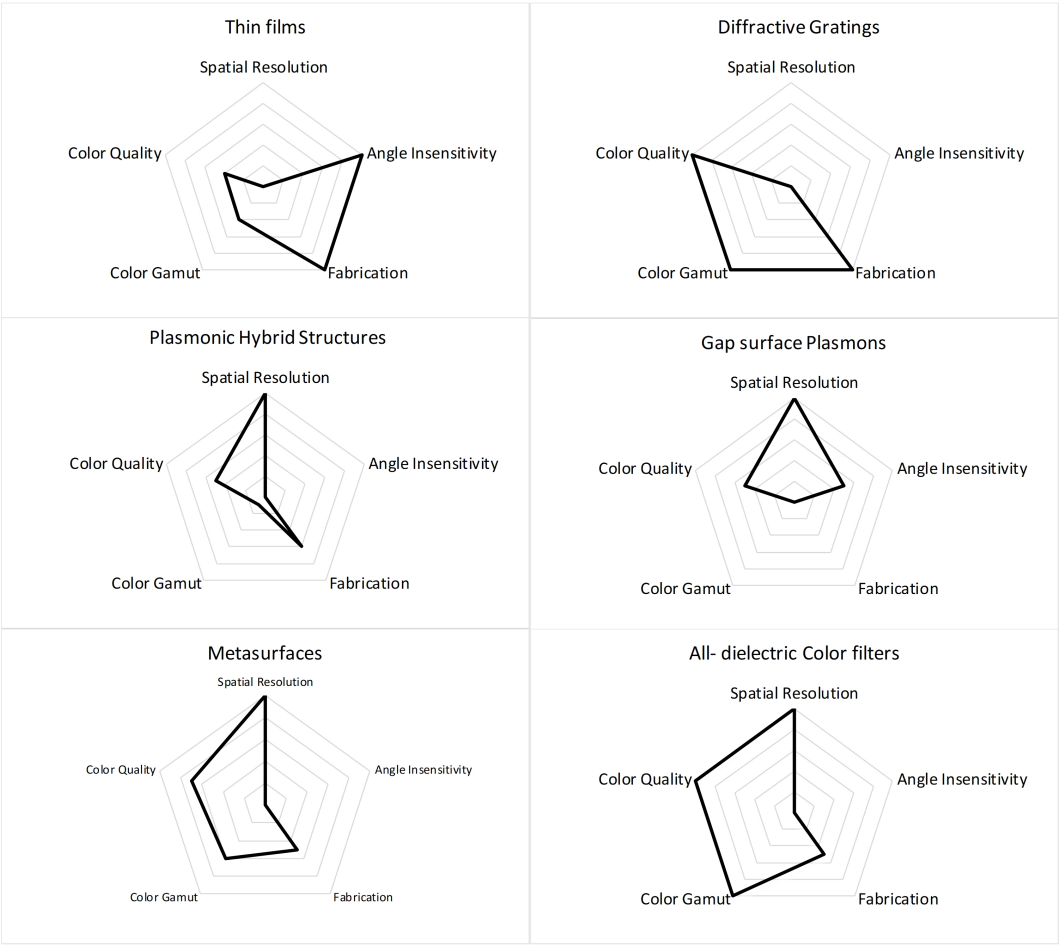

FIGURE 3.11: Key Performance Indicator charts for nanostructure colour filters

A-Si, TiO_2 and Si_3N_4 etc.) nanoresonators are studied. It has already sought its due attention because of its compatibility with the CMOS technology. In general,

dielectric-based colour filters are very angle sensitive, but they offer high spatial resolution due to nanoresonators' high refractive index contrast and their surroundings. Amorphous/crystalline silicon offers broad gamut coverage, but the colour absorption at a lower wavelength makes it unsuitable for blue colours. Although TiO_2based colour filters were demonstrated to avoid absorption for red colour (at 650 nm), it invited higher-order modes at non-resonant wavelength. Lately, the performance of other dielectric materials Si_3N_4-based cubic nanostructures showed praiseworthy performance by suppressing higher modes and enhancing the monochromaticity of higher resonant wavelengths by employing Rayleigh anomalies at short wavelengths. Hence, pointing towards the research opportunities in this field.

The last section of the review includes LC-based active plasmonic colour filters, which allows colour tuning in plasmonic structures; this helps to move the λ_{res} across the visible regime without any change in its dimensions. This technique has research potential. Therefore liquid crystal with large birefringence, fast switching between states, and its implementation with efficient designs like nanohole-nanodisk hybrid structures and dielectric metamaterials for colour filtering, etc., needs to be explored further.

3.6 Knowledge Gap

The literature review presented in this chapter suggests that, besides the CMOS-compatibility, fabrication steps and performance of the thin film design are also important. Generally, the fabrication steps in thin films are minimum and the fabricated/deposited films are insensitive to the light polarization. However, the films show high dependency on the incident angle of light. This issue has been addressed by many researchers [195–198] using high refractive index materials, such as A-Si that allows high angle invariance by blocking a big portion of the visible region. In another approach, Ji et. al [199] used seven layer stack of Si_3N_4 and A-Si to block visible region, but allowed NIR transmission. In the visible region the blocking of the light is a drawback, however this could be a useful feature for NIR filtering. Therefore, considering this as a research gap, we manipulate thicknesses and number of layers of the stack, to demonstrate NIR filtering with high transmission efficiency and narrow bandwidth.

The literature also reveals that asymmetric FP nanocavity color filters with different novel materials, such as platinum (Pt), and nickle (Ni) [62, 200] produce valuable results.

However, these materials are CMOS incompatible and to fully benefit from the successful FP nanocavity designs for varied applications, it is prudent to investigate and implement them using CMOS compatible materials. Since this has not been presented in the existing literature to the best of the authors' knowledge. Considering this a research gap, tungsten (W) is used as a candidate material due to its chemical and physical properties along with its CMOS compatibility.

Chapter 4

Simulation and Fabrication of the Multilayered Thin Films Cascaded Filter

This chapter covers the steps required to perform simulations and fabrication of the proposed design.

The first section explains the adapted FDTD solutions with its brief theoretical background. The complete algorithm for FDTD methodology is described in detail in Appendix B.

The use of Ansys FDTD solutions is demonstrated with the help of diagrams in the next section. This includes mandatory initial steps such as simulator's environment for the proposed design, mesh settings, script writing to avoid redundant steps and preferences for structures containing overlapping objects, suitable boundary conditions and placement of incident light in the simulation volume. The result requisition for the device is also included in this part.

The following section includes the design of the proposed device, its theoretical background, and the steps required to reach the final design are demonstrated with the help of simulation plots. The performance of the final design is evaluated by varying incident and polarization angles of incident light. In the last section, the working principle of employed fabrication techniques, including CVD and PECVD, are explained, followed by the proposed design's fabrication procedure.

4.1 Finite Difference Time Domain Method

Simulation with the help of fundamental principles of modelling, mathematics, physics and computer science allows the engineer to foresee the anticipated results of the proposed design. Hence it reduces the overall fabrication and testing cost and saves time. Moreover, this has opened avenues for innovation and allowed the designer to think to look further.

In electromagnetic problems, the FDTD algorithm is primarily used to simulate photonic crystals, plasmonics and nanophotonic devices. In this particular study case, FDTD methodology is adapted for simulating nanophotonic spectral filters. It was first presented by mathematician Kayne S.Yee [201] in 1966. It is based on the applications of the time-domain differential Maxwell's equations and suitable boundary conditions. The FDTD method belongs to the grid-based differential numerical modelling methods (finite difference methods). The time-dependent Maxwell's equations (in partial differential form) are discretized using central-difference approximations to the space and time partial derivatives.

Figure 4.1 illustrates a 3D spatial grid or Yee unit cell where electric and magnetic field vectors are precisely arranged. The electric field component is placed at the edge's centre and points parallel to the edge itself. In contrast, the magnetic field is placed at the centre of each face and is orthogonal to the face's plane. Hence, allowing Ampere's and Faraday's law to fill the interlinked space. Here, both time and space are discretized, and magnetic and electric fields are sampled at discrete alternate half-time steps to exploit the leapfrog scheme. It is to be noted that the associated material constitutive parameters of the field are also distributed over the discretized grid of the cell [7].

4.2 Setting-up the Simulation Environment

In this thesis, the proposed design is finalized by thoroughly studying and evaluating already reported work demonstrated in the literature review in Chapter 3. Furthermore, different structures with CMOS compatible materials were simulated to obtain the desired goal. The final design of a multilayered thin film cascaded filter is simulated by employing the Ansys FDTD simulator. It is a user-friendly simulator with dynamic characteristics and an expandable default material database. Typically, a simulation

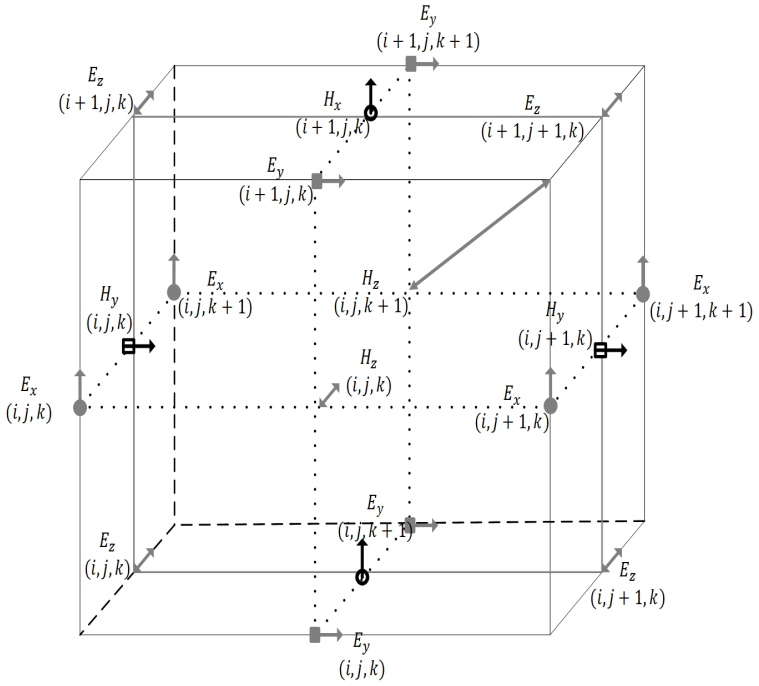

FIGURE 4.1: Yee cell: In FDTD methods, different field components of electric (E_x,E_y,E_z) and magnetic field (H_x,H_y and H_z) are stored at different field sites, and this discretization of the electromagnetic field is called the Yee lattice. The electric field components are stored on the edges of cubes; however, H components are placed on the face of the cube. The arrangement is made in such a way that four E components surround each H component, and each H component is surrounded by four H components.

setup requires defining a set of objects, simulation region, position of monitors and source. The spatial grid size has a trade-off with the computation time needed to run the simulation. Hence, special care is taken off in choosing the mesh size. Typically mesh size is relatively kept low at the critical regions (such as metal and dielectric interface) of the simulation volume, as it helps in saving computation time. Since the proposed design comprises all-dielectric material, a mesh is kept constant around the multilayered films.

Likewise, the user-defined mesh order for any object, at the material level or the object level, is highly significant, as it governs how the overlapping objects mesh in the simulation. Figure 4.2 demonstrates the impact of mesh order 'm' on the partially overlapping objects. It is evident from the figure that mesh order determines the design's architecture which is being simulated. However, the objects with the shape of the overlapping objects with the same mesh order is dependent on their location in the object tree. The objects at the bottom of the tree have higher priority than the object at the top. Therefore, it is recommended to organize the designed structure in an object tree.

Since the proposed 1D crystals are composed of a non-overlapping stack of different material layers with specific thicknesses on top of one another, the mesh order is negligible.

Typically, simulation of thin films is more straightforward because it does not include complicated structures like arrays of nano-objects (holes, spheres, diffraction gratings) or other metasurfaces [202–204].

Figure 4.3 demonstrate a unit cell of multilayers thin film and its simulation volume in the Ansys environment. A broadband plane wave source with a wavelength range of 200 nm to 2500 nm as incident light is placed above the structure and is pointing towards the structure along the z-axis, where the azimuthal, incident and polarization angle is chosen to be at 0°. In transverse magnetic (TM) polarization, the direction of polarization is along the x-axis. The mesh is 4 nm in all directions along the defined area around the film stack.

The transmission and reflection data are recorded as a function of frequency by employing two dimensional (2D)-frequency domain field monitors. The transmission and reflection monitors are placed below and above the structure, respectively, inside the defined simulation region. It is to be noted that sources require a specific amount of room to inject the electric and magnetic fields (2-3 grid cells). Hence it is prohibited to place monitors in that region. In contrast, multiple monitors in a simulation do not interface.

Moreover, it is permissible to place sources at layers, where layers interact or have monitors crossing through several objects. However, some types of projections, like far-field projections, require the monitor to be in a homogeneous material. A 2D index monitor is also employed to check the refractive index of each object.

Using a suitable set of boundary conditions is vital to acquire reliable simulation results.

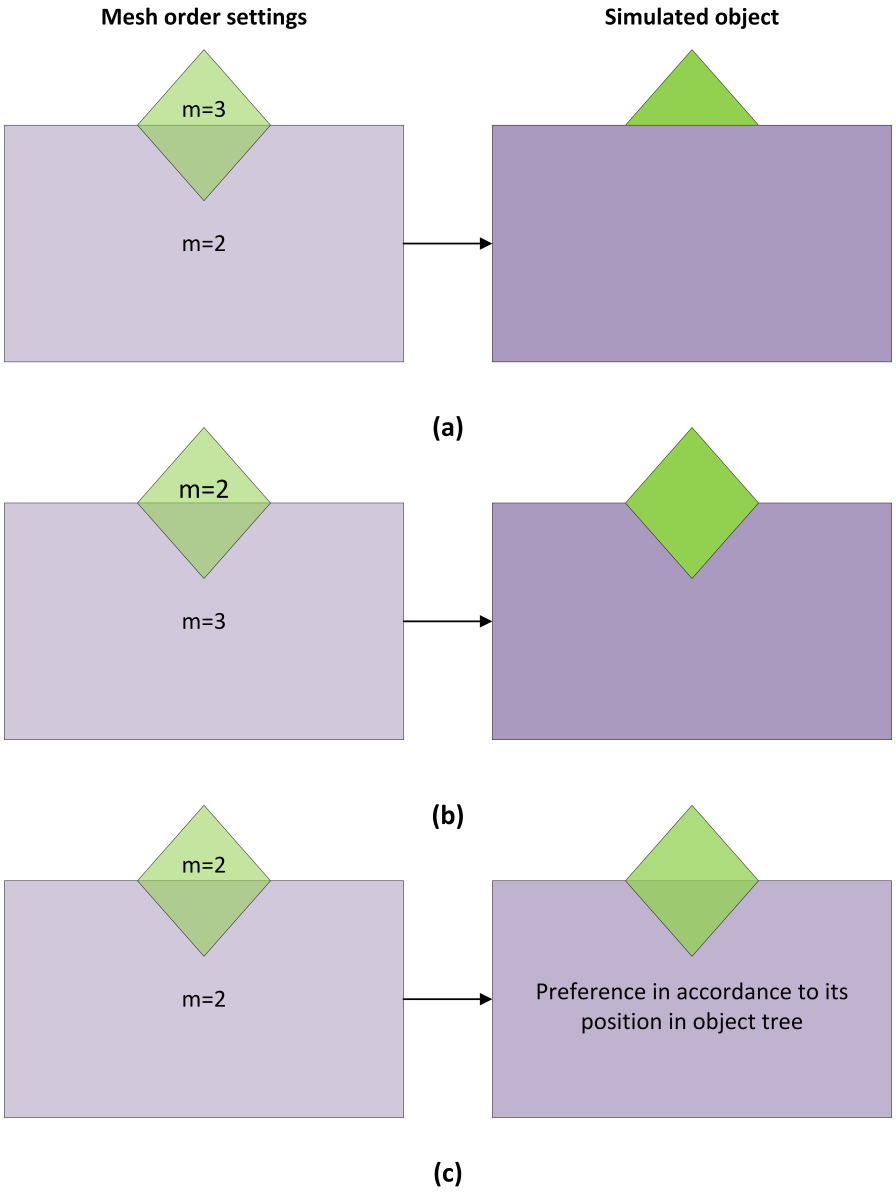

FIGURE 4.2: Mesh order and overlapping object: Figure a) and b) illustrate that the object with higher mesh order has least priority. The shape of the simulated shape is determined by the position of object in object tree

FDTD solutions support numerous categories of boundary conditions, but here the relevant ones are discussed only. The perfectly matched layer (PML) conditions are used for open boundaries conditions below and above the cascaded etalon's structure. It reduces the possibility of multiple reflections at the bottom and top boundaries of the simulation region by absorbing incident electromagnetic waves, allowing reflection-less boundaries. Moreover, the amount of absorption can be further controlled with the help of several parameters, such as the number of layers. The periodicity of both the structure and electromagnetic field is reproduced by implementing periodic boundary

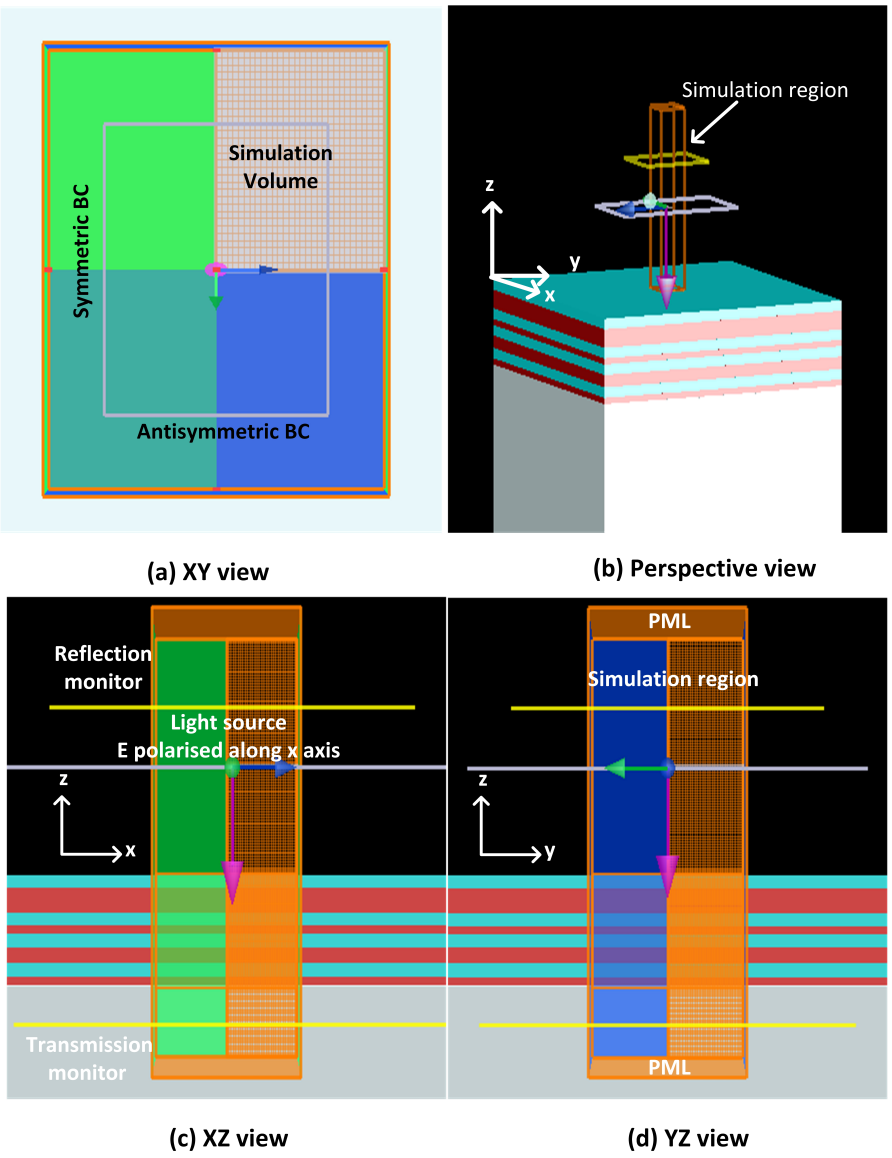

FIGURE 4.3: Ansys simulation setup of multilayered cascaded hybrid etalons: Ansys simulation setup of multilayered cascaded hybrid etalons represent the a) XY view, b) Perspective view, c) XZ view, and d)YZ view of the Ansys simulation model. A TM polarized light source is injected from the top of the structure and points in the '-z' direction.

conditions in the direction(s) of interest (x-y plane). Lastly, the symmetric and anti-symmetric boundary conditions are employed due to mirror and anti-mirror symmetry, respectively, and it is beneficial in reducing simulation factor by 2, 4 or 8. Since both the source and structure are symmetric, their boundaries mirror the electric or magnetic fields. Therefore, the source and the boundary conditions must have exact symmetry. However, in the case of oblique incidence of a plane wave, the boundary condition should be changed to Bloch because the electromagnetic fields will not be symmetric/anti-symmetric along the same plane of symmetry of the structure anymore.

Ansys FDTD solutions also offer a robust scripting language to manoeuver the simulation's objects, define parameters, launch simulation and analyze results. Since optimization, development, and analysis require many simulations, it can be sequentially run with the help of a written script. The transmission, reflection, and absorbance spectra are plotted and are saved as JPEG images. Likewise, the data is imported into .mat files, which allows figure formatting such as line colour, legends, font size, etc. The script is saved as a .lsf file, and the project is saved with the .fsp extension.

4.3 Proposed Design with its Theoretical Background and Simulated Results

Following on from the literature presented in Chapter 3, it has been concluded that thin film filters have the following advantages over their counterparts:

- Fabrication process of thin film filter is a single-step process that does not require complicated fabrication steps. Thus the design's fabrication is easy and cost-effective [205, 206].
- Due to the symmetrical nature of the design, the outcome is always insensitive to the angle of polarization of incident light.
- The light incident angle independent response of the filter can be achieved with the inclusion of a high refractive index cavity (such as A-Si, Cr etc.) in the stack [53, 60].

Due to the advantages mentioned earlier, this thesis pursues a filter design approach with thin films. The design is inspired by generally adopted methods [195, 204], where a substrate is used as the starting material and layers of lower (L) and higher (H) refractive indices materials, with specific thicknesses 't', are added successively on one side till the desired characteristics are achieved (Figure 4.4). This process can be analytically developed or achieved through extensive simulations in the appropriate software. Usually, fabrication and testing do not precede the simulation or analytical design stage as it is impractical to design a filter without the simulation/analytical steps. To achieve CMOS compatibility, only those materials that can be processed in a nano-fabrication facility are considered, such as dielectrics etc. The result of our simulations

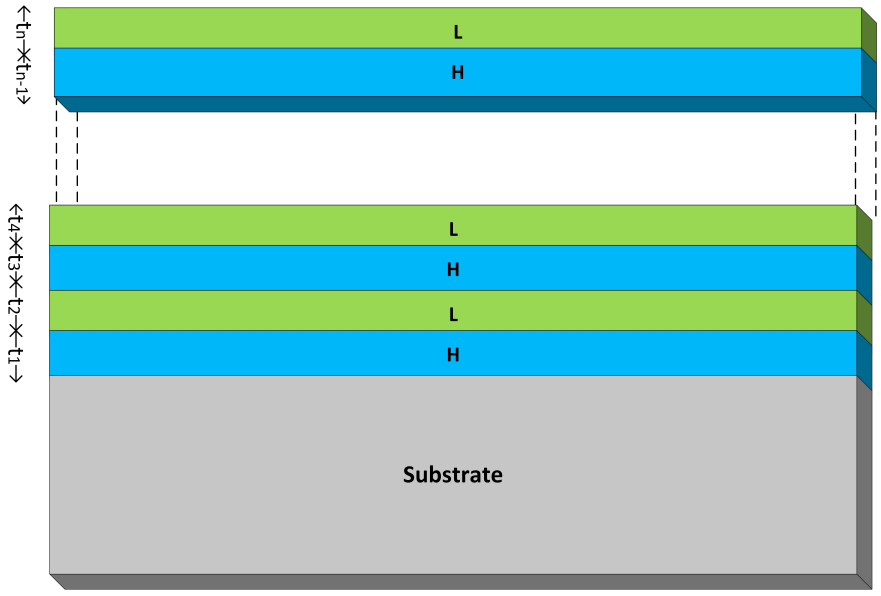

FIGURE 4.4: Schematic diagram of stack of films: Successively deposited thin film layers of low (L) and high (H) refractive indices materials with thicknesses 't'.

is an all-dielectric multilayered cascaded thin film for NIR filtering. It comprises amorphous silicon (A-Si) and silicon nitride (Si_3N_4) layers. Through simulations and reported work, it has been proved that the combination of these materials produces maximum efficiency in the NIR region with zero transmission in visible region [204]. The behaviour of incident light at an angle θ_i in all dielectric single etalon with A-Si cavity sandwiched between two Si_3N_4 layers is depicted in Figure 4.5. Here, the angle of refraction (θ_1) due to Si_3N_4 - air interface is determined with the help of Snell's law.

According to Fresnel 's equation the periodic peak transmission (T) of the refracted light through the cavity is given as [207]

$$T = \frac{(1-R)^2}{(1-R)^2 + 4R\sin^2(\frac{n_2 L\cos\theta_2\pi}{\lambda+2\phi})}. \tag{4.1}$$

Here R is the induced reflectance comes from the partially reflecting Si_3N_4/A-Si interface θ_2 is the propagation angle inside A-Si cavity, λ is the wavelength, n_2 is the refractive index of A-Si cavity and ϕ the phase shift due to internal reflection at the interface. The optical thickness of the cavity at different angles can be expressed as

$$\delta = \frac{2\pi n_2 L\cos\theta_i}{m\lambda}. \tag{4.2}$$

Here 'm' is the number of resonating modes inside the cavity. It can be implied from equation 4.2 that δ reduces with the increase in the angle of incident light. The resonant

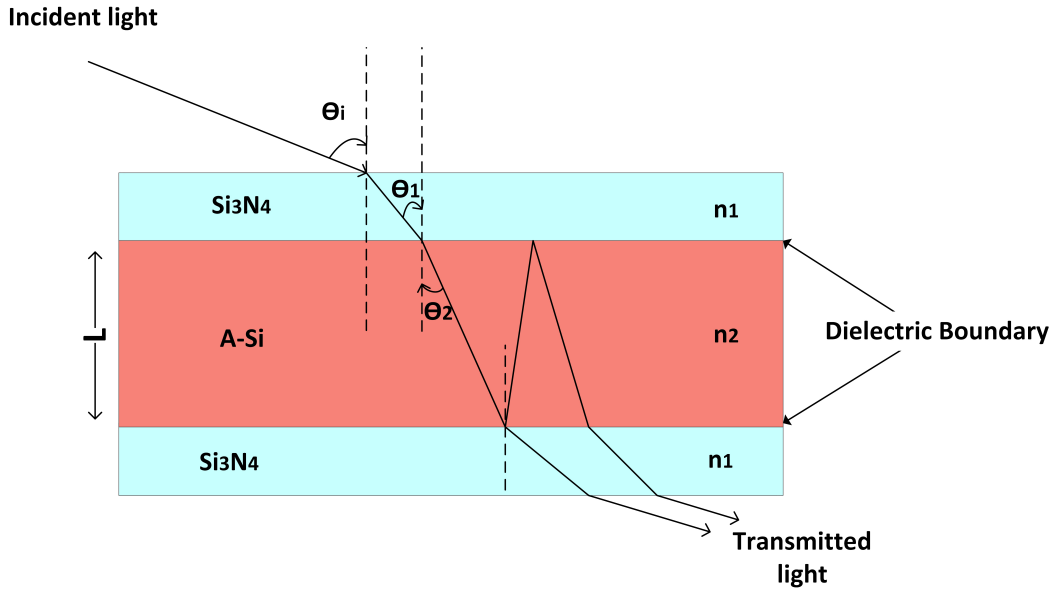

FIGURE 4.5: Response of incident light in a 1D ternary photonic crystal with low (Si_3N_4) and high A-Si refractive indices layers.

wavelength of the cavity is given as [207]

$$\lambda_o = 2\pi L\sqrt{n_2^2 - \cos\theta_i^2}. \tag{4.3}$$

The change in phase shift at the interface causes fractional wavelength shift ($\frac{\delta\lambda_o}{\lambda_o}$), and the rate of change in fractional wavelength shift concerning θ_i is inversely proportional to the refractive index of the cavity.

Mathematically [207],

$$\frac{\partial\frac{(\delta\lambda_o}{\lambda_o})}{\partial\theta_i} = \frac{-2Lsin\theta_i\cos\theta_i}{\sqrt{n_2^2 - sin\theta_i^2}}. \tag{4.4}$$

It can be deduced from equation 4.4 that high refractive index material shows negligible wavelength shift concerning change in incident angle; it also justifies the usage of A-Si for the proposed design.

4.3.1 Hybrid Etalon

A simple hybrid etalon with three deposited layers is presented and studied first. Figure 4.6 shows the design of simple hybrid etalons with two asymmetric cavities, cavity I comprise of A-Si layer with cavity thickness d_l ('l' subscript is for lower cavity) and is sandwiched between Si_3N_4 and substrate (SiO_2) from both ends respectively, while

cavity II with thickness d_u ('u' subscript is for upper cavity) is sandwiched between Si_3N_4 and air from the lower and upper end respectively. Here the thickness of Si_3N_4 is given as h.

For simulating the design, a TM polarized plane wave source is perpendicularly injected from the top of the device i.e., along '-z' direction. The direction of polarization is parallel to the plane of incidence, and the magnetic field is along the y axis. As per the requirement of the proposed design, the wavelength of the plan wave varies from 250 to 2500 nm (UV-NIR). In order to reduce the computational time, the boundary conditions for the x and y-axis are anti-symmetrical and symmetrical, respectively. However, PML is used along the z-axis, and the mesh size is 4 nm in all directions. A similar simulation setup is used to extract all results in this chapter.

The refractive index of A-Si is taken from Pailk [208], where the refractive index for

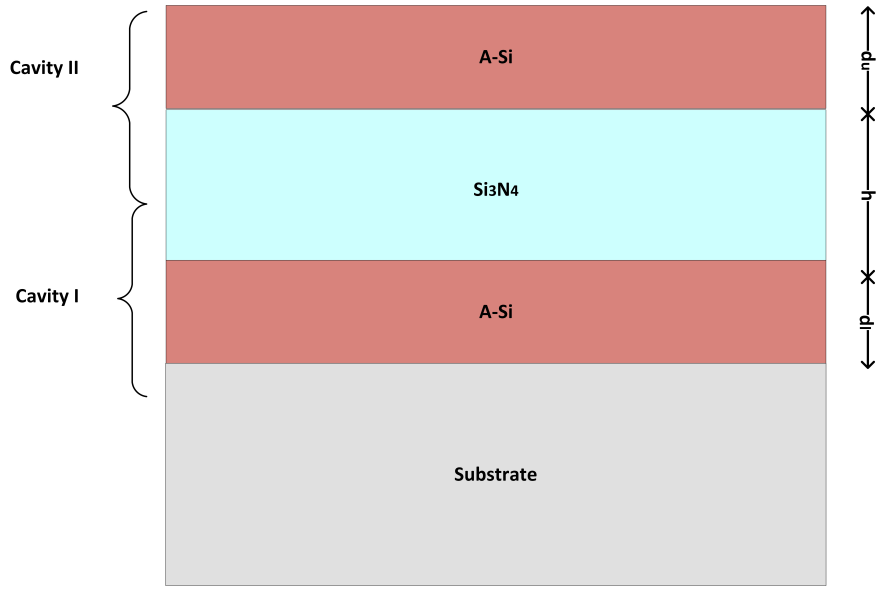

FIGURE 4.6: A simple hybrid filter with two asymmetric etalons joined at a common Si_3N_4.

Si_3N_4 is obtained through spectroscopic ellipsometey, are given in Figure 4.7 and 4.8. Moreover, the results for the reflection and transmission spectra, when $d_u = d_l = 40$ nm, and h=100 nm, are shown in Figure 4.9 respectively.

It is to be noticed from Figures 4.7 and 4.8 that the extinction co-efficient (k) is negligible for Si_3N_4 and A-Si in NIR region, hence allowing low absorption in the regime, which is also seen in Figure 4.9.

The impact of cavity thicknesses d_l and d_u on the filtering response of design is demonstrated with the help of Figures 4.10, and 4.11. It is evident from Figure 4.10 that

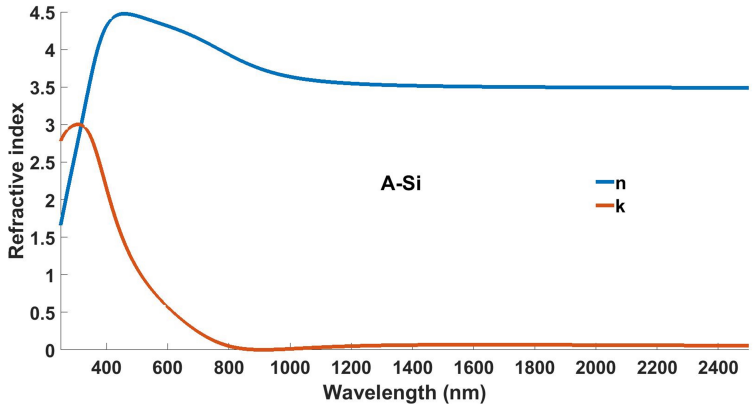

FIGURE 4.7: Refractive index (n,k) values of A-Si from 250 to 2400 nm obtained from Palik.

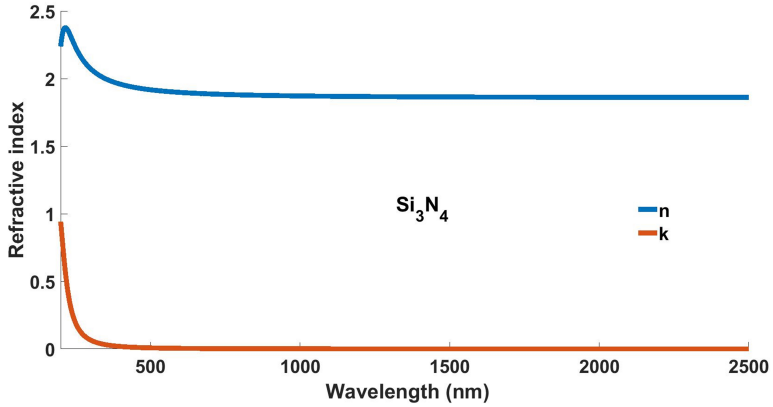

FIGURE 4.8: Refractive index (n,k) values of Si_3N_4 from 250 to 2400 nm.

the increase in d_u, from 40 to 240 nm at d_l=40 nm and h=100 nm shows a decrease in bandwidth and free spectral range of multiple resonances because of increase in cavity thickness, which is inversely proportional to free spectral range between resonances [195]. Likewise, the increase in d_l from 40 to 240 nm shows the same behaviour of reduced spectral range at d_u=40 nm and h= 100 nm (Figure 4.11).

With the help of analysis from Figures 4.10 and 4.11, it is demonstrated in Figure 4.12 at $d_l = d = 40nm$, $h = 200nm$ and $d_u = 2d$. The results show that a simple hybrid etalon can filtration; however, the presence of sidebands at a higher wavelength is inevitable. In order to produce more useful results, it is highly desired to produce a distinct peak at λ_{res} with well-suppressed sidebands; therefore, a cascaded filter with two hybrid etalons is further evaluated.

Figure 4.13 shows a design of hybrid etalon having a cavity with fundamental thickness d, responsible for the position of resonance in NIR range, and another cavity with thickness d_n (multiple of d), where a dielectric layer of Si_3N_4 of thickness h=100 nm

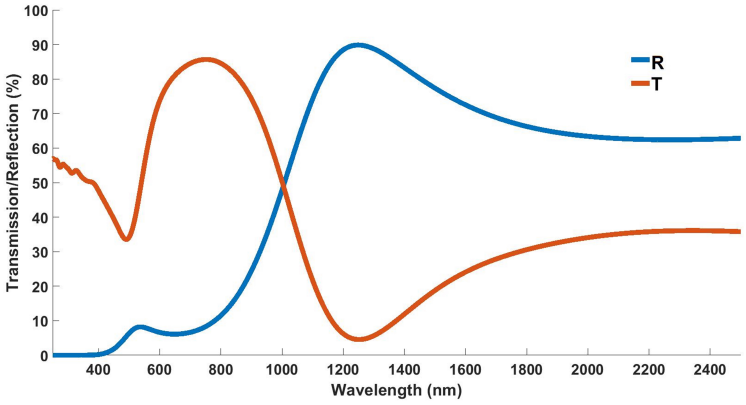

FIGURE 4.9: Transmission and Reflection spectrum of hybrid etalon.

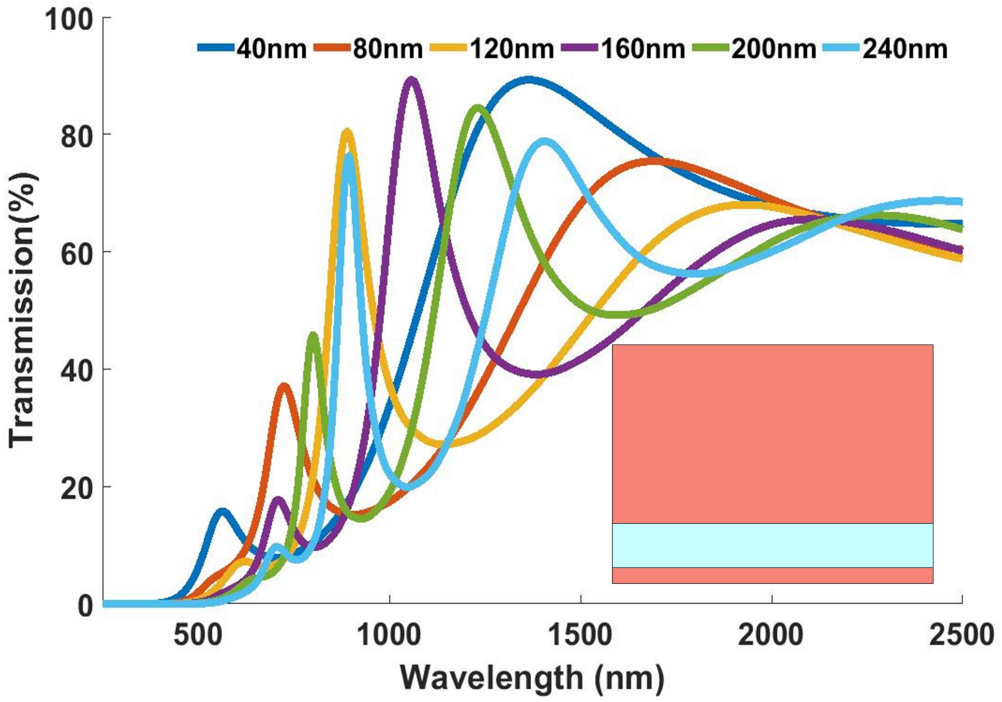

FIGURE 4.10: The impact of increase in thickness d_u of upper cavity of hybrid etalon.

is connecting both the cavities. As observed in Figures 4.10 and 4.11, the simulated results in Figure 4.13b with $d_1 = d = 80$ nm and $d_n = 2d$ and $3d$ show a decrease in free spectral range with an increase in the cavity thickness [195], and results in constructive interference at a distinct peak with λ_{res}= 1050 nm. However, the side bands are inevitable.

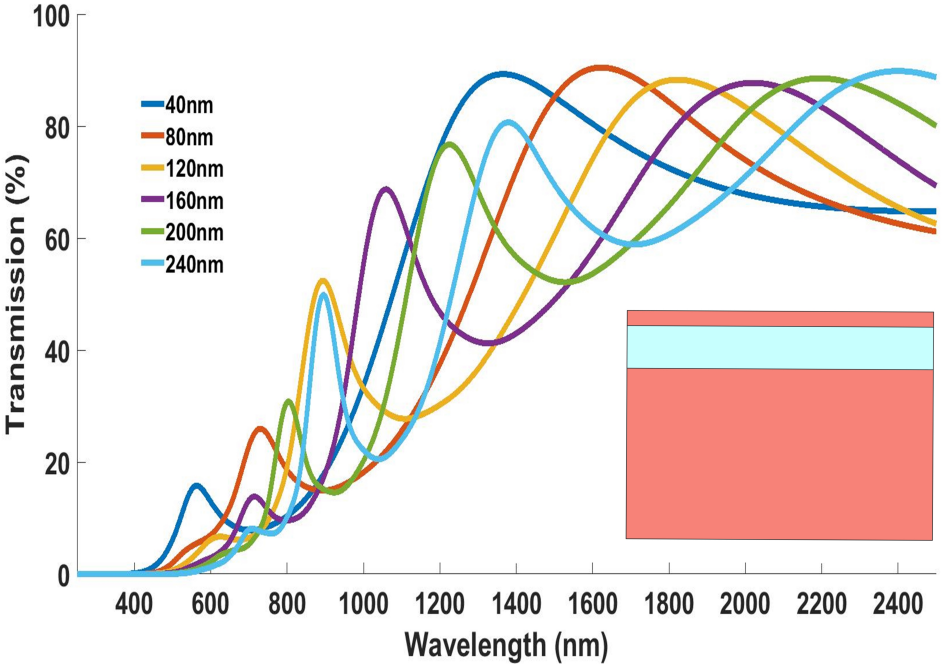

FIGURE 4.11: The impact of increase in thickness d_l of upper cavity of hybrid etalon.

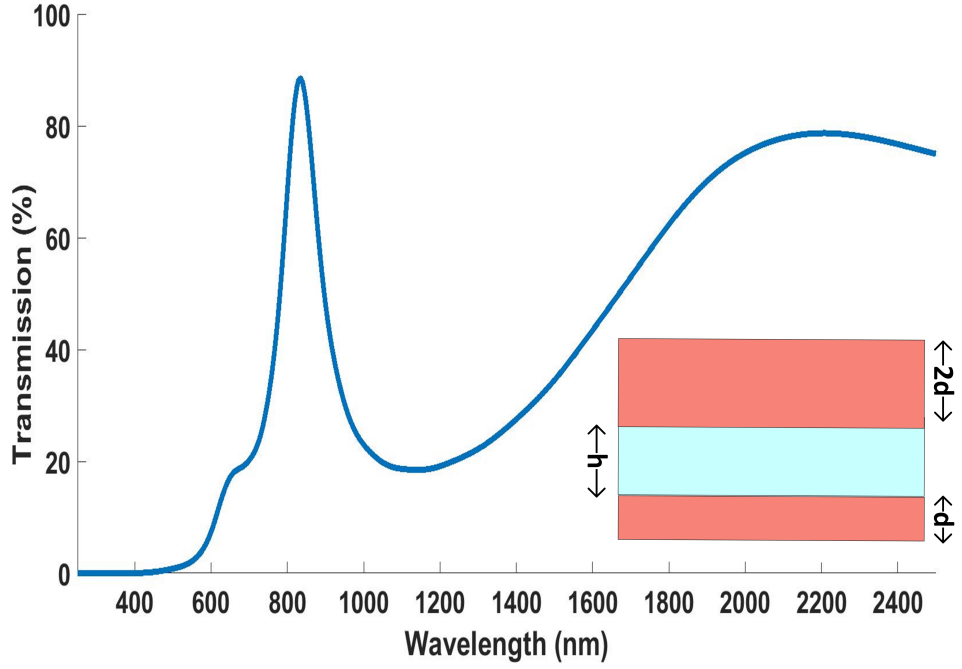

FIGURE 4.12: The impact of film thicknesses on the designed device when $d_u = 2d_l$.

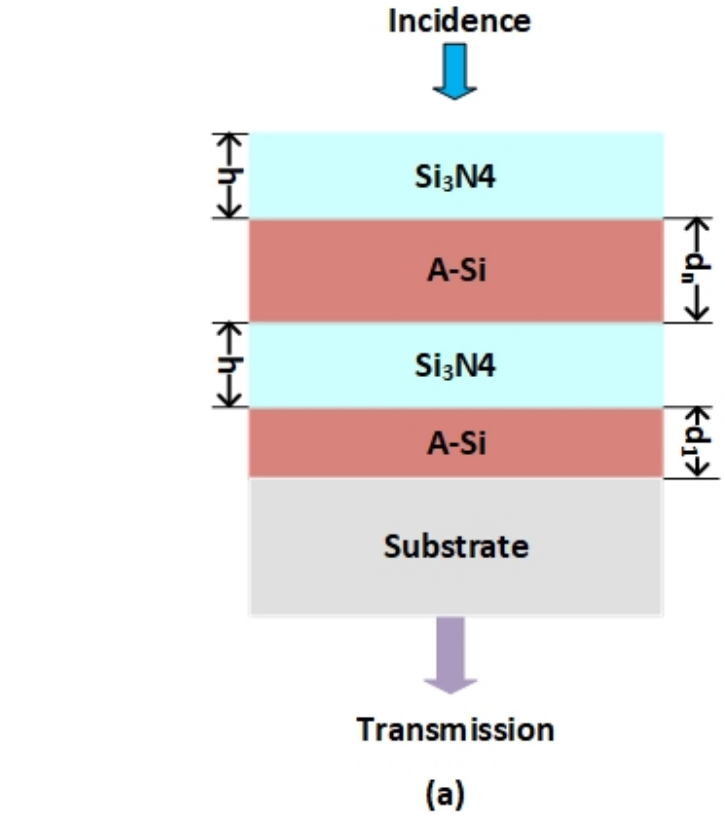

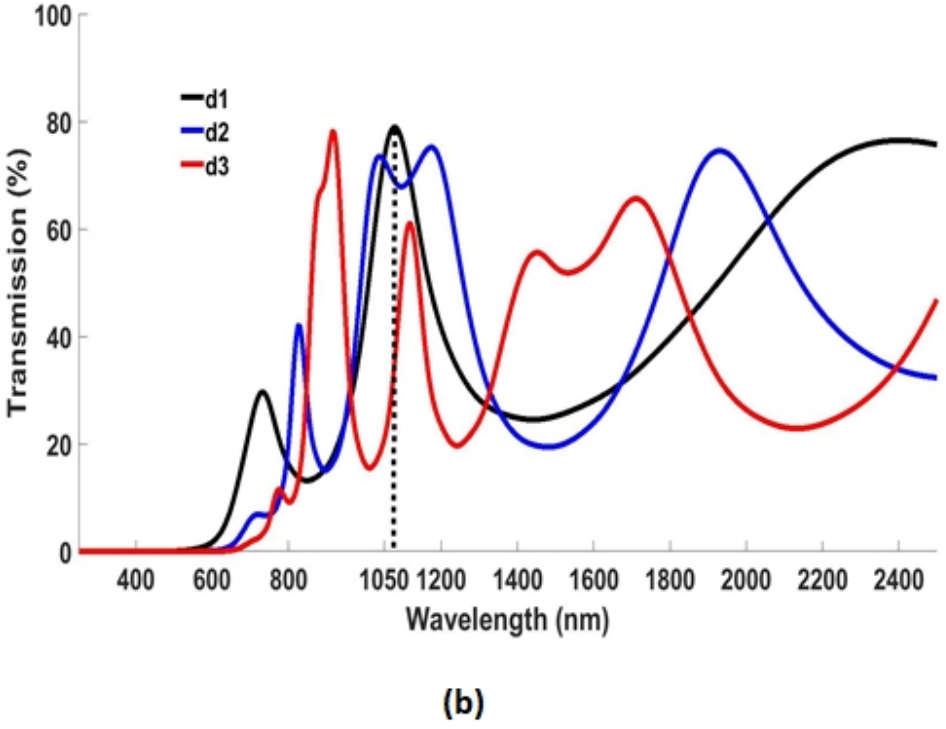

FIGURE 4.13: a) Schematic of hybrid etalon with different cavity thicknesses and b) Transmission spectrum of hybrid etalon with different cavity thicknesses such that $d_n = d_1$,d_2 and d_3, where $d_1 = d = 80$ nm is the fundamental cavity thickness, while d_2 and d_3 are its multiples.

4.4 Multilayered thin film Cascaded Filters

To suppress the sidebands, two hybrid filters are cascaded as shown in Figure 4.14a. The obtained results in Figure 4.14b demonstrate a distinct peak at 1050 nm with 70 % efficiency, FWHM at 77 nm and well-suppressed sidebands. It is accredited to increase in destructive interference from transmission spectrum of d_1, d_2 and d_3, which occurs everywhere in the VIS-NIR spectrum, other than the desired resonant wavelength λ_{res}.

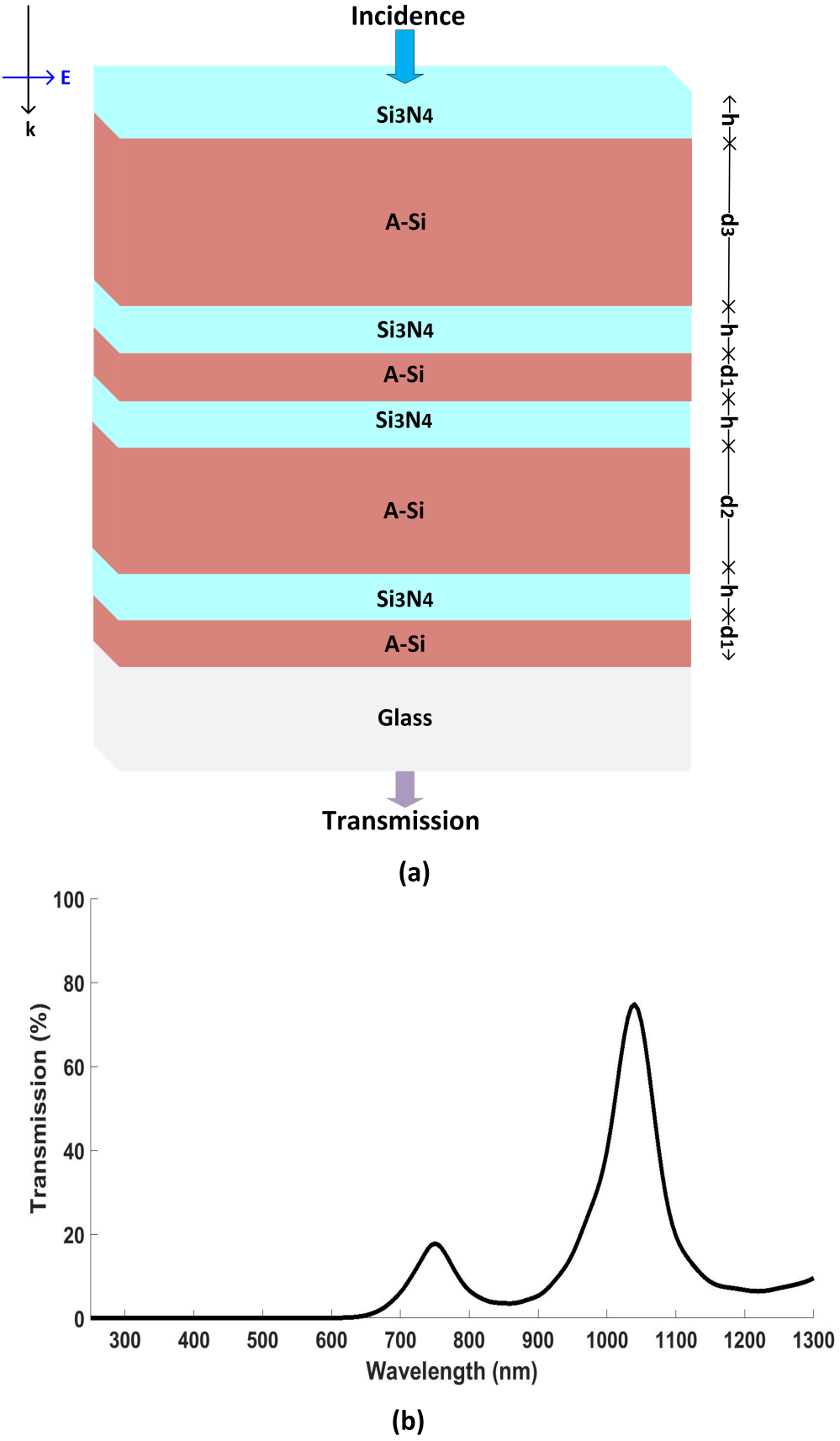

FIGURE 4.14: a) Schematic of multilayered thin film cascaded filter, where $d_1 = d = 80nm$ is the fundamental cavity thickness, while d_2 and d_3 are its multiples. b)Transmission spectrum of the cascaded multilayered thin film filter

4.5 Dual Mode Operation

The design was further evaluated for its operation in reflection mode. The results in Figure 4.15 show that the cascaded multilayered thin film filter is capable of operating in transmission and reflection modes.

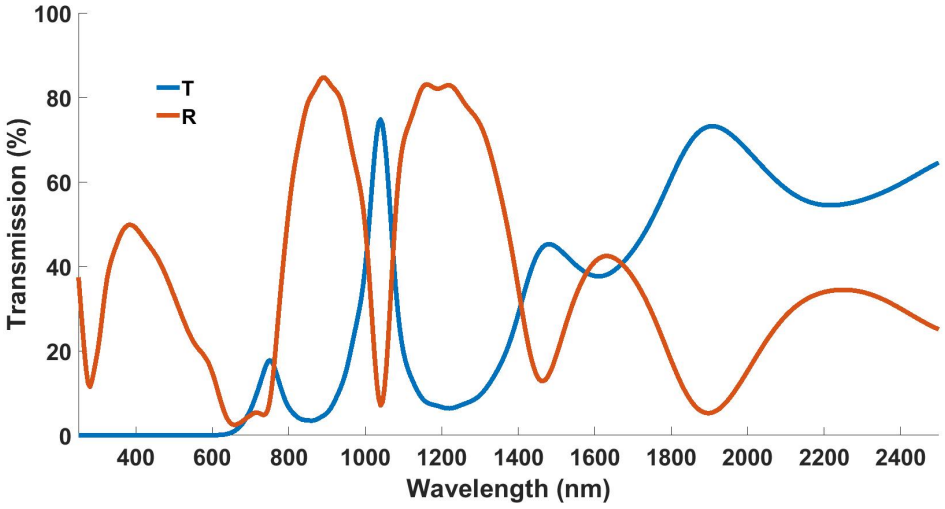

FIGURE 4.15: Response of cascaded multilayered thin film filters in transmission and reflection mode.

4.6 At Various Light Polarization and Incident Angles

Figures 4.16 and 4.17 show the impact of incident angle (θ) of incident light on the device's performance, where light polarization is in TM and TE mode, respectively. Likewise, Figure 4.18 shows the dependency of transmission spectrum on the polarization of incident light when the angle of incident is 0°.

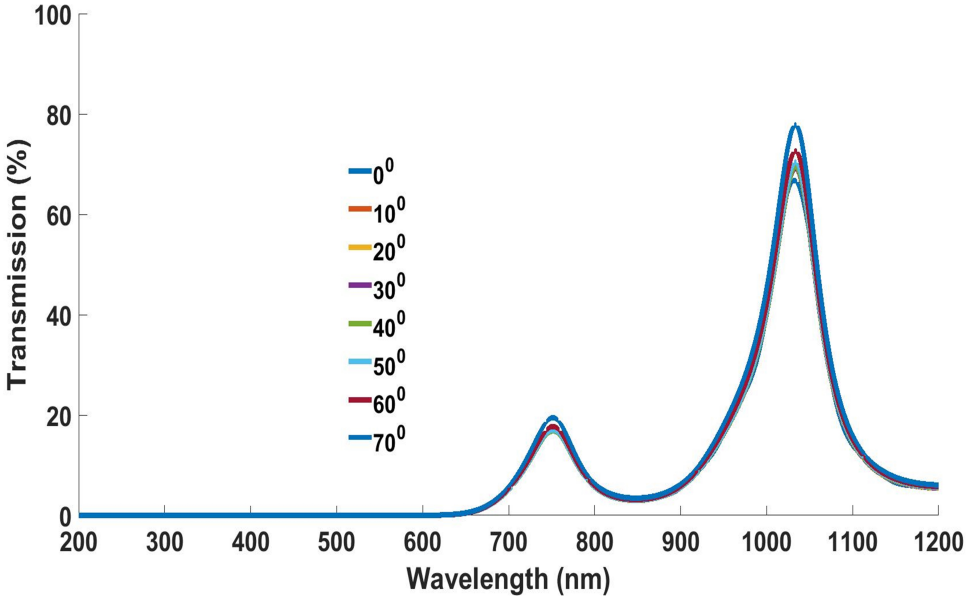

FIGURE 4.16: a) The transmission spectrum, when angle of incident is varied from 0° to 70° in TM mode.

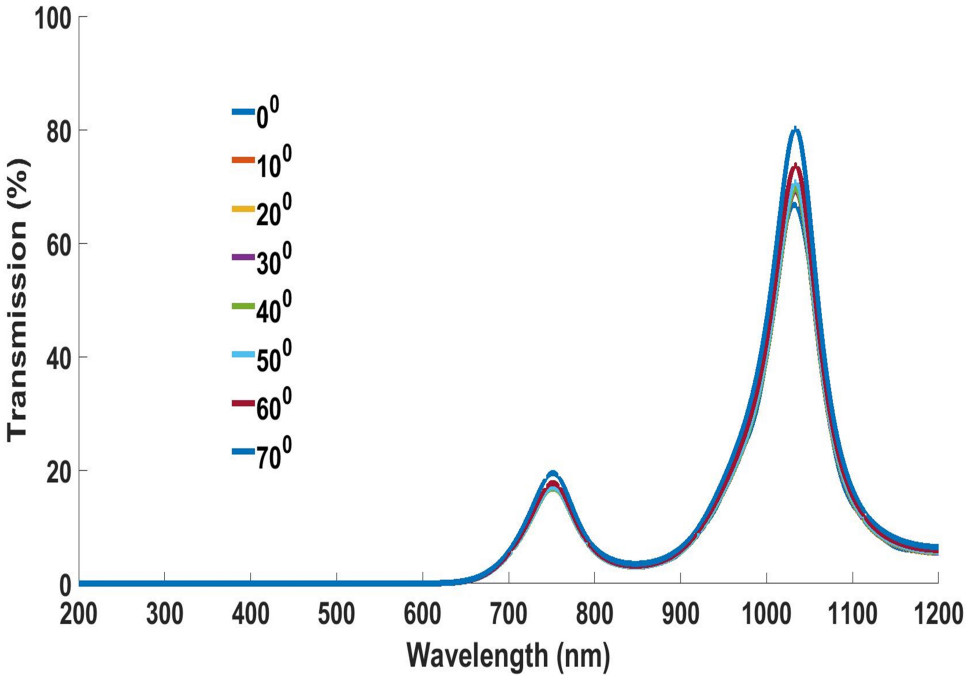

FIGURE 4.17: a) The transmission spectrum, when angle of incident is varied from 0° to 70° in TE mode.

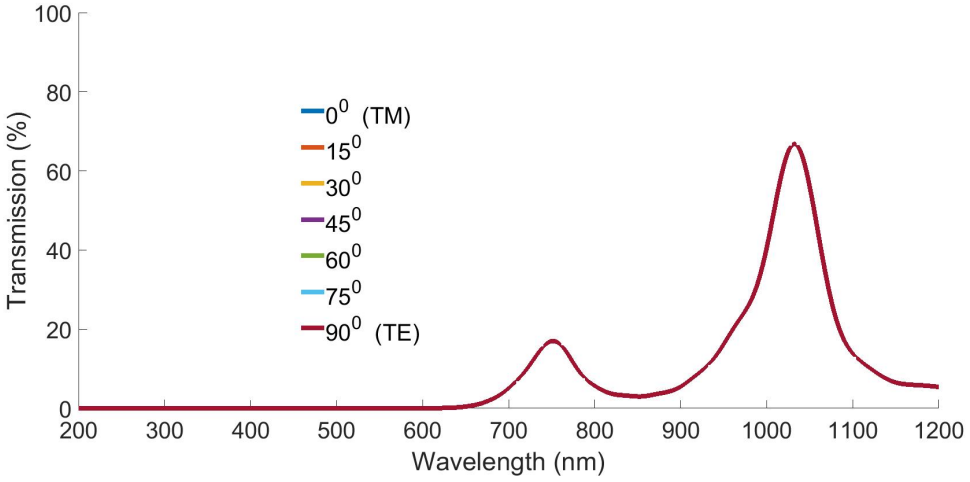

FIGURE 4.18: a) The impact of varying polarization angle(ϕ) of incident light, when it varies from 0° to 90°, where angle of incident is 0°

4.7 Nanofabrication

Nanofabrication is used to materialize the simulated design, which can be further validated via optical characterization. In this thesis, due to unavailability of fabrication facility at Massey University, film depositions were carried out at the Australian National Fabrication Facility (ANFF), at the University of New South Wales (UNSW) in Sydney, Australia.

Upon the completion of the filter designs as described earlier, fabrication recipes were created referring to the relevant published literature. Then the fabrication recipes were thoroughly discussed with the ANFF/UNSW technical team to understand their capabilities and limitations of the processes. This led to some modification in the fabrication steps even before starting the deposition and other processes. Once the fabrication steps were finalized, the technicians started the fabrication process. During this stage a close communication channel (via email and phone) was kept to support the technicians with any questions or challenges they faced that required further research and literature review on our part. All the fabrications and characterization were done under our guidance and as per the design requirements.

4.7.1 Thin Film Deposition

Thin film deposition is the core the required fabrication steps for the designed filter. The procedure to deposit desired material with certain thickness on a substrate is referred as thin film deposition. On the basis of its operation, it is mainly divided into Physical vapour deposition (PVD) and chemical vapour deposition (CVD) [209].

4.7.1.1 Physical Vapour Deposition

Metallization, also known as physical vapour deposition (PVD), is a method to have thin films of metals or alloys onto a coolant substrate under high vacuum conditions. The accumulation or condensation of vapours attains the desired thickness onto the substrate. This process involves four steps:

- Evaporation of the desired material via high energy source.

- Transportation of the vapours to be deposited onto the substrate.
- The reaction between the suitable gas (like oxygen, methane or nitrogen) and the metal atoms during transportation.
- Deposition at the target.

The PVD techniques can be classified into two categories: 1) sputtering; and 2) evaporation. The latter has further subcategories known as thermal and electron beam (e-beam) evaporation in the case of Design II, where titanium oxide (TiO_2) was deposited by employing reactive DC sputter deposition. Here, titanium was deposited in the oxygen environment to obtain TiO_2 film on aluminium.

4.7.2 Chemical Vapour Deposition

Deposition of dielectric materials in this thesis is attained by employing Chemical Vapour Deposition (CVD). It is a chemical process procedure to grow high-purity, high-performance coatings. CVD fits an extensive range of materials, from metals to semiconductors to insulators. In CVD, the substrate is exposed to one or more volatile precursors, which react and decompose onto the substrate surface to deposit the desired film of a certain thickness. Based on its operation, CVD can be further categorized as Metal-Organic CVD (MOCVD), Low Pressure CVD (LPCVD), Atomic-Layer CVD (ALCVD), Plasma -Enhanced CVD (PECVD), Atmospheric pressure CVD(APCVD), Ultrahigh vacuum CVD (UVCVD) and many more [209]. For this study, PECVD is employed to deposit dielectric thin films; therefore, here we explain PECVD led by a fundamental mechanism of CVD.

The CVD process is generally carried out at a high temperature and at low pressure. A basic CVD carries a gas delivery system to supply precursors to the reactor chamber, where deposition takes place. It has a built-in system for installing or removing the substrate in the chamber. It employs an energy source to decompose or react to the precursors. The by-products produced during the chemical reactions are vented out of the exhaust with the help of an exhaust and vacuum system. The temperature, pressure and other parameters are controlled and monitored with the help of control equipment. Figure 4.19 shows the steps involved in a CVD mechanism in the chamber. The procedure can be divided into five steps.

Firstly the chemical or chemicals (also referred to as precursors) to be deposited are

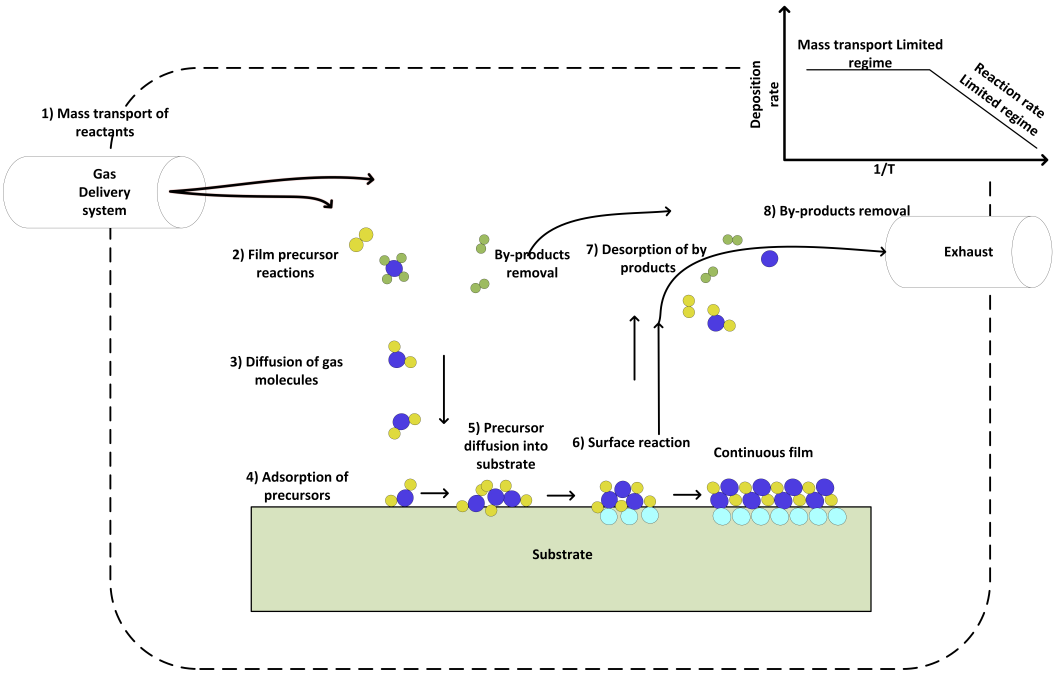

FIGURE 4.19: Depiction of surface reaction mechanism involved in CVD: Precursor gas or gases are pumped into a vacuum chamber containing one or more hot substrates to be coated. Gas particles are adsorbed and chemically react with the heated surfaces when they travel near the substrate. Surface diffusion causes reactive species to persist at surface sites or migrate along the surface, resulting in nucleation and island formation. Clusters (or nuclei) collide and merge to form a continuous film. Surface reaction by-products that are volatile are desorbed and flushed away at the end of the process. Deposition rate vs. substrate temperature is shown in the inset.

transported safely with the help of a gas delivery system. Safety is ensured to maintain its original state and form- chemically and physically. It is more likely that the precursor can react with the walls of the materials through which it is transported, especially at high temperatures. Hence the choice of the precursor is crucial and is mainly taken in its gaseous form for transportation. The transportation to the substrate is achieved through convection.

In general, the substrate is heated to provide the required energy for chemical reaction; however, the precursor may react with each other and decompose before reaching the substrate. The adsorption of the reactants on or near the hot surface is followed by a chemical reaction, which either gets fixed at one spot or migrates along the substrate surface due to surface diffusion resulting in nucleation and island growth. Once the distance between the island growth decreases due to increase bonding between the surface and the molecules, it results in a continuous film.

The film deposition rate is the total reaction rate and reactant arrival time. The reaction

rate is directly proportional to temperature; therefore, at high temperatures, the film deposition rate is mainly dependent on the reactant arrival time due to the fast reaction rate and slow reactant arrival time. Hence this regime is called mass-transport limited, and the deposition rate considers a constant value depending on the reactant arrival time. Similarly, the deposition rate is governed by the slow reaction rate at low temperatures because of comparatively fast reactant arrival time. Hence, this regime is called reaction rate limited.

4.7.2.1 Plasma-Enhanced CVD

As the name suggests, PECVD is a CVD process that exploits plasma for thin film deposition. Figure 4.20 illustrates the working principle of PECVD. Here a mixture of reacting and inert gas is supplied between the cathode and the ground substrate. The supplied RF power at the cathode ionizes the inert gas to capacitive coupling between the cathode and substrate. This ionized gas containing an approximately equal positive ions and electrons is called plasma. It helps in the decomposing the reactant gas and allows further reaction with other gas molecules or substrate material. The radicals generated at this stage can come back to their ground state by emitting photons producing a visible glow, which is associated with the type of gases being used. The ionization process is the same as the recombination process at a steady state. However, the radicals that make it to the substrate chemically react and are adsorbed on its surface. Furthermore, the reactive molecules remain on the surface and form a thin coating, and the by-products are desorbed and exhausted out of the chamber.

The temperature requirement of PECVD generally lies in the range of $250C^{\circ}$ to $350C^{\circ}$, which is relatively low compared to high temperature is driven CVD operations. PECVD also has many other advantages over CVD, such as it has good deposition on steps and corners, more flexibility in the deposition of different materials and less porosity etc. Moreover, the better control of PECVD process parameters allows customization of optical, electrical, and mechanical properties, stoichiometry, and residual stresses of the deposition. However, the high cost and generation of toxic by-products in PECVD materials are inevitable, and it is also not suitable for metal deposition [210].

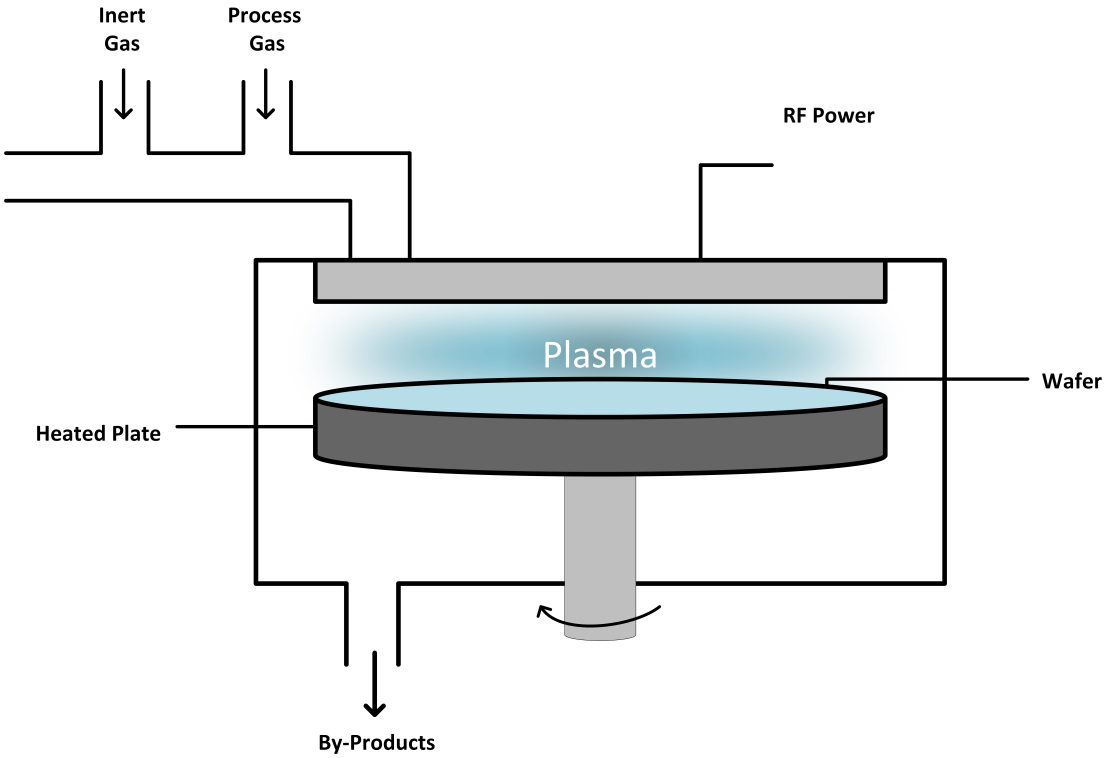

FIGURE 4.20: Typical PECVD process: An insulating or conducting layer on the surface of a wafer is formed using one or more gaseous reactants in PECVD. At lower temperatures, the effectiveness of this layer is further boosted by the addition of a vapour containing electrically charged particles or plasma.

4.8 Deposition of Hybrid Etalon and Cascaded Multilayered Thin Film Filter

As the design used in this thesis comprises dielectric thin films, therefore PECVD is the right choice. In the deposition, an adhesive layer of SiO_2 of 5 nm thickness is deposited for better adhesion between A-Si and Bk7 glass substrate.

Due to the unavailability of tools at Massy University's School of Food and Advanced Technology, the design was sent to the ANFF UNSW campus in Sydney, Australia. The depositions were carried out using an Oxford instrument system 100 PECVD module at $300C^{\circ}$ on Bk7 substrate, without breaking the chamber. The deposition rate for Si_3N_4 and A-Si are 35,3nm/min and 53nm/min,respectively. The specifications of the tool used by the ANFF UNSW team are provided in Appendix C.

4.9 Summary

In this chapter, the detailed simulation study on thin films has been a directive to reach the cascaded multilayered thin-film filter's design. The studied impact of cavity thickness on hybrid etalon helped suppress the sidebands at a higher wavelength. The resultant transmission spectrum demonstrated efficiency up to 70 % with 77 nm FWHM value. The obtained results are independent of the angle of incidence and polarization of the incident light. The evaluation of transmission spectrum at varying incident angles from 0° to 60° in steps of 10° shows a constant peak. Likewise, the design showed the same results when the angle of polarization of incident light varied in steps of 10° from 0° (TM mode) to 90° (TE mode). Furthermore, the design is capable of operating in reflection and transmission modes. Hence, this chapter's study helped produce the simulated results for a lithography-free, omnidirectional, polarization-insensitive narrowband cascaded multilayered thin films filter for NIR filtering.

Chapter 5

Physical and Optical Characterization of Multilayered Thin Films Cascaded Filter

After the thin film depositions were completed, it was necessary to characterize their physical properties. To determine the thickness of the deposited layers, they were cut, and a scanning electron microscope (SEM) was used to image their profiles. However, the conditioning of the samples for enhancing their physical features prior to image taking is vital in this research. Therefore, the sample's dry reactive ion etching (DRIE) etching is done first.

The optical characteristics (transmission, reflection, and absorbance profiles) of the hybrid etalon and cascaded multilayered thin films are obtained by customizing a spectrofluorometer available at the chemistry lab of Massy's School of Food and Advanced Technology. However, the results were unsatisfactory due to unavoidable human, environmental and equipment errors. Therefore, the results were acquired at the ANFF UNSW branch in Sydney, Australia, in a controlled environment.

The physical characteristics of the design are also obtained through Spectroscopic Ellipsometry (SE). It is further employed for investigating the dependence of the transmission spectrum on the incident angle and polarisation direction of the incident light.

Furthermore, the employed physical and optical characterization processes for this thesis,

such as SEM, DRIE, and spectroscopic ellipsometry, are also explained in this chapter. Similarly, the working principles of the spectrophotometer and spectrofluorometer are also elaborated.

5.1 Physical Characterization

The physical characterization methods for examining devices at nanoscales can be divided into three broad categories: spectroscopy, which includes Raman, Fourier-transform infrared (FTIR), and UV-VIS spectroscopy. Second is scattering methods which cover small angle neutron scattering (SANS), small-angle X-ray (SAXS) dynamic light (DLS) scattering etc., and the third is microscopy which includes optical, scanning electron (SEM), transmission electron microscopy (TEM) etc [209].
As multilayered thin films' cascaded filter s' design contains films of A-Si, Silicon dioxide (SiO_2) and silicon nitride (Si_3N_4) with thicknesses varying from 5 to 240 nm, it becomes difficult to distinguish the layers with nearly equal average atomic number. Therefore dry reactive ion etching (DRIE) is carried out to enhance the contrast. Afterwards, the cross-sectional SEM image of the PECVD deposited layers is used to determine the thicknesses of each layer.

5.1.1 Dry Etching

Reactive ion etching (RIE) is employed in the fabrication of topographical structures in micro-and nano-system technologies due to its outstanding process control (etch-rate, selectivity, etch-profile, homogeneity), which is critical for high-fidelity pattern-transfer. RIE is made from a blend of chemical and physical etching, allowing for the removal of isotropic and anisotropic (uni-directional) materials and is categorized into dry and wet etching. Dry etching or DRIE (illustrated in Figure 5.1) is a form of plasma etching wherein the materials are bombarded with ions in a gaseous environment. This act dislocates material particles from the surface, and the etch profile can be isotropic and anisotropic without utilizing crystal direction. Moreover, it is controllable and has stable functioning with vast processing space. Likewise, it has many advantages over its counterpart, i.e., wet (acid) etching which is as follow [211]:

- It helps in improving the physical properties of the materials.

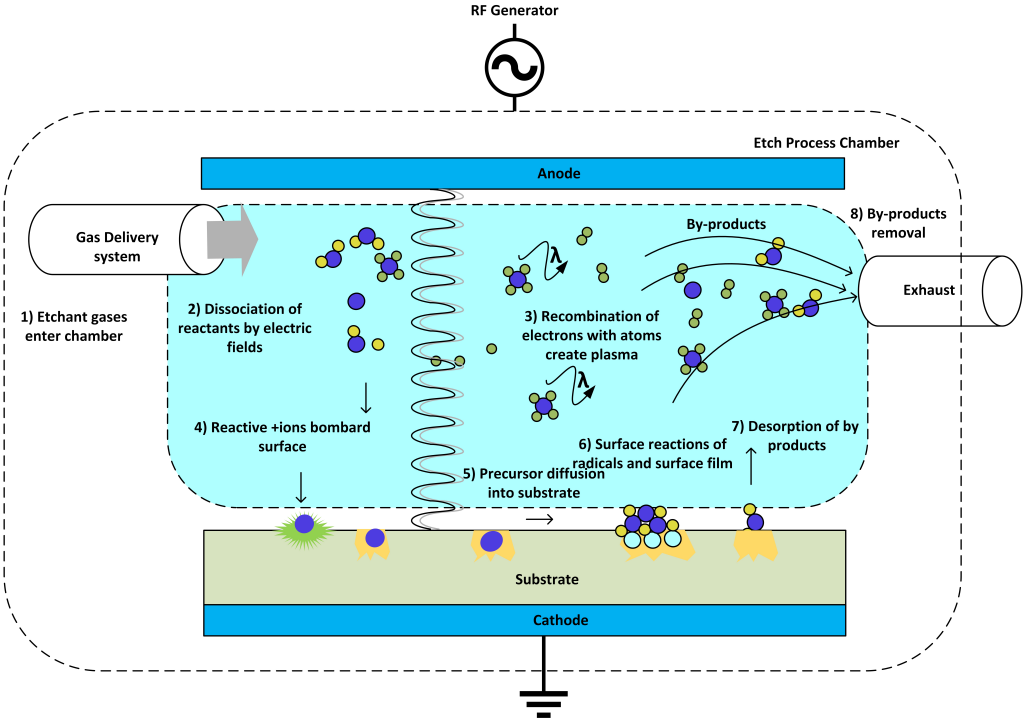

FIGURE 5.1: Demonstration of dry reactive ion etching (DRIE): A reactant gas or gases are pumped into a vacuum chamber. The reactants are dissociated into high-energy electrons, ions, and free radicals due to the electric fields. The plasma is created and maintained by the recombination of electrons with atoms. Because the substrate is placed on a negatively charged electrode, positively charged ions speed towards the sample's surface, generating physical etching by high-energy impact. Chemical etching occurs when reactive ions are adsorbed on the surface and react. Surface reaction by-products that are volatile are desorbed and flushed away at the end of the process.

- It is useful in post-treatment adherence with glues and paints.
- It cleans and eradicates the undesirable organic residues from the metal surface.
- The physical and chemical properties are improved only when none of the properties is changed in the process. Likewise, the treatment of fragile semiconducting wafers and substrates is carried out with the help of dry etchants.
- It sticks two surfaces better than the wet etchants.
- Handling of the dry etchant is easier than acids (wet).
- Although it requires expensive equipment, the process is highly reliable with high resolution and neat lithography.
- Volatile by-products can be flushed out easily.

In this thesis, reactive ion etching (RIE) exploits sulfur hexafluoride (SF_6) etchant in DRIE tool Oxford Instruments RIE 80 at ANFF UNSW facility.

5.1.2 Electron Microscopy

An electronic microscope differs from a conventional microscope by using a focused beam of an accelerated electron as a source of illumination instead of a beam of light. It is useful in obtaining high resolution images of biological and non-biological samples. It is also exploited in particle counting, size determination, and process control. Due to its exceptionally detailed morphological details, this methodology is primitive for investigating and characterization of nanostructural devices. The higher resolving power and resolution is accredited to the 100,000 times shorter wavelength of electrons than that of visible photons [212].

Figure 5.2 shows the occurring events in a specimen when struck by a highly accelerated

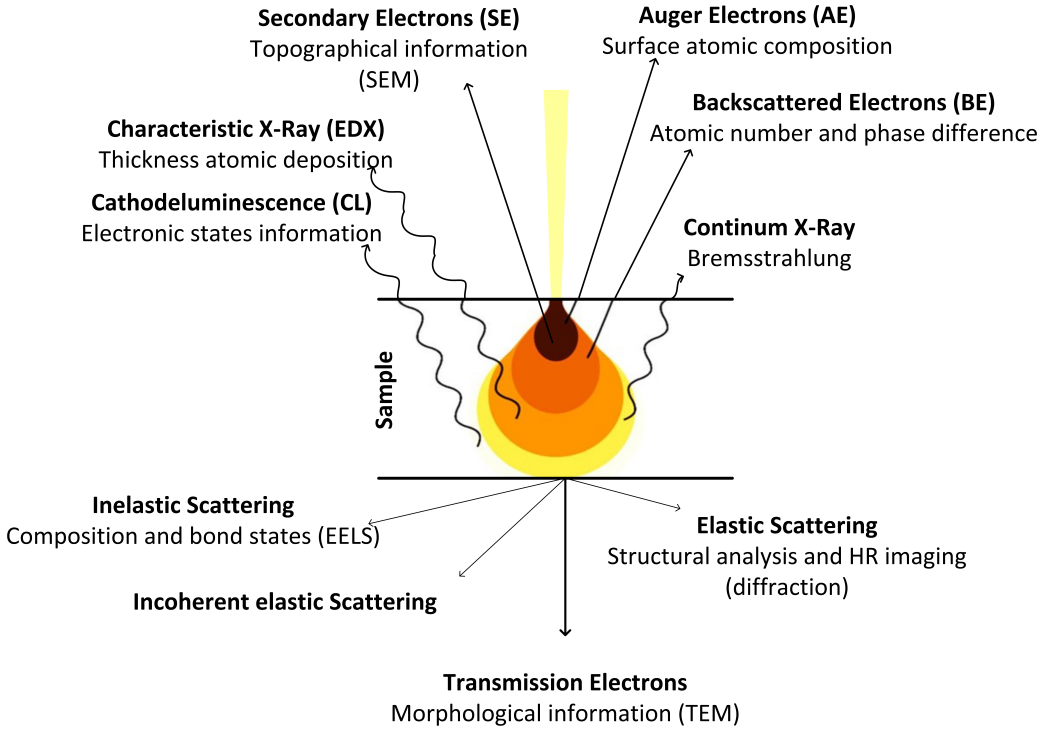

FIGURE 5.2: The electron interaction volume: When high energy electrons enter a material, they encounter numerous scattering events, and the resulting electron interactions create a variety of signals. Each signal is the consequence of electron beam interactions at different depths within the sample and so provides varied information about its surface topography and composition.

electron beam. The specimen volume where these events occur is known as specimen

interaction volume. The nature of interaction depends on the energy transferred from the incident electrons to the sample and results in elastic or inelastic interaction. It is illustrated in Figure 5.2 that electron interactions produce unique signals named Auger electrons (AE), secondary electrons (SE), reflected or back-scattered electrons (BSE), X-rays, photons, cathodoluminescence (CL), plasmons, transmitted electrons, etc. These signals result due to the interaction of electron beams at different depths within the sample. It is to be noted that the reaction at the top of the sample is exploited while investigating thick or bulk specimens and is known as SEM. However, the reaction on the bottom of the sample for examining thin or foil specimens is named TEM.

Here, back-scattered electrons disassociate from their parent atom, occurring normal to the incident electron beam and is scattered backwards with the same energy as the incident beam and can easily penetrate the sample. The back-scattered signals depend on the atomic number of the material (higher atomic number elements emerge brighter as compared to lower atomic number elements) and hence help differentiate different materials coming across. In contrast, the electrons with smaller energy, such as Auger and other secondary electrons, contain information only about a sample's surface.

Typically an electron microscope contains : (i) an electron source (gun) to generate the beam, (ii) two or more stages of electromagnetic lenses to align and collimate the beam, (iii) deflection coils to deviate the beam during the exposure, (iv) apertures to limit and define the beam size, (v) objective lenses to focus the beam on the sample, and finally (vi) electron detectors to provide real-time observation and image recording of the specimen surface. Typically two types of electron microscopes are used, i.e., scanning electron microscope (SEM) and transmission electron microscope (TEM) [213]. Although in this study SEM is used to measure deposited films' thicknesses, TEM is also explained and compared briefly here .

Figures 5.3a and b show the SEM and TEM schematic diagrams, respectively. As explained earlier, the electrons employed for microscopy determine its nature. In SEM, inelastic matter-electron interactions are primarily exploited in SEM, while elastic interactions are predominately exploited in TEM along with electron diffraction methods. Since SEM collects the information from the electrons reflected from the specimen's surface, its thickness does not matter and requires a lesser acceleration voltage range from 1 to 30 KV. The sample preparation for SEM images is straightforward because of no constraints on the sample's thickness. The beam of electrons is focused to a fine point and then scanned line by line over the specimen's surface in a rectangular

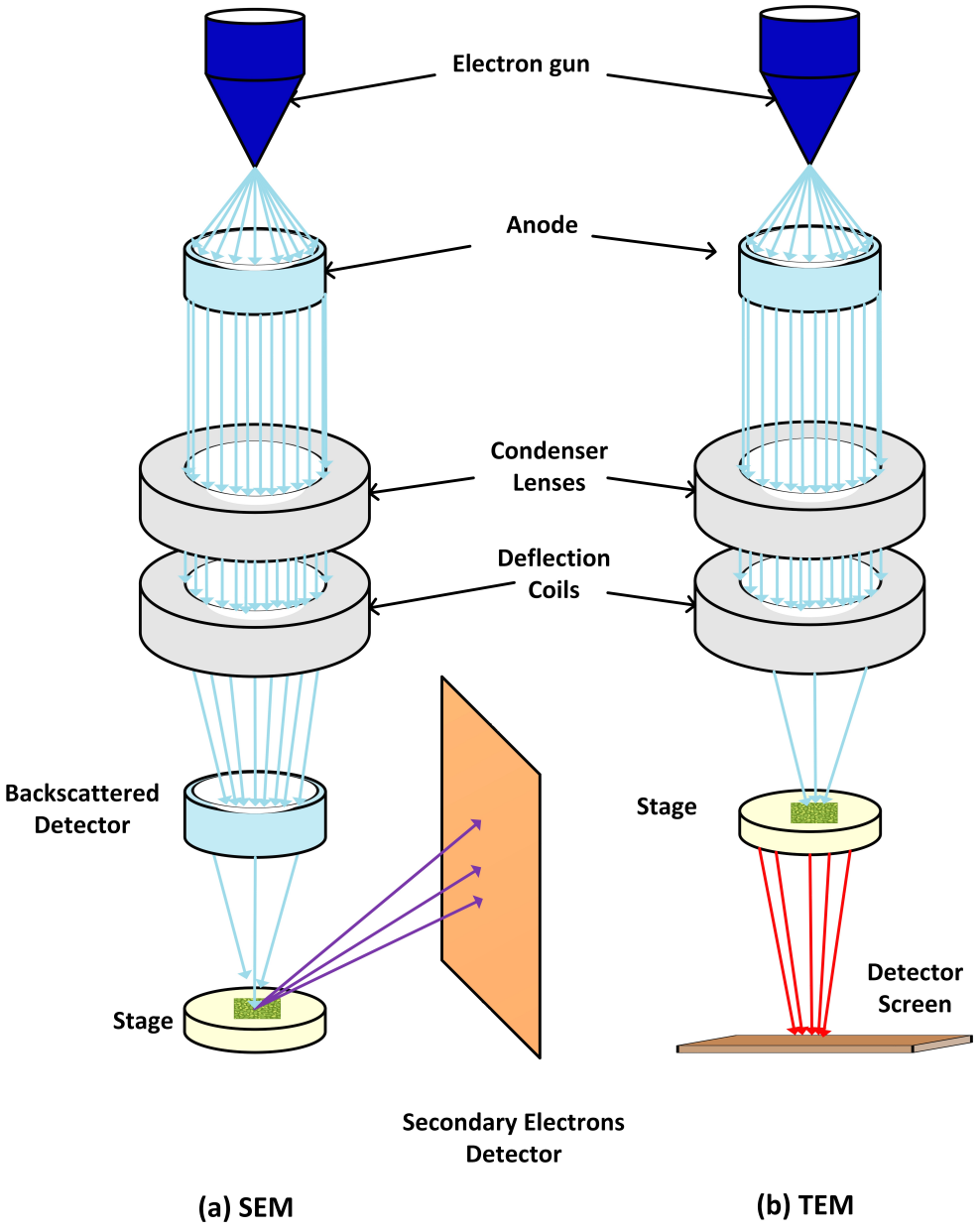

FIGURE 5.3: Schematics of a conventional Scanning Electron Microscope (SEM) and a Transmission Electron Microscope(TEM): A typical electron microscope consists of: i) an electron source (gun) to generate the beam, (ii) two or more stages of electromagnetic lenses to align and collimate the beam, (iii) deflection coils to deviate the beam during the exposure, (iv) apertures to limit and define the beam size, (v) objective lenses to focus the beam on the sample, and finally (vi) electron detectors to provide real-time observation and image recording of the specimen surface. The primary distinction between an SEM and a TEM is in the sort of particles utilized to generate a picture, as well as in the image production process itself.

raster pattern. These electrons are seized and counted by detectors at each point, and the image is displayed on the computer screen. It provides the information about the composition of the materials contained in a sample.

On the other hand, TEM identifies the electrons transmitted through the specimen, with higher penetrating voltages, usually in the range of 60 to 300KVA, and requires a thin sample, as flat as possible. This results in quite challenging and complex sample preparation techniques. It uses a broader, static beam hence only a small area of the sample can be analyzed at a time. After emergence from the sample, an objective lens collect and magnify the electron information. Furthermore, the image is recorded by projecting the magnified electron image onto an imaging device like a sensor of fluorescent screen connected to a CCD camera. Consequently, TEM provides beneficial information on the inner structure of the specimen like morphology, stress state information and crystal structure. Since this thesis is focused on multilayered thin films and to see layers of different materials, SEM is ideal.

5.2 SEM images for Hybrid Etalon and Cascaded Multilayered Thin Film Filters

The cross-sectional image of an SEM image of the deposited thin films is shown in Figures 5.4a and 5.4b for a single hybrid etalon and cascaded multilayered thin film filter, respectively. It is difficult to distinguish the deposited layer, therefore DRIE is applied to the sample. The reactive ion etching in the presence of Sulphur tetra-fluoride (SF_6) is applied to the sample. Before etching, gold (Au) was sputtered in the presence of Argon (Ar) gas with a flow rate of 15 sccm and 18 mTorr at 100 W RF power for 2 minutes. Later, DRIE is performed for 20 seconds with SF_6 at a flow rate of 20 sccm and 100 mTorr at a fixed RF power of 20 W.

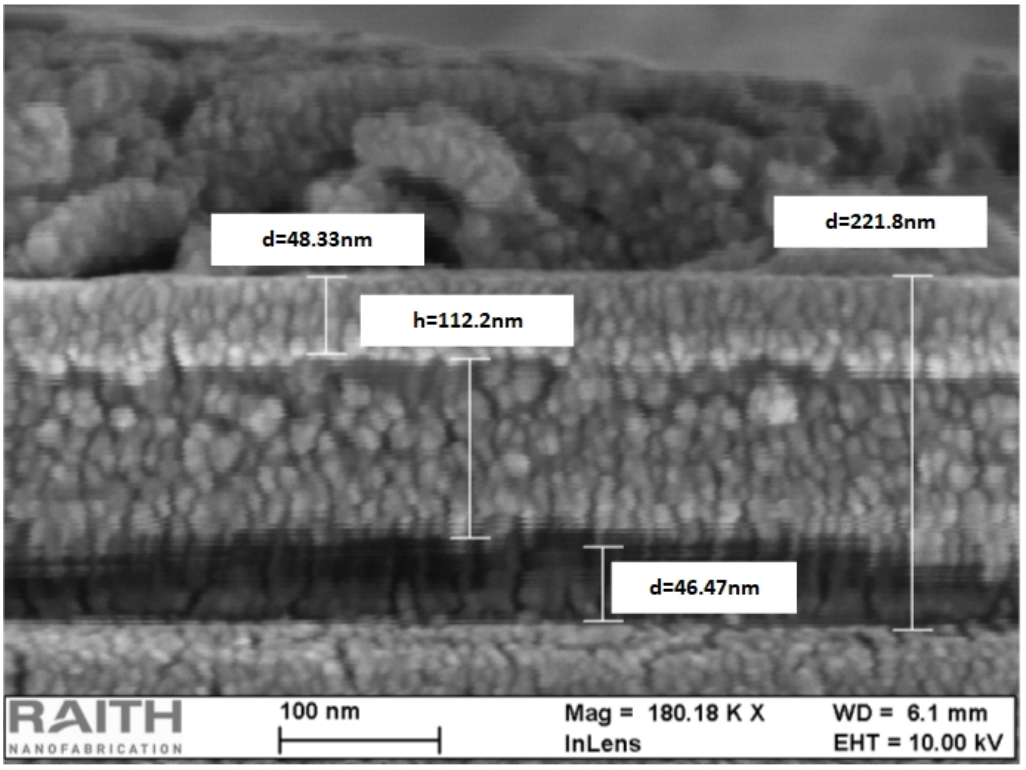

(a)

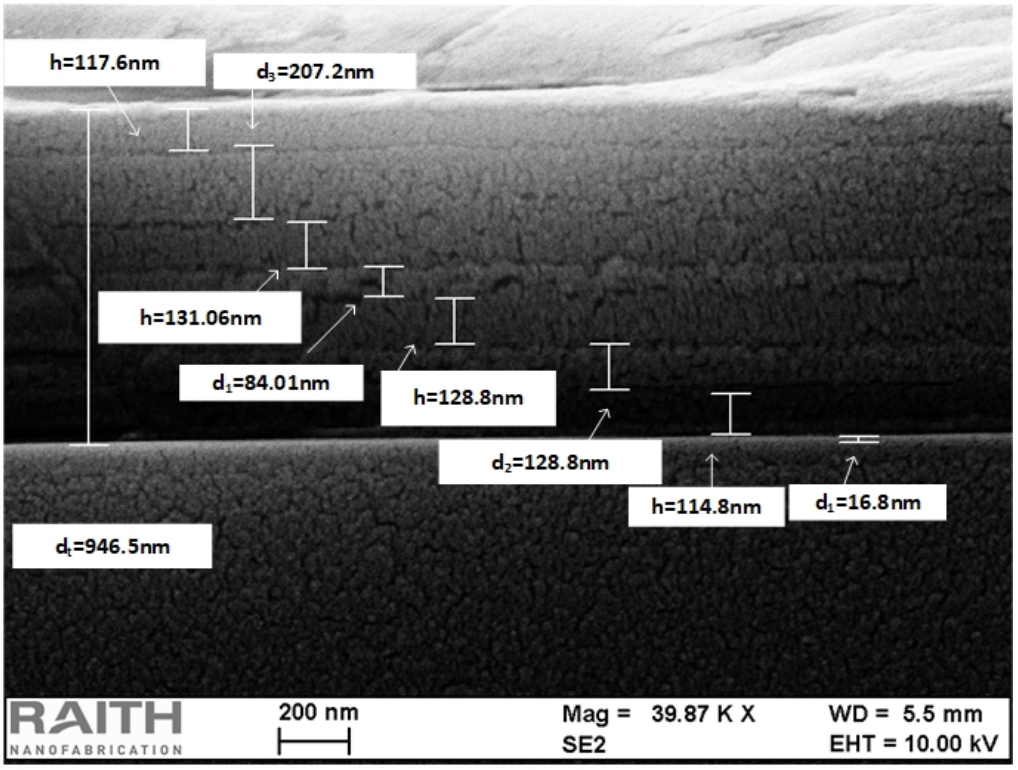

(b)

FIGURE 5.4: SEM images for a) hybrid etalon and b) cascaded multilayered thin film filters.

5.3 Optical Characterization

The optical characterization of thin film requires a UV-NIR spectrophotometer. Due to the unavailability of a spectrophotometer at Massey University's Sensors lab, a spectrofluorometer (RF-6000 Shimadzu) at the Chemistry lab was customized to be used as a spectrophotometer for this particular study.

5.3.1 Spectrophotometer

A spectrophotometer is an analytical equipment used to quantify the transmission or reflection of ultraviolet (UV) light, visible light or infrared (IR) light. It takes light in,

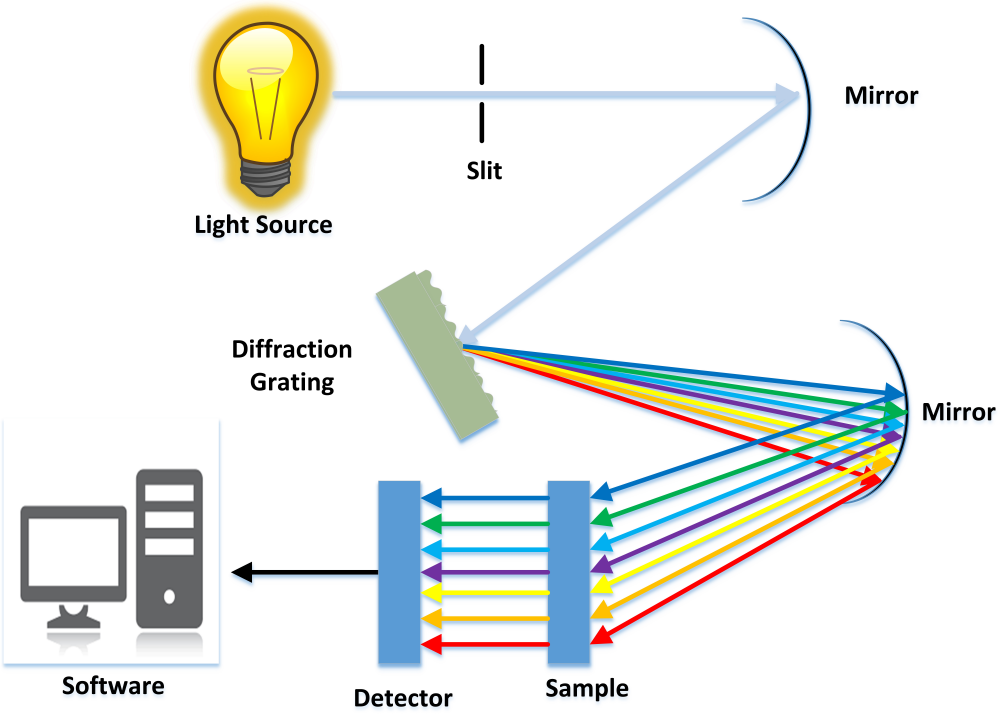

FIGURE 5.5: Ray Diagram of a typical Spectrophotometer: The light source after passing through the entrance slit reflects onto the diffraction grating with the help of the mirror, where it disperse into its component. The dispersed light is directed towards the sample and then to the detector, which captures and evaluates the light as a function of wavelength.

breaks it into spectral components, discretizes the signal as a function of wavelength, reads and displays the result on the screen. Figure 5.5 depicts the working principle of a typical spectrophotometer. The components required to fulfil the functionality are:

- ***Entrance slit*** **:** In general a tungsten halogen , LED, xenon (Xe) arc laser or mercury argon (Ar) are used as a light source in spectrometer. The amount of light measured by the equipment is determined by the width of the slit. It has a direct relation to the optical resolution of the system. The smaller the slit size, the better the optical resolution is. Once the light source passes through the slit, it becomes divergent and travels towards the collimated mirror, reflecting it to the diffraction grating.

- ***Grating*** **:** The diffraction grating allows colour dispersion and transmits the divergent and fragmented beam to another collimating mirror, which directs it towards the sample.

- ***Detector*** **:** It captures the light spectra and evaluates the intensity of light as a function of wavelength. The captured data is further processed and plotted on the screen with the help of software.

Due to the unavailability of spectrophotometers in the lab, a spectrofluorometer was customized to be used as a spectrometer. Figure 5.6 demonstrate the ray diagram of RF- 6000 Schimadzu UV-NIR spectrofluorometer. It mainly consists of five components explained as follows:

- ***Light Source*** A high intensity xenon lamp is used to have high intensity fluorescence.

- ***Excitation Monochromator*** A monochromatic excitation setup is implemented to irradiate the sample with monochromatic excitation light. The input light from the Xenon lamp is directed towards the diffraction grating (DG) with the help of a mirror (M). Here the light is diffracted into fragments, and monochromatic light through a slit is directed to the cell compartment.

- ***Cell compartment*** The cell compartment contains the sample to be tested. Since it is a single beam instrument, the cell compartment holds a single sample cell. The monochromatic light from the excitation monochromator is directed towards the sample, which emits light at different wavelengths. The fluorescence light is emitted in all directions and is directed perpendicularly towards the emission monochromator. This arrangement is ideal for minimizing the effect of excitation light on the fluorescence spectrum is recorded.

- ***Emission Monochromator*** The fluorescence signal is perpendicularly fed to the emission monochromator, from here the light is diffracted to the detector.
- ***Detector*** A highly sensitive photo-multiplier tube (PMT)-based detector is used to detect and amplify weak photon signals from emission monochromator [214].

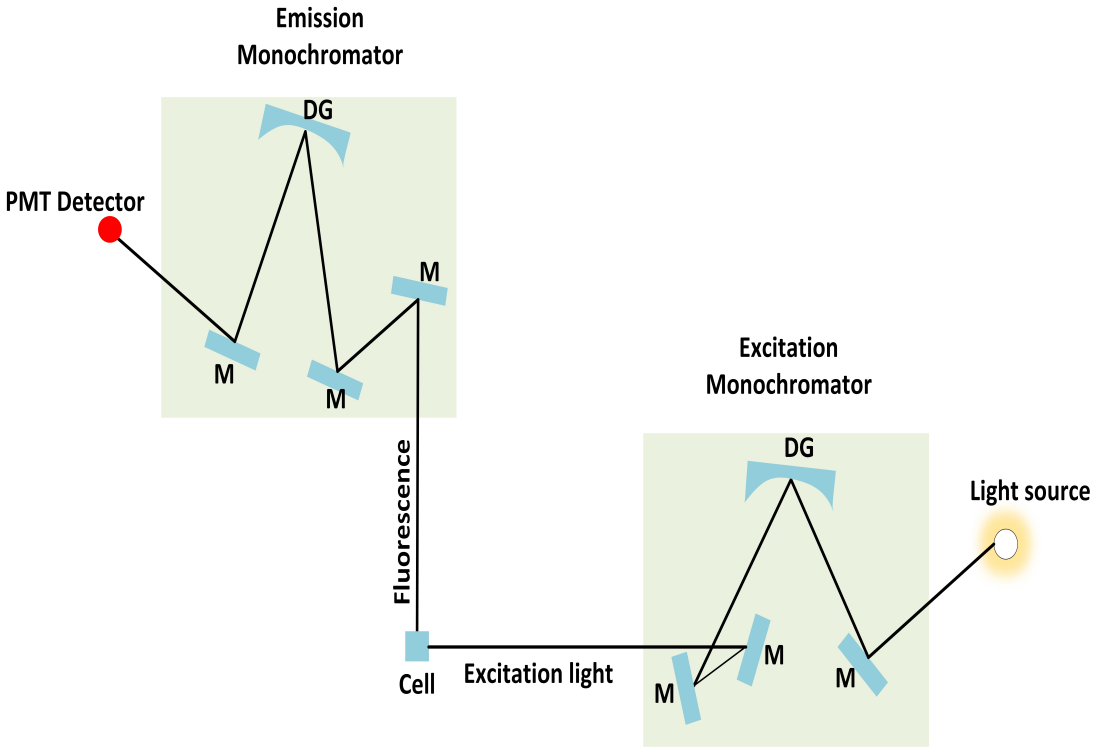

FIGURE 5.6: A typical spectrofluorometer with cell compartment between excitation and emission monochromators.Light with the help of mirror (M) is directed towards the diffraction grating (DG), which split light into fragments, and allows an appropriate excitation light is directed to the cell compartment(sample). The perpendicular fluorescence light falls in the M in emission monochromator, from where after diffraction from DG it is directed to the PMT.

Since the available equipment has a built-in monochromator (excitation), which comes in the path of the light source, it is unsuitable for this particular study.

5.4 Customization of Spectrofluorometer

To overcome the constraints mention in previous section, an optical setup was built inside the cell compartment for implementing a broad light source in the available spectrofluorometer body. The broad light is directed to the sample with the help of an

optical system and a microcontroller controlled rotational stage is designed to examine thin films performance at different angles. A stepper motor (Appendix C), governed with the help of a microcontroller, is used to rotate the rotational stage. The initial position (or home) for the rotating stage is determined with the help of a phototransistor.

Figure 5.7 shows the ray diagram of the designed setup inside the cell compartment. A white light source is impinged on the mirror face of the prism and is directed to the sample (multilayered thin films). Here an iris is used, a movable opening that controls how much light enters the camera. The PMT detector detects the filtered light from the other end of the sample, and the results appear on the screen with the help of LabSolutions RF software.

The installation of the designed setup, in the cell compartment of the spectrofluorom-

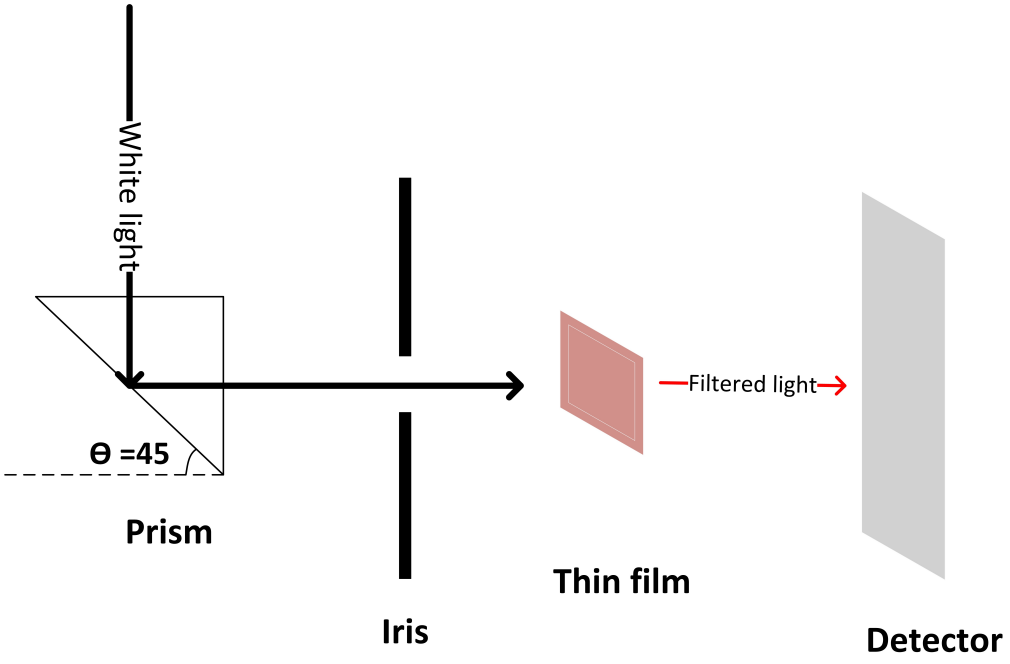

FIGURE 5.7: An L-shaped ray diagram of installed setup inside the cell compartment. Here a broad light source is directed towards the sample by striking the mirror face of the prism. It is further directed towards the sample with the help of an iris, and the output is collected with the help of a PMT detector.

eter, is illustrated with the help of a labelled computer-aided design (CAD) diagram in Figure 5.8. Here the monochromatic light from the excitation monochromator (from Figure 5.6) is blocked.

Figure 5.9a shows the in-house built set-up, designed for installing inside the spectrofluorometer. Figure 5.9b shows the fabricated wafer diced in 25 mm^2 specimens. However, the obtained experimental results with the customized setup in spectrofluorometer were

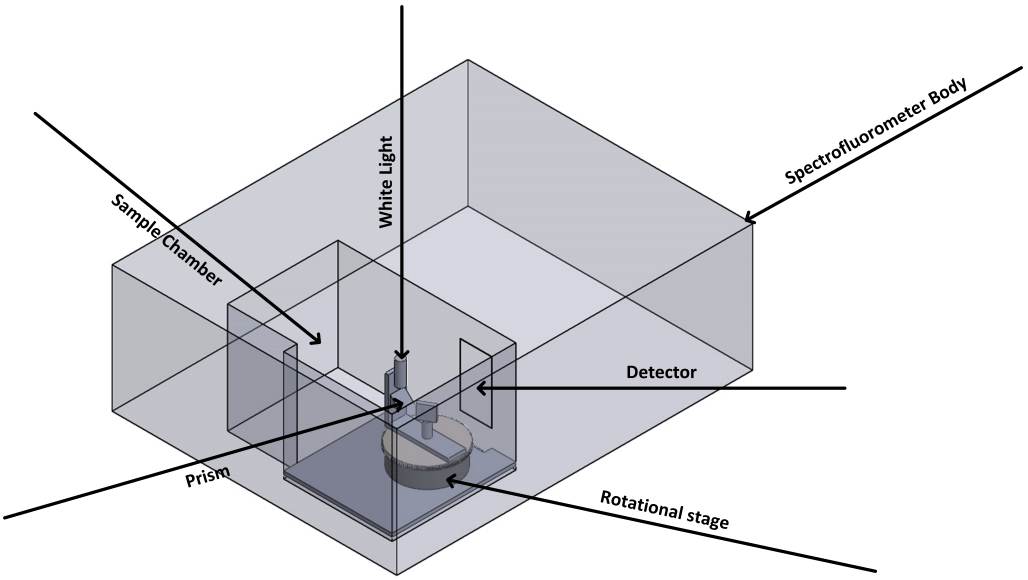

FIGURE 5.8: 3D illustration of the assembled design of customized spectrofluorometer with a white light source.

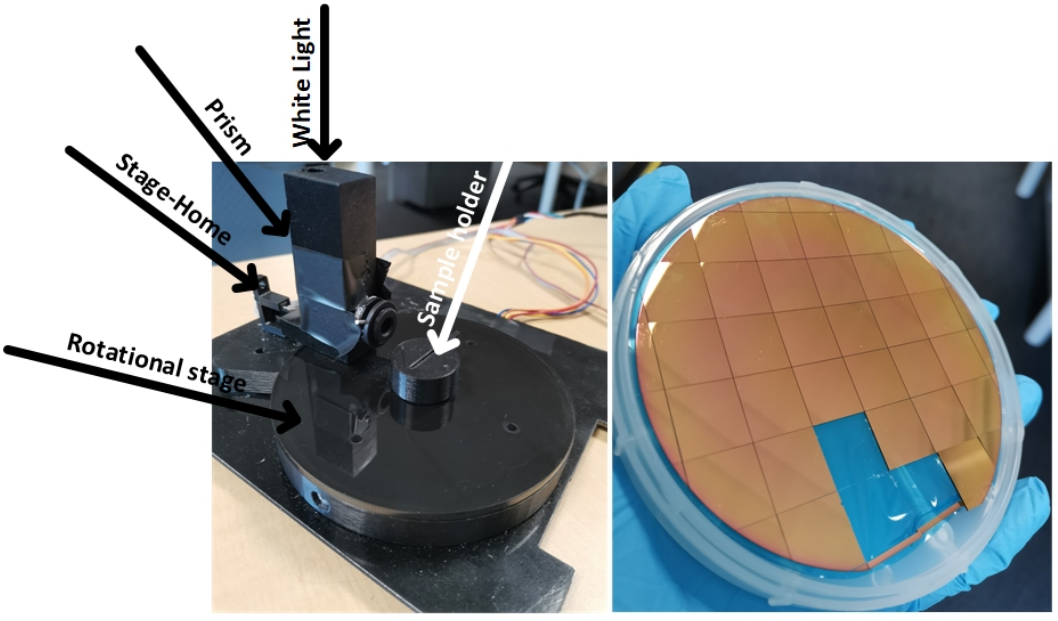

FIGURE 5.9: a) The in-house built system for customizing spectrofluorometer to spectrophotometer. b) Diced wafer after fabrication.

unsatisfactory due to various reasons such as equipment, environment and human error. Therefore the designs were sent to ANFF UNSW for testing in a standard environment.

5.5 Result Analysis of SEM

In this section, simulation results using the deposited layer thicknesses obtained/observed through SEM images are compared with the experimental results (obtained through spectrophotometer). The simulated results are called "theoretical results" and the measured results are called "experimental results" throughout this section.

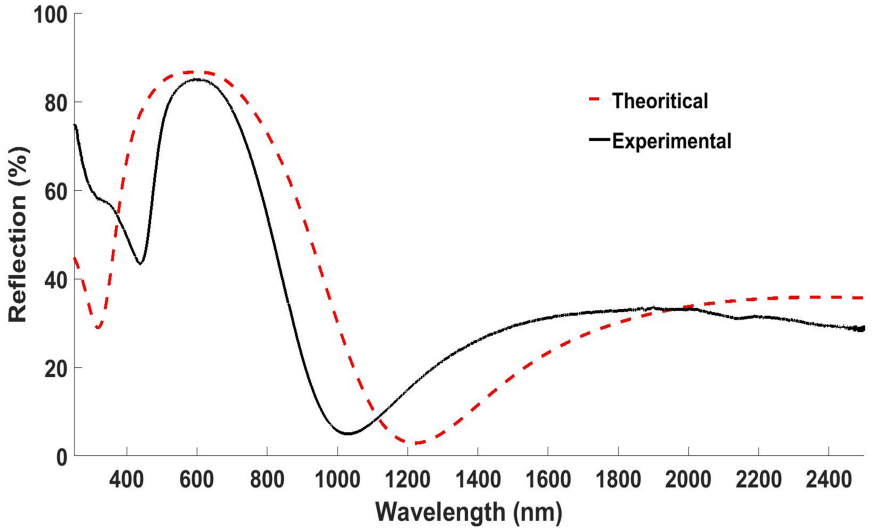

FIGURE 5.10: Theoretical (dotted line) and experimental (solid line) results for reflection spectrum of hybrid etalon with d=40 nm and h= 100 nm.

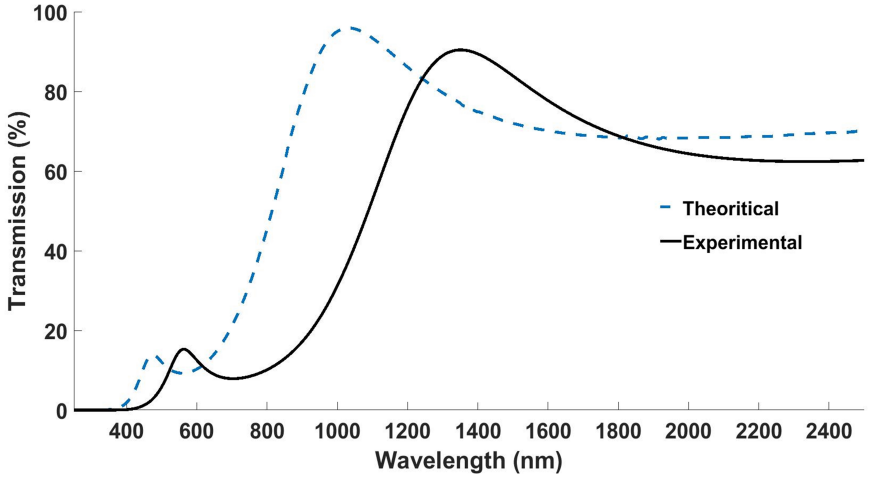

FIGURE 5.11: Theoretical (dotted line) and experimental (solid line) results for transmission spectrum of hybrid etalon with d=40 nm and h= 100 nm.

The theoretical (simulated with measured layer thicknesses) and experimental (obtained via spectrophotometer) results for the reflection and transmission spectra of a single etalon are presented in Figures 5.10 and 5.11, respectively. Here, the discrepancy in the

experimental and theoretical results is accredited to the close average atomic mass of Si_3N_4 and A-Si, which led to the difficulty in distinguishing the deposited layers as seen in Figure 5.4a, section 5.2.

A similar situation is faced in obtaining the accurate thicknesses of the deposited layers of cascaded filters, as shown in Figure 5.12.

It can be observed in the SEM image (Figure 5.4b, section 5.2) that d_1= 16.8 nm, which is nowhere close to the proposed design (Figure 4.14a, section 4.4 where d_1 = 80 nm). The same discrepancies can be seen in the other 7 layers. It highlights the difficulty in determining the exact thicknesses of the deposited layers through SEM, which has also impacted the transmission spectrum, as shown in Figure 5.12.

Alternatively, the thickness of such designs, where material constituents are close in average atomic mass, can be obtained through spectroscopic ellipsometry (SE) [215]. It is discussed in detail in the next section.

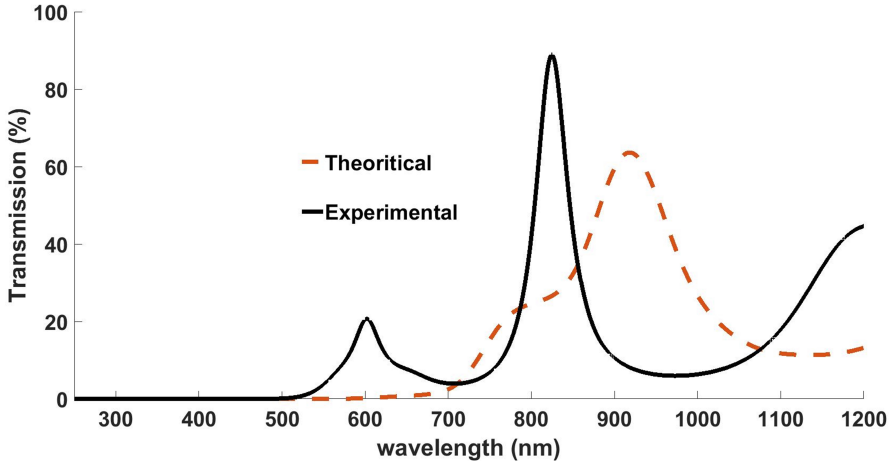

FIGURE 5.12: Theoretical (dotted line) and experimental (solid line) results for multilayered thin films cascaded filter.

5.6 Spectroscopic Ellipsometry

Spectroscopic ellipsometry, or simply ellipsometry, is a technique for characterizing thin films and bulk materials that use polarised light. It has been used to calculate optical constants, thin film thickness, doping concentration, surface and interfacial roughness, alloy ratio, crystallinity, optical anisotropy, material depths profile, growth or etch rate (in-situ), or temperature (in-situ). The combination of SE with changing the

angle of incidence is an incredibly robust measuring method. It offers several benefits over comparable optical characterization techniques, for instance, single wavelength ellipsometry, reflectometry etc.

The essential steps required to derive results through ellipsometry are discussed first here.

As the light interacts with a sample's structure, its polarisation changes (Figure 5.13). This change in polarization is represented by Psi (ψ) (reflection amplitude ratio angle of incident TM polarization and TE polarization) and Delta (Δ) (phase difference between the TM and TE polarization).

In Figure 5.13 the plane of incidence (grey area) is defined as the plane including the input and output beams, as well as has direction normal to the sample surface. The polarization of incident light is given as electric fields parallel (p- or TM mode) and perpendicular (s- or TE mode) to the plane of incidence [215].

Mathematically, this is expressed by an amplitude ratio ($\tan\psi$) as well as a phase

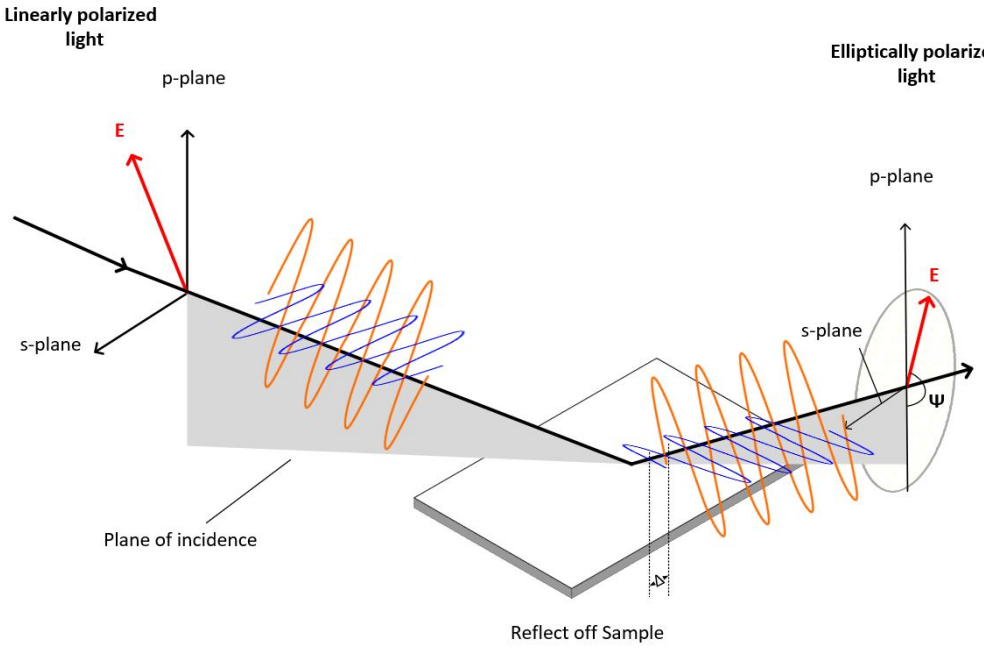

FIGURE 5.13: The ellipsometric experiment's measurement geometry. In the p-s coordinate system, the coordinate system is used to describe the ellipse of polarisation. The s-direction is defined as parallel to the sample surface and perpendicular to the direction of propagation. The p-direction is assumed to be perpendicular to the direction of propagation and lies inside the plane of incidence. The plane of incidence (grey area) is defined as the plane including the input and output beams and the direction normal to the sample surface.

difference (Δ):

$$tan(\psi)e^{\iota\Delta} = \frac{\tilde{r}_p}{\tilde{r}_s}; \tag{5.1}$$

where $\tilde{r}_p$ and $\tilde{r}_s$ are the Fresnel reflection coefficients for p– and s– polarized light, respectively.

An ellipsometer is used to collect the ellipsometric parameters (ψ, Δ) within a given spectral range and incident angles. However, the measured data (ψ, Δ) does not provide direct information. A data analysis procedure is required to extract meaningful physical information about the sample. The following steps are usually included in the data analysis procedure [216–218], as outlined in the flow chart in Figure 5.14.

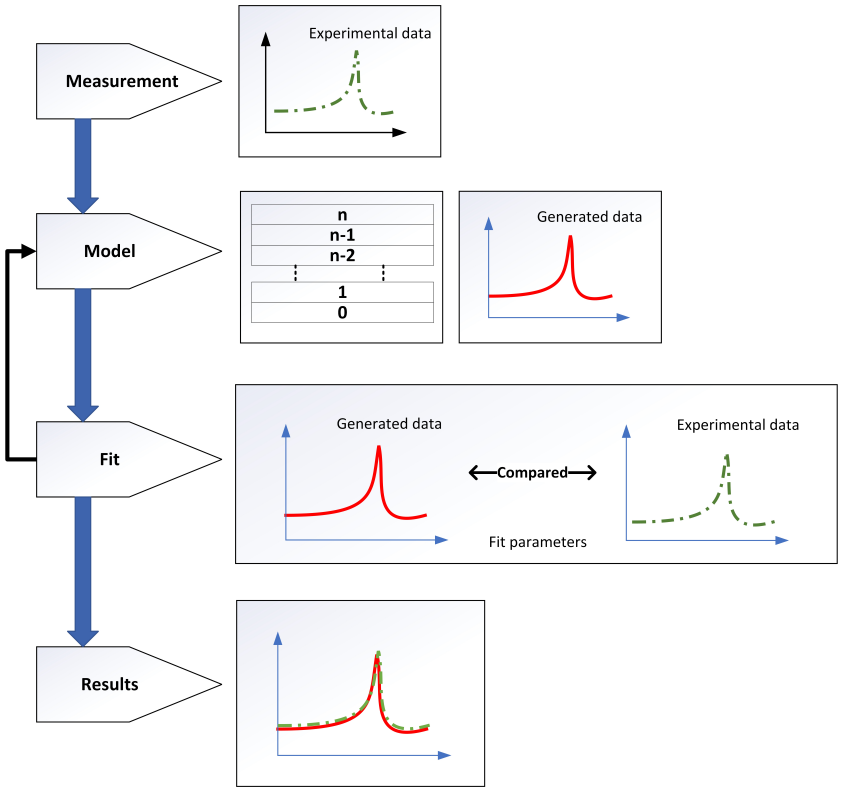

FIGURE 5.14: Flow chart for ellipsometry data analysis.

1. The first step is to acquire experimental data of the sample. In this particular case, a Perkin Elmer Lambda 1050 UV-Vis-NIR spectrophotometer is used to collect the transmission and reflection experimental data.

2. The second step is to create an accurate optical model of the sample system. Here, every material in the system, such as the substrate, A-Si and Si_3N_4 layer, is viewed as a "layer." This model is used to generate SE data.

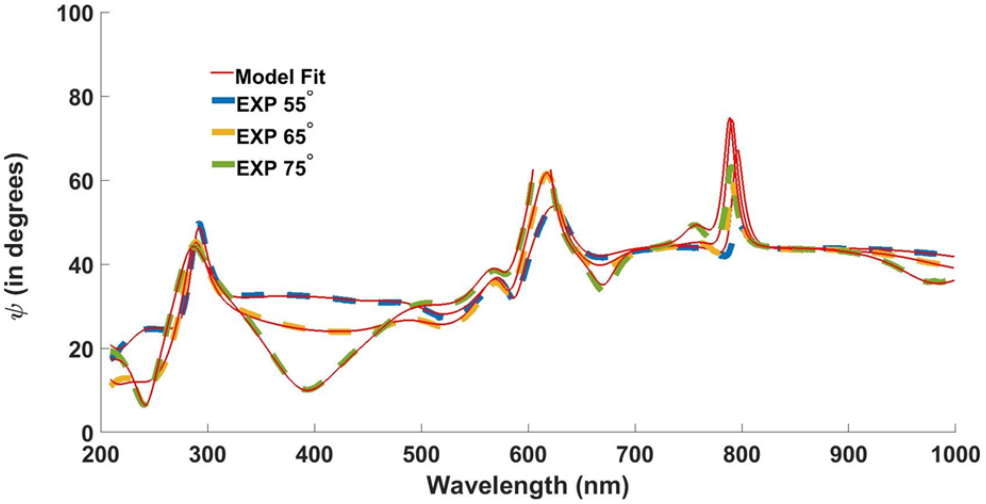

FIGURE 5.15: Ellipsometric fit to the proposed design extracted at 55°, 65°, and 75°.

3. In third step model fit parameters (such as n&k values of each layer, thickness etc.) are defined, and the software adjusts them automatically to improve the agreement between measured and model-generated SE data. This is referred to as 'fitting' the data.

4. The fit's outcomes are assessed. If the results aren't satisfactory, the optical model and/or fit parameters are modified, and the data is re-fit. Mean-Squared Error (MSE) is a parameter that evaluates the quality of the match between the generated and the experimental data [219]. Mathematically,

$$MSE = \sqrt{\frac{1}{2N-M}\sum_{i=1}^{N}\left[\left(\frac{\psi_i^{mod}-\psi_i^{exp}}{\sigma_{\psi,i}^{exp}}\right)^2+\left(\frac{(\Delta_i^{mod}-\Delta_i^{exp}}{\sigma_{\psi,i}^{exp}}\right)^2\right]}; \tag{5.2}$$

where, N is the number of (ψ, Δ) pairs, M is the number of variable parameters in the model, and σ is the standard deviation on the experimental data points. MSE should be positive and near zero for the maximum likelihood estimate. Figure 5.15 shows the model fit to the experimental data with mean-squared error (MSE) = 30.51, when the light is incident at 55°,65° and 75° angles.

The obtained thicknesses of the cascaded filter via SE are provided in Table 5.1.

Figure 5.16 provides the comparative analysis for ellipsometric data, experimental and simulated data for multilayered thin films cascaded filter. It is to be notified that simulated results are obtained by employing thicknesses provided in Table 5.1. Hence, it

TABLE 5.1: Thicknesses of deposited films extracted with the help of ellipsometry

Layer numbers	Symbol	Material	Thicknesses (nm)
1	L_1	A-Si	54.730
2	L_2	Si_3N_4	84.430
3	L_3	A-Si	112.557
4	L_4	Si_3N_4	112.043
5	L_5	A-Si	52.043
6	L_6	Si_3N_4	106.518
7	L_7	A-Si	165.611
8	L_8	Si_3N_4	101.408

can be deduced that the the SE obtained thicknesses for each of the deposited layers are in unison to the PECVD deposited layers. Figure 5.17 illustrates the angle invariance

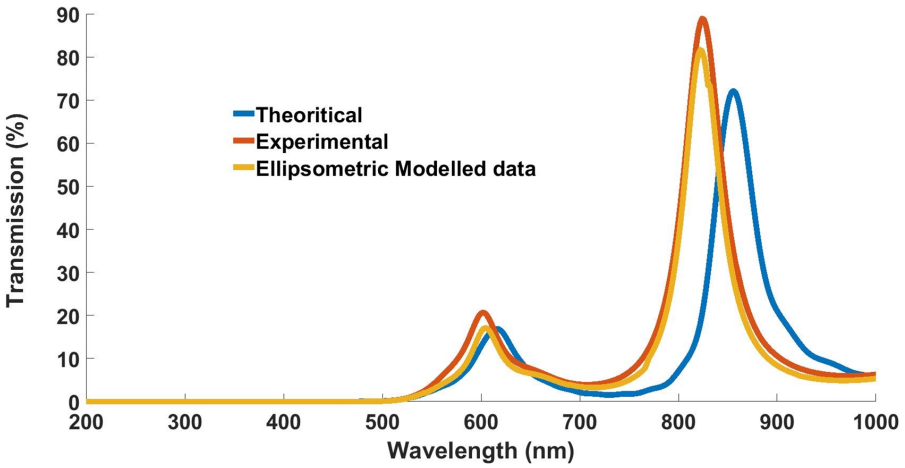

FIGURE 5.16: Transmission spectrum produced with the help of theoritical, experimental and ellipsometry derived data.

of the proposed design when the incident angle varied from 0° to 60° in TM mode. Likewise, the angle invariance of the proposed design when the incident angle varied from 0° to 60° in TE polarization is demonstrated in Figure 5.18. It is observed from the obtained results that λ_{res} varies from 823 nm to 794 nm from 0° to 50°; however, the maximum resonant shift is observed at the highest angle, i.e., 60°.

5.7 Summary

In this chapter, the proposed design has been explained with the help of simulated and experimental results obtained by physical and optical characterization. An existing spectrofluorometer was customized for the optical characterizations; however, the

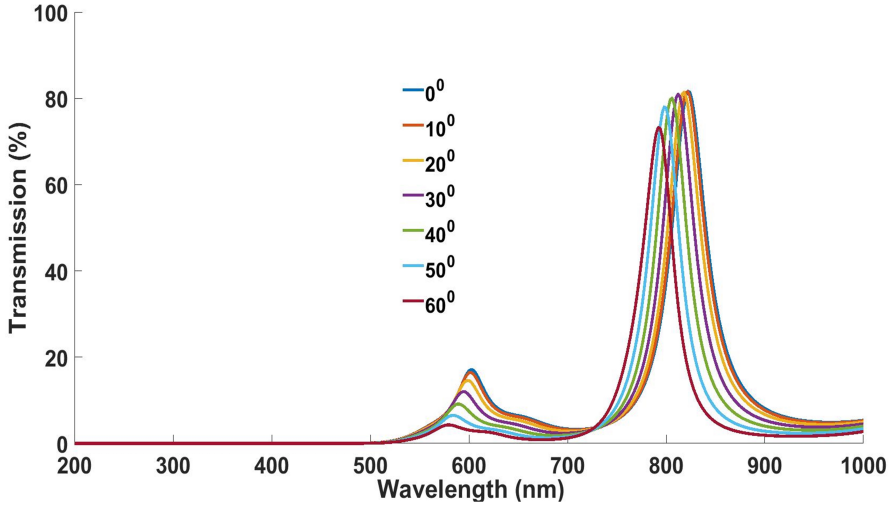

FIGURE 5.17: Transmission spectrum when incident angle varies from 0° to 60° in TM mode polarization.

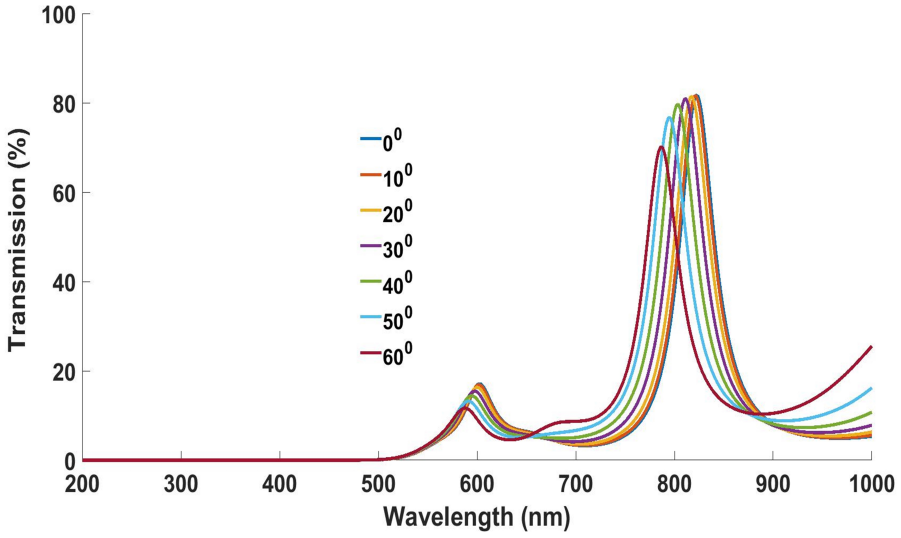

FIGURE 5.18: Transmission spectrum when incident angle varies from 0° to 60° in TE mode polarization.

customization did not work as desired due to the lab/workshop access limitations. This led to the decision to get the characterizations done at UNSW ANFF.

The thicknesses obtained with the help of SEM were not helpful and resulted in discrepancy in simulated and experimental results. These discrepancies are accredited to the SEM limitations in distinguishing between the layers of same average atomic mass. However, alternatively, film thicknesses were obtained through SE and the simulated results were in agreement with the experimental results. Furthermore, the results for polarization insensitivity and angle invariance up to 50° were also produced with the help of SE, which have a reasonable agreement with the experimental results.

Chapter 6

Design of Asymmetric Fabry-Pérot (FP) Nanocavity Incorporating CMOS compatible Tungsten

This chapter presents an analytical and experimental study of a subtractive colour filter by proposing a novel thin film colour filter design capable of producing vivid subtractive colours.

The first section covers the design specifications, including its constituents and film thicknesses' requirements for achieving the desired results. Likewise, the resonance conditions for CMY colour filters is investigated in detail. The reflection spectrum at different cavity thicknesses is observed to obtain a vivid colour palette. The reflection response of the design is further evaluated at a different incident and polarization angles of insensitivity. The film deposition for vivid colours and its physical and optical characteristics are also part of this chapter.

6.1 Design of Asymmetric FP Nanocavity Incorporating CMOS compatible Tungsten

Here an analytical study of subtractive colour filter based on a CMOS compatible tungsten (W) material is presented. There are examples where W and tungsten trioxide (WO_3) are used for broadband light absorption for dynamic temperature applications and dynamic colour filtering in nanostructural colour filters, respectively [220–222]. However, the proposed design is inspired by the work done in the nanostructural colour filtration where asymmetric FṔ nanocavities are used to present the impact of novel materials such as nickel (Ni) and platinum (Pt) [62, 200] on filters' performance.
Here, we have studied the same design by employing W in an asymmetric FP' etalon for subtractive colour filtration. W has a high degree of flexibility, a low evaporation rate, a high melting point, and a strong electron emission ability. Moreover, tungsten and its alloys are often employed in nanoelectronics because of its CMOS compatibility [223]. The proposed design comprises an asymmetric FP cavity with titanium oxide (TiO_2) of thickness d sandwiched between W of thickness t and Al films of thickness h. The cavity is deposited on a silicon (Si) substrate, as illustrated in Figure 6.1.

For simulating the design, a TM polarized plane wave source is perpendicularly injected from the top of the device i.e., along '-z' direction. The direction of polarization is parallel to the plane of incidence, and the magnetic field is along the y axis. As per the requirement of the proposed design, the wavelength of the plan wave varies from 400 to 700 nm (visible region). To reduce the computational time, the boundary conditions for the x and y-axis are anti-symmetrical and symmetrical, respectively. However, PML is used along the z-axis, and the mesh size is 4 nm in all directions.
The refractive indices of Al and W are extracted from Paliks' database [208], while the refractive index of TiO_2 is obtained through ellipsometry using a spectroscopic ellipsometer (M-2000D, J.A. Woollam). Figures 6.2, 6.3 and 6.4 show the plot of real (n) and imaginary (k) values of refractive index versus wavelength values of TiO_2, W and Al respectively. The thickness of the bottom Al layer h is set to 50 nm such that incident light could be sufficiently reflected throughout the visible band and transmission is blocked.

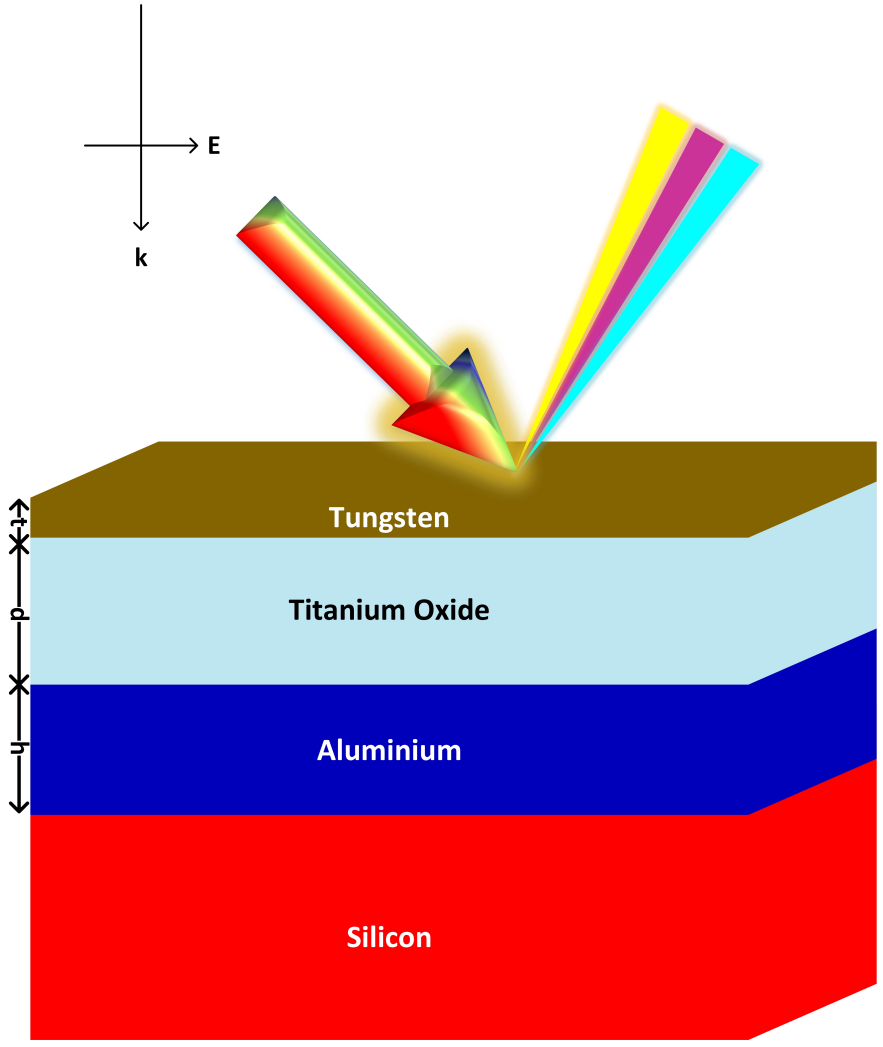

FIGURE 6.1: Schematic diagram of the proposed design. A 3D perspective of the proposed design of asymmetric Fabry-Pérot cavity with a TiO_2 of thickness d is sandwiched between thin tungsten (W) of thickness t and thick aluminium (Al), grown on a Si substrate.

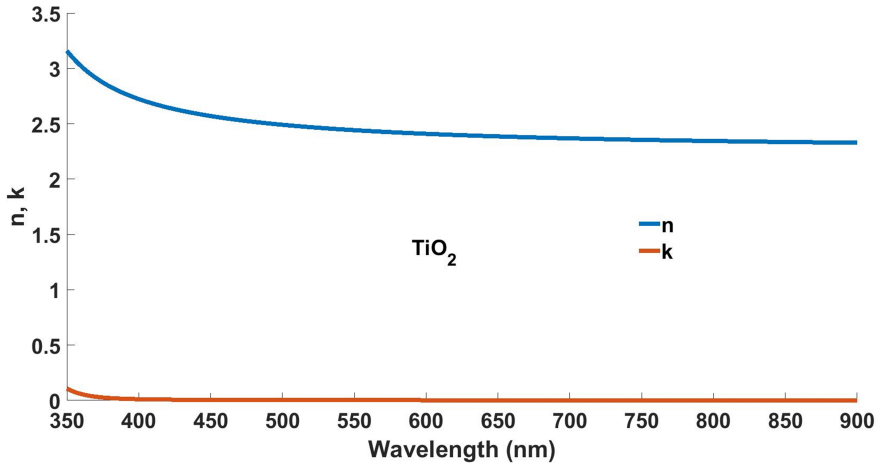

FIGURE 6.2: Refractive index of Titanium oxide (TiO_2) obtained through ellipsometry.

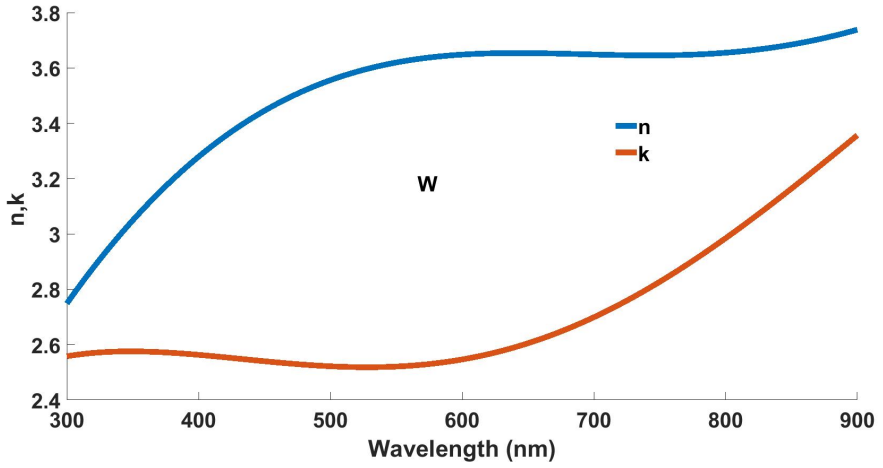

FIGURE 6.3: Refractive index of tungsten (W) obtained from Palik's database [208].

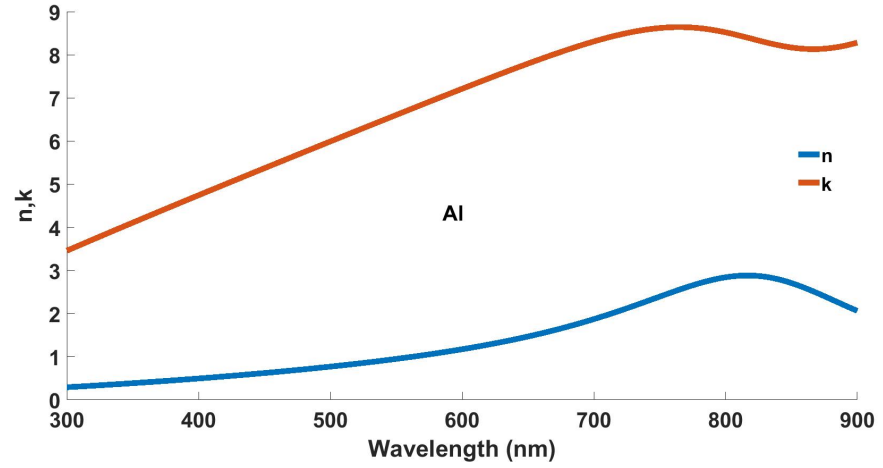

FIGURE 6.4: Refractive index of aluminium (Al) obtained from Palik's database [208].

6.1.1 Thickness d of TiO_2

At 5 nm thin tungsten (i.e., t=5 nm), the impact of cavity thickness 'd' on the device performance is investigated by sweeping d from 0 to 300 nm in the visible region of the electromagnetic spectrum. Figure 6.5 illustrates the contour plot of the visible reflection spectra in accordance with the TiO_2 thickness. An increase in d invites higher modes into the spectrum. The white dotted lines on the contour point to the probable locations of resonant wavelength (λ_{res}) at different d.

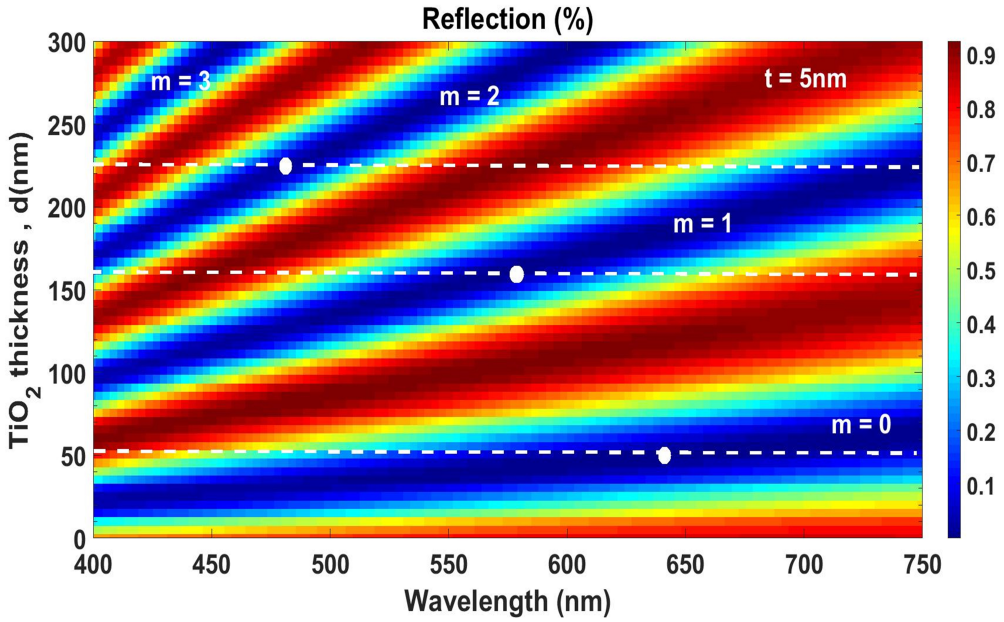

FIGURE 6.5: Contour plot of the visible reflection spectra in accordance to the TiO_2 cavity thickness at t=5 nm.

6.1.2 Thickness t of W

It is learnt from previous section that resonance (λ_{res}) sweeps across visible regime by sweeping cavity thickness from 0 to 300 nm. In this section thickness of W layer 't' is varied to see its influence on the reflection spectra for cyan (C), magenta (M) and yellow (Y) colours.

From Figure 6.5 the $\lambda_{res} \approx 550$ nm (for magenta colour) can be achieved when $d \approx 150nm$ and $t = 5nm$. Figure 6.7 shows the effect on reflection dip when at $d = 150nm$ W thickness 't' is varied from 0 to 20 nm. It is obvious from Figure 6.7 that at d= 150 nm and t=5 nm a resonance occur at $\lambda_{res} = 544$ nm with minimum reflection(R) dip up to and 0.6 % and 99.4 % absorption. It can also be seen that as the tungsten value

increases, the reflection dip increases and results in lower colour quality. Hence, t=5 nm is the optimum thickness of the W layer.

Furthermore, the same effect is also noticed for λ_{res} for cyan(C) and yellow (Y) colours in Figures 6.6 and 6.8 respectively. The contour plot for cyan colour shows reflection dip at 0.6 % and absorbance peak at 99.4 % at $\lambda_{res} = 625nm$. However, the contour plot for the yellow colour shows reflection dip at 2.4 % and absorbance peak at 97.6 % at $\lambda_{res} = 433nm$.

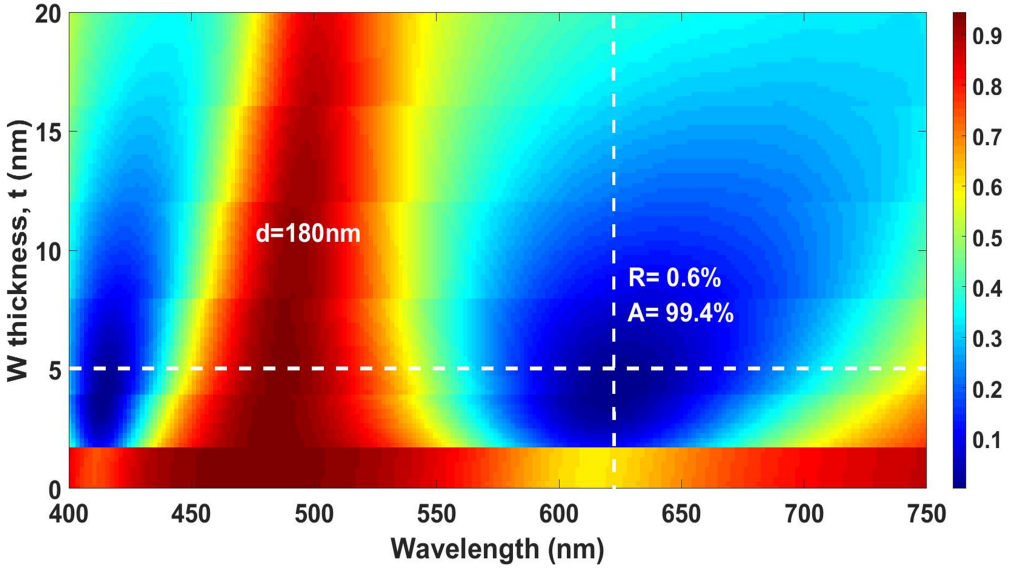

FIGURE 6.6: The reflection dip and absorption peak occur at the resonance wavelength $\lambda_{res} = 625nm$ for cyan colour.

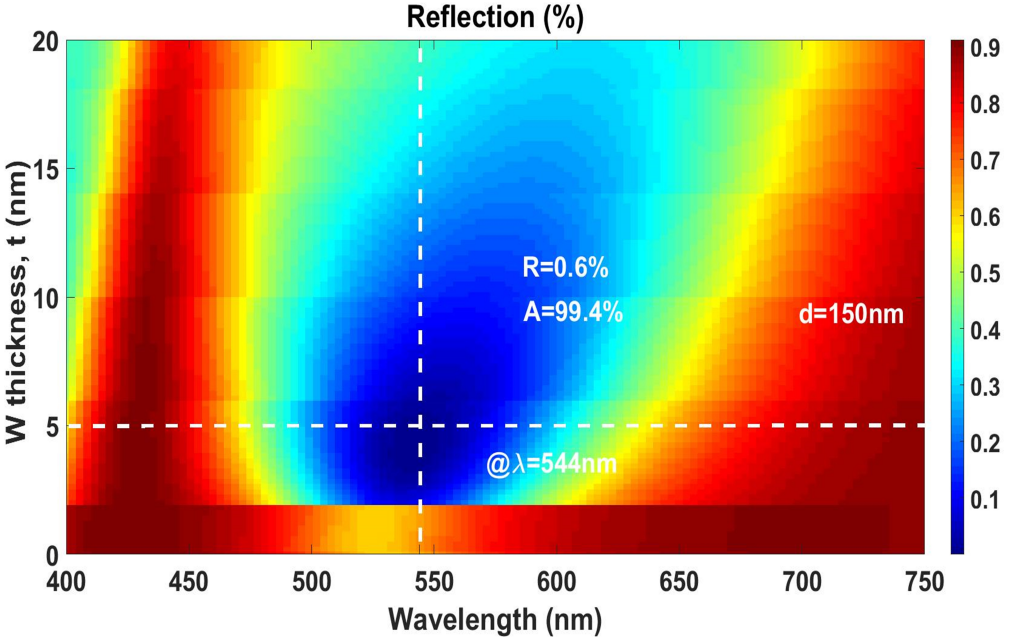

FIGURE 6.7: The reflection dip and absorption peak occur at the resonance wavelength $\lambda_{res} = 544nm$ for magenta colour.

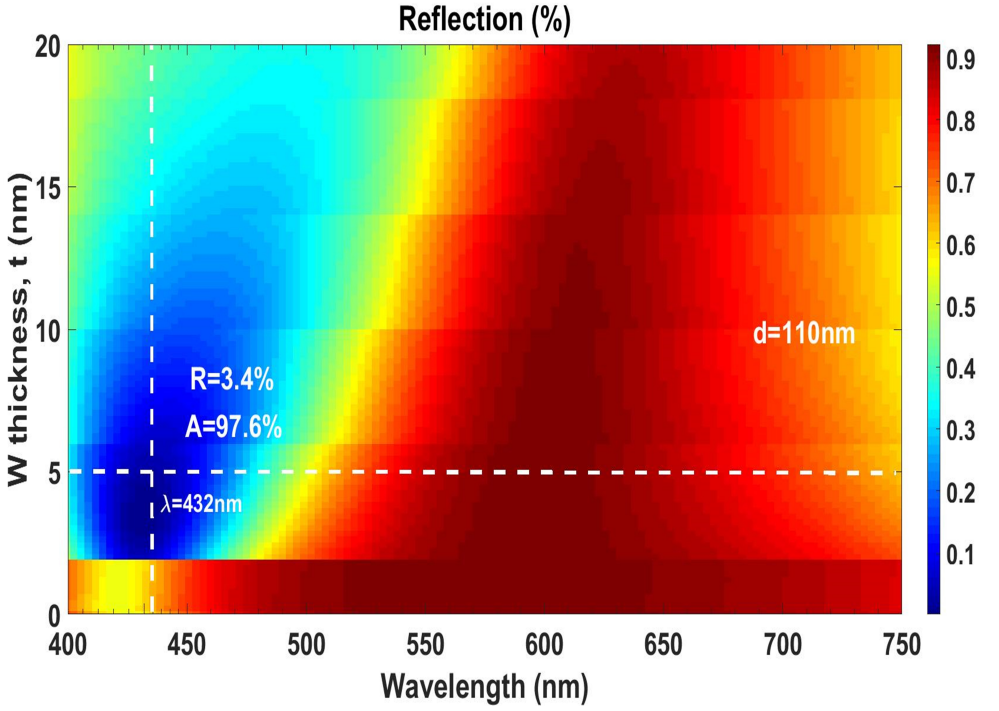

FIGURE 6.8: The effect of the thickness of W on the reflection spectrum at d = 110 nm. The reflection dip and absorption peak occur at the resonance wavelength $\lambda_{res} = 433nm$ for yellow colour.

6.2 Resonance Conditions for CMY Subtractive Colours

The resonant conditions for vivid CMY colours are further investigated in this section. In the case of the proposed design, transmission (T) through the device is negligible due to opaque aluminium film in the light's path. Hence, W's total reflection (R) is R= 1 - A, where A is the absorbance.

The reflection (R) behaviour of incident light at the film interface, in asymmetric FP-cavity for the proposed design, can be calculated by Fresnel equation [207] given as:

$$R = \frac{2\sqrt{(R_a R_b)}(1 - cos\delta)}{1 + R_a R_b - 2\sqrt{(R_a R_b)}cos\delta}. \tag{6.1}$$

Here R_a and R_b corresponds to the reflection at W-TiO_2 and Al-TiO_2 interfaces, respectively. The total phase accumulated during a single round trip in the TiO_2 (FP cavity) 'δ' is equivalent to $\delta = \phi_{prop} - \phi_a - \phi_b$, where ϕ_{prop}, ϕ_a and ϕ_b are the phase shift at the top and bottom interface of cavity, however, ϕ_{prop} is the round-trip propagation phase equals to $\frac{4\pi}{\lambda} n h_c$. The reflection is minimum when δ is be a multiple of 2π i.e., $2m\pi$ where m is an integer. The values for ϕ_a, ϕ_b can be calculated from equation 3.3 and 3.4 in chapter 3 in TM polarization.

Figure 6.9 shows the phase shift for cyan colour when d=180 nm. It is evident from Figure 6.9b that the wide cavity has more modes, and the reflection dip at λ=450 and 625 nm are due to m= 3 and 2, respectively.

In contrast, from Figures 6.10 and 6.11, it is evident that at d= 150 nm and d= 110 nm for magenta and yellow colours the reflection dips occur due to m=1 at λ_{res}= 544 nm and 433 nm, respectively.

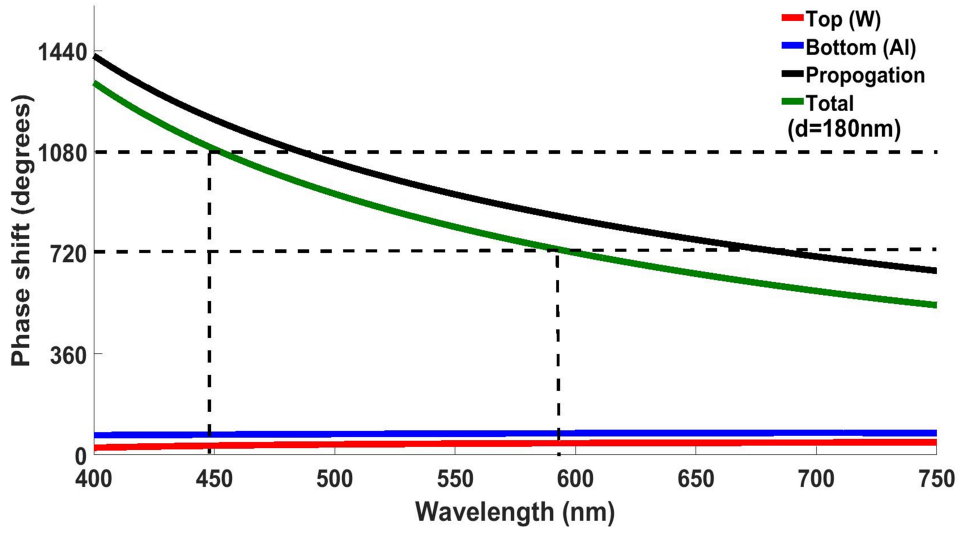

(a)

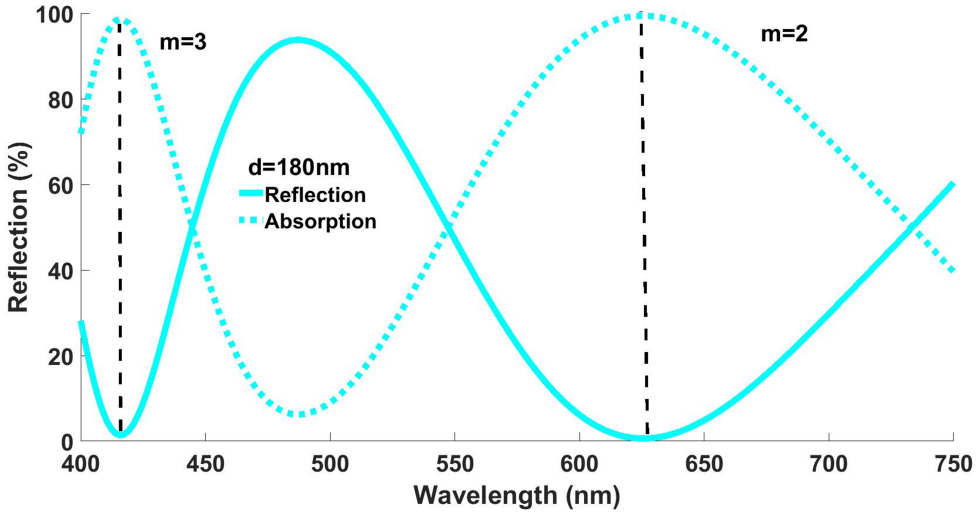

(b)

FIGURE 6.9: Resonance conditions for magenta colour at d=180 nm and t=5 nm. a) Calculated phase shift and the b) corresponding reflection (solid lines) and absorption (dotted line) spectra.

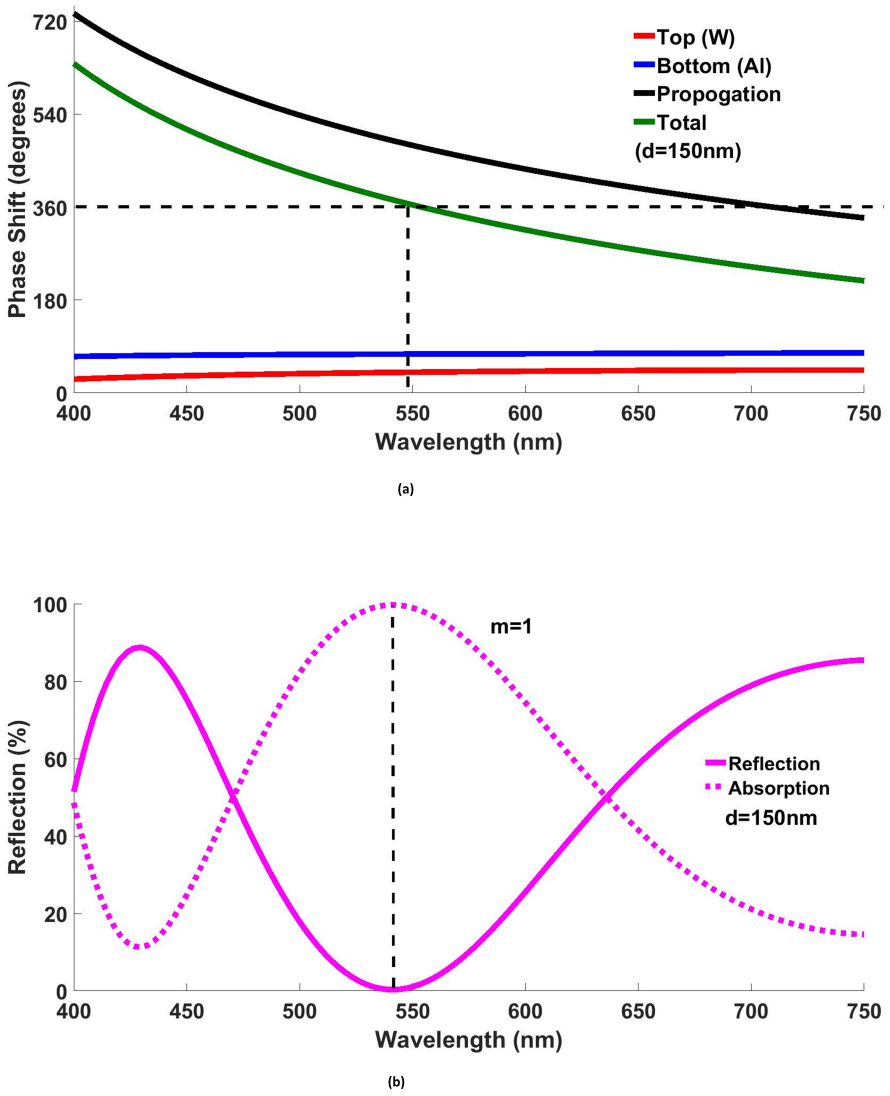

FIGURE 6.10: Resonance conditions for magenta colour at d=150 nm and t=5 nm. a) Calculated phase shift and the b) corresponding reflection (solid lines) and absorption (dotted line) spectra.

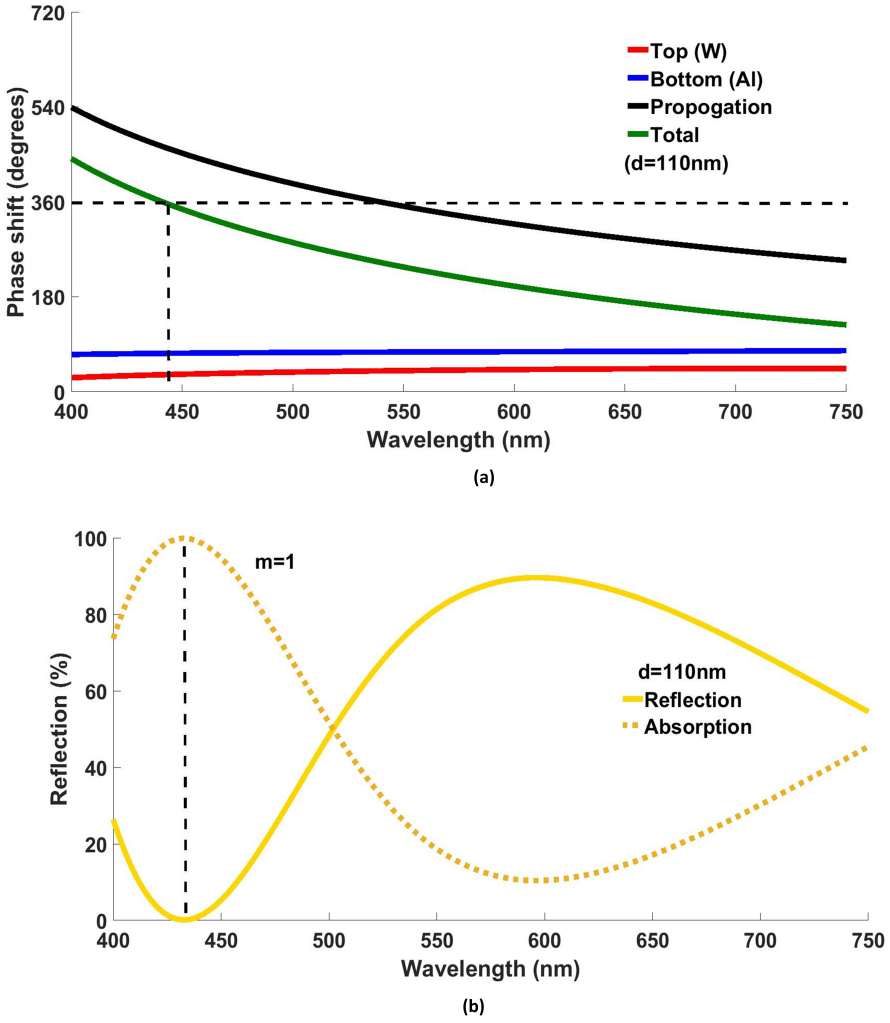

FIGURE 6.11: Resonance conditions for yellow colour at d=110 nm and t=5 nm. a) Calculated phase shift and the b) corresponding reflection (solid lines) and absorption (dotted line) spectra.

6.3 Commission Internationale del' Elcairage (CIE) 1931 Chromaticity Map

The entire colour gamut can be easily reproduced by colour mixing of either additive (red, green, blue (RGB)) or subtractive (cyan, magenta, yellow (CMY)) colours. The term subtraction is associated with CMY because they are produced by subtracting one of the RGB colours from the white light. Hence (1-red) creates cyan, (1-green) creates magenta and (1-blue) creates yellow. Likewise, the pure values of CMY, in terms of RGB values, can also be written as (0, 255, 255), (255, 0, 255) and (255, 255, 0), respectively. These RGB values can be plotted on Commission Internationale del' Elcairage (CIE) 1931 chromaticity map, and this process requires the following steps [224]:

1. Conversion of RGB values to XYZ coordinates: This can be done by employing conversion matrix given as

$$\begin{bmatrix} X \\ Y \\ Z \end{bmatrix} = \begin{bmatrix} 0.4124564 & 0.3575761 & 0.1804375 \\ 0.2126729 & 0.7151522 & 0.0721750 \\ 0.0193339 & 0.1191920 & 0.9503041 \end{bmatrix} \begin{bmatrix} R \\ G \\ B \end{bmatrix}. \tag{6.2}$$

2. Conversion of XYZ coordinated to Yxy values for CIE 1931 plot:

$$x = \frac{X}{X+Y+Z}, \qquad y = \frac{Y}{X+Y+Z}, \tag{6.3}$$

where $z = 1 - x - y$.

The location of pure CMY colour filters on CIE 1931 map are (0.22466, 0.32876), (0.32094, 0.15419) and (0.41932, 0.50525) respectively. The dimensions, RGB and xy values for CIE 1931 map for designed CMY colour filters are provided in Table 6.1. The

TABLE 6.1: CMY colours due to asymmetric FP nanocavities

colour	**d (nm)**	**t (nm)**	λ_{res}	**R**	**G**	**B**	**x**	**y**
C	180	5	620	0	254	248	0.18306	0.33726
M	150	5	544	228	29	255	0.29394	0.14244
Y	110	5	433	255	214	63	0.43585	0.46599

location of the obtained colours on CIE 1931 xy colour space are shown in Figure 6.12.

The response of asymmetric FP nanocavity is further investigated by plotting xy coordinates for colours at different cavity thicknesses. The colours obtained by varying cavity thickness d from 0 to 400 nm in 5 nm steps are illustrated in Figure 6.13, which resulted in 41.3 % coverage of sRGB gamut on CIE 1931 map .

Furthermore, the palette for produced vivid colours at different d is produced in Figure 6.14.

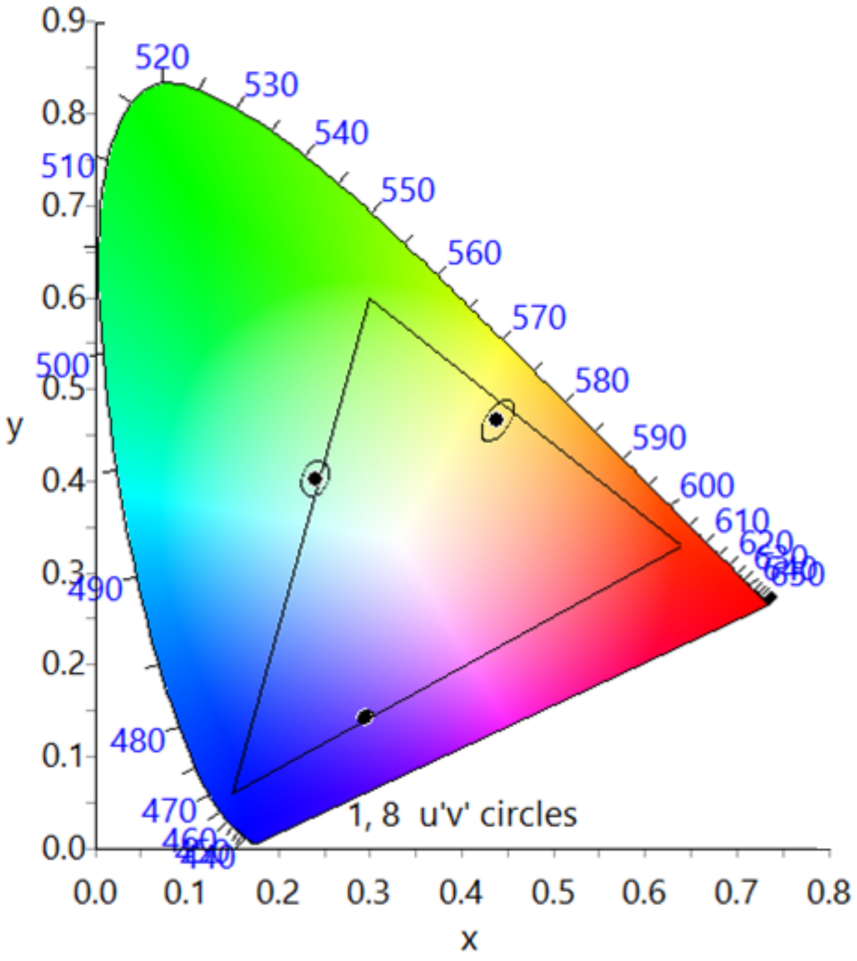

FIGURE 6.12: CIE 1931 chromaticity map for obtained CMY colour filters.

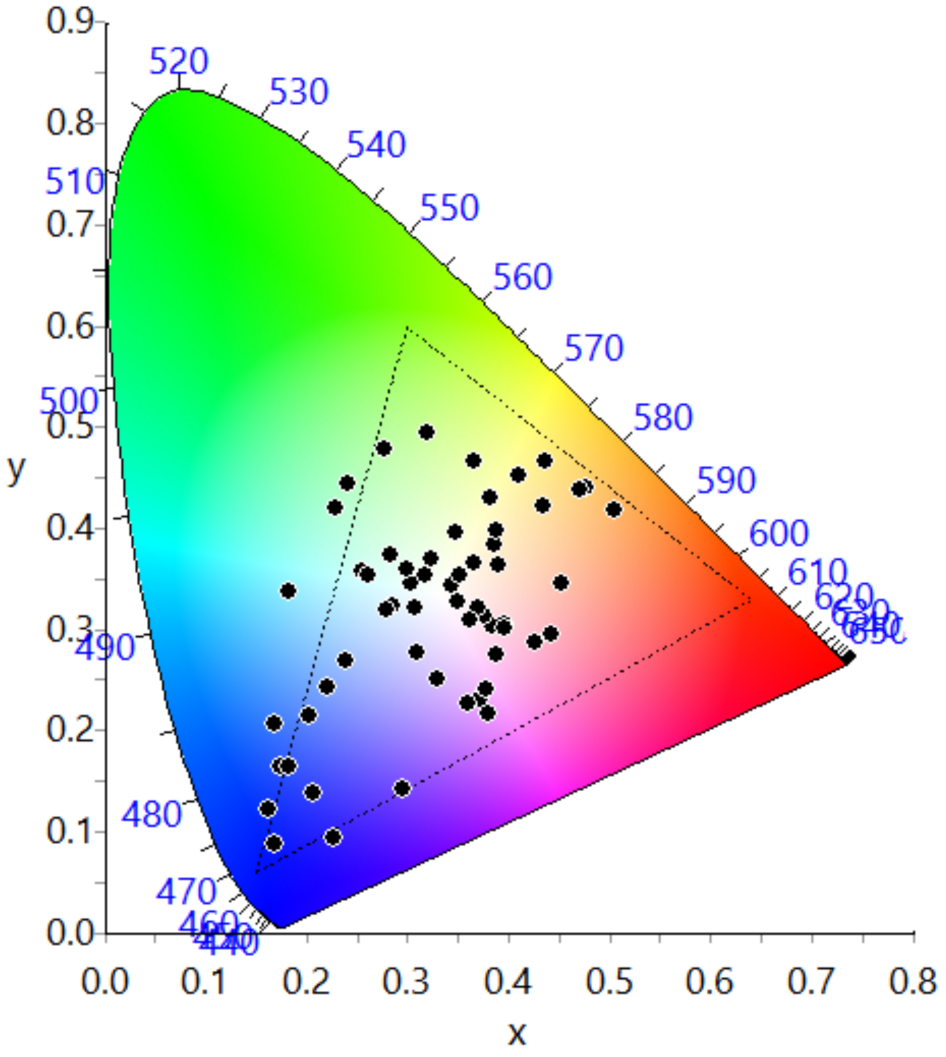

FIGURE 6.13: CIE 1931 chromaticity map for colour filters obtained by varying cavity thickness d from 0 to 500 nm.

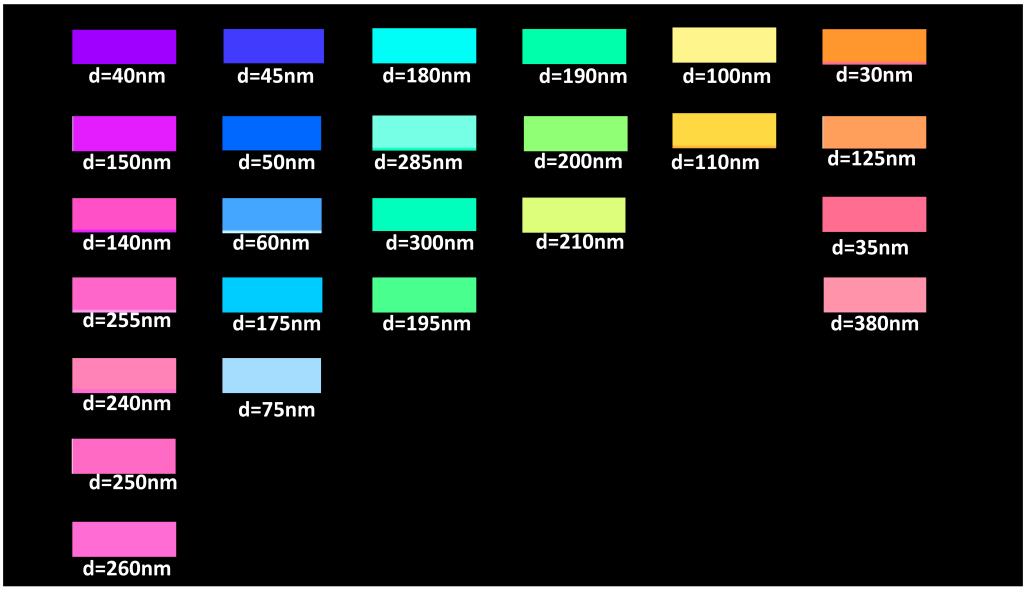

FIGURE 6.14: Palette of vivid colours obtained by varying nanocavity thickness from 0 to 400 nm.

6.3.1 At Various Light Polarization and Incident Angles

The results obtained for CMY colour filters are further evaluated at varying incident and polarization angles of incident light.

The contour plot of reflection spectrum at d=180 nm (for cyan colour), with the angle of incident varied from 0° to 60°, is shown in Figure 6.15. It is evident from obtained contour that the reflection dip will remain constant from 0° to 40°, however with the increase of incident angle from 40° onwards, the reflection spectrum gets distorted due to the emergence of peaks in the spectrum. Likewise, the exact impact is seen in Figures 6.16 and 6.17 for magenta and yellow colours, respectively.

Due to the symmetric nature of thin films' design, the design is expected to show polarization insensitivity, and this property is verified by varying polarization angle of incident light from 0° (TM mode) to 90° (TE mode) in steps of 15°. Figures 6.18, 6.19 and 6.20 demonstrate polarization angle insensitivity of CMY colour filters respectively.

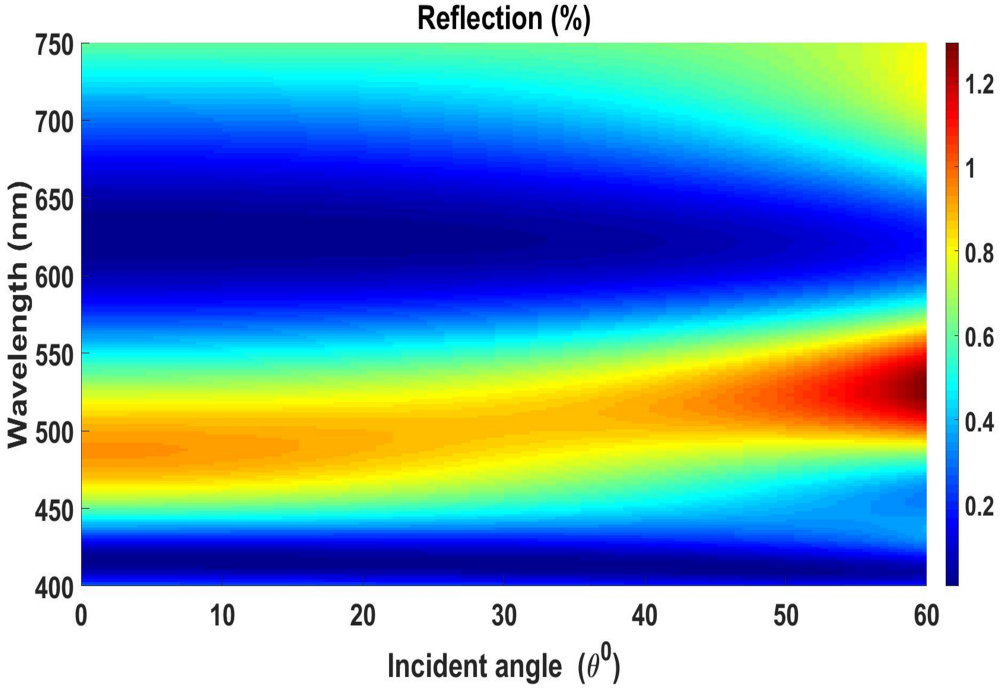

FIGURE 6.15: Reflection spectrum of cyan colour at d=180 nm, when incident angle varies from 0° to 60°.

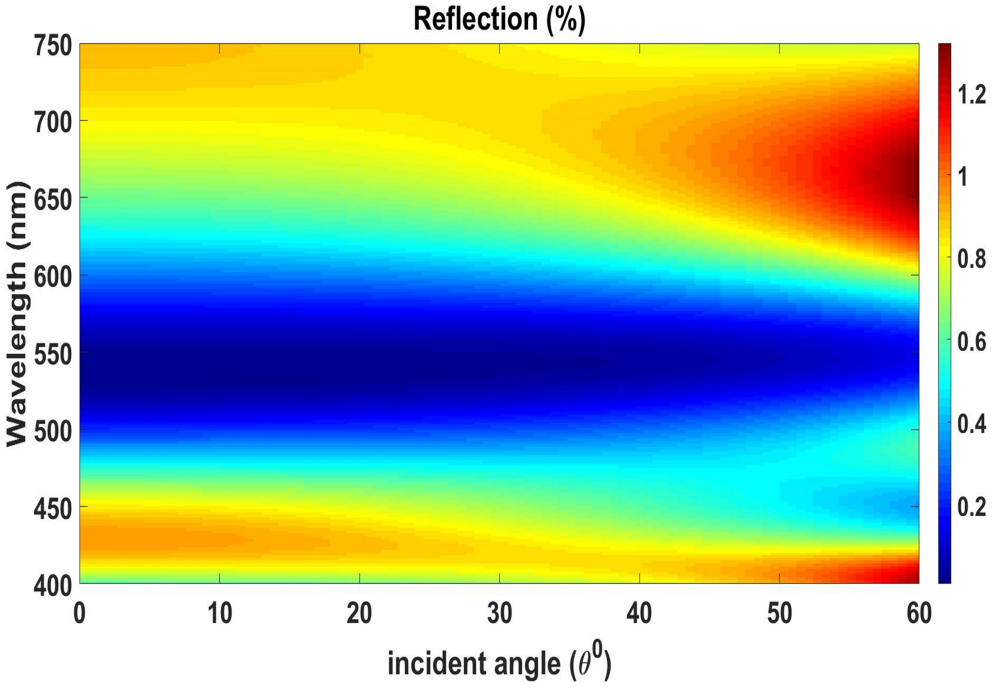

FIGURE 6.16: Reflection spectrum of magenta colour at d=150 nm, when incident angle varies from 0° to 60°.

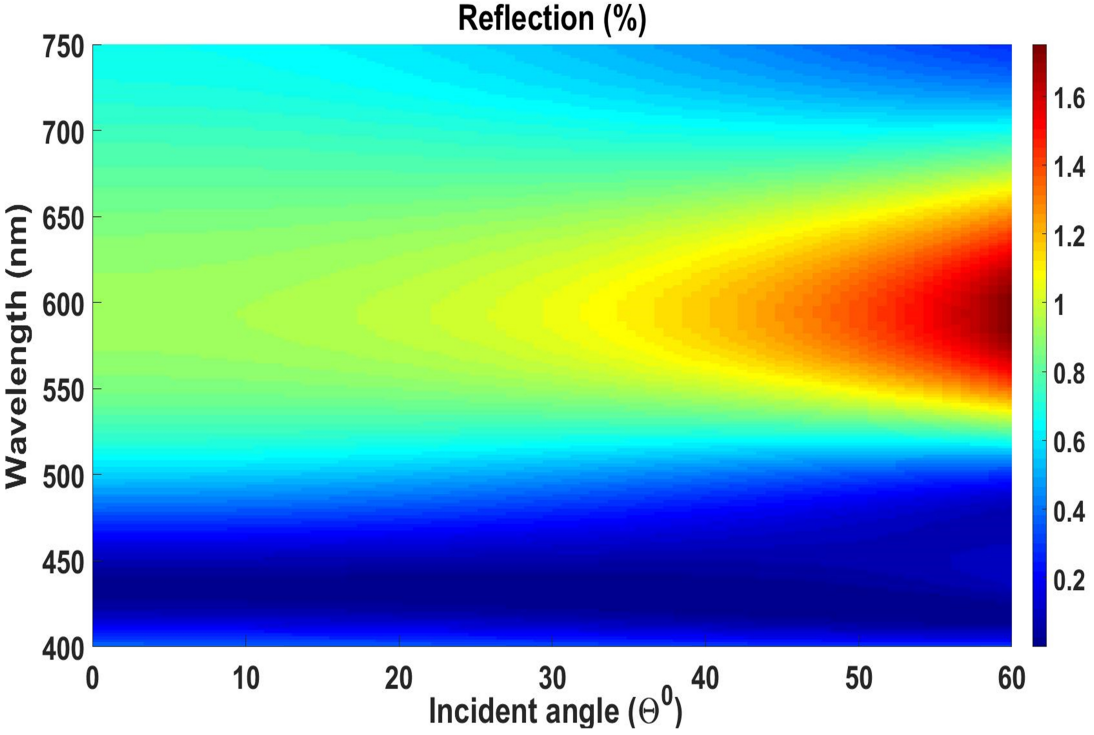

FIGURE 6.17: Reflection spectrum of yellow colour at d=110 nm, when incident angle varies from 0° to 60°.

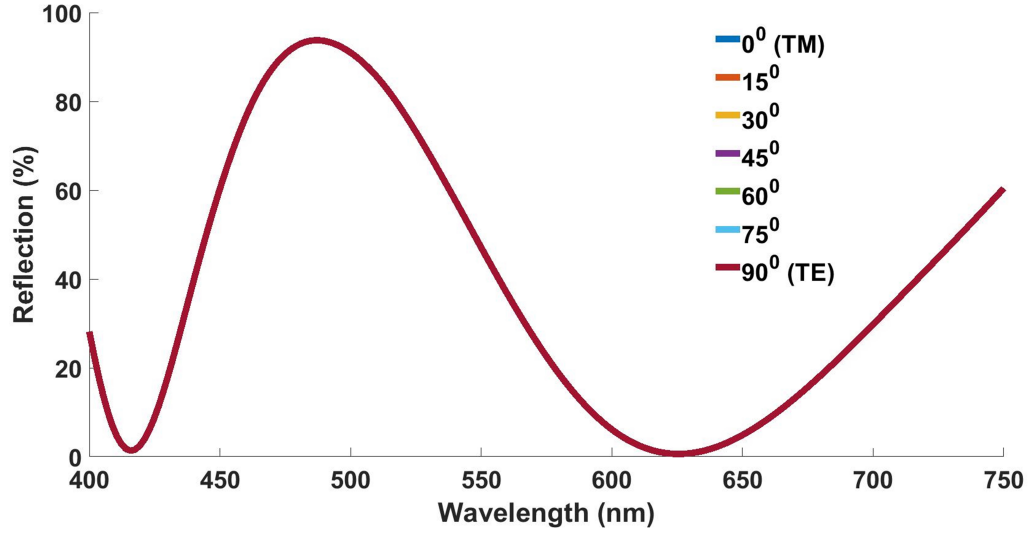

FIGURE 6.18: Reflection spectrum of cyan colour filter (at d=180 nm) when angle of light polarization varied from TM to TE mode in steps of 15°.

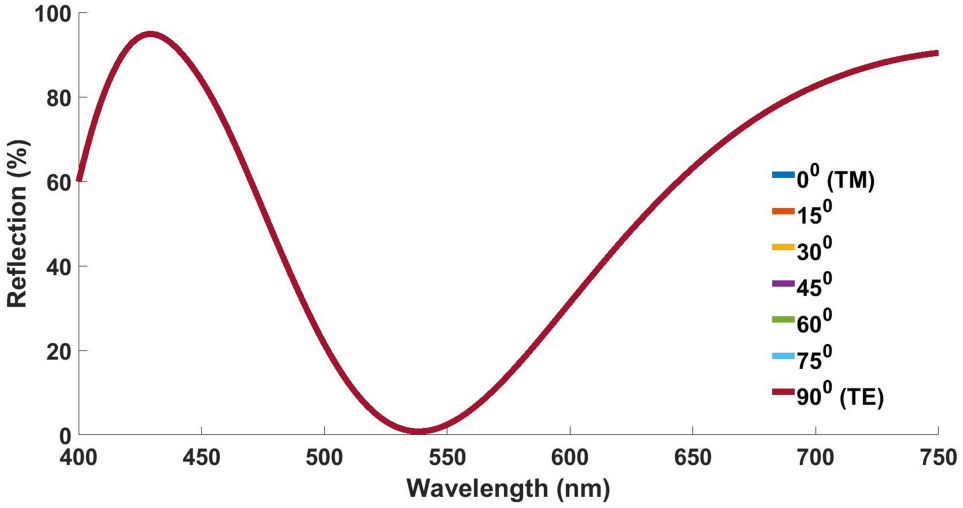

FIGURE 6.19: Reflection spectrum of magenta (at d=150 nm) colour filter when angle of light polarization varied from TM to TE mode in steps of 15°.

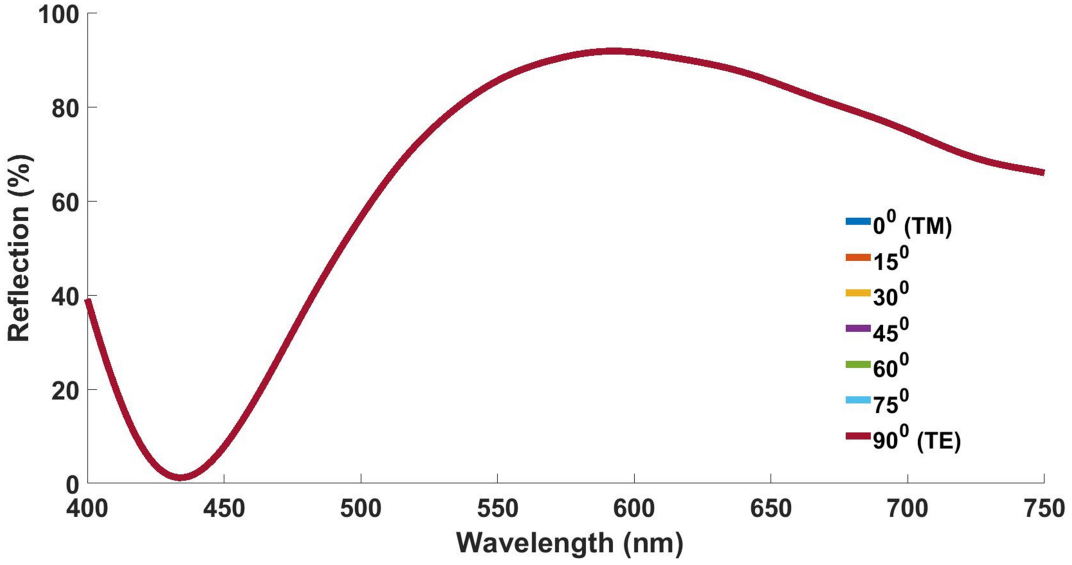

FIGURE 6.20: Reflection spectrum of yellow colour filter (at d=110 nm) when angle of light polarization varied from TM to TE mode in steps of 15°.

6.4 Film Deposition

For obtaining the experimental results, a nanocavity capable of producing cyan colour at t=5 nm, d=150 nm and h=100 nm is fabricated. The films were deposited at the ANFF facility (UNSW Australia).

A Hind High Vacuum (HHV) TF600 magnetron sputterer was used for deposition in asymmetric FP nanocavity. The chamber base pressure was kept at 3.0x10$^-$7 Torr. For Al, 200 W (DC) is used, and deposition is performed at room temperature with an Argon (Ar) flow of 10 sccm at 2.6mTorr process pressure with a run-time of 28 minutes and 40seconds. Next, for TiO_2, 300 W (RF) was employed, and the sample holder was heated up to 395^oC, the Ar flow was at 20 sccm along with oxygen (O_2) flow 1 sccm at 2.5 mTorr process pressure with run time 2 hours 20 minutes and 30 seconds. Afterwards, W was deposited with W 50 W(RF) and the deposition was performed at room temperature with Ar flow of 20 sccm at 2.1mTorr process pressure with a run-time of 4 minutes.

6.5 Physical Characterization

For physical characterisation, the SEM images of the fabricated sample were extracted to find out the thicknesses of the deposited film. Figure 6.21 shows the SEM image of the sample's cross-section. The image only shows one film with thickness ≈ 100 nm, probably the deposited Al film. However, W and TiO_2 cannot be seen. It indicates that either the sample needs conditioning or the layers on top of Al are not deposited. Therefore, spectroscopic analysis was carried out, which showed TiO_2 film only 30 nm thick. From Figure 6.14 of section 6.3 it can be deduced that at 30 nm, the sample reflects a mix of red and yellow colour, i.e., orange. Through diagnostic efforts, it was found out that there was an issue with the pressure gauge, which gave erroneous readings throughout and deposited only 30 nm film of TiO_2 instead of 150 nm.

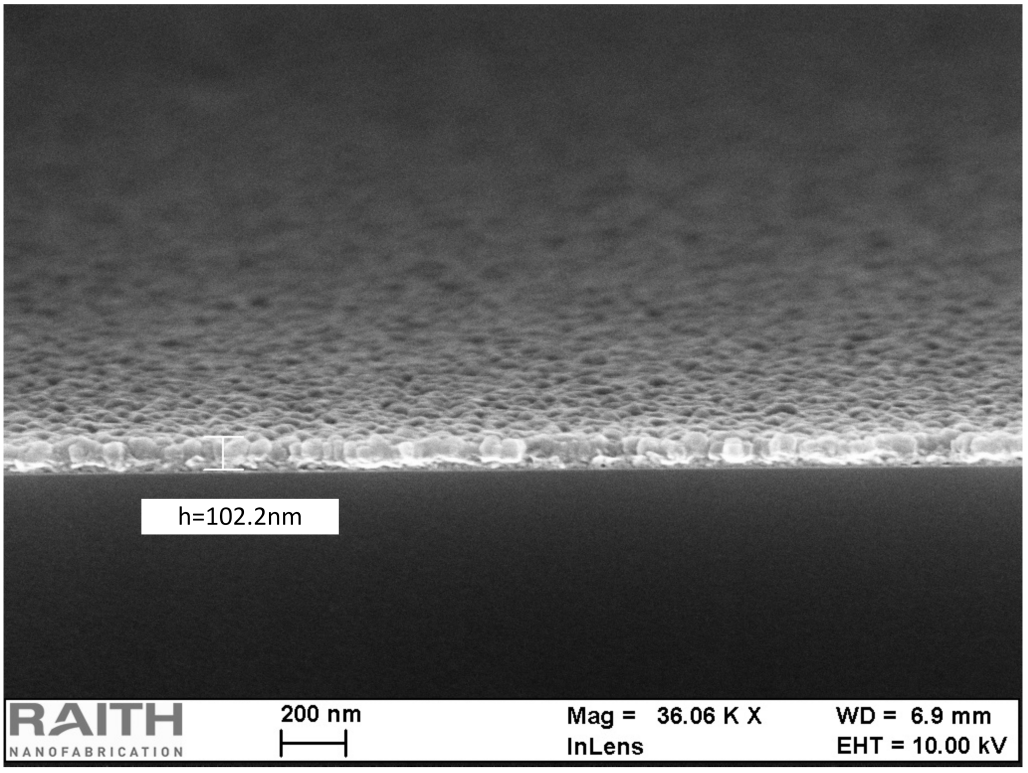

FIGURE 6.21: SEM image for Asymmetric FP nanocavity incorporating CMOS compatible tungsten

6.6 Optical Characterization

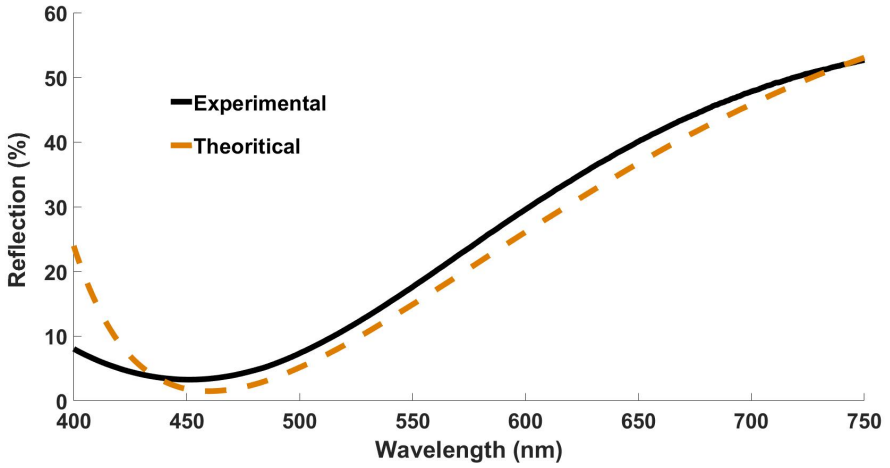

FIGURE 6.22: Experimental and theoretical results of asymmetric FP nanocavity at d=30 nm

Figure 6.22 illustrates the curve obtained by optical characterization of the sample, which is close to the curve obtained at 30 nm cavity (dotted line).

6.7 Summary

The analytical and experimental study of asymmetric FP nanocavity incorporating. CMOS compatible tungsten has been carried out in this chapter. The obtained reflection spectrum produced vivid colours with angle invariance up to 40° and insensitivity to the light polarization. The colours are limited to the primary CMY subtractive colours; in fact, the flexible design allows 41.3 % of sRGB gamut coverage on CIE 1931 chromaticity map and produces a palette of vivid bright colours.

Although the thicknesses obtained from SEM were not helpful to see all three layers, the thicknesses obtained from spectroscopic ellipsometry agreed with the experimental results.

Chapter 7

Conclusion and Future Work

7.1 Conclusion

This research aimed to explore CMOS compatible colour filters for NIR and visible regions. For this purpose, a novel all dielectric thin film filter with well-suppressed sidebands, transmission up to 70 % at all polarization angles of the incident light, narrow bandwidth and angle invariance up to 60° was developed. These traits make it a suitable candidate for CMOS compatible spectral image sensing applications. Through extensive simulation studies, several of the physical mechanisms involved in the transmission process of the cascaded filter were identified, and the effect of each layer and constitutive parameter on the device's optical response was established.
Furthermore, an analytical and experimental study on an asymmetric FP nanocavity incorporating CMOS compatible tungsten (W) for vivid colouration was also carried out. The analytical study produced reflection spectra for vivid colours, and a palette of vivid colours at different cavity thicknesses was also produced. The device demonstrated angle invariance up to 40°, and it was insensitive to change in light polarization.

The salient aspects and novelties/contributions of the proposed filters are briefly presented below:

- The filter design material database was narrowed down to the CMOS compatible materials only. This was accompanied by selecting a thin film filter design due to its

easy layer deposition steps. Additionally, the design was chosen to be symmetrical to make it insensitive to the polarization of incident light. A high refractive index material is chosen for the design's cavity, as it produces omnidirectional response due to insensitivity to variation in incident angle [53, 60].

- Through extensive literature review and rigorous simulation process, a dielectric omnidirectional, lithography-free, and polarization-insensitive multilayered thin films cascaded filter was designed for the NIR region. It can be applied in spectral imaging devices for many applications, such as food sciences, agricultural industry, medical sciences and many more.

  The results were evaluated at different incident and polarization angles of incident light and showed the same results at all incident and polarization angles. The nature of the chosen design allows polarization insensitivity for the transmission response through these devices; however, the invariant angle response is accredited to the usage of high dielectric material (i.e., A-Si in our case) for the design's cavity. The simulation results built confidence for materializing the design and led to the fabrication process.

- For fabrication, it only required successive deposition of Si_3N_4 and A-Si on a glass substrate. The deposition of layers was done at the ANFF by employing plasma-enhanced chemical vapour deposition (PECVD) [225].

  For testing purposes, cross-sectional scanning electron microscope (SEM) images were needed to obtain the thicknesses of the deposited films. However, due to the same average atomic masses of Si_3N_4 and A-Si, it was not possible to obtain the correct thicknesses of deposited films. Therefore, the sample needed to go through dry reactive ion etching (DRIE) in the presence of sulphur hexafluoride (SF_6) for enhancing the layers' contrast.

- For optical characterization, an in-house setup was built by customizing the available spectrofluorometer to the spectrophotometer. A rotating stage was designed and placed in the spectrofluorometer chamber, and the white light source was allowed to enter it through an inlet. This allowed observing the transmission spectra at different angles of incident light. Despite all these efforts, the results obtained through the established setup suffered from instrumental, environmental and human error.Hence the experimental results for the transmission spectrum of

the films were obtained at the ANFF. The thicknesses obtained via SEM image showed a discrepancy in the simulated and experimental values, which is accredited to the usage of materials with close properties, i.e., Si_3N_4 and A-Si.
Hence, the spectroscopic ellipsometry was employed to obtain the thicknesses of the deposited films, and simulated the transmission spectrum with the derived thicknesses. The simulated results showed a reasonable unison with the experimental results. The sample's response was further investigated for different incident angles; however, due to tools' constraints, it cannot be done through an available spectrophotometer (Perkin Elmer Lambda 1050 UV-Vis-NIR Spectrophotometer) at ANFF; therefore, spectroscopic ellipsometry was also utilized to obtain the filter's response at different incident angles. However, the results showed angle invariance up to 50°.

- Besides NIR filter, an asymmetric FP nanocavity incorporating CMOS compatible tungsten (W) for subtractive colour filtering was also carried out. In its analytical study, the simulations were carried out for investigating the thicknesses for each layer i.e., cavity (TiO_2) and W. Through rigorous simulations; it was observed that 5 nm thick W layer allowed vivid colour filtration when cavity thickness varied from 0 to 400 nm. The resonance conditions for cyan, magenta and yellow (CMY) colours were further investigated. It was shown that the resonance occurred when the propagation delay due to a light ray trip was multiple of 2π. The obtained results covered 41.3 % of the sRGB gamut on CIE 1931 chromaticity map. The results were further evaluated at different light incident angles, and the reflection spectrum showed angle invariance up to 40°. Moreover, the design was immune to change in the polarization angle of incident light.
  The design deposition was carried out at ANFF. The layers were sputtered using a magnetron sputterer. The results obtained through optical characterization agreed with the simulated results; however, the captured SEM image showed only one layer.

7.2 Future Work

While the design and fabrication of the filters for NIR and visible region resulted in narrowing down the material choice to some commonly used CMOS compatible materials

and fabrication steps, there is still room for further improvements. Notably in the area of fabrication and characterization.

The first design consisted of a multilayered thin film cascaded filter and produced discrepancies in experimental and simulated results. The main reason for this was the difficulty in measuring each layer's thickness due to the materials' close composition, i.e., Si_3N_4 and A-Si, which led to misleading dimensions in the SEM images. Since the dimensions from the fabricated structures could not be correctly obtained, simulations with the fabricated dimensions were not possible. It is suggested that new materials and/or other design parameters be considered to circumvent the issue resulting from the inability of the equipment to measure the dimensions correctly.
The second design consisted of an asymmetric FP nanocavity incorporating CMOS compatible tungsten. The analytical study agreed with the data obtained from spectroscopic ellipsometry. In contrast, the poor SEM images indicated the difficulty experienced in obtaining the exact thicknesses of the layers. To ascertain the root cause of this anomaly, it is planned to deposit more films, including CMY colours based nanocavities, and carefully observe and compare their physical and optical characterization performances. Moreover, further investigations for designs performance at the different incidence and polarization angles of incident light are also needed to be carried out in future.

7.3 Reflection

Reflecting upon this research, it can be inferred that a deeper understanding of the micro/nanofabrication techniques/technologies is necessary to effectively design structures that can be fabricated and characterized in accessible facilities. As a minimum, the designer has to closely work with the fabrication team so that the designs can be modified before running the fabrication steps. Since this was not an option from the beginning of this research due to the limited resources (and the inability of the researcher to travel to the fabrication facility due to the Covid-19 lockdowns), the disparity between the simulated and fabricated results is not unexpected. However, the filter designs and resulting findings are considered valid and a significant contribution in the area of CMOS compatible colour filters. It is strongly expected that the results can

be easily improved with appropriate access to the fabrication facilities and the ability to travel and work with the fabrication team.

Bibliography

[1] Gamal ElMasry, Ramadan ElGamal, Nasser Mandour, Pere Gou, Salim Al-Rejaie, Etienne Belin, and David Rousseau. Emerging thermal imaging techniques for seed quality evaluation: Principles and applications. *Food Research International*, 131:109025, 2020. ISSN 0963-9969. doi: https://doi.org/10.1016/j.foodres.2020.109025. URL https://www.sciencedirect.com/science/article/pii/S0963996920300508.

[2] Naeeme Modir, Maysam Shahedi, James Dormer, and Baowei Fei. Development of a real-time spectral imaging system using in-site led-based illumination for endoscopic applications.

[3] Dionysios Bitas, Kyriakos Papastavros, and Dimitris Tsipianitis. A smart cablebot for spectral imaging and micro-climate measurements inside greenhouses. In *2020 11th International Conference on Information, Intelligence, Systems and Applications (IISA*, pages 1–4. IEEE. ISBN 0738123463.

[4] Wen-Hao Su and Da-Wen Sun. Multispectral imaging for plant food quality analysis and visualization. *Comprehensive reviews in food science and food safety*, 17(1):220–239, 2018. ISSN 1541-4337.

[5] Yasushi Hiraoka, John W Sedat, and David A Agard. The use of a charge-coupled device for quantitative optical microscopy of biological structures. *Science*, 238 (4823):36–41, 1987. ISSN 0036-8075.

[6] Ahmed Nabil Belbachir and Peter Michael Göbel. *Smart cameras: A historical evolution*, pages 3–17. Springer, 2009.

[7] A Elsherbeni and Veysel Demir. *The Finite-Difference Time-Domain Method for Electromagnetics with MATLAB Simulations. ACES Series.* SciTech Publishing, Edison, NJ, 2016.

[8] P. Cambou and J. Jaffard. Status of the cmos image sensor industry 2021 report. *Yole Développement,*, 2021.

[9] Abbas El Gamal and Helmy Eltoukhy. Cmos image sensors. *IEEE Circuits and Devices Magazine*, 21(3):6–20, 2005. ISSN 8755-3996.

[10] Guolan Lu and Baowei Fei. Medical hyperspectral imaging: a review. *Journal of biomedical optics*, 19(1):010901, 2014. ISSN 1083-3668.

[11] Suparshya Babu Sukhavasi, Susrutha Babu Sukhavasi, Khaled Elleithy, Shakour Abuzneid, and Abdelrahman Elleithy. Human body-related disease diagnosis systems using cmos image sensors: A systematic review. *Sensors*, 21(6):2098, 2021.

[12] Susrutha Babu Sukhavasi, Suparshya Babu Sukhavasi, Khaled Elleithy, Shakour Abuzneid, and Abdelrahman Elleithy. Cmos image sensors in surveillance system applications. *Sensors*, 21(2):488, 2021.

[13] Nadia Pinton. *Metal-insulator-metal plasmonic colour filters for CMOS image sensor applications.* Thesis, 2020.

[14] Kim Cooper CJ Kazilek. Rods and cones. asu - ask a biologist, October 2021. URL https://askabiologist.asu.edu/rods-and-cones.

[15] Jim Adams, Ken Parulski, and Kevin Spaulding. Color processing in digital cameras. *IEEE micro*, 18(6):20–30, 1998. ISSN 0272-1732.

[16] Henrique S Malvar, Li-wei He, and Ross Cutler. High-quality linear interpolation for demosaicing of bayer-patterned color images. In *2004 IEEE International Conference on Acoustics, Speech, and Signal Processing*, volume 3, pages iii–485. IEEE. ISBN 0780384849.

[17] Eric A Newman and Peter H Hartline. The infrared" vision" of snakes. *Scientific American*, 246(3):116–127, 1982. ISSN 0036-8733.

[18] James D Crall, Callin M Switzer, Robert L Oppenheimer, Ashlee N Ford Versypt, Biswadip Dey, Andrea Brown, Mackay Eyster, Claire Guérin, Naomi E Pierce, and Stacey A Combes. Neonicotinoid exposure disrupts bumblebee nest behavior, social networks, and thermoregulation. *Science*, 362(6415):683–686, 2018. ISSN 0036-8075.

[19] Dennis Wirth, Brook Byrd, Boyu Meng, Rendall R Strawbridge, Kimberley S Samkoe, and Scott C Davis. Hyperspectral imaging and spectral unmixing for improving whole-body fluorescence cryo-imaging. *Biomedical Optics Express*, 12 (1):395–408, 2021. ISSN 2156-7085.

[20] J Tsai, AL Chien, JU Kang, S Leung, S Kang, and LA Garza. Hyperspectral measurement of skin reflectance detects differences in the visible and near-infrared regions according to race, gender and body site. *Journal of the European Academy of Dermatology and Venereology: JEADV*, 35(5):e330, 2021.

[21] Zhenfeng Yang, Juncang Tian, Kepeng Feng, Xue Gong, and Jiabin Liu. Application of a hyperspectral imaging system to quantify leaf-scale chlorophyll, nitrogen and chlorophyll fluorescence parameters in grapevine. *Plant Physiology and Biochemistry*, 166:723–737, 2021. ISSN 0981-9428.

[22] Luca Giannoni, Frédéric Lange, Marija Sajic, Kenneth J Smith, and Ilias Tachtsidis. A hyperspectral imaging system for mapping haemoglobin and cytochrome-c-oxidase concentration changes in the exposed cerebral cortex. *IEEE Journal of Selected Topics in Quantum Electronics*, 27(4):1–11, 2021. ISSN 1077-260X.

[23] Silvia Serranti, Roberta Palmieri, Giuseppe Bonifazi, and Andrés Cózar. Characterization of microplastic litter from oceans by an innovative approach based on hyperspectral imaging. *Waste Management*, 76:117–125, 2018. ISSN 0956-053X.

[24] Yasser Fawzy and Haishan Zeng. Spectral imaging technology-a review on skin and endoscopy applications. *Recent Patents on Medical Imaging (Discontinued)*, 4(2):101–109, 2014. ISSN 2210-6847.

[25] Jason M Eichenholz and John Dougherty. Ultracompact fully integrated megapixel multispectral imager. In *Integrated Optics: Devices, Materials, and Technologies XIII*, volume 7218, page 721814. International Society for Optics and Photonics.

[26] Thomas W Ebbesen, H J Lezec, HF Ghaemi, Tineke Thio, and PA Wolff. Extraordinary optical transmission through sub-wavelength hole arrays. *Nature*, 391(6668):667, 1998. ISSN 1476-4687.

[27] H Angus Macleod and H Angus Macleod. *Thin-film optical filters*. CRC press, 2010. ISBN 1420073036.

[28] Stephen Y Chou, Peter R Krauss, and Preston J Renstrom. Nanoimprint lithography. *Journal of Vacuum Science Technology B: Microelectronics and Nanometer Structures Processing, Measurement, and Phenomena*, 14(6):4129–4133, 1996. ISSN 1071-1023.

[29] Chul-Soon Park, Vivek Raj Shrestha, Sang-Shin Lee, and Duk-Yong Choi. Transreflective color filters based on a phase compensated etalon enabling adjustable color saturation. *Scientific reports*, 6:25496, 2016. ISSN 2045-2322.

[30] Manish Chhowalla, KBK Teo, C Ducati, NL Rupesinghe, GAJ Amaratunga, AC Ferrari, D Roy, J Robertson, and WI Milne. Growth process conditions of vertically aligned carbon nanotubes using plasma enhanced chemical vapor deposition. *Journal of applied physics*, 90(10):5308–5317, 2001. ISSN 0021-8979.

[31] Helen Ghiradella. Light and color on the wing: structural colors in butterflies and moths. *Applied Optics*, 30(24):3492–3500, 1991. doi: 10.1364/AO.30.003492. URL http://ao.osa.org/abstract.cfm?URI=ao-30-24-3492.

[32] Amnon Yariv and Pocji Yeh. *Photonics: optical electronics in modern communications*. Oxford Univ., 2006. ISBN 0195179463.

[33] Max Born and Emil Wolf. *Principles of optics: electromagnetic theory of propagation, interference and diffraction of light*. Elsevier, 2013. ISBN 148310320X.

[34] Craig F Bohren and Donald R Huffman. *Absorption and scattering of light by small particles*. John Wiley Sons, 2008. ISBN 3527618163.

[35] Graça Minas, JC Ribeiro, Júlio S Martins, RF Wolffenbuttel, and JH Correia. An array of fabry-perot optical-channels for biological fluids analysis. *Sensors and Actuators A: Physical*, 115(2-3):362–367, 2004. ISSN 0924-4247.

[36] Graça Minas, RF Wolffenbuttel, and JH Correia. An array of highly selective fabry–perot optical channels for biological fluid analysis by optical absorption using

a white light source for illumination. *Journal of Optics A: pure and applied optics*, 8(3):272, 2006. ISSN 1464-4258.

[37] A. Spisser, R. Ledantec, C. Seassal, J. L. Leclercq, T. Benyattou, D. Rondi, R. Blondeau, G. Guillot, and P. Viktorovitch. Highly selective and widely tunable 1.55-m inp/air-gap micromachined fabry-perot filter for optical communications. *IEEE Photonics Technology Letters*, 10(9):1259–1261, 1998. ISSN 1941-0174. doi: 10.1109/68.705609.

[38] Peng-Hsiao Lee and Yung-Chiang Lan. Plasmonic waveguide filters based on tunneling and cavity effects. *Plasmonics*, 5(4):417–422, 2010. ISSN 1557-1963. doi: 10.1007/s11468-010-9159-2. URL https://doi.org/10.1007/s11468-010-9159-2.

[39] Qingxu Yu and Xinlei Zhou. Pressure sensor based on the fiber-optic extrinsic fabry-perot interferometer. *Photonic Sensors*, 1(1):72–83, 2011. ISSN 2190-7439. doi: 10.1007/s13320-010-0017-9. URL https://doi.org/10.1007/s13320-010-0017-9.

[40] Md Islam, Muhammad Mahmood Ali, Man-Hong Lai, Kok-Sing Lim, and Harith Ahmad. Chronology of fabry-perot interferometer fiber-optic sensors and their applications: a review. *Sensors*, 14(4):7451–7488, 2014.

[41] Raquel Flores, Ricardo Janeiro, and Jaime Viegas. Optical fibre fabry-pérot interferometer based on inline microcavities for salinity and temperature sensing. *Scientific Reports*, 9(1):9556, 2019. ISSN 2045-2322. doi: 10.1038/s41598-019-45909-2. URL https://doi.org/10.1038/s41598-019-45909-2.

[42] N I Landy, S Sajuyigbe, Jack J Mock, David R Smith, and Willie J Padilla. Perfect metamaterial absorber. *Physical review letters*, 100(20):207402, 2008.

[43] Yingran He, Huixu Deng, Xiangyang Jiao, Sailing He, Jie Gao, and Xiaodong Yang. Infrared perfect absorber based on nanowire metamaterial cavities. *Optics Letters*, 38(7):1179–1181, 2013. doi: 10.1364/OL.38.001179. URL http://ol.osa.org/abstract.cfm?URI=ol-38-7-1179.

[44] Zhengqi Liu, Xiaoshan Liu, Shan Huang, Pingping Pan, Jing Chen, Guiqiang Liu, and Gang Gu. Automatically acquired broadband plasmonic-metamaterial black absorber during the metallic film-formation. *ACS Applied Materials Interfaces*, 7

(8):4962–4968, 2015. ISSN 1944-8244. doi: 10.1021/acsami.5b00056. URL https://doi.org/10.1021/acsami.5b00056.

[45] Habibe Durmaz, Arif E Cetin, Yuyu Li, and Roberto Paiella. A polarization insensitive wide-band perfect absorber. *Advanced Engineering Materials*, 21(8): 1900188, 2019. ISSN 1438-1656.

[46] Wei Wang, Yurui Qu, Kaikai Du, Songang Bai, Jingyi Tian, Meiyan Pan, Hui Ye, Min Qiu, and Qiang Li. Broadband optical absorption based on single-sized metal-dielectric-metal plasmonic nanostructures with high- metals. *Applied Physics Letters*, 110(10):101101, 2017. ISSN 0003-6951.

[47] Yeo-Taek Yoon and Sang-Shin Lee. Transmission type color filter incorporating a silver film based etalon. *Optics Express*, 18(5):5344–5349, 2010. doi: 10.1364/OE.18.005344. URL http://www.opticsexpress.org/abstract.cfm?URI=oe-18-5-5344.

[48] Zhongyang Li, Serkan Butun, and Koray Aydin. Large-area, lithography-free super absorbers and color filters at visible frequencies using ultrathin metallic films. *ACS Photonics*, 2(2):183–188, 2015. doi: 10.1021/ph500410u. URL https://doi.org/10.1021/ph500410u.

[49] Chul-Soon Park, Vivek Raj Shrestha, Sang-Shin Lee, Eun-Soo Kim, and Duk-Yong Choi. Omnidirectional color filters capitalizing on a nano-resonator of ag-tio 2-ag integrated with a phase compensating dielectric overlay. *Scientific reports*, 5: 8467, 2015. ISSN 2045-2322.

[50] Chul-Soon Park, Vivek Raj Shrestha, Sang-Shin Lee, and Duk-Yong Choi. Trans-reflective color filters based on a phase compensated etalon enabling adjustable color saturation. *Scientific reports*, 6:25496, 2016. ISSN 2045-2322.

[51] Debasish Banerjee and Minjuan Zhang. Quarter-wave design criteria for omni-directional structural colors. *Journal of Modern Optics*, 57(13):1180–1188, 2010. ISSN 0950-0340.

[52] Jaeyong Kim, Harim Oh, Beomseung Kang, Jongill Hong, Jong-Joo Rha, and Myeongkyu Lee. Broadband visible and near-infrared absorbers implemented with planar nanolayered stacks. *ACS Applied Nano Materials*, 2020. doi: 10.1021/acsanm.0c00265. URL https://doi.org/10.1021/acsanm.0c00265.

[53] Kyu-Tae Lee, Sungyong Seo, Jae Yong Lee, and L Jay Guo. Strong resonance effect in a lossy medium-based optical cavity for angle robust spectrum filters. *Advanced Materials*, 26(36):6324–6328, 2014. ISSN 0935-9648.

[54] Mikhail A Kats, Romain Blanchard, Patrice Genevet, and Federico Capasso. Nanometre optical coatings based on strong interference effects in highly absorbing media. *Nature materials*, 12(1):20, 2013. ISSN 1476-4660.

[55] Seyed Sadreddin Mirshafieyan and Junpeng Guo. Silicon colors: spectral selective perfect light absorption in single layer silicon films on aluminum surface and its thermal tunability. *Optics express*, 22(25):31545–31554, 2014. ISSN 1094-4087.

[56] Kyu-Tae Lee, Sungyong Seo, Jae Yong Lee, and L Jay Guo. Strong resonance effect in a lossy medium-based optical cavity for angle robust spectrum filters. *Advanced Materials*, 26(36):6324–6328, 2014. ISSN 0935-9648.

[57] Kyu-Tae Lee, Sung Yong Han, and Hui Joon Park. Omnidirectional flexible transmissive structural colors with high-color-purity and high-efficiency exploiting multicavity resonances. *Advanced Optical Materials*, 5(14):1700284, 2017. ISSN 2195-1071.

[58] Kyu-Tae Lee, Sung Yong Han, and Hui Joon Park. Omnidirectional flexible transmissive structural colors with high-color-purity and high-efficiency exploiting multicavity resonances. *Advanced Optical Materials*, 5(14):1700284, 2017. ISSN 2195-1071.

[59] Kyu-Tae Lee, Sung Yong Han, Zijia Li, Hyoung Won Baac, and Hui Joon Park. Flexible high-color-purity structural color filters based on a higher-order optical resonance suppression. *Scientific Reports*, 9(1):14917, 2019. ISSN 2045-2322. doi: 10.1038/s41598-019-51165-1. URL https://doi.org/10.1038/s41598-019-51165-1.

[60] Zhongyang Li, Edgar Palacios, Serkan Butun, Hasan Kocer, and Koray Aydin. Omnidirectional, broadband light absorption using large-area, ultrathin lossy metallic film coatings. *Scientific Reports*, 5(1):15137, 2015. ISSN 2045-2322. doi: 10.1038/srep15137. URL https://doi.org/10.1038/srep15137.

[61] Chenying Yang, Weidong Shen, Yueguang Zhang, Kan Li, Xu Fang, Xing Zhang, and Xu Liu. Compact multilayer film structure for angle insensitive color filtering. *Scientific reports*, 5:9285, 2015. ISSN 2045-2322.

[62] Zhengmei Yang, Yanming Zhou, Yiqin Chen, Yasi Wang, Peng Dai, Zhaogang Zhang, and Huigao Duan. Reflective color filters and monolithic color printing based on asymmetric fabry–perot cavities using nickel as a broadband absorber. *Advanced Optical Materials*, 4(8):1196–1202, 2016. ISSN 2195-1071.

[63] Jaeyong Kim, Harim Oh, Minseok Seo, and Myeongkyu Lee. Generation of reflection colors from metal–insulator–metal cavity structure enabled by thickness-dependent refractive indices of metal thin film. *ACS Photonics*, 6(9):2342–2349, 2019. ISSN 2330-4022.

[64] Manas Ranjan Gartia, Austin Hsiao, Anusha Pokhriyal, Sujin Seo, Gulsim Kulsharova, Brian T Cunningham, Tiziana C Bond, and Gang Logan Liu. Colorimetric plasmon resonance imaging using nano lycurgus cup arrays. *Advanced Optical Materials*, 1(1):68–76, 2013. ISSN 2195-1071.

[65] Shinji Hayashi, Akimichi Maekawa, Suk Chan Kim, and Minoru Fujii. Mechanism of enhanced light emission from an emitting layer embedded in metal-insulator-metal structures. *Physical Review B*, 82(3):035441, 2010.

[66] Yuanyuan Tian, Lei Zhang, and Lianhui Wang. Dna-functionalized plasmonic nanomaterials for optical biosensing. *Biotechnology journal*, 15(1):1800741, 2020. ISSN 1860-6768.

[67] Xue Han, Kun Liu, and Changsen Sun. Plasmonics for biosensing. *Materials (Basel, Switzerland)*, 12(9):1411, 2019. ISSN 1996-1944. doi: 10.3390/ma12091411. URL https://pubmed.ncbi.nlm.nih.gov/31052240https://www.ncbi.nlm.nih.gov/pmc/articles/PMC6539671/.

[68] Dongshi Zhang and Koji Sugioka. Hierarchical microstructures with high spatial frequency laser induced periodic surface structures possessing different orientations created by femtosecond laser ablation of silicon in liquids. *Opto-Electronic Advances*, 2(03):190002, 2019. ISSN 2096-4579.

[69] Jun Yang, Jingbi You, Chun-Chao Chen, Wan-Ching Hsu, Hai-ren Tan, Xing Wang Zhang, Ziruo Hong, and Yang Yang. Plasmonic polymer tandem solar cell. *ACS nano*, 5(8):6210–6217, 2011. ISSN 1936-0851.

[70] Tao Tao, Ting Zhi, Bin Liu, Peng Chen, Zili Xie, Hong Zhao, Fangfang Ren, Dunjun Chen, Youdou Zheng, and Rong Zhang. Electron-beam-driven iii-nitride plasmonic nanolasers in the deep-uv and visible region. *Small*, 16(1):1906205, 2020. ISSN 1613-6810.

[71] Sen Yan, Ran An, Yongjin Zou, Nan Yang, and Ying Zhang. Fabrication of polymer colloidal/au composite nanofilms for stable and reusable sers-active substrates with highly-dense hotspots. *Sensors and Actuators B: Chemical*, 302: 127107, 2020. ISSN 0925-4005.

[72] SI Bozhevolnyi. Plasmonic nanoguides and circuits (singapore: Pan stanford). 2009.

[73] Xiangang Luo and Teruya Ishihara. Surface plasmon resonant interference nanolithography technique. *Applied Physics Letters*, 84(23):4780–4782, 2004. ISSN 0003-6951.

[74] Robert Williams Wood. On a remarkable case of uneven distribution of light in a diffraction grating spectrum. *Proceedings of the Physical Society of London*, 18 (1):269, 1902. ISSN 1478-7814.

[75] Ugo Fano. The theory of anomalous diffraction gratings and of quasi-stationary waves on metallic surfaces (sommerfeld's waves). *JOSA*, 31(3):213–222, 1941.

[76] Andreas Otto. Excitation of nonradiative surface plasma waves in silver by the method of frustrated total reflection. *Zeitschrift für Physik A Hadrons and nuclei*, 216(4):398–410, 1968. ISSN 0939-7922.

[77] Bo Liedberg, Claes Nylander, and Ingemar Lunström. Surface plasmon resonance for gas detection and biosensing. *Sensors and Actuators*, 4:299–304, 1983. ISSN 0250-6874. doi: https://doi.org/10.1016/0250-6874(83)85036-7. URL http://www.sciencedirect.com/science/article/pii/0250687483850367.

[78] M Born and E Wolf. Principles of optics: Electromagnetic theory of propagation, interference, and diffraction of light 7th edition cambridge university press. *Cambridge, UK*, pages 752–758, 1999.

[79] Jakub Dostálek, Jiří Homola, and Miroslav Miler. Rich information format surface plasmon resonance biosensor based on array of diffraction gratings. *Sensors and Actuators B: Chemical*, 107(1):154–161, 2005. ISSN 0925-4005. doi: https://doi.org/10.1016/j.snb.2004.08.033. URL http://www.sciencedirect.com/science/article/pii/S0925400504006811.

[80] La Wang, Tian Sang, Jian Gao, Xin Yin, and Honglong Qi. High-performance sensor achieved by hybrid guide-mode resonance/surface plasmon resonance platform. *Applied optics*, 57(25):7338–7343, 2018. ISSN 2155-3165.

[81] Onur Tokel, Umit Hakan Yildiz, Fatih Inci, Naside Gozde Durmus, Okan Oner Ekiz, Burak Turker, Can Cetin, Shruthi Rao, Kaushik Sridhar, and Nalini Natarajan. Portable microfluidic integrated plasmonic platform for pathogen detection. *Scientific reports*, 5(1):1–9, 2015. ISSN 2045-2322.

[82] Jiří Homola and Marek Piliarik. *Surface plasmon resonance (SPR) sensors*, pages 45–67. Springer, 2006.

[83] Thitirat Putnin, Chutiparn Lertvachirapaiboon, Ryousuke Ishikawa, Kazunari Shinbo, Keizo Kato, Sanong Ekgasit, Kontad Ounnunkad, and Akira Baba. Enhanced organic solar cell performance: Multiple surface plasmon resonance and incorporation of silver nanodisks into a grating-structure electrode. *Opto-Electronic Advances*, 2(07):190010, 2019. ISSN 2096-4579.

[84] Sanathanan S Muttikulangara, Maciej Baranski, Shakil Rehman, Liangxing Hu, and Jianmin Miao. Mems tunable diffraction grating for spaceborne imaging spectroscopic applications. *Sensors*, 17(10):2372, 2017.

[85] Feng Wang and Y. Ron Shen. General properties of local plasmons in metal nanostructures. *Physical Review Letters*, 97(20):206806, 2006. doi: 10.1103/PhysRevLett.97.206806. URL https://link.aps.org/doi/10.1103/PhysRevLett.97.206806.

[86] Chang-Hyun Park, Yeo-Taek Yoon, and Sang-Shin Lee. Polarization-independent visible wavelength filter incorporating a symmetric metal-dielectric resonant structure. *Optics Express*, 20(21):23769–23777, 2012. ISSN 1094-4087.

[87] Alex F Kaplan, Ting Xu, and L Jay Guo. High efficiency resonance-based spectrum filters with tunable transmission bandwidth fabricated using nanoimprint lithography. *Applied Physics Letters*, 99(14):143111, 2011. ISSN 0003-6951.

[88] Stephen Y Chou, Peter R Krauss, and Preston J Renstrom. Imprint lithography with 25-nanometer resolution. *Science*, 272(5258):85–87, 1996. ISSN 0036-8075.

[89] Yi-Kuei Ryan Wu, Andrew E. Hollowell, Cheng Zhang, and L. Jay Guo. Angle-insensitive structural colours based on metallic nanocavities and coloured pixels beyond the diffraction limit. *Scientific Reports*, 3(1):1194, 2013. ISSN 2045-2322. doi: 10.1038/srep01194. URL https://doi.org/10.1038/srep01194.

[90] Ishwor Koirala, Vivek Raj Shrestha, Chul-Soon Park, Song Gao, Sang-Shin Lee, and Duk-Yong Choi. All dielectric transmissive structural multicolor pixel incorporating a resonant grating in hydrogenated amorphous silicon. *Scientific reports*, 7(1):1–7, 2017. ISSN 2045-2322.

[91] Yeo-Taek Yoon, Chang-Hyun Park, and Sang-Shin Lee. Highly efficient color filter incorporating a thin metal–dielectric resonant structure. *Applied Physics Express*, 5(2):022501, 2012. ISSN 1882-0786.

[92] Daniel B. Mazulquim, Kyu Jin Lee, Jae Woong Yoon, Leone V. Muniz, Ben-Hur V. Borges, Luiz G. Neto, and Robert Magnusson. Efficient band-pass color filters enabled by resonant modes and plasmons near the rayleigh anomaly. *Optics Express*, 22(25):30843–30851, 2014. doi: 10.1364/OE.22.030843. URL http://www.opticsexpress.org/abstract.cfm?URI=oe-22-25-30843.

[93] Lord Rayleigh. On the dynamical theory of gratings. *Proceedings of the Royal Society of London. Series A, Containing Papers of a Mathematical and Physical Character*, 79(532):399–416, 1907. ISSN 0950-1207.

[94] Mohammad Jalal Uddin and Robert Magnusson. Efficient guided-mode-resonant tunable color filters. *IEEE Photonics Technology Letters*, 24(17):1552–1554, 2012. ISSN 1041-1135.

[95] Ishwor Koirala, Vivek Raj Shrestha, Chul-Soon Park, Sang-Shin Lee, and Duk-Yong Choi. Polarization-controlled broad color palette based on an ultrathin one-dimensional resonant grating structure. *Scientific reports*, 7:40073, 2017. ISSN 2045-2322.

[96] Kyu-Tae Lee, Ji-Yun Jang, Sang Jin Park, Ujwal Kumar Thakur, Chengang Ji, L. Jay Guo, and Hui Joon Park. Subwavelength nanocavity for flexible structural transmissive color generation with a wide viewing angle. *Optica*, 3(12):1489–1495, 2016. doi: 10.1364/OPTICA.3.001489. URL http://www.osapublishing.org/optica/abstract.cfm?URI=optica-3-12-1489.

[97] Beibei Zeng, Yongkang Gao, and Filbert J. Bartoli. Ultrathin nanostructured metals for highly transmissive plasmonic subtractive color filters. *Scientific Reports*, 3: 2840, 2013. doi: 10.1038/srep02840https://www.nature.com/articles/srep02840#supplementary-information. URL https://doi.org/10.1038/srep02840.

[98] D Reibold, F Shao, A Erdmann, and U Peschel. Extraordinary low transmission effects for ultra-thin patterned metal films. *Optics express*, 17(2):544–551, 2009. ISSN 1094-4087.

[99] Ting Xu, Haofei Shi, Yi-Kuei Wu, Alex F Kaplan, Jong G Ok, and L Jay Guo. Structural colors: from plasmonic to carbon nanostructures. *Small*, 7(22):3128–3136, 2011. ISSN 1613-6810.

[100] Ting Xu, Yi-Kuei Wu, Xiangang Luo, and L Jay Guo. Plasmonic nanoresonators for high-resolution colour filtering and spectral imaging. *Nature communications*, 1(1):1–5, 2010. ISSN 2041-1723.

[101] Chang-Hyun Park, Yeo-Taek Yoon, and Sang-Shin Lee. Polarization-independent visible wavelength filter incorporating a symmetric metal-dielectric resonant structure. *Optics Express*, 20(21):23769–23777, 2012. ISSN 1094-4087.

[102] Guoguo Kang, Qiaofeng Tan, Xiaoling Wang, and Guofan Jin. Achromatic phase retarder applied to mwir lwir dual-band. *Optics express*, 18(2):1695–1703, 2010. ISSN 1094-4087.

[103] Vivek Raj Shrestha, Chul-Soon Park, and Sang-Shin Lee. Enhancement of color saturation and color gamut enabled by a dual-band color filter exhibiting an

adjustable spectral response. *Optics express*, 22(3):3691–3704, 2014. ISSN 1094-4087.

[104] Luc Duempelmann, Angelique Luu-Dinh, Benjamin Gallinet, and Lukas Novotny. Four-fold color filter based on plasmonic phase retarder. *ACS Photonics*, 3(2): 190–196, 2016. ISSN 2330-4022.

[105] Gustav Mie. Contributions to the optics of turbid media, particularly of colloidal metal solutions. *Ann.Phys*, 25(3):377–445, 1976.

[106] V. G. Kravets, A. V. Kabashin, W. L. Barnes, and A. N. Grigorenko. Plasmonic surface lattice resonances: A review of properties and applications. *Chemical Reviews*, 118(12):5912–5951, 2018. ISSN 0009-2665. doi: 10.1021/acs.chemrev.8b00243. URL https://doi.org/10.1021/acs.chemrev.8b00243.

[107] William L Barnes. Particle plasmons: Why shape matters. *American Journal of Physics*, 84(8):593–601, 2016. ISSN 0002-9505.

[108] Naomi J Halas, Surbhi Lal, Wei-Shun Chang, Stephan Link, and Peter Nordlander. Plasmons in strongly coupled metallic nanostructures. *Chemical reviews*, 111(6): 3913–3961, 2011. ISSN 0009-2665.

[109] Vadim A Markel. Divergence of dipole sums and the nature of non-lorentzian exponentially narrow resonances in one-dimensional periodic arrays of nanospheres. *Journal of Physics B: Atomic, Molecular and Optical Physics*, 38(7):115, 2005. ISSN 0953-4075.

[110] SRK Rodriguez, MC Schaafsma, A Berrier, and J Gómez Rivas. Collective resonances in plasmonic crystals: Size matters. *Physica B: Condensed Matter*, 407(20):4081–4085, 2012. ISSN 0921-4526.

[111] AM Lopatynskyi, VK Lytvyn, IV Mogylnyi, OE Rachkov, OP Soldatkin, and VI Chegel. Smart nanocarriers for drug delivery: controllable lspr tuning. *Semiconductor physics quantum electronics optoelectronics*, (19,№ 4):358–365, 2016. ISSN 1560-8034.

[112] Lin Pang, Lindsay M. Freeman, H. Matthew Chen, Qing Gu, and Yeshaiahu Fainman. volume 4, pages 399–428. North-Holland, 2014. ISBN 1573-4331.

doi: https://doi.org/10.1016/B978-0-444-59526-3.00014-8. URL http://www.sciencedirect.com/science/article/pii/B9780444595263000148.

[113] Daisuke Inoue, Atsushi Miura, Tsuyoshi Nomura, Hisayoshi Fujikawa, Kazuo Sato, Naoki Ikeda, Daiju Tsuya, Yoshimasa Sugimoto, and Yasuo Koide. Polarization independent visible color filter comprising an aluminum film with surface-plasmon enhanced transmission through a subwavelength array of holes. *Applied Physics Letters*, 98(9):093113, 2011. ISSN 0003-6951.

[114] Kuang-Li Lee, Pei-Wen Chen, Shu-Han Wu, Jhih-Bin Huang, Sen-Yeu Yang, and Pei-Kuen Wei. Enhancing surface plasmon detection using template-stripped gold nanoslit arrays on plastic films. *ACS nano*, 6(4):2931–2939, 2012. ISSN 1936-0851.

[115] Markus A Schmidt, Dang Yuan Lei, Lothar Wondraczek, Virginie Nazabal, and Stefan A Maier. Hybrid nanoparticle–microcavity-based plasmonic nanosensors with improved detection resolution and extended remote-sensing ability. *Nature communications*, 3(1):1–8, 2012. ISSN 2041-1723.

[116] Stephen Y Chou, Peter R Krauss, and Preston J Renstrom. Imprint lithography with 25-nanometer resolution. *Science*, 272(5258):85–87, 1996. ISSN 0036-8075.

[117] Beibei Zeng, Xufeng Yang, Changtao Wang, and Xiangang Luo. Plasmonic interference nanolithography with a double-layer planar silver lens structure. *Optics Express*, 17(19):16783–16791, 2009. ISSN 1094-4087.

[118] LB Sun, XL Hu, Y Xu, QJ Wu, B Shi, M Ye, LS Wang, J Zhao, XL Li, and YQ Wu. Influence of structural parameters to polarization-independent color-filter behavior in ultrathin ag films. *Optics Communications*, 333:16–21, 2014. ISSN 0030-4018.

[119] Yun Seon Do, Jung Ho Park, Bo Yeon Hwang, Sung-Min Lee, Byeong-Kwon Ju, and Kyung Cheol Choi. Plasmonic color filter and its fabrication for large-area applications. *Advanced Optical Materials*, 1(2):133–138, 2013. ISSN 2195-1071.

[120] Xiao Ming Goh, Yihan Zheng, Shawn J. Tan, Lei Zhang, Karthik Kumar, Cheng-Wei Qiu, and Joel K. W. Yang. Three-dimensional plasmonic stereoscopic prints in full colour. *Nature Communications*, 5(1):5361, 2014. ISSN 2041-1723. doi: 10.1038/ncomms6361. URL https://doi.org/10.1038/ncomms6361.

[121] J. Parsons, E. Hendry, C. P. Burrows, B. Auguié, J. R. Sambles, and W. L. Barnes. Localized surface-plasmon resonances in periodic nondiffracting metallic nanoparticle and nanohole arrays. *Physical Review B*, 79(7):073412, 2009. doi: 10.1103/PhysRevB.79.073412. URL https://link.aps.org/doi/10.1103/PhysRevB.79.073412.

[122] Hong-Shik Lee, Yeo-Taek Yoon, Sang-Shin Lee, Sang-Hoon Kim, and Ki-Dong Lee. Color filter based on a subwavelength patterned metal grating. *Optics express*, 15 (23):15457–15463, 2007. ISSN 1094-4087.

[123] Xiaokang Li, Maria Soler, Cenk I. Özdemir, Alexander Belushkin, Filiz Yesilköy, and Hatice Altug. Plasmonic nanohole array biosensor for label-free and real-time analysis of live cell secretion. *Lab on a Chip*, 17(13):2208–2217, 2017. ISSN 1473-0197. doi: 10.1039/C7LC00277G. URL http://dx.doi.org/10.1039/C7LC00277G.

[124] Yanqin Wang, Xiaoliang Ma, Xiong Li, Mingbo Pu, and Xiangang Luo. Perfect electromagnetic and sound absorption via subwavelength holes array. *Opto-Electronic Advances*, 1(08):180013, 2018. ISSN 2096-4579.

[125] Yu Horie, Seunghoon Han, Jeong-Yub Lee, Jaekwan Kim, Yongsung Kim, Amir Arbabi, Changgyun Shin, Lilong Shi, Ehsan Arbabi, Seyedeh Mahsa Kamali, Hong-Seok Lee, Sungwoo Hwang, and Andrei Faraon. Visible wavelength color filters using dielectric subwavelength gratings for backside-illuminated cmos image sensor technologies. *Nano Letters*, 17(5):3159–3164, 2017. ISSN 1530-6984. doi: 10.1021/acs.nanolett.7b00636. URL https://doi.org/10.1021/acs.nanolett.7b00636.

[126] R. Rüther, J. Livingstone, and N. Dytlewski. Large-grain polycrystalline silicon thin films obtained by low-temperature stepwise annealing of hydrogenated amorphous silicon. *Thin Solid Films*, 310(1):67–74, 1997. ISSN 0040-6090. doi: https://doi.org/10.1016/S0040-6090(97)00362-3. URL http://www.sciencedirect.com/science/article/pii/S0040609097003623.

[127] Mark L. Brongersma, Yi Cui, and Shanhui Fan. Light management for photovoltaics using high-index nanostructures. *Nature Materials*, 13(5):451–460,

2014. ISSN 1476-4660. doi: 10.1038/nmat3921. URL https://doi.org/10.1038/nmat3921.

[128] Zhibo Li, Alasdair W. Clark, and Jonathan M. Cooper. Dual color plasmonic pixels create a polarization controlled nano color palette. *ACS Nano*, 10(1):492–498, 2016. ISSN 1936-0851. doi: 10.1021/acsnano.5b05411. URL https://doi.org/10.1021/acsnano.5b05411.

[129] Fei Cheng, Jie Gao, Ting S Luk, and Xiaodong Yang. Structural color printing based on plasmonic metasurfaces of perfect light absorption. *Scientific reports*, 5: 11045, 2015. ISSN 2045-2322.

[130] S. T. Davies and B. Khamsehpour. Focused ion beam machining and deposition for nanofabrication. *Vacuum*, 47(5):455–462, 1996. ISSN 0042-207X. doi: https://doi.org/10.1016/0042-207X(95)00235-9. URL http://www.sciencedirect.com/science/article/pii/0042207X95002359.

[131] Xin He, Yajing Liu, Paul Beckett, Hemayet Uddin, Ampalavanapillai Nirmalathas, and Ranjith Rajasekharan Unnithan. Transmission enhancement in plasmonic nanohole array for colour imaging applications. In *AOS Australian Conference on Optical Fibre Technology (ACOFT) and Australian Conference on Optics, Lasers, and Spectroscopy (ACOLS) 2019*, volume 11200, page 112003M. International Society for Optics and Photonics.

[132] Karthik Kumar, Huigao Duan, Ravi S Hegde, Samuel CW Koh, Jennifer N Wei, and Joel KW Yang. Printing colour at the optical diffraction limit. *Nature nanotechnology*, 7(9):557, 2012. ISSN 1748-3395.

[133] Boris Luk'yanchuk, Nikolay I Zheludev, Stefan A Maier, Naomi J Halas, Peter Nordlander, Harald Giessen, and Chong Tow Chong. The fano resonance in plasmonic nanostructures and metamaterials. *Nature materials*, 9(9):707–715, 2010. ISSN 1476-4660.

[134] Hua Qi, Dimitri Alexson, Orest Glembocki, and SM Prokes. The effect of size and size distribution on the oxidation kinetics and plasmonics of nanoscale ag particles. *Nanotechnology*, 21(21):215706, 2010. ISSN 0957-4484.

[135] Shawn J Tan, Lei Zhang, Di Zhu, Xiao Ming Goh, Ying Min Wang, Karthik Kumar, Cheng-Wei Qiu, and Joel KW Yang. Plasmonic color palettes for

photorealistic printing with aluminum nanostructures. *Nano letters*, 14(7):4023–4029, 2014. ISSN 1530-6984.

[136] Jiancun Zhao, Xiaochang Yu, Kui Zhou, Xiaoming Yang, and Yiting Yu. Wide-gamut and polarization-independent structural color at optical sub-diffraction-limit spatial resolution based on uncoupled lspps. *Nanoscale research letters*, 14 (1):1–7, 2019. ISSN 1556-276X.

[137] Jiancun Zhao, Xiaochang Yu, Xiaoming Yang, Quan Xiang, Huigao Duan, and Yiting Yu. Polarization independent subtractive color printing based on ultrathin hexagonal nanodisk-nanohole hybrid structure arrays. *Optics express*, 25(19): 23137–23145, 2017. ISSN 1094-4087.

[138] David Woolf, Marko Loncar, and Federico Capasso. The forces from coupled surface plasmon polaritons in planar waveguides. *Optics express*, 17(22):19996–20011, 2009. ISSN 1094-4087.

[139] Peng Dai, Yasi Wang, Xupeng Zhu, Huimin Shi, Yiqin Chen, Shi Zhang, Wenhong Yang, Zhiquan Chen, Shumin Xiao, and Huigao Duan. Transmissive structural color filters using vertically coupled aluminum nanohole/nanodisk array with a triangular-lattice. *Nanotechnology*, 29(39):395202, 2018. ISSN 0957-4484.

[140] Jeppe S. Clausen, Emil Højlund-Nielsen, Alexander B. Christiansen, Sadegh Yazdi, Meir Grajower, Hesham Taha, Uriel Levy, Anders Kristensen, and N. Asger Mortensen. Plasmonic metasurfaces for coloration of plastic consumer products. *Nano Letters*, 14(8):4499–4504, 2014. ISSN 1530-6984. doi: 10.1021/nl5014986. URL https://doi.org/10.1021/nl5014986.

[141] Santiago García-Cuevas Carrillo, Liam Trimby, Yat-Yin Au, V Karthik Nagareddy, Gerardo Rodriguez-Hernandez, Peiman Hosseini, Carlos Ríos, Harish Bhaskaran, and C David Wright. A nonvolatile phase-change metamaterial color display. *Advanced Optical Materials*, 7(18):1801782, 2019. ISSN 2195-1071.

[142] Xin Huang, Fan Yang, Bing Gao, Qi Yang, Jiamin Wu, and Wei He. Metamaterial absorber with independently tunable amplitude and frequency in the terahertz regime. *Optics express*, 27(18):25902–25911, 2019. ISSN 1094-4087.

[143] Wei Zhu, Ruisheng Yang, Yuancheng Fan, Quanhong Fu, Hongjing Wu, Peng Zhang, Nian-Hai Shen, and Fuli Zhang. Controlling optical polarization conversion

with ge2sb2te5-based phase-change dielectric metamaterials. *Nanoscale*, 10(25): 12054–12061, 2018. ISSN 2040-3364. doi: 10.1039/C8NR02587H. URL http://dx.doi.org/10.1039/C8NR02587H.

[144] Tiancheng Han, Xue Bai, Dongliang Gao, John TL Thong, Baowen Li, and Cheng-Wei Qiu. Experimental demonstration of a bilayer thermal cloak. *Physical Review Letters*, 112(5):054302, 2014.

[145] C. Menzel, C. Helgert, C. Rockstuhl, E. B. Kley, A. Tünnermann, T. Pertsch, and F. Lederer. Asymmetric transmission of linearly polarized light at optical metamaterials. *Physical Review Letters*, 104(25):253902, 2010. doi: 10.1103/PhysRevLett.104.253902. URL https://link.aps.org/doi/10.1103/PhysRevLett.104.253902.

[146] Zhaowei Liu, Hyesog Lee, Yi Xiong, Cheng Sun, and Xiang Zhang. Far-field optical hyperlens magnifying sub-diffraction-limited objects. *science*, 315(5819): 1686–1686, 2007. ISSN 0036-8075.

[147] Jiaming Hao, Jing Wang, Xianliang Liu, Willie J Padilla, Lei Zhou, and Min Qiu. High performance optical absorber based on a plasmonic metamaterial. *Applied Physics Letters*, 96(25):251104, 2010. ISSN 0003-6951.

[148] Chenying Yang, Weidong Shen, Jing Zhou, Xu Fang, Ding Zhao, Xing Zhang, Chengang Ji, Bo Fang, Yueguang Zhang, and Xu Liu. Angle robust reflection/-transmission plasmonic filters using ultrathin metal patch array. *Advanced Optical Materials*, 4(12):1981–1986, 2016. ISSN 2195-1071.

[149] Gururaj V Naik, Vladimir M Shalaev, and Alexandra Boltasseva. Alternative plasmonic materials: beyond gold and silver. *Advanced Materials*, 25(24):3264–3294, 2013. ISSN 0935-9648.

[150] Jana Olson, Alejandro Manjavacas, Lifei Liu, Wei-Shun Chang, Benjamin Foerster, Nicholas S King, Mark W Knight, Peter Nordlander, Naomi J Halas, and Stephan Link. Vivid, full-color aluminum plasmonic pixels. *Proceedings of the national academy of sciences*, 111(40):14348–14353, 2014. ISSN 0027-8424.

[151] Ming Ye, Libin Sun, Xiaolin Hu, Bin Shi, Beibei Zeng, Liansheng Wang, Jun Zhao, Shumin Yang, Renzhong Tai, and Hans-Jorg Fecht. Angle-insensitive plasmonic

color filters with randomly distributed silver nanodisks. *Optics letters*, 40(21): 4979–4982, 2015. ISSN 1539-4794.

[152] Vivek R. Shrestha, Sang-Shin Lee, Eun-Soo Kim, and Duk-Yong Choi. Aluminum plasmonics based highly transmissive polarization-independent subtractive color filters exploiting a nanopatch array. *Nano Letters*, 14(11):6672–6678, 2014. ISSN 1530-6984. doi: 10.1021/nl503353z. URL https://doi.org/10.1021/nl503353z.

[153] Jana Olson, Alejandro Manjavacas, Tiyash Basu, Da Huang, Andrea E Schlather, Bob Zheng, Naomi J Halas, Peter Nordlander, and Stephan Link. High chromaticity aluminum plasmonic pixels for active liquid crystal displays. *ACS nano*, 10(1):1108–1117, 2016. ISSN 1936-0851.

[154] QJ Wu, H Jia, XL Hu, LB Sun, LS Wang, SM Yang, RZ Tai, Hans-Jörg Fecht, LQ Wang, and DX Zhang. Plasmonic reflection color filters with metallic random nanostructures. *Nanotechnology*, 28(8):085203, 2017. ISSN 0957-4484.

[155] Anders Pors and Sergey I Bozhevolnyi. Plasmonic metasurfaces for efficient phase control in reflection. *Optics express*, 21(22):27438–27451, 2013. ISSN 1094-4087.

[156] Wenshan Cai, Uday K Chettiar, Hsiao-Kuan Yuan, Vashista C de Silva, Alexander V Kildishev, Vladimir P Drachev, and Vladimir M Shalaev. Metamagnetics with rainbow colors. *Optics express*, 15(6):3333–3341, 2007. ISSN 1094-4087.

[157] Michael G. Nielsen, Dmitri K. Gramotnev, Anders Pors, Ole Albrektsen, and Sergey I. Bozhevolnyi. Continuous layer gap plasmon resonators. *Optics Express*, 19(20):19310–19322, 2011. doi: 10.1364/OE.19.019310. URL http://www.opticsexpress.org/abstract.cfm?URI=oe-19-20-19310.

[158] Anders Pors, Michael G Nielsen, René Lynge Eriksen, and Sergey I Bozhevolnyi. Broadband focusing flat mirrors based on plasmonic gradient metasurfaces. *Nano letters*, 13(2):829–834, 2013. ISSN 1530-6984.

[159] Hai Zhu, Fei Yi, and Ertugrul Cubukcu. Plasmonic metamaterial absorber for broadband manipulation of mechanical resonances. *Nature Photonics*, 10(11):709–714, 2016. ISSN 1749-4893. doi: 10.1038/nphoton.2016.183. URL https://doi.org/10.1038/nphoton.2016.183.

[160] Benny Walther, Christian Helgert, Carsten Rockstuhl, Frank Setzpfandt, Falk Eilenberger, Ernst-Bernhard Kley, Falk Lederer, Andreas Tünnermann, and Thomas Pertsch. Spatial and spectral light shaping with metamaterials. *Advanced Materials*, 24(47):6300–6304, 2012. ISSN 0935-9648.

[161] Zhongyang Li, Edgar Palacios, Serkan Butun, and Koray Aydin. Visible-frequency metasurfaces for broadband anomalous reflection and high-efficiency spectrum splitting. *Nano letters*, 15(3):1615–1621, 2015. ISSN 1530-6984.

[162] Jing Wang, Yiting Chen, Xi Chen, Jiaming Hao, Min Yan, and Min Qiu. Photothermal reshaping of gold nanoparticles in a plasmonic absorber. *Optics express*, 19(15):14726–14734, 2011. ISSN 1094-4087.

[163] Pin Chieh Wu, Wei-Yi Tsai, Wei Ting Chen, Yao-Wei Huang, Ting-Yu Chen, Jia-Wern Chen, Chun Yen Liao, Cheng Hung Chu, Greg Sun, and Din Ping Tsai. Versatile polarization generation with an aluminum plasmonic metasurface. *Nano letters*, 17(1):445–452, 2017. ISSN 1530-6984.

[164] Anders Pors, Michael G. Nielsen, Thomas Bernardin, Jean-Claude Weeber, and Sergey I. Bozhevolnyi. Efficient unidirectional polarization-controlled excitation of surface plasmon polaritons. *Light: Science Applications*, 3(8):e197–e197, 2014. ISSN 2047-7538. doi: 10.1038/lsa.2014.78. URL https://doi.org/10.1038/lsa.2014.78.

[165] Alexander S. Roberts, Anders Pors, Ole Albrektsen, and Sergey I. Bozhevolnyi. Subwavelength plasmonic color printing protected for ambient use. *Nano Letters*, 14(2):783–787, 2014. ISSN 1530-6984. doi: 10.1021/nl404129n. URL https://doi.org/10.1021/nl404129n.

[166] Hao Wang, Xiaolong Wang, Chen Yan, Hua Zhao, Jingwen Zhang, Christian Santschi, and Olivier J. F. Martin. Full color generation using silver tandem nanodisks. *ACS Nano*, 11(5):4419–4427, 2017. ISSN 1936-0851. doi: 10.1021/acsnano.6b08465. URL https://doi.org/10.1021/acsnano.6b08465.

[167] Masashi Miyata, Hideaki Hatada, and Junichi Takahara. Full-color subwavelength printing with gap-plasmonic optical antennas. *Nano Letters*, 16(5):3166–3172, 2016. ISSN 1530-6984. doi: 10.1021/acs.nanolett.6b00500. URL https://doi.org/10.1021/acs.nanolett.6b00500.

[168] Hendrik Christoffel Hulst and Hendrik C van de Hulst. *Light scattering by small particles*. Courier Corporation, 1981. ISBN 0486642283.

[169] Darko Kajfez and Pierre Guillon. Dielectric resonators. *Norwood, MA, Artech House, Inc., 1986, 547 p. No individual items are abstracted in this volume.*, 1986.

[170] Andrey B. Evlyukhin, Sergey M. Novikov, Urs Zywietz, René Lynge Eriksen, Carsten Reinhardt, Sergey I. Bozhevolnyi, and Boris N. Chichkov. Demonstration of magnetic dipole resonances of dielectric nanospheres in the visible region. *Nano Letters*, 12(7):3749–3755, 2012. ISSN 1530-6984. doi: 10.1021/nl301594s. URL https://doi.org/10.1021/nl301594s.

[171] James C Ginn, Igal Brener, David W Peters, Joel R Wendt, Jeffrey O Stevens, Paul F Hines, Lorena I Basilio, Larry K Warne, Jon F Ihlefeld, and Paul G Clem. Realizing optical magnetism from dielectric metamaterials. *Physical review letters*, 108(9):097402, 2012.

[172] RB Greegor, CG Parazzoli, K Li, and MH Tanielian. Origin of dissipative losses in negative index of refraction materials. *Applied Physics Letters*, 82(14):2356–2358, 2003. ISSN 0003-6951.

[173] Shang Sun, Zhenxing Zhou, Chen Zhang, Yisheng Gao, Zonghui Duan, Shumin Xiao, and Qinghai Song. All-dielectric full-color printing with tio2 metasurfaces. *ACS Nano*, 11(5):4445–4452, 2017. ISSN 1936-0851. doi: 10.1021/acsnano.7b00415. URL https://doi.org/10.1021/acsnano.7b00415.

[174] Yusuke Nagasaki, Masafumi Suzuki, and Junichi Takahara. All-dielectric dual-color pixel with subwavelength resolution. *Nano Letters*, 17(12):7500–7506, 2017. ISSN 1530-6984. doi: 10.1021/acs.nanolett.7b03421. URL https://doi.org/10.1021/acs.nanolett.7b03421.

[175] Bo Yang, Wenwei Liu, Zhancheng Li, Hua Cheng, Duk-Yong Choi, Shuqi Chen, and Jianguo Tian. Ultrahighly saturated structural colors enhanced by multipolar-modulated metasurfaces. *Nano Letters*, 19(7):4221–4228, 2019. ISSN 1530-6984. doi: 10.1021/acs.nanolett.8b04923. URL https://doi.org/10.1021/acs.nanolett.8b04923.

[176] Jhen-Hong Yang, Viktoriia E. Babicheva, Min-Wen Yu, Tien-Chang Lu, Tzy-Rong Lin, and Kuo-Ping Chen. Structural colors enabled by lattice resonance on silicon

nitride metasurfaces. *ACS Nano*, 14(5):5678–5685, 2020. ISSN 1936-0851. doi: 10.1021/acsnano.0c00185. URL https://doi.org/10.1021/acsnano.0c00185.

[177] Vishal Vashistha, Gayatri Vaidya, Ravi S. Hegde, Andriy E. Serebryannikov, Nicolas Bonod, and Maciej Krawczyk. All-dielectric metasurfaces based on cross-shaped resonators for color pixels with extended gamut. *ACS Photonics*, 4(5): 1076–1082, 2017. doi: 10.1021/acsphotonics.6b00853. URL https://doi.org/10.1021/acsphotonics.6b00853.

[178] Yusuke Nagasaki, Masafumi Suzuki, and Junichi Takahara. All-dielectric dual-color pixel with subwavelength resolution. *Nano Letters*, 17(12):7500–7506, 2017. ISSN 1530-6984. doi: 10.1021/acs.nanolett.7b03421. URL https://doi.org/10.1021/acs.nanolett.7b03421.

[179] Yusuke Nagasaki, Ikuto Hotta, Masafumi Suzuki, and Junichi Takahara. Metal-masked mie-resonant full-color printing for achieving free-space resolution limit. *ACS Photonics*, 5(9):3849–3855, 2018. doi: 10.1021/acsphotonics.8b00895. URL https://doi.org/10.1021/acsphotonics.8b00895.

[180] Wenjing Yue, Song Gao, Sang-Shin Lee, Eun-Soo Kim, and Duk-Yong Choi. Subtractive color filters based on a silicon-aluminum hybrid-nanodisk metasurface enabling enhanced color purity. *Scientific Reports*, 6(1):29756, 2016. ISSN 2045-2322. doi: 10.1038/srep29756. URL https://doi.org/10.1038/srep29756.

[181] Hongliang Li, Song Gao, Yang Li, Chunwei Zhang, and Wenjing Yue. Dielectric metasurfaces based on a rectangular lattice of a-si:h nanodisks for color pixels with high saturation and stability. *Optics Express*, 27(24):35027–35040, 2019. doi: 10.1364/OE.27.035027. URL http://www.opticsexpress.org/abstract.cfm?URI=oe-27-24-35027.

[182] Chul-Soon Park, Vivek Raj Shrestha, Wenjing Yue, Song Gao, Sang-Shin Lee, Eun-Soo Kim, and Duk-Yong Choi. Structural color filters enabled by a dielectric metasurface incorporating hydrogenated amorphous silicon nanodisks. *Scientific Reports*, 7(1):2556, 2017. ISSN 2045-2322. doi: 10.1038/s41598-017-02911-w. URL https://doi.org/10.1038/s41598-017-02911-w.

[183] Julien Proust, Frédéric Bedu, Bruno Gallas, Igor Ozerov, and Nicolas Bonod. All-dielectric colored metasurfaces with silicon mie resonators. *ACS Nano*, 10(8):

7761–7767, 2016. ISSN 1936-0851. doi: 10.1021/acsnano.6b03207. URL https://doi.org/10.1021/acsnano.6b03207.

[184] Jing Yang, Fangfang Luo, Tsung Sheng Kao, Xiong Li, Ghim Wei Ho, Jinghua Teng, Xiangang Luo, and Minghui Hong. Design and fabrication of broadband ultralow reflectivity black si surfaces by laser micro/nanoprocessing. *Light: Science Applications*, 3(7):e185–e185, 2014. ISSN 2047-7538. doi: 10.1038/lsa.2014.66. URL https://doi.org/10.1038/lsa.2014.66.

[185] Yanhui Zhao, Qingzhen Hao, Yi Ma, Mengqian Lu, Bingxin Zhang, Michael Lapsley, Iam-Choon Khoo, and Tony Jun Huang. Light-driven tunable dual-band plasmonic absorber using liquid-crystal-coated asymmetric nanodisk array. *Applied Physics Letters*, 100(5):053119, 2012. ISSN 0003-6951.

[186] G Geandier, P-O Renault, E Le Bourhis, Ph Goudeau, D Faurie, Christophe Le Bourlot, Ph Djémia, O Castelnau, and SM Cherif. Elastic-strain distribution in metallic film-polymer substrate composites. *Applied Physics Letters*, 96(4): 041905, 2010. ISSN 0003-6951.

[187] Annette Böhme, Florian Sterl, Elinor Kath, Monika Ubl, Venla Manninen, and Harald Giessen. Electrochemistry on inverse copper nanoantennas: Active plasmonic devices with extraordinarily large resonance shift. *ACS Photonics*, 6 (8):1863–1868, 2019. doi: 10.1021/acsphotonics.9b00716. URL https://doi.org/10.1021/acsphotonics.9b00716.

[188] Yue Bing Zheng, Ying-Wei Yang, Lasse Jensen, Lei Fang, Bala Krishna Juluri, Amar H Flood, Paul S Weiss, J Fraser Stoddart, and Tony Jun Huang. Active molecular plasmonics: controlling plasmon resonances with molecular switches. *Nano Letters*, 9(2):819–825, 2009. ISSN 1530-6984.

[189] Shin-Tson Wu. Birefringence dispersions of liquid crystals. *Physical Review A*, 33 (2):1270, 1986.

[190] Guangyuan Si, Yanhui Zhao, Eunice Sok Ping Leong, and Yan Jun Liu. Liquid-crystal-enabled active plasmonics: a review. *Materials*, 7(2):1296–1317, 2014.

[191] Chang-Hyun Park, Yeo-Taek Yoon, Vivek Raj Shrestha, Chul-Soon Park, Sang-Shin Lee, and Eun-Soo Kim. Electrically tunable color filter based on a

polarization-tailored nano-photonic dichroic resonator featuring an asymmetric subwavelength grating. *Optics Express*, 21.

[192] Youngjin Lee, Min-Kyu Park, Seunguk Kim, Jeong Hee Shin, Cheil Moon, Jae Youn Hwang, Jun-Chan Choi, Heewon Park, Hak-Rin Kim, and Jae Eun Jang. Electrical broad tuning of plasmonic color filter employing an asymmetric-lattice nanohole array of metasurface controlled by polarization rotator. *ACS Photonics*, 4(8):1954–1966, 2017. doi: 10.1021/acsphotonics.7b00249. URL https://doi.org/10.1021/acsphotonics.7b00249.

[193] Deng-Ke Yang and Shin-Tson Wu. *Fundamentals of liquid crystal devices*. John Wiley Sons, 2014. ISBN 1118752007.

[194] Zu-Wen Xie, Jhen-Hong Yang, Vishal Vashistha, Wei Lee, and Kuo-Ping Chen. Liquid-crystal tunable color filters based on aluminum metasurfaces. *Optics express*, 25(24):30764–30770, 2017. ISSN 1094-4087.

[195] Chul-Soon Im and Sang-Shin Lee. Highly efficient and angle-tolerant mid-infrared filter based on a cascaded etalon resonator. *Optics express*, 25(14):16083–16091, 2017. ISSN 1094-4087.

[196] Vivek Raj Shrestha, Sang-Shin Lee, Eun-Soo Kim, and Duk-Yong Choi. Non-iridescent transmissive structural color filter featuring highly efficient transmission and high excitation purity. *Scientific reports*, 4(1):1–8, 2014. ISSN 2045-2322.

[197] Tae-Hui Noh, Yeo-Taek Yoon, Hong-Shik Lee, Sang-Shin Lee, and Duk-Yong Choi. Highly angle tolerant filter incorporating serially cascaded a-si based etalons and its application to a compact receiver. *Optics express*, 21 1:1301–9, 2013.

[198] Hwa-Seub Lee, Gyu-Weon Hwang, Tae-Yeon Seong, Jongkil Park, Jae Wook Kim, Won Mok Kim, Inho Kim, and Kyeong-Seok Lee. Design of mid-infrared filter array based on plasmonic metal nanodiscs array and its application to on-chip spectrometer. *Scientific reports*, 11(1):1–10, 2021.

[199] Chengang Ji, Chenying Yang, Weidong Shen, Kyu-Tae Lee, Yueguang Zhang, Xu Liu, and L. Jay Guo. Decorative near-infrared transmission filters featuring high-efficiency and angular-insensitivity employing 1d photonic crystals. *Nano Research*, 12(3):543–548, 2019. ISSN 1998-0000. doi: 10.1007/s12274-018-2249-8. URL https://doi.org/10.1007/s12274-018-2249-8.

[200] Chul-Soon Park and Sang-Shin Lee. Vivid coloration and broadband perfect absorption based on asymmetric fabry–pérot nanocavities incorporating platinum. *ACS Applied Nano Materials*, 4(4):4216–4225, 2021. doi: 10.1021/acsanm.1c00699. URL https://doi.org/10.1021/acsanm.1c00699.

[201] Kane Yee. Numerical solution of initial boundary value problems involving maxwell's equations in isotropic media. *IEEE Transactions on antennas and propagation*, 14(3):302–307, 1966. ISSN 0018-926X.

[202] Wenchao Qian, Yilin Wang, Song Zhang, Maowen Song, Yi Zou, and Ting Xu. Lithography-free nanofilm color filters composed of cmos-compatible materials. *IEEE Photonics Technology Letters*, 2021. ISSN 1041-1135.

[203] Kenneth Diest, Jennifer A. Dionne, Merrielle Spain, and Harry A. Atwater. Tunable color filters based on metalinsulatormetal resonators. *Nano Letters*, 9 (7):2579–2583, 2009. ISSN 1530-6984. doi: 10.1021/nl900755b. URL https://doi.org/10.1021/nl900755b.

[204] Chengang Ji, Chenying Yang, Weidong Shen, Kyu-Tae Lee, Yueguang Zhang, Xu Liu, and L. Jay Guo. Decorative near-infrared transmission filters featuring high-efficiency and angular-insensitivity employing 1d photonic crystals. *Nano Research*, 12(3):543–548, 2019. ISSN 1998-0000. doi: 10.1007/s12274-018-2249-8. URL https://doi.org/10.1007/s12274-018-2249-8.

[205] Mikhail A Kats, Steven J Byrnes, Romain Blanchard, Mathias Kolle, Patrice Genevet, Joanna Aizenberg, and Federico Capasso. Enhancement of absorption and color contrast in ultra-thin highly absorbing optical coatings. *Applied Physics Letters*, 103(10):101104, 2013. ISSN 0003-6951.

[206] Zhongyang Li, Serkan Butun, and Koray Aydin. Large-area, lithography-free super absorbers and color filters at visible frequencies using ultrathin metallic films. *Acs Photonics*, 2(2):183–188, 2015. ISSN 2330-4022.

[207] Max Born. E. wolf principles of optics. *Pergamon Press*, 6(188):36–111, 1980.

[208] Edward D Palik. *Handbook of optical constants of solids*, pages 429–443. Elsevier, 1997.

[209] Stephanie L. Brock. Nanostructures and nanomaterials: Synthesis, properties and applications, 2004.

[210] AK Sinha. Plasma-enhanced chemical vapor-deposition-review. In *JOURNAL OF THE ELECTROCHEMICAL SOCIETY*, volume 123, pages C262–C263. ELECTROCHEMICAL SOC INC 10 SOUTH MAIN STREET, PENNINGTON, NJ 08534. ISBN 0013-4651.

[211] Pradeep Dixit and Jianmin Miao. Effect of sf6flow rate on the etched surface profile and bottom grass formation in deep reactive ion etching process. *Journal of Physics: Conference Series*, 34:577–582, 2006. ISSN 1742-6588 1742-6596. doi: 10.1088/1742-6596/34/1/095. URL http://dx.doi.org/10.1088/1742-6596/34/1/095.

[212] Rolf Erni, Marta D Rossell, Christian Kisielowski, and Ulrich Dahmen. Atomic-resolution imaging with a sub-50-pm electron probe. *Physical review letters*, 102 (9):096101, 2009.

[213] Ray F Egerton. *Physical principles of electron microscopy*, volume 56. Springer, 2005.

[214] AE Owen. Fundamentals of uv-visible spectroscopy. 1996.

[215] Hiroyuki Fujiwara. *Spectroscopic ellipsometry: principles and applications*. John Wiley Sons, 2007. ISBN 0470060182.

[216] John A Woollam, James N Hilfiker, Corey L Bungay, Ron A Synowicki, Thomas E Tiwald, and Daniel W Thompson. Spectroscopic ellipsometry from the vacuum ultraviolet to the far infrared. In *AIP Conference Proceedings*, volume 550, pages 511–518. American Institute of Physics. ISBN 156396967X.

[217] Harland Tompkins and Eugene A Irene. *Handbook of ellipsometry*. William Andrew, 2005. ISBN 0815517475.

[218] Hiroyuki Fujiwara. *Spectroscopic ellipsometry: principles and applications*. John Wiley Sons, 2007. ISBN 0470060182.

[219] Jorge J Moré. *The Levenberg-Marquardt algorithm: implementation and theory*, pages 105–116. Springer, 1978.

[220] Manohar Chirumamilla, Alexander S Roberts, Fei Ding, Deyong Wang, Peter Kjær Kristensen, Sergey I Bozhevolnyi, and Kjeld Pedersen. Multilayer tungsten-alumina-based broadband light absorbers for high-temperature applications. *Optical Materials Express*, 6(8):2704–2714, 2016. ISSN 2159-3930.

[221] Yohan Lee, Jeongse Yun, Minjee Seo, Sun-Je Kim, Jaehyun Oh, Chung Mu Kang, Ho-Jung Sun, Taek Dong Chung, and Byoungho Lee. Full-color-tunable nanophotonic device using electrochromic tungsten trioxide thin film. *Nano Letters*, 20(8):6084–6090, 2020. ISSN 1530-6984. doi: 10.1021/acs.nanolett.0c02097. URL https://doi.org/10.1021/acs.nanolett.0c02097.

[222] Yiyang Li, Jorik van de Groep, A Alec Talin, and Mark L Brongersma. Dynamic tuning of gap plasmon resonances using a solid-state electrochromic device. *Nano letters*, 19(11):7988–7995, 2019. ISSN 1530-6984.

[223] S. Z. Ali, F. Udrea, W. I. Milne, and J. W. Gardner. Tungsten-based soi microhotplates for smart gas sensors. *Journal of Microelectromechanical Systems*, 17(6):1408–1417, 2008. ISSN 1941-0158. doi: 10.1109/JMEMS.2008.2007228.

[224] G · Wyszecki and Walter Stanley Stiles. *Color science: concepts and methods, quantitative data and formulae*. John Wiley Sons, 1982. ISBN 0471021067.

[225] Yasaman Hamedani, Prathyushakrishna Macha, Timothy J Bunning, Rajesh R Naik, and Milana C Vasudev. *Plasma-enhanced chemical vapor deposition: Where we are and the outlook for the future*. InTech, 2016.

[226] James Clerk Maxwell. Viii. a dynamical theory of the electromagnetic field. *Philosophical transactions of the Royal Society of London*, (155):459–512, 1865. ISSN 0261-0523.

Appendix A

List of Publications

nanomaterials

MDPI

Review

Nanostructured Color Filters: A Review of Recent Developments

Ayesha Shaukat [1,2], Frazer Noble [1] and Khalid Mahmood Arif [1,*]

[1] Department of Mechanical and Electrical Engineering, SF&AT, Massey University, Auckland 0632, New Zealand; a.shaukat@massey.ac.nz (A.S.); f.k.noble@massey.ac.nz (F.N.)
[2] Engineering and Management Sciences, Balochistan University of Information Technology, Quetta 87100, Pakistan
* Correspondence: k.arif@massey.ac.nz; Tel.: +64-9-414-0800

Received: 21 June 2020; Accepted: 23 July 2020; Published: 7 August 2020

check for updates

Abstract: Color plays an important role in human life: without it life would be dull and monochromatic. Printing color with distinct characteristics, like hue, brightness and saturation, and high resolution, are the main characteristic of image sensing devices. A flexible design of color filter is also desired for angle insensitivity and independence of direction of polarization of incident light. Furthermore, it is important that the designed filter be compatible with the image sensing devices in terms of technology and size. Therefore, color filter requires special care in its design, operation and integration. In this paper, we present a comprehensive review of nanostructured color filter designs described to date and evaluate them in terms of their performance.

Keywords: color filters; photonic crystals; nanoholes; mie scattering; liquid crystal display

1. Introduction

The incoming electromagnetic waves of the visible spectrum (400–700 nm) are capable of stimulating the photo-receptor cells of the human retina, which enables color perception. In image sensing devices (cameras, scanners, printers, etc.), which replicate the eye operation, color recognition plays an imperative part to store accurate color information at each pixel of the captured image. The produced color quality via filters is subject to full wave half width maximum value, efficiency and distinct location of transmission peak/reflection dip in the visible spectrum. Hence, all aforementioned characteristics play role in positioning the output color on the CIE Map 1931 [1].

Typically, additive or subtractive color and Bayer filter [2], along with polymer-based filter technologies, have been exploited for image sensing. Over the last three decades, synthetic dyes and pigment-based colors [3] have been extensively used for decorating objects, printing ink, synthetic fibers and identification [4–6]. Nevertheless, these filters have many disadvantages such as non-recyclability, non-affordability, and cause environmental damage. Likewise, their performance as image sensors [7,8] also has limitations such as inadequate resolution and fragility. However, recent progress in color filter design, along with the evolution in optical physics [9,10] and fabrication technology [11–13], has revolutionized color filtering process and replaced the conventional dry/pigment-based coloring, due to its color tunability, durability, high resolution and environmental friendliness.

In the past Charged Coupled Devices (CCD) were mainly used for different image sensing devices like cameras, microscopes and detectors in the field of life sciences, astronomy and optical microscopy. However, in recent times, Complementary Metal Oxide Semiconductor (CMOS) based sensing devices have out-dated their predecessors in performance by demonstrating low power consumption and higher miniaturization capability.

FIGURE A.1: Journal paper: Nanostructured Colour Filters: A Review of Recent Developments.

ANZCOP
8th - 12th December 2019, Melbourne

MASSEY UNIVERSITY
TE KUNENGA KI PŪREHUROA
UNIVERSITY OF NEW ZEALAND

Design of CMOS Compatible Plasmonic Colour Filter for High Selectivity

Ayesha Shaukat and Khalid M. Arif
Department of Mechanical and Electrical Engineering, SF&AT, Massey University, Auckland 0632, New Zealand

Abstract

A theoretical study of highly selective plasmonic color filter is demonstrated. The filter design consist of a thin perforated aluminium film, where nanoholes are arranged in a rectangular lattice. This allows it to obtain different resonant wavelengths at different polarization. A hybrid substrate is implemented as a dielectric layer which suppresses unwanted modes in spectrum, hence allowing high selectivity and minimum spectral cross talk.

Design Features

- The implementation of hybrid substrate (glass (SiO_2) and Silicon nitrate(Si_3N_4)) exhibits high transmission and high selectivity for additive color filtration.
- A thin perforated aluminium layer on the hybrid substrate makes the device CMOS compatible.
- Due to one fold symmetry of rectangular lattice the device exhibits different results in transverse magnetic (TE) and transverse electric (TM) modes. Hence the designed filter demonstrate different color in each mode.

The proposed design can be realized by simple fabrication methods. The schematic of the proposed design is given in Figure 1.

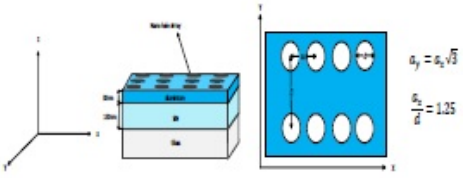

Fig. 1 schematic of the proposed design

The resonance wavelength(λ_{res}) for a rectangular lattice is given as follows

$$\lambda_{res} = \left(\frac{m^2}{{a_x}^2} + \frac{n^2}{{a_y}^2}\right)^{-\frac{1}{2}} \sqrt{\frac{{n_d}^2 + \varepsilon_m}{\varepsilon_m {n_d}^2}}$$

Here a_x and a_y are the periodicity of the lattice along x and y axis respectively, (m, n) are the diffraction grating modes between the metal and dielectric medium, whereas n_d and ε_m are the refractive index and relative permittivity of the dielectric and metal respectively. The diameter of nanohole is given as 'd'.
The wavelength and polarization dependent transmission $T(\Phi,\lambda)$ is given as

$$T_{(\Phi,\lambda)} = T_o(\lambda)cos^2\Phi + T_{90}(\lambda)sin^2\Phi$$

Here λ is the wavelength of light in free space and Φ is the angle of light polarization. T_o and T_{90} are light transmission along TM and TE mode respectively.

Conclusion

An analytical study of highly selective polarization controlled plasmonic color filter is presented here. The results show a distinct resonance peak in TM and TE mode of polarization . Hence, this design can be implemented for filtering two colors by simply changing the direction of polarization of impinging light.

Acknowledgement

We would like to thank Massey University, Department of Mechanical and Electrical Engineering, SF&AT, for providing financial support for this project.

References

Cetin, A. E., Etezadi, D., Galarreta, B. C., Busson, M. P., Eksioglu, Y., & Altug, H. (2015). Plasmonic Nanohole Arrays on a Robust Hybrid Substrate for Highly Sensitive Label-Free Biosensing. ACS Photonics, 2(8), 1167-1174. doi:10.1021/acsphotonics.5b00242
Guo, R., Hakala, T. K., & Törmä, P. (2017). Geometry dependence of surface lattice resonances in plasmonic nanoparticle arrays. *Physical Review B, 95*(15), 155423.

Simulation Region

Fig. 2 shows view of the simulation region in 2D XZ view. A TM polarized plane wave source is perpendicularly injected from the substrate side of the device i.e., along '+z' direction. The direction of polarization is parallel to the plane of incidence, and magnetic field is along the y axis. The wavelength of the plan wave varies from 400 to 700nm (visible regime) . The position of transmission and reflection monitors is also highlighted.

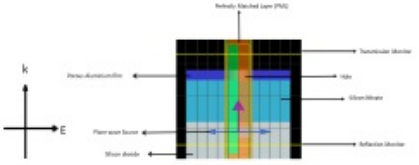

Fig. 2 Simulation region

Simulation Results

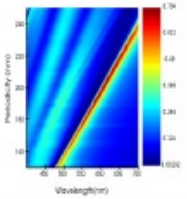

Fig. 3 Transmission Spectra in visible regime in TM mode

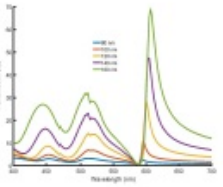

Fig. 4 Transmission Spectra when hole diameter changed from 80 to 160nm

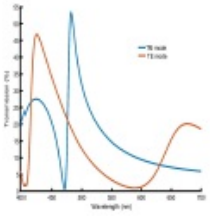

Fig. 5a

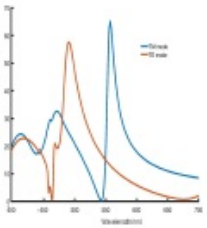

Fig. 5b

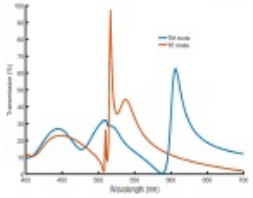

Fig. 5c

Fig. 5 Transmission spectra at a) a_y=150nm, b) 180nm and c) 210nm

Sensor Lab, Department of Mechanical and Electrical Engineering, SF&AT, Massey University, Auckland 0632, New Zealand
Telephone: +64(09) 414 0800 ext. 43580; Email: k.arif@massey.ac.nz

FIGURE A.2: Poster Presentation: Design of CMOS Compatible Plasmonic Colour Filter for High Selectivity.

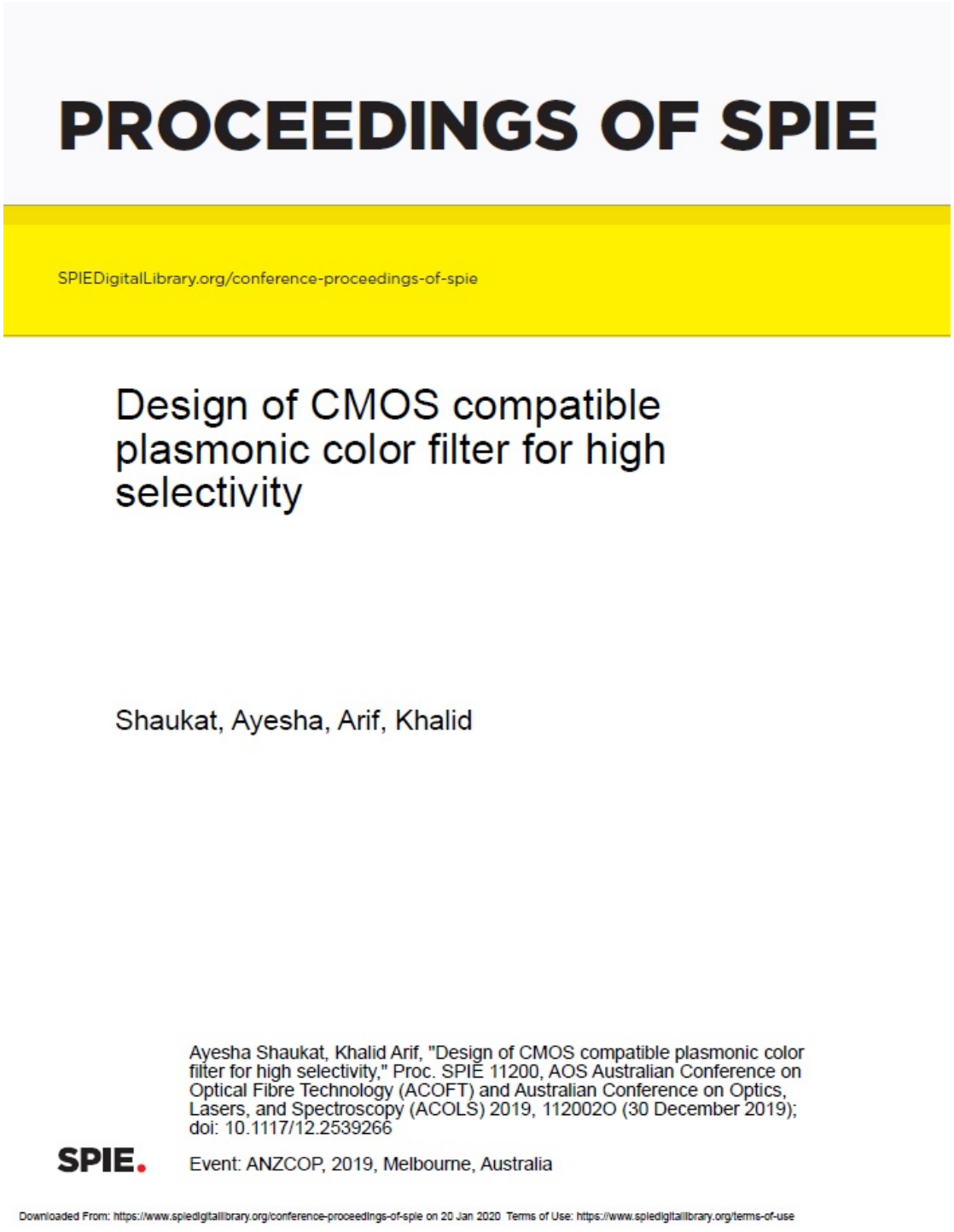

PROCEEDINGS OF SPIE

SPIEDigitalLibrary.org/conference-proceedings-of-spie

Design of CMOS compatible plasmonic color filter for high selectivity

Shaukat, Ayesha, Arif, Khalid

Ayesha Shaukat, Khalid Arif, "Design of CMOS compatible plasmonic color filter for high selectivity," Proc. SPIE 11200, AOS Australian Conference on Optical Fibre Technology (ACOFT) and Australian Conference on Optics, Lasers, and Spectroscopy (ACOLS) 2019, 112002O (30 December 2019); doi: 10.1117/12.2539266

SPIE.

Event: ANZCOP, 2019, Melbourne, Australia

Downloaded From: https://www.spiedigitallibrary.org/conference-proceedings-of-spie on 20 Jan 2020 Terms of Use: https://www.spiedigitallibrary.org/terms-of-use

FIGURE A.3: Conference Paper: Design of CMOS Compatible Plasmonic Colour Filter for High Selectivity.

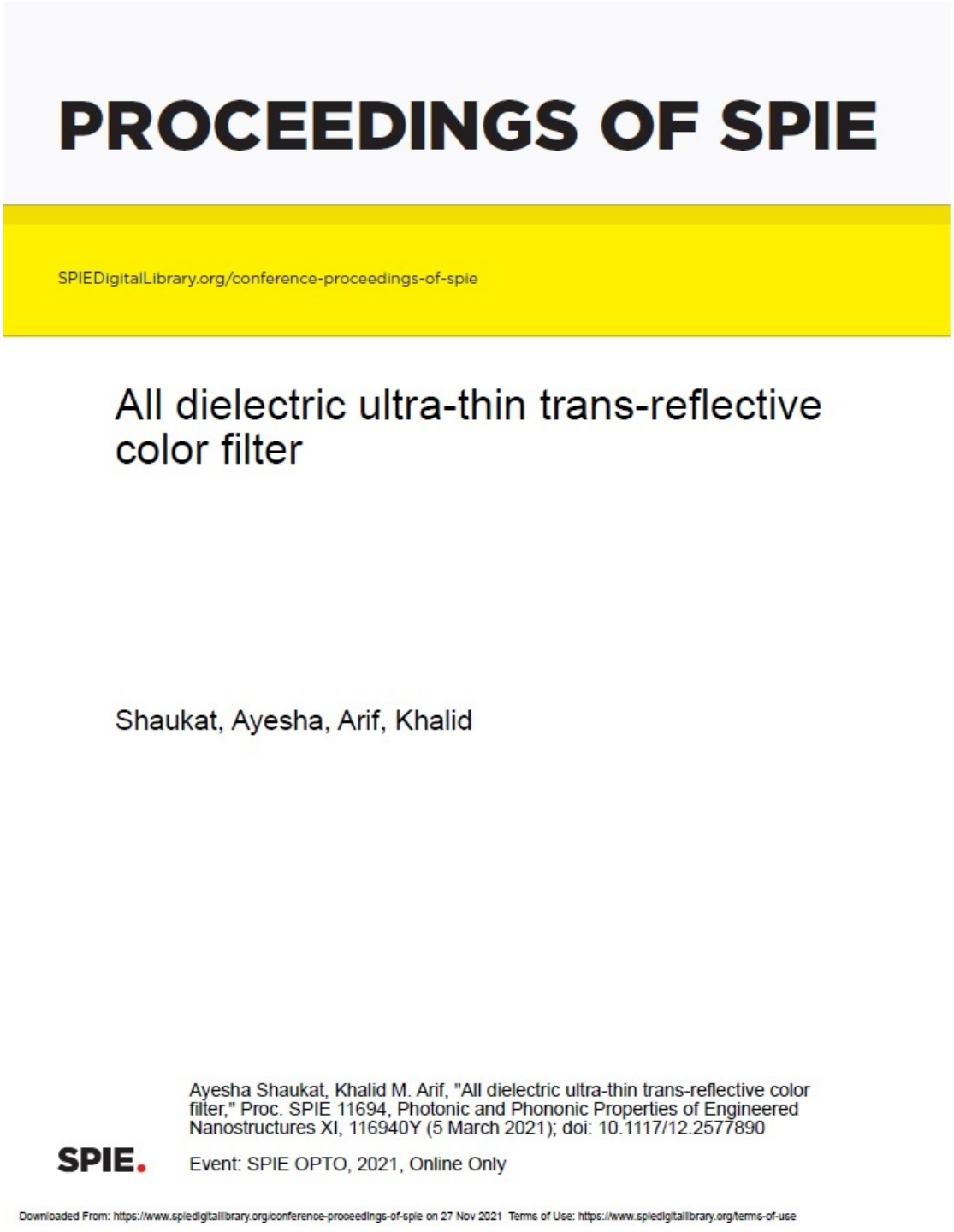

PROCEEDINGS OF SPIE

SPIEDigitalLibrary.org/conference-proceedings-of-spie

All dielectric ultra-thin trans-reflective color filter

Shaukat, Ayesha, Arif, Khalid

Ayesha Shaukat, Khalid M. Arif, "All dielectric ultra-thin trans-reflective color filter," Proc. SPIE 11694, Photonic and Phononic Properties of Engineered Nanostructures XI, 116940Y (5 March 2021); doi: 10.1117/12.2577890

SPIE.

Event: SPIE OPTO, 2021, Online Only

Downloaded From: https://www.spiedigitallibrary.org/conference-proceedings-of-spie on 27 Nov 2021 Terms of Use: https://www.spiedigitallibrary.org/terms-of-use

FIGURE A.4: All dielectric ultra-thin trans-reflective colour filter.

Appendix B

FDTD Background

Maxwell equations by James Clerk Maxwell [226], which govern all classical electromagnetic phenomenon which in its differential form is given as :

$$\frac{\partial \bar{\mathcal{B}}}{\partial t} = -\nabla \times \bar{\mathcal{E}}, \qquad \text{Faraday 's Law} \tag{B.1}$$

$$\nabla \cdot \bar{\mathcal{B}} = 0, \qquad \text{Guass 's Law} \tag{B.2}$$

$$\frac{\partial \bar{\mathcal{D}}}{\partial t} + \bar{\mathcal{J}} = \nabla \times \bar{\mathcal{H}}, \qquad \text{Ampere 's Law} \tag{B.3}$$

$$\nabla \cdot \bar{\mathcal{D}} = \tilde{\rho}, \qquad \text{Columb's Law} \tag{B.4}$$

Here $\mathcal{E}$ $\mathcal{B}$, $\mathcal{D}$,$\mathcal{H}$ and $\bar{\rho}$ are electric field intensity, magnetic field intensity, electric flux density, magnetic flux density and electrical current density respectively. And each of the fields is a function of time and space i.e., $\bar{\mathcal{E}} = \bar{\mathcal{E}}(x, y, z, t)$ It is to be notified here that the conservation of charge in differential form can be derived with the help of Equation 3.3 and 3.4, and is given as

$$\nabla \cdot \bar{\mathcal{J}} = -\frac{\partial \tilde{\rho}}{\partial t}, \tag{B.5}$$

Likewise, Equation 3.2 can be derived by using Equation 3.3 and 3.5.Hence, it indicates that Maxwell 's equations are not entirely independent.

However, the relation of electric field intensity to electric flux density D, and magnetic field intensity to magnetic field intensity is given as

$$\bar{\mathcal{D}} = \tilde{\epsilon}\bar{\mathcal{E}}, \tag{B.6}$$

$$\bar{\mathcal{B}} = \tilde{\mu}\bar{\mathcal{H}}, \tag{B.7}$$

Here $\tilde{\epsilon}$ and $\tilde{\mu}$ are electric and magnetic permeability of the material. In case of inhomogeneous, anisotropic and/or linear, dispersive materials the constitutive relations valid at each pont at all time and are expressed as:

$$\mathcal{D}(\bar{\mathbf{r}}, t) = \tilde{\epsilon}(\mathbf{r}, t)\bar{\mathcal{E}}(\mathbf{r}, t), \tag{B.8}$$

$$\mathcal{B}(\bar{\mathbf{r}}, t) = \tilde{\mu}(\mathbf{r}, t)\bar{\mathcal{H}}(\mathbf{r}, t), \tag{B.9}$$

$$\mathcal{J}(\bar{\mathbf{r}}, t) = \tilde{\sigma}(\mathbf{r}, t)\tilde{\epsilon}(\mathbf{r}, t), \tag{B.10}$$

For accurate modelling of wave interactions with scattering object, in FDTD methodology the enforcement of boundary condition is of considerable importance. It has been recommended that for the interface between two media(region 1 and 2) the following boundary conditions must hold:

$$\begin{aligned} \mathcal{E}_{1t} = \mathcal{E}_{2t} \qquad & \mathcal{D}_{1n} - \mathcal{D}_{2n} = \rho_s, \\ \mathcal{B}_{1n} = \mathcal{B}_{2n} \qquad & \mathcal{H}_{1t} - \mathcal{H}_{2t} = \bar{\mathcal{J}}_s, \\ \bar{\mathcal{J}}_{1n} - \bar{\mathcal{J}}_{1n} = -\frac{\delta\rho_s}{\delta t}, & \end{aligned} \tag{B.11}$$

where 'n' and 't' refer to the normal and tangential components of each fields.
The Maxwell equations further leads to the equation of propagating wave in a simple medium given as:

$$\Delta^2\bar{\mathcal{E}} - \mu\epsilon\frac{\delta^2\mathcal{E}}{\delta t^2} = 0, \tag{B.12}$$

However the phase velocity with $\omega = 2\pi f$ is the wave angular velocity and wavenumber $k = \frac{2\pi}{\lambda}$ is given as

$$v_p = \frac{\omega}{k}, \tag{B.13}$$

Likewise the velocity of energy propogation along the electromagnetic wave through the medium is given as

$$v_g = \frac{\delta\omega}{\delta k}, \tag{B.14}$$

In a simple medium in which the wave number is not a function of frequency $v_g = v_p$.

B.1 FDTD Algorithm

FDTD is largely the discretization of Maxwell 's equation in time domain using the central differences techniques. In 1966, Kane Shee-Gong Yee, was the one who introduced Yee algorithm for microwave applications. Later on, it waas utilized for optical structures.

The Cartesian discretization of the electric and magnetic field based on Yee 's algorithm is given as:

$$E_x|_{i,j,k}^{n+1} = C_a(i,j,k)E_x|_n^{i,j,k} + C_b(i,j,k)\Bigg[\frac{H_z|_{i,j,k}^{n+0.5} - H_z|_{i,j-1,k}^{n+0.5}}{\Delta y} - \frac{H_y|_{i,j,k}^{n+0.5} - H_y|_{i,j,k-1}^{n+0.5}}{\Delta z} - \bar{\mathcal{J}}_{ex}|_{i,j,k}^{n+0.5}\Bigg], \tag{B.15}$$

$$E_y|_{i,j,k}^{n+1} = C_a(i,j,k)E_y|_n^{i,j,k} + C_b(i,j,k)\Bigg[\frac{H_z|_{i,j,k}^{n+0.5} - H_z|_{i,j,k-1}^{n+0.5}}{\Delta y} - \frac{H_z|_{i,j,k}^{n+0.5} - H_z|_{i-1,j,k}^{n+0.5}}{\Delta x} - \bar{\mathcal{J}}_{ey}|_{i,j,k}^{n+0.5}\Bigg], \tag{B.16}$$

$$E_z|_{i,j,k}^{n+1} = C_a(i,j,k)E_z|_n^{i,j,k} + C_b(i,j,k)\Bigg[\frac{H_y|_{i-1,j,k-1}^{n+0.5} - H_y|_{i,j,k}^{n+0.5}}{\Delta x} - \frac{H_x|_{i,j,k}^{n+0.5} - H_x|_{i,j-1,k}^{n+0.5}}{\Delta y} - \bar{\mathcal{J}}_{ez}|_{i,j,k}^{n+0.5}\Bigg], \tag{B.17}$$

$$C_a(i,j,k) = \frac{1 - \frac{\sigma(i,j,k)\Delta t}{2\epsilon(i,j,k)}}{1 + \frac{\sigma(i,j,k)\Delta t}{2\epsilon(i,j,k)}}, \tag{B.18}$$

$$C_b(i,j,k) = \frac{\frac{\Delta t}{\epsilon(i,j,k)}}{1 + \frac{\sigma(i,j,k)\Delta t}{2\epsilon(i,j,k)}}, \tag{B.19}$$

$$H_x|_{i,j,k}^{n+0.5} = D_a(i,j,k)H_x|_{n-0.5}^{i,j,k} + D_b(i,j,k)\Bigg[\frac{E_z|_{i-1,j,k}^{n} - H_z|_{i,j+1,k}^{n}}{\Delta y} - \frac{E_y|_{i,j,k}^{n} - E_y|_{i,j,k+1}^{n}}{\Delta} z\Bigg], \tag{B.20}$$

$$H_y|_{i,j,k}^{n+0.5} = D_a(i,j,k)H_x|_{n-0.5}^{i,j,k} + D_b(i,j,k)\left[\frac{E_x|_{i,j,k}^{n} - E_x|_{i,j,k+1}^{n}}{\Delta z} - \frac{E_z|_{i,j,k}^{n} - E_z|_{i+1,j,k}^{n}}{\Delta x}\right], \tag{B.21}$$

$$H_z|_{i,j,k}^{n+0.5} = D_a(i,j,k)H_x|_{n-0.5}^{i,j,k} + D_b(i,j,k)\left[\frac{E_y|_{i,j,k}^{n} - E_y|_{i,j+1,k}^{n}}{\Delta x} - \frac{E_x|_{i,j=1,k}^{n} - E_x|_{i,j,k}^{n}}{\Delta} y\right], \tag{B.22}$$

where

$$D_a(i,j,k) = \frac{1 - \frac{\sigma_m(i,j,k)\Delta t}{2\mu(i,j,k)}}{1 + \frac{\sigma_m(i,j,k)\Delta t}{2\mu(i,j,k)}}, \tag{B.23}$$

$$D_b(i,j,k) = \frac{\frac{\Delta t}{\mu(i,j,k)}}{1 + \frac{\sigma_m(i,j,k)\Delta t}{2\mu(i,j,k)}}, \tag{B.24}$$

Figure 4.1, (Chapter 4) depicts the Yee cell, which adopts leapfrog methodology by having the electric and magnetic field components located at alternative half space. However, for stability, Courant relationship is implemented to impose a constraint on the time step is given as

$$\Delta t \leq \frac{1}{C\sqrt{\frac{1}{(\Delta x)^2} + \frac{1}{(\Delta y)^2} + \frac{1}{(\Delta z)^2}}}, \tag{B.25}$$

Here C is the speed of light i.e $3 \times 10^8 msec^{-}1$. It is evident from the stability equation B.25 that the time step of the algorithm is directly proportional to the spatial grid size. Hence the algorithms with fine details such as nanophotonic devices , requires longer time to converge.

Appendix C

Data sheets

C.1 Stepper Motor

C.2 Oxford PlasmaLab 100 PECVD

SANYO DENKI

SANMOTION

New Product Information

2-phase Stepping Motor 42 mm square by 11.6 thin



SANYO DENKI *EUROPE SA.* is pleased to introduce its new 2-phase 1.8° per step very thin stepping motor serie «**SANMOTION F2 - SS24**». This serie has achieved industry-leading thinness of 11.6 mm among 42 mm square size motors.

Specifications

Basic angle : 1.8°
Winding : bipolar (unipolar models available upon request) with lead wire output
Rated current : 1A/phase

Model No.		Size		Holding torque at 2-phase energization	Mass
Single shaft	*Double shaft*	*Flange size*	*Motor length*		
SS2421-5041	SS2421-5011	42 mm	11.6 mm	0.083 Nm min.	0.07 kg
SS2422-5041	SS2422-5011	42 mm	18.6 mm	0.186 Nm min.	0.14 kg
SS2423-5041	SS2423-5011	42 mm	25.6 mm	0.24 Nm min.	0.2 kg

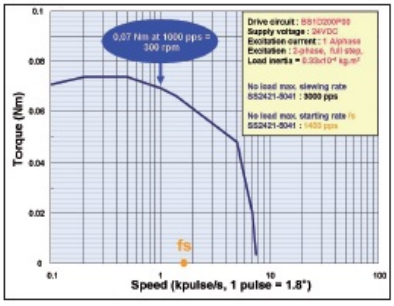

Figure 1 : SS2421 Torque - Speed Curve

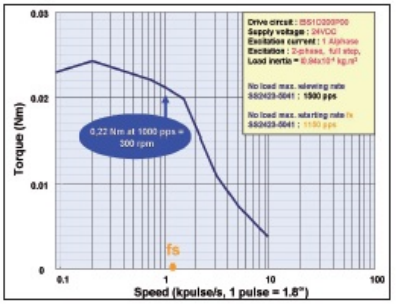

Figure 2 : SS2423 Torque - Speed Curve

Main features

Industry Leading Thinness 11.6 mm with high torque
The first motor of this serie is the higher torque hybrid stepping motor of the market with such small thickness of 11,6 mm and a weight of 0,07 kg. Easily installed into very compact devices, it contributes to downsizing of equipments and offer new design possibilities for device manufacturers.

Target Applications

Small surveillance camera, chip mounter and semiconductor manufacturing device, general-purpose mounter, medical inspection device, etc.

SANMOTION F2

Stepping motor Specifications



2-phase stepping motor

42mm sq: 1.65inch sq.

SS2421

1.8 / step Bipolar winding

Unipolar winding Lead wire type

Model		Holding torque at 2-phase energization	Rated current	Wiring resistance	Winding inductance	Rotor inertia	Mass Weight
Single shaft	Double shafts	[N m oz in MIN.]	A/phase	/phase	mH/phase	[10 kg m oz in]	[kg lbs]
SS2421-5041	**-5011**	0.083 11.75	1	3.5	1.2	0.015 0.082	0.07 0.15
SS2422-5041	**-5011**	0.186 26.33	1	5.4	2.9	0.028 0.153	0.14 0.31
SS2423-5041	**-5011**	0.240 33.98	1	7.3	5	0.038 0.208	0.20 0.44

Pulse rate-torque characteristics

SS2421-50

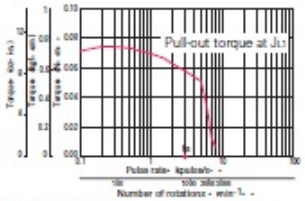

Constant current circuit
Source voltage : DC24V operating current : 1A/phase,
2-phase energization full-step
J_{L1} = 0.33x10^{-4}kg m^2 4.80 oz in^2 Inertia of rubber coupling is included
J_{L2} = 0.94x10^{-4}kg m^2 5.14 oz in^2 Inertia of rubber coupling is included
fs: No load maximum starting pulse rate

SS2422-50

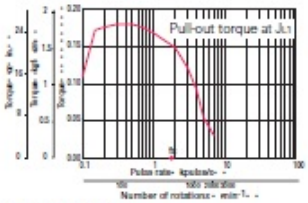

Constant current circuit
Source voltage : DC24V operating current : 1A/phase,
2-phase energization full-step
J_{L1} = 0.33x10^{-4}kg m^2 4.80 oz in^2 Inertia of rubber coupling is included
J_{L2} = 0.94x10^{-4}kg m^2 5.14 oz in^2 Inertia of rubber coupling is included
fs: No load maximum starting pulse rate

SS2423-50

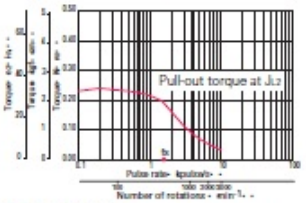

Constant current circuit
Source voltage : DC24V operating current : 1A/phase,
2-phase energization full-step
J_{L1} = 0.33x10^{-4}kg m^2 4.80 oz in^2 Inertia of rubber coupling is included
J_{L2} = 0.94x10^{-4}kg m^2 5.14 oz in^2 Inertia of rubber coupling is included
fs: No load maximum starting pulse rate

The data are measured under the drive condition of our company. The drive torque may vary depending on the accuracy of customer-side equipment.

SANMOTION F2

Dimensions

Motors· Unit: mm· inch····

··28mm ··1.10inch·· ·

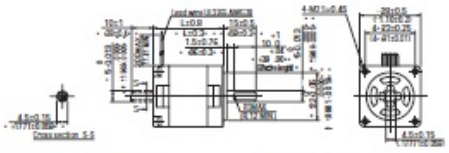

Connector type Lead wire type

	Set part number	Motor model number	Motor length mm· inch·· ·	Cable type
Unipolar	DU14S281··	SH2281-51··	32 1.26··	Lead wire
	DU14S281··	SH2281-52··	32 1.26··	Lead wire
	DU14S285··	SH2285-51··	51.5 2.03··	Lead wire
	DU14S285··	SH2285-52··	51.5 2.03··	Lead wire
Bipolar	DB14S281··	SH2281-56··	32 1.26··	Lead wire
	DB14S281··	SH2281-57··	32 1.26··	Lead wire
	DB14S285··	SH2285-56··	51.9 2.03··	Lead wire
	DB14S285··	SH2285-57··	51.5 2.03··	Lead wire

··35mm ··1.65inch·· ·

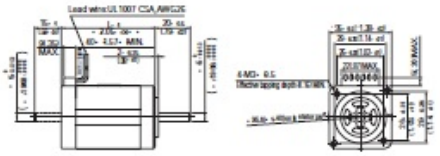

Lead wire type

	Set part number	Motor model number	Motor length mm· inch·· ·	Cable type
Unipolar	··	SH3533-12U··	33 1.25··	Lead wire
	··	SH3537-12U··	33 1.54··	Lead wire
	··	SH3552-12U··	52 1.89··	Lead wire

··42mm ··1.65inch·· ·

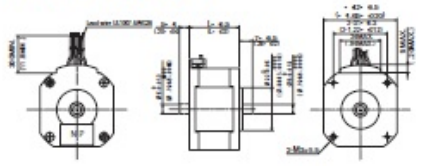

Lead wire type

	Set part number	Motor model number	Motor length mm· inch·· ·	Cable type
Bipolar	··	SS2421-50··	11.6 0.457··	Lead wire
	··	SS2422-50··	18.6 0.732··	Lead wire
	··	SS2423-50··	25.8 1.008··	Lead wire

··42mm ··1.65inch·· ·

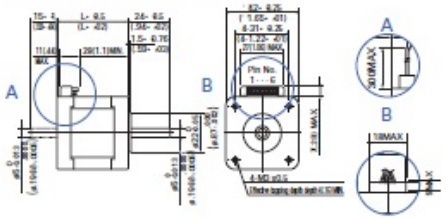

Connector type Lead wire type

	Set part number	Motor model number	Motor length mm· inch·· ·	Cable type
Unipolar	DU15H521··	103H5205-04··	33 1.25··	Connector
	DU15H522··	103H5208-04··	39 1.54··	Connector
	DU15H524··	103H5210-04··	49 1.89··	Connector
	··	103H5209-04··	41 1.61··	Connector

··42mm ··1.65inch·· ·



Connector type Lead wire type

	Set part number	Motor model number	Motor length mm· inch·· ·	Cable type
Bipolar	DB14H521··	103H5205-52··	33 1.25··	Lead wire
	DB14H522··	103H5208-52··	39 1.54··	Lead wire
	DB14H524··	103H5210-52··	49 1.89··	Lead wire
	··	103H5205-50··	33 1.25··	Lead wire
	··	103H5205-51··	33 1.25··	Lead wire
	··	103H5208-50··	39 1.54··	Lead wire
	··	103H5208-51··	39 1.54··	Lead wire
	··	103H5209-50··	41 1.61··	Lead wire
	··	103H5209-51··	41 1.61··	Lead wire
	··	103H5209-52··	41 1.61··	Lead wire
	··	103H5210-50··	49 1.89··	Lead wire
	··	103H5210-51··	49 1.89··	Lead wire

··42mm ··1.65inch·· ·

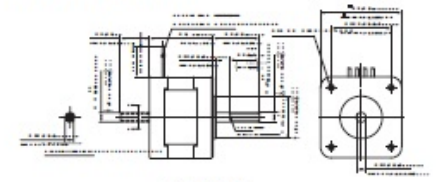

Lead wire type

	Set part number	Motor model number	Motor length mm· inch·· ·	Cable type
Unipolar	DU15S141··	SH1421-04··	33 1.25··	Lead wire
	DU15S142··	SH1422-04··	39 1.54··	Lead wire
	DU15S144··	SH1424-04··	49 1.89··	Lead wire
Bipolar	DB16H141··	SH1421-52··	33 1.25··	Lead wire
	DB16H142··	SH1422-52··	39 1.54··	Lead wire
	DB16H144··	SH1424-52··	49 1.89··	Lead wire

·· Motor shaft specification code

Motor shaft spec	Set type code	Motor type code
Single shaft	S	7
Double shafts	D	3

·· Motor shaft specification code

Motor shaft spec	Set type code	Motor type code
Single shaft	S	4
Double shafts	D	1

Deposition Process Modules 100

Plasma Enhanced Chemical Vapour Deposition (PECVD)

The PECVD process modules are specifically designed to produce excellent uniformity and high rate films, with control of film properties such as refractive index, stress, electrical characteristics and wet chemical etch rate.

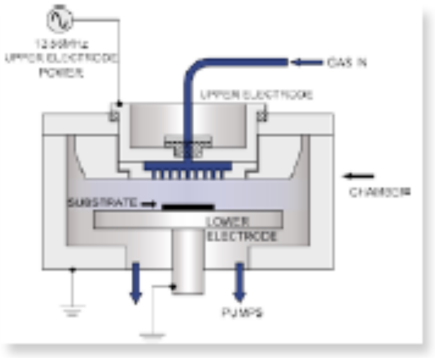

PECVD process chamber

PECVD features:

- In-situ chamber cleaning and end-pointing
- Electrically grounded lower electrodes available:
  - 400°C electrode - typical processes are SiO_2, Si_3N_4 and SiON, amorphous Si and SiC
  - 1200°C electrode - In addition to processes above, the electrode enables Si Nanowires, high temperature PECVD films with a wide variety of chemistries
- An optimised upper electrode design , operating in high pressure, high RF power, high flow regimes, enables SiO_2, Si_3N_4 and SiON, amorphous Si deposition at increased rates whilst maintaining excellent film properties and uniformity across the wafer
- RF powered showerhead with optimised gas delivery, provides uniform plasma processing with LF/RF switching allowing precise control of film stress

Options:

- Flexible liquid source delivery module with capacity for up to 3 precursors delivered by:
  - Vapour pressure regulated by heated vapour mass flow controller
  - or Bubbled using argon
- The module is capable of delivering a wide range of precursors including:
  - TEOS, TMA, TMB, TMP, ...

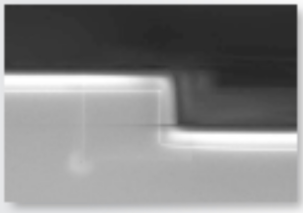

SiO_2 deposited using TEOS and O_2 plasma gives excellent conformality



FIGURE C.1: Oxford PlasmaLab 100 PECVD

Appendix D

DRC Froms

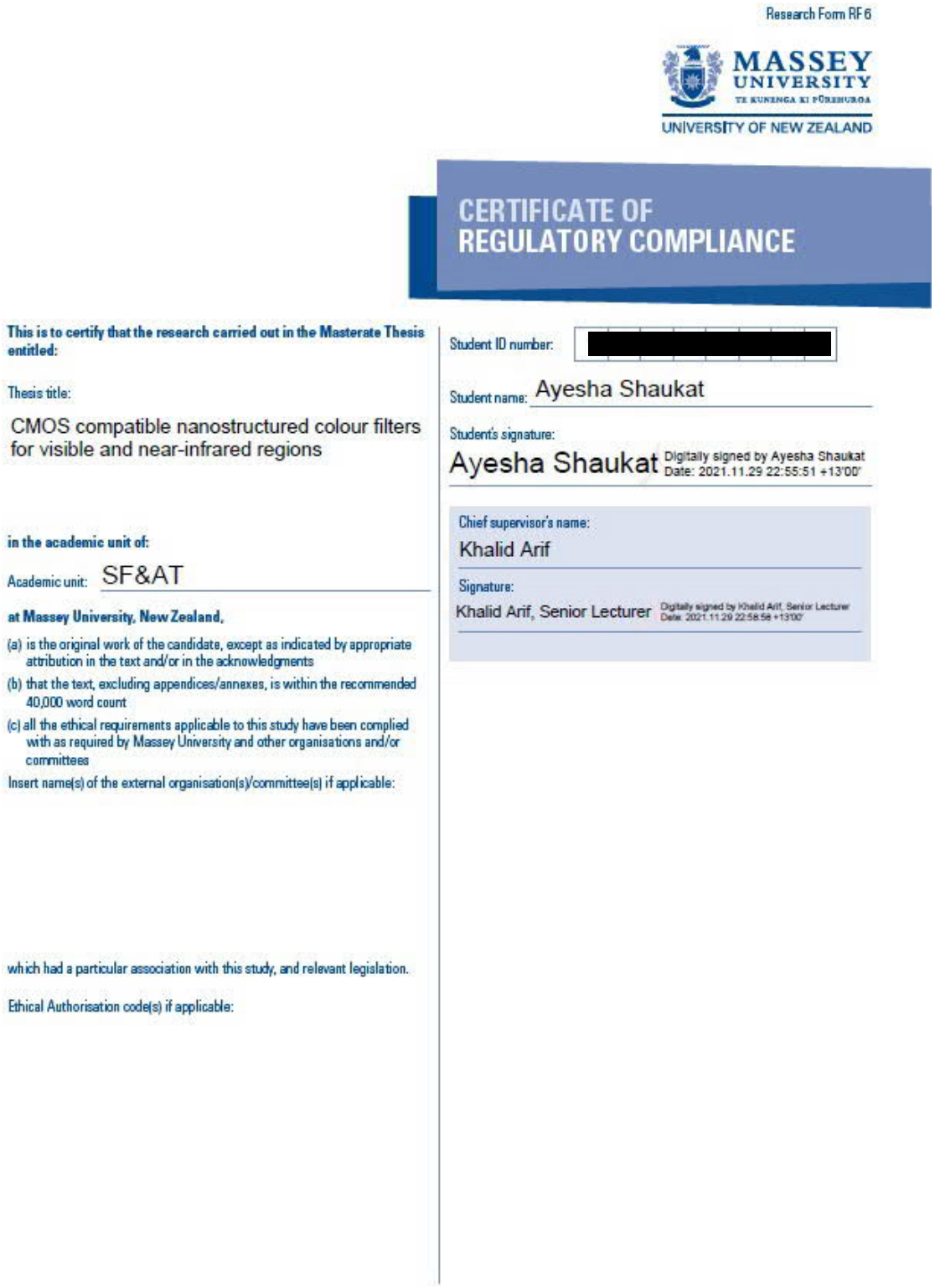

Research Form RF 6

MASSEY UNIVERSITY
TE KUNENGA KI PŪREHUROA
UNIVERSITY OF NEW ZEALAND

CERTIFICATE OF REGULATORY COMPLIANCE

This is to certify that the research carried out in the Masterate Thesis entitled:

Thesis title:

CMOS compatible nanostructured colour filters for visible and near-infrared regions

Student ID number: [redacted]

Student name: Ayesha Shaukat

Student's signature:

Ayesha Shaukat Digitally signed by Ayesha Shaukat Date: 2021.11.29 22:55:51 +13'00'

Chief supervisor's name:

Khalid Arif

Signature:

Khalid Arif, Senior Lecturer Digitally signed by Khalid Arif, Senior Lecturer Date: 2021.11.29 22:58:56 +13'00'

in the academic unit of:

Academic unit: SF&AT

at Massey University, New Zealand,

(a) is the original work of the candidate, except as indicated by appropriate attribution in the text and/or in the acknowledgments

(b) that the text, excluding appendices/annexes, is within the recommended 40,000 word count

(c) all the ethical requirements applicable to this study have been complied with as required by Massey University and other organisations and/or committees

Insert name(s) of the external organisation(s)/committee(s) if applicable:

which had a particular association with this study, and relevant legislation.

Ethical Authorisation code(s) if applicable:

FIGURE D.1: RF06 Form

DRC 16

MASSEY UNIVERSITY
TE KUNENGA KI PŪREHUROA
UNIVERSITY OF NEW ZEALAND

GRADUATE RESEARCH SCHOOL

STATEMENT OF CONTRIBUTION
DOCTORATE WITH PUBLICATIONS/MANUSCRIPTS

We, the candidate and the candidate's Primary Supervisor, certify that all co-authors have consented to their work being included in the thesis and they have accepted the candidate's contribution as indicated below in the *Statement of Originality*.

Name of candidate:	Ayesha Shaukat
Name/title of Primary Supervisor:	Dr. Khalid Arif
In which chapter is the manuscript /published work:	Chapter 4,5,6

Please select one of the following three options:

○ The manuscript/published work is published or in press

- Please provide the full reference of the Research Output:

Shaukat, A., & Arif, KM. (2021). All dielectric ultra-thin trans-reflective color filter. Proceedings of SPIE - The International Society for Optical Engineering. Vol. 11694

○ The manuscript is currently under review for publication – please indicate:

- The name of the journal:

- The percentage of the manuscript/published work that was contributed by the candidate:

- Describe the contribution that the candidate has made to the manuscript/published work:

◉ It is intended that the manuscript will be published, but it has not yet been submitted to a journal

Candidate's Signature:	Ayesha Shaukat Digitally signed by Ayesha Shaukat Date: 2021.11.28 10:47:03 +13'00'
Date:	28-Nov-2021
Primary Supervisor's Signature:	Khalid Arif, Senior Lecturer Digitally signed by Khalid Arif, Senior Lecturer Date: 2021.11.28 12:14:29 +13'00'
Date:	28-Nov-2021

This form should appear at the end of each thesis chapter/section/appendix submitted as a manuscript/ publication or collected as an appendix at the end of the thesis.

GRS Version 5 – 13 December 2019
DRC 19/09/10

FIGURE D.2: DRC 16 Form1

DRC 16

MASSEY UNIVERSITY
TE KUNENGA KI PŪREHUROA
UNIVERSITY OF NEW ZEALAND

GRADUATE RESEARCH SCHOOL

STATEMENT OF CONTRIBUTION
DOCTORATE WITH PUBLICATIONS/MANUSCRIPTS

We, the candidate and the candidate's Primary Supervisor, certify that all co-authors have consented to their work being included in the thesis and they have accepted the candidate's contribution as indicated below in the *Statement of Originality*.

Name of candidate:	Ayesha Shaukat
Name/title of Primary Supervisor:	Dr. Khalid Arif
In which chapter is the manuscript /published work:	Chapter 4,5,6

Please select one of the following three options:

◯ **The manuscript/published work is published or in press**

- **Please provide the full reference of the Research Output:**

Shaukat, A., & Arif, K. (2019). Design of CMOS compatible plasmonic color filter for high selectivity. Proceedings of SPIE - The International Society for Optical Engineering. Vol. 11200

◯ **The manuscript is currently under review for publication – please indicate:**

- **The name of the journal:**

- **The percentage of the manuscript/published work that was contributed by the candidate:**

- **Describe the contribution that the candidate has made to the manuscript/published work:**

◉ **It is intended that the manuscript will be published, but it has not yet been submitted to a journal**

Candidate's Signature:	Ayesha Shaukat Digitally signed by Ayesha Shaukat Date: 2021.11.28 10:47:03 +13'00'
Date:	28-Nov-2021
Primary Supervisor's Signature:	Khalid Arif, Senior Lecturer Digitally signed by Khalid Arif, Senior Lecturer Date: 2021.11.28 12:14:48 +13'00'
Date:	28-Nov-2021

This form should appear at the end of each thesis chapter/section/appendix submitted as a manuscript/ publication or collected as an appendix at the end of the thesis.

GRS Version 5 – 13 December 2019
DRC 19/09/10

FIGURE D.3: DRC 16 Form2

DRC 16

MASSEY UNIVERSITY
TE KUNENGA KI PŪREHUROA
UNIVERSITY OF NEW ZEALAND

GRADUATE RESEARCH SCHOOL

STATEMENT OF CONTRIBUTION
DOCTORATE WITH PUBLICATIONS/MANUSCRIPTS

We, the candidate and the candidate's Primary Supervisor, certify that all co-authors have consented to their work being included in the thesis and they have accepted the candidate's contribution as indicated below in the *Statement of Originality*.

Name of candidate:	Ayesha Shaukat
Name/title of Primary Supervisor:	Dr. Khalid Arif
In which chapter is the manuscript /published work:	Chapter 03

Please select one of the following three options:

(●) **The manuscript/published work is published or in press**

- **Please provide the full reference of the Research Output:**

A.Shaukat, F.Noble, K.M Arif, "Nanostructured Color Filters: A Review of Recent Developments", Nanomaterials 10,1-36 (2020)

( ) **The manuscript is currently under review for publication – please indicate:**

- **The name of the journal:**

- **The percentage of the manuscript/published work that was contributed by the candidate:**

- **Describe the contribution that the candidate has made to the manuscript/published work:**

Conceptualization, methodology and investigation.
Visualization and original draft preparation

( ) **It is intended that the manuscript will be published, but it has not yet been submitted to a journal**

Candidate's Signature:	Ayesha Shaukat Digitally signed by Ayesha Shaukat Date: 2021.11.28 10:42:12 +13'00'
Date:	28-Nov-2021
Primary Supervisor's Signature:	Khalid Arif, Senior Lecturer Digitally signed by Khalid Arif, Senior Lecturer Date: 2021.11.28 12:09:00 +13'00'
Date:	28-Nov-2021

This form should appear at the end of each thesis chapter/section/appendix submitted as a manuscript/ publication or collected as an appendix at the end of the thesis.

GRS Version 5 – 13 December 2019
DRC 19/09/10

FIGURE D.4: DRC 16 Form3

DRC 16

MASSEY UNIVERSITY
TE KUNENGA KI PŪREHUROA
UNIVERSITY OF NEW ZEALAND

GRADUATE RESEARCH SCHOOL

STATEMENT OF CONTRIBUTION
DOCTORATE WITH PUBLICATIONS/MANUSCRIPTS

We, the candidate and the candidate's Primary Supervisor, certify that all co-authors have consented to their work being included in the thesis and they have accepted the candidate's contribution as indicated below in the *Statement of Originality*.

Name of candidate:	Ayesha Shaukat
Name/title of Primary Supervisor:	Dr. Khalid Arif
In which chapter is the manuscript /published work:	Chapter 4 and 5

Please select one of the following three options:

○ The manuscript/published work is published or in press

- Please provide the full reference of the Research Output:

○ The manuscript is currently under review for publication – please indicate:

- The name of the journal:
- The percentage of the manuscript/published work that was contributed by the candidate:
- Describe the contribution that the candidate has made to the manuscript/published work:

◉ It is intended that the manuscript will be published, but it has not yet been submitted to a journal

Candidate's Signature:	Ayesha Shaukat Digitally signed by Ayesha Shaukat Date: 2021.11.28 10:45:47 +13'00'
Date:	28-Nov-2021
Primary Supervisor's Signature:	Khalid Arif, Senior Lecturer Digitally signed by Khalid Arif, Senior Lecturer Date: 2021.11.28 12:10:22 +13'00'
Date:	28-Nov-2021

This form should appear at the end of each thesis chapter/section/appendix submitted as a manuscript/ publication or collected as an appendix at the end of the thesis.

GRS Version 5 – 13 December 2019
DRC 19/09/10

FIGURE D.5: DRC 16 Form4

DRC 16

MASSEY UNIVERSITY
TE KUNENGA KI PŪREHUROA
UNIVERSITY OF NEW ZEALAND

GRADUATE RESEARCH SCHOOL

STATEMENT OF CONTRIBUTION
DOCTORATE WITH PUBLICATIONS/MANUSCRIPTS

We, the candidate and the candidate's Primary Supervisor, certify that all co-authors have consented to their work being included in the thesis and they have accepted the candidate's contribution as indicated below in the *Statement of Originality*.

Name of candidate:	Ayesha Shaukat
Name/title of Primary Supervisor:	Dr. Khalid Arif
In which chapter is the manuscript /published work:	Chapter 06

Please select one of the following three options:

○ The manuscript/published work is published or in press

- Please provide the full reference of the Research Output:

○ The manuscript is currently under review for publication – please indicate:

- The name of the journal:
- The percentage of the manuscript/published work that was contributed by the candidate:
- Describe the contribution that the candidate has made to the manuscript/published work:

◉ It is intended that the manuscript will be published, but it has not yet been submitted to a journal

Candidate's Signature:	Ayesha Shaukat Digitally signed by Ayesha Shaukat Date: 2021.11.28 10:47:03 +13'00'
Date:	28-Nov-2021
Primary Supervisor's Signature:	Khalid Arif, Senior Lecturer Digitally signed by Khalid Arif, Senior Lecturer Date: 2021.11.28 12:11:19 +13'00'
Date:	28-Nov-2021

This form should appear at the end of each thesis chapter/section/appendix submitted as a manuscript/ publication or collected as an appendix at the end of the thesis.

GRS Version 5 – 13 December 2019
DRC 19/09/10

FIGURE D.6: DRC 16 Form5